Modeling Multiple Scattering and Absorption for a Differential Absorption LIDAR System

by

Daniel D. Blevins

B.S., Wright State University, 1994
M.S., University of Michigan, 1999

A dissertation submitted in partial fulfillment of the
requirements for the degree of Doctor of Philosophy
in the Chester F. Carlson Center for Imaging Science

College of Science

Rochester Institute of Technology

2005

Signature of the Author _____

Daniel D. Blevins

Accepted by _____

Coordinator, Ph.D. Degree Program

Report Documentation Page

Form Approved
OMB No. 0704-0188

Public reporting burden for the collection of information is estimated to average 1 hour per response, including the time for reviewing instructions, searching existing data sources, gathering and maintaining the data needed, and completing and reviewing the collection of information. Send comments regarding this burden estimate or any other aspect of this collection of information, including suggestions for reducing this burden, to Washington Headquarters Services, Directorate for Information Operations and Reports, 1215 Jefferson Davis Highway, Suite 1204, Arlington VA 22202-4302. Respondents should be aware that notwithstanding any other provision of law, no person shall be subject to a penalty for failing to comply with a collection of information if it does not display a currently valid OMB control number.

1. REPORT DATE	2. REPORT TYPE	3. DATES COVERED
30 MAR 2006	**N/A**	**-**

4. TITLE AND SUBTITLE	5a. CONTRACT NUMBER
Modeling Multiple Scattering and Absorption for a Differential Absorption LIDAR System	5b. GRANT NUMBER
	5c. PROGRAM ELEMENT NUMBER
6. AUTHOR(S)	5d. PROJECT NUMBER
	5e. TASK NUMBER
	5f. WORK UNIT NUMBER
7. PERFORMING ORGANIZATION NAME(S) AND ADDRESS(ES) **Rochester Institute of Technology**	8. PERFORMING ORGANIZATION REPORT NUMBER
9. SPONSORING/MONITORING AGENCY NAME(S) AND ADDRESS(ES)	10. SPONSOR/MONITOR'S ACRONYM(S)
	11. SPONSOR/MONITOR'S REPORT NUMBER(S)

12. DISTRIBUTION/AVAILABILITY STATEMENT
Approved for public release, distribution unlimited

13. SUPPLEMENTARY NOTES
The original document contains color images.

14. ABSTRACT

15. SUBJECT TERMS

16. SECURITY CLASSIFICATION OF:			17. LIMITATION OF ABSTRACT	18. NUMBER OF PAGES	19a. NAME OF RESPONSIBLE PERSON
a. REPORT	b. ABSTRACT	c. THIS PAGE			
unclassified	**unclassified**	**unclassified**	**UU**	**340**	

Standard Form 298 (Rev. 8-98)
Prescribed by ANSI Std Z39-18

CHESTER F. CARLSON
CENTER FOR IMAGING SCIENCE
COLLEGE OF SCIENCE
ROCHESTER INSTITUTE OF TECHNOLOGY
ROCHESTER, NEW YORK

CERTIFICATE OF APPROVAL

Ph.D. DEGREE DISSERTATION

The Ph.D. Degree Dissertation of Daniel D. Blevins
has been examined and approved by the dissertation
committee as satisfactory for the dissertation
requirement for the Ph.D. degree in Imaging Science

Dr. John R. Schott, Dissertation Advisor

Dr. Roger Easton

Dr. John Kerekes

Dr. Andrew Robinson

Date

DISSERTATION RELEASE PERMISSION
ROCHESTER INSTITUTE OF TECHNOLOGY
COLLEGE OF SCIENCE
CHESTER F. CARLSON CENTER FOR IMAGING SCIENCE

Title of Dissertation:

Modeling Multiple Scattering and Absorption for a
Differential Absorption LIDAR System

I, Daniel D. Blevins, hereby grant permission to the Wallace Memorial Library of the Rochester Institute of Technology to reproduce my thesis in whole or in part. Any reproduction will not be for commercial use or profit.

Signature _____

Date _____

Modeling Multiple Scattering and Absorption for a
Differential Absorption LIDAR System

by

Daniel D. Blevins

Chester F. Carlson Center for Imaging Science
Rochester Institute of Technology

Abstract

The Digital Image and Remote Sensing Image Generation (DIRSIG) model has been developed and utilized to support research at the Rochester Institute of Technology (RIT) for over a decade. The model is an established, first-principles-based scene simulation tool that has been focused on passive multi- and hyper-spectral sensing from the visible to long wave infrared (0.4 to 14 μm). Leveraging photon mapping techniques utilized by the computer graphics community, a first-principles-based elastic Light Detection and Ranging (LIDAR) model was incorporated into the passive radiometry framework so that the model calculates arbitrary, time-gated photon counts at the sensor for atmospheric, topographic, and backscattered returns. The active LIDAR module handles a wide variety of complicated scene geometries, a diverse set of surface and participating media optical characteristics, multiple bounce and multiple scattering effects, and a flexible suite of sensor models. This robust modeling environment allows the researcher to evaluate sensor design trades for topographic systems and the impact that scattering constituents (e.g. water vapor, dust, sediment, soot, etc.) may have on a Differential Absorption LIDAR (DIAL) system's ability to detect and quantify constituents of interest within volumes including water and atmospheric plumes.

The interest in modeling DIAL sensor engagements involving participating media such as gaseous plumes presented significant challenges that were overcome using the photon mapping paradigm. Intuitively, researchers suspect that multiple scattering effects from additional constituents as simple as water vapor or soot could impact a DIAL sensor's ability to detect and quantify effluents of interest within a participating medium.

Traditional techniques, however, are not conducive to modeling the multiple scattering and absorption within a non-homogenous finite volume, such as a plume. Specific numerical approaches are presented for predicting sensor-reaching photon counts, including the effects of multiple scattering and absorption within a realistic plume. These approaches are discussed and benchmarked against analytically predicted results using a non-stationary, diffusion approximation. The analytical development and consistency of this new variant of photon mapping is explored along with the underlying physics and radiative transfer theory for participating media. Additionally, a LIDAR equation that accounts for multiple scattering effects is presented in conjunction with a discussion of the importance of accounting for these effects.

Representative datasets generated via DIRSIG for both a topographical LIDAR and DIAL system are then shown. The results from some interesting phenomenological case studies including standard terrain topography, forest canopy penetration, plume interrogation with scattering and absorbing constituents, and camouflaged hard targets are also presented. Based upon a limited number of case studies, the effects of multiple scattering on DIAL sensor performance are also qualitatively discussed.

Disclaimer

The views expressed in this dissertation are those of the author and do not reflect the official policy or position of the United States Air Force, Department of Defense, or the U.S. Government.

Contents

List of Figures viii

List of Tables xvi

Nomenclature 1

1. Introduction 9

2. Objectives 13
2.1 Success Criteria 13
2.2 Goals 15

3. Background and Theory 17
3.1 DIAL/DAS Systems 18
3.1.1 Principles of the DIAL Method 19
3.1.2 DIAL LIDAR Equation 22
3.1.3 Typical System Configuration 27
3.1.3.1 Transmitter 27
3.1.3.2 Receiver 29
3.1.3.3 Detector 30
3.1.3.4 Data Processor 30
3.1.4 Detection Limit and Concentration Sensitivity 32
3.1.4.1 Detection Limit for Aerosol Return 32
3.1.4.2 Detection Limit for a Topographic Return 35
3.1.4.3 Concentration Sensitivity and Interfering Constituents 37
3.2 Multiple Scattering LIDAR Equation 40
3.2.1 Key Assumptions 40
3.2.2 Simplified Approximation of Multiple Scattering 42
3.2.3 Generalized Multiply Scattered Model 46
3.2.4 Implications for DIAL Measurements 60
3.3 Radiative Transfer in Participating Media 62
3.3.1 Fundamentals and Properties for Participating Medium 63
3.3.2 Radiative Transfer Equation 70
3.3.3 Radiative Transfer Equation for a Plane-Parallel Gaseous Layer 74
3.3.3.1 Thin Layers 78
3.3.3.2 Thick, Homogenous Non-absorbing Layer 80
3.3.4 General Solutions and Approximations for Plane-Parallel Layers 81
3.3.4.1 Diffusion Approximation 82
3.3.4.2 Small Angle Approximation 87
3.3.4.3 Small-Angle Diffusion Approximation 88
3.3.4.4 Discrete Ordinate Approximation 89
3.3.4.5 Approximation Applicability Diagram 95
3.3.4.6 Non-stationary Diffusion Approximation 96

3.4 Photon mapping 101
3.4.1 Governing Radiative Transfer Equations for Photon Mapping 103
3.4.2 Photon Mapping Concept 107
3.4.3 Photon Tracing (Phase 1) 109
3.4.4 Rendering in Participating Medium (Phase 2) 113
3.4.4.1 Volume Radiance Estimate 113
3.4.4.2 Surface Radiance Estimate 117
3.4.5 Sample Results 117
3.4.6 Time-dependent Photon Mapping 122
3.5 Particles and Polydiverse Media 124
3.6 Scattering Theory for Spheres of Arbitrary Size (Mie Theory) 129
3.6.1 Mie Formulation 130
3.6.2 Practical Mie Calculations 138
3.6.3 Performance and Accuracy 146
3.7 Plume Dynamics Modeling 148
3.7.1 Governing Equations (Navier-Stokes Equations) 150
3.7.2 JPL Gaussian Plume Model 152
3.7.3 LANL QUIC-PLUME Model 158
3.7.4 Blackadar Plume Model 160
3.8 Summary 162

4. Approach 165
4.1 Model History 165
4.1.1 Historical Modeling Approach 166
4.1.2 Active System Justification 168
4.1.3 Prototype DIRSIG LIDAR Model 169
4.1.3.1 Description 170
4.1.3.2 Prototype Limitations and the Path Forward 174
4.2 DIRSIG LIDAR Module (New and Improved) 176
4.2.1 Numerical Modeling Approach 180
4.2.2 Source and Sensor Modeling 183
4.2.3 Modified Photon Mapping 184
4.2.3.1 Forward Propagation – Tracing 184
4.2.3.2 Backward Propagation – Rendering 187
4.2.4 Passive and Thermal Contributions 192
4.2.5 Backscattered Atmospheric Returns 196
4.2.6 Instrument and Platform 197
4.2.7 Generalized Modeling Process 198
4.2.8 Practical Implementation Issues 200
4.2.8.1 Multiple Photon Maps and Required Photon Density 200
4.2.8.2 Optical Parameter Generation Methodology 202
4.3 Topographic and DIAL Processor 214
4.4 Model Development and Verification 215
4.4.1 Time-gated Topographic Return and Temporal Pulse Spread 218
4.4.2 Impact of an Absorbing Layer 219
4.4.3 Impact of an Scattering Layer 219
4.4.4 Atmospheric, Passive, and Emissive Contributions 221

4.5 Phenomenological Case Studies 221
4.6 DIAL Case Studies and Representative Datasets 223

5. Results 229
5.1 Analytical Model Verification 230
5.1.1 Temporal Pulse Broadening 231
5.1.2 Topographic Return from a Lambertian Plate 234
5.1.3 Absorption by a Gaseous Layer 245
5.1.3.1 Statistical Analysis 246
5.1.3.2 Integrated Return Signal 249
5.1.4 Scattering by a Gaseous Layer 252
5.1.4.1 Statistical Analysis 253
5.1.4.2 Temporal Signature of Backscattered Power 262
5.1.5 Passive/Thermal Contributions 265
5.2 Phenomenological Demonstrations 269
5.2.1 Multi-Bounce and "Late" Photons 270
5.2.2 Forest Canopy Penetration 272
5.2.3 Camouflage/Concealed Hard Targets 274
5.2.4 End-to-End Topographic Mapping Demonstrations 277
5.2.4.1 Microscene 277
5.2.4.2 Spotlight-mode, Extended Dwell and Canopy Penetration 281
5.3 Impact of Scattering Constituents on DIAL Measurements 283
5.3.1 Controlled Scattering Case Study 284
5.4 End-to-end DIAL Demonstration 288
5.4.1 Megascene Tile 4 Water Treatment Plant with a CH_4 Plume 288

6. Conclusions 293
6.1 Findings 294
6.2 Recommendations for Future Research 296
6.2.1 Model Validation 296
6.2.2 Model Enhancements 297
6.2.3 Model Applications 299

Appendix A - Mie Code Performance 301

References 311

List of Figures

Figure 1: Illustration of DIAL principles 21

Figure 2: Example of DIAL measurement of SO_2 (Measures, 1988) (a) Absorption LIDAR signal, (b) Reference LIDAR signal, (c) DIAL curve, and (d) Calculated concentrations 21

Figure 3: Configuration of typical DIAL system 27

Figure 4: Generalized DIAL processing algorithm 32

Figure 5: Simplified multiple scattering setup 43

Figure 6: Geometry for a photon emitted by the laser and scattered once at a slab at a distance x_1 from the maximum range R 48

Figure 7: Geometry for a photon returning to the receiver from the area $\xi\, d\xi\, d\psi$ 52

Figure 8: Multiple scattering geometry for a cloud located at a distance R_c from the LIDAR 55

Figure 9: C1 Cloud multiple-to-single scatter power ratio for a WFOV LIDAR at different penetration depths 59

Figure 10: Comparison of multiple scattering and single scattering LIDAR equation 60

Figure 11: Radiance attenuation through a participating medium of volume dV 64

Figure 12: Henyey-Greenstein phase functions for g=0, 0.3, and 0.9 68

Figure 13: Scattering phase function for water using Mie theory (log scale, λ=650 nm, m=1.33, a_{eff}=6 μm) 69

Figure 14: Scattering into direction $\vec{\Omega}$ through distance dS in a participating medium 72

Figure 15: Geometrical construct for RTE of plane-parallel layer 75

Figure 16: Reflection function of a water cloud with different liquid water paths (a_{eff}=6 μm, μ=1, μ_0=0.707, r_s=0) 81

Figure 17: Geometry for virtual sources in a diffusion approximation of an isotropic point source in a semi-infinite medium for an observation point M 87

Figure 18: Reflection function of water clouds at τ=30, μ=1, μ_0=0.707, a_{eff}=6 μm for different ground albedos 94

Figure 19: Reflection function of water clouds from DISORT and Kokhanvosky's cloud approximation (Equation 127) (τ=30, μ=1, μ_0=0.707, a_{eff}=6 μm) 94

Figure 20: Reflection function of water clouds from DISORT and Kokhanvosky's cloud approximation (Equation 127) 95

Figure 21: Applicability domains of approximation methods (Zege, et al., 1991) 96

Figure 22: Predicted backscattered return from a laser pulse for (1) BSN diffusion approximation, (2) Multiple scatter LIDAR equation, and (3) Single scatter LIDAR equation 101

Figure 23: Illustration of key terms in radiance calculation for a participating medium 106

Figure 24: Pass 1 - Photon tracing 108

Figure 25: Pass 1 - Recorded photon map 108

Figure 26: Pass 2 - Rendering 109

Figure 27: Importance sampling of $f(x)$ with uniform distributions 112

Figure 28: Importance sampling of $f(x)$ with distribution $h(x)$ 113

Figure 29: Photon mapping volume radiance estimate 115

Figure 30: Adaptive ray tracing calculation of radiance at points x_k 116

Figure 31: Photon mapping surface radiance estimate 117

Figure 32: Photon mapping simulation of a non-homogeneous cloud (Jensen and Christensen, 1998) 119

Figure 33: "Little Fluffy Clouds" over mountain landscape (Jensen 2001) 120

Figure 34: Dusty room illuminated by sunlight through a stained glass window (Jensen and Christensen, 1998) 121

Figure 35: Photon mapping rendering of smoke (Fedkiw, Stam, and Jensen, 2001) 122

Figure 36: Photographs of typical irregular terrestrial particles (Kokhansky, 2001) 125

Figure 37: Gamma and Log-normal particle PSDs (a_{eff}=6 μm and coefficient of variance Δ=0.38) 128

Figure 38: Geometry of incident and scattered fields for spherical particle and plane wave 131

Figure 39: Polar plots of first six angle-dependent functions for π_n 133

Figure 40: Polar plots of first six angle-dependent functions for τ_n 134

Figure 41: Spherical Bessel functions of the first (J_n) and second (Y_n) kind for $n = \{0,1,2,3\}$ 136

Figure 42: Normalized Rayleigh scattering amplitude functions 147

Figure 43: Decomposition of a simple shear flow into fundamental invariants 151

Figure 44: Gaussian plume approximated by successive point sources 153

Figure 45: Reflected plume created by use of a virtual source at $z=-h_{eff}$ 154

Figure 46: ACAD of JPL "Wander" Gaussian Plume Model 155

Figure 47: Gaussian plume model diagrams for σ_y and σ_z for release heights of 100m over rough terrain (Blackadar, 1997) 157

Figure 48: Rendered snapshots of a QUIC-PLUME simulation of a release in West Villiage area of New York City (Qui, et al., 1997) 159

Figure 49: Rendered close-up views for a QUIC-PLUME simulation of a release in West Villiage area of New York City (Qui, et al., 1997) 159

Figure 50: Conceptual diagram for DIRSIG's Blackadar plume model 161

Figure 51: Annotated DIRSIG truth map image of a Blackadar plume 162

Figure 52: Representative DIRSIG passive images 168

Figure 53: Prototype DIRSIG LIDAR module time slices for a T-72 tank (Burton, 2002) 170

Figure 54: Illustration of the prototype DIRSIG LIDAR model approach in 2002 172

Figure 55: DIRSIG passive simulation of a T-72 tank on a flat plate (λ=768 nm) 179

Figure 56: DIRSIG LIDAR module time slices for a T-72 tank on a flat plate 179

Figure 57: Key DIRSIG LIDAR source and sensor model inputs 184

Figure 58: Sample volume scattering photon map profile 187

Figure 59: Initial recorded photon map after forward ray tracing.....188

Figure 60: Collection Step 1 – Trace ray from detector and project FOV 189

Figure 61: Collection Step 2 – Apply phase function and scattering probability 190

Figure 62: Collection Step 3 – Sum, range-gate, and sample photon stream 191

Figure 63: Range-gated and sampled backscattered pulse 192

Figure 64: General passive contributions for the LIDAR return signal 194

Figure 65: Passive contributions to the LIDAR return signal modeled in DIRSIG.....195

Figure 66: DIRSIG simulation of passive solar contribution for a pulse fired a Lambertian plate with different reflectances (mid-latitude summer atmosphere; Rochester, NY).....196

Figure 67: Conceptual end-to-end DIRSIG LIDAR simulation process flow.....200

Figure 68: Scattering phase function generation methodology.....202

Figure 69: Typical atmospheric complex indices of refraction (MODTRAN database) 205

Figure 70: C1 water cloud complex indices of refraction (Segelstein, 1981).....207

Figure 71: Sample particle size distribution for C1 cloud water vapor (gamma[a_{eff}=6.0;a_0=4.0]) 207

Figure 72: C1 water cloud extinction, scattering, and absorption cross-sections 208

Figure 73: C1 water cloud asymmetry parameter 208

Figure 74: Complex indices of refraction for soot (Chang, 1990 and Kokhanovsky, 2001) 209

Figure 75: Soot aerosol particle size distribution (lognormal[a_m=0.5;σ=1.09527]) 210

Figure 76: Optical properties for soot using Chang's indices of refraction.....211

Figure 77: Optical properties for soot aerosol using Kokhanvosky's indices of refraction.....212

Figure 78: Sample particle size distribution for fly ash (gamma[a_{eff}=6.7; a_0=10.8]).....213

Figure 79: Optical properties for fly ash using Chang's indices of refraction.....214

Figure 80: Simplified verification scene setup.....217

Figure 81: Illustrated comparison of the signal returns from a tipped and flat plate..... 219

Figure 82: Illustrated averaged return signal from a tree..... 222

Figure 83: DIRSIG emissivity texture map used for MWIR grass spectrum (Peterson, 2004)..... 225

Figure 84: Sample emissivity curves for brown field grass (field1_brngrass_grass_mix300.ems)..... 225

Figure 85: Absorbance for CH_4 gas at 25°C in ppm/m..... 226

Figure 86: Absorbance for CH_4 gas at 25°C in ppm/m in MWIR region (3.3-3.4 μm)..... 227

Figure 87: DIRSIG panchromatic image of a CH_4 gas plume inserted into the RIT's Megascene 1 water treatment facility..... 228

Figure 88: Simplified verification scene setup..... 231

Figure 89: Illustration of temporal pulse broadening due to tilted plate for a Gaussian pulse..... 233

Figure 90: Temporal pulse broadening due to tilted plate for a 1 ns Gaussian pulse (10 deg)..... 233

Figure 91: DIRSIG integrated number of photons detected for a single pulse reflected from a Lambertian surface at 1200 m downrange for various detector sizes..... 236

Figure 92: Error for DIRSIG integrated number of photons detected for a single pulse reflected from a Lambertian surface at 1200 m downrange for various detector sizes..... 237

Figure 93: Error for DIRSIG integrated number of photons detected for a single pulse reflected from a Lambertian surface at 1200 m downrange for a 50 mm detector..... 240

Figure 94: Error for DIRSIG integrated number of photons detected for a single pulse reflected from a Lambertian surface at 1200 m downrange for a 1 mm detector..... 241

Figure 95: Error for DIRSIG integrated number of photons detected for a single pulse reflected from a Lambertian surface at 1200 m downrange for a 0.5 mm detector..... 242

Figure 96: Normalized histogram of photon events recorded for a single LIDAR pulse intersecting a flat Lambertian plate 1200 m downrange..... 243

Figure 97: Detector size impact on the integrated number of photons detected from a Lambertian surface of varying reflectances at 1200 m downrange for a single pulse 245

Figure 98: Analytical and modeled vertical distribution statistics of photons fired into different absorbing layers 247

Figure 99: Absolute error for modeled vertical distribution statistics of photons fired into different absorbing layers 247

Figure 100: Analytical and LIDAR model vertical distribution of photons for different absorbing layers (penetration depth distribution) 248

Figure 101: Modeling error for vertical distribution of photons for different absorbing layers (penetration depth distribution) 248

Figure 102: DIRSIG integrated number of photons detected for a single pulse reflected from a Lambertian surface at 1200 m downrange and attenuated by an absorbing gaseous layer of varying optical depths 250

Figure 103: DIRSIG error for integrated number of photons detected for a single pulse reflected from a Lambertian surface at 1200 m downrange and attenuated by an absorbing gaseous layer of varying optical depths 251

Figure 104: Fraction of photon bundles cast into a thick scattering layer that are reflected or transmitted as the asymmetry parameter is varied (τ = 10.0; ω_0 = 0.9928; μ=0.707) 255

Figure 105: Average number of scattering events within a cloud layer with an optical thickness of 10.0 and a scattering albedo of 0.9928 for all (a) reflected and (b) transmitted photons for various asymmetry parameters 257

Figure 106: Average number of scattering events in a scattering layer for reflected and transmitted photons as the asymmetry parameter is varied (τ = 10.0; ω_0 = 0.9928; μ=0.707) 258

Figure 107: Horizontal displacement distribution for photon bundles cast into a scattering layer (τ = 10.0; ω_0 = 0.9928; ; μ=0.707; g_{sca} = {0.0, 0.5, 0.85, 0.95}) 259

Figure 108: Histogram image of absorption events at the surface 2 m beneath the layer occurring within ±35 m of the scene center for horizontal displacement calculation (τ = 10.0; ω_0 = 0.9928; μ=0.707) 260

Figure 109: Theoretical and DIRSIG average number of scattering events within a cloud layer with an optical thickness of 8.0 for all (a) reflected and (b) transmitted photons for two common remote sensing spectral bands (Platnick, 2001) 261

Figure 110: Normalized backscattered power from a semi-infinite scattering layer 264

Figure 111: Passive solar contribution for a pulse fired a Lambertian plate with different reflectances (mid-latitude summer atmosphere; Rochester, NY) 267

Figure 112: Error for passive solar contribution for a pulse fired a Lambertian plate with different reflectances (mid-latitude summer atmosphere; Rochester, NY) 268

Figure 113: Photons collected at midnight from a pulse fired at a Lambertian plate with a 1m gaseous layer for different absorption coefficients including the thermal contributions (mid-latitude summer atmosphere; Rochester, NY) 269

Figure 114: CAD model of "grown" grass blades for Microscene burm (Barcomb, 2004) 271

Figure 115: Microscene topographic LIDAR time-gated returns with "late" photons 271

Figure 116: Canopy penetration/multi-bounce demonstration setup 273

Figure 117: DIRSIG photon map for canopy penetration/multi-bounce demonstration 273

Figure 118: Canopy penetration and multi-bounce demonstration for a single, deciduous tree 274

Figure 119: HMVVV, spreaders, and camouflage netting CAD models for DIRSIG simulation (Barcomb, 2004) 275

Figure 120: DIRSIG overhead passive simulation of HMVVV and camouflaged HMVVV 276

Figure 121: DIRSIG scene distance truth map for camouflaged HMVVV 276

Figure 122: DIRSIG time-gated LIDAR returns for camouflaged HMVVV 277

Figure 123: Microscene topographic LIDAR product and passive simulation (overhead) 279

Figure 124: Microscene topographic LIDAR product and passive simulation (slant view) 280

Figure 125: Topographic product for extended dwell (45 deg) collect of concealed targets at 30 deg grazing angle 282

Figure 126: Vehicle close-ups for extended dwell (45 deg) topographic product 282

Figure 127: DIAL concentration path length error due to scattering for a gaseous layer 100 above a grassy surface 287

Figure 128: DIRSIG MWIR image of Megascene-Tile4 waterplant with a Blackadar plume 290

Figure 129: Processed CPL maps from DIRSIG LIDAR cubes for Megascene-Tile4 waterplant with a CH_4 Blackadar plume (λ_{off}=3.3060 μm; λ_{on}=3.3151 μm) 291

Figure 130: Processed CPL maps from DIRSIG LIDAR cubes for Megascene-Tile4 waterplant with a CH_4 and water vapor Blackadar plume (λ_{off}=3.3060 μm; λ_{on}=3.3151 μm) 291

Figure 131: Normalized Rayleigh scattering amplitude functions 307

List of Tables

Table 1: Sample lasers used in LIDAR systems (Zanzotera, 1990) 29

Table 2: Particle size distributions of selected disperse media (Kokhanovsky, 2001) 127

Table 3: Operational restrictions for MIEV0, BHMIE, and MIEDU 146

Table 4: Comparison of MIEDU and MIEV0 results 148

Table 5: Comparison of MIEDU and BHMIE results 148

Table 6: Comparison of MIEV0 and BHMIE results 148

Table 7: Pasquill Stability Classes 156

Table 8: Pasquill Stability Types Guidance 157

Table 9: DIRSIG LIDAR modeling requirements and development status 178

Table 10: Particle size distribution description for typical plume constituents 206

Table 11: LIDAR system configurations for DIRSIG verification runs 218

Table 12: LIDAR system configuration for scattering case study 227

Table 13: LIDAR system configurations for DIRSIG verification runs 231

Table 14: Photons represented by each bundle given the number of bundles shot in DIRSIG 240

Table 15: Scattering parameters averaged over typical remote sensing instrument spectral response functions for a cloud droplet size spectra (Platnick, 2001) 261

Table 16: Average number of scattering events for reflected and transmitted photons cast into cloud layer with an optical thickness of 8.0 and optical parameters in Table 15 262

Table 17: LIDAR system parameters and MODTRAN output data for solar verification scenes 266

Table 18: Breakdown of key contributors for solar verification scenes 266

Table 19: LIDAR system configuration for scattering case study 286

Table 20: Optical depth of gas box for DIAL and scattering case study at the OFF wavelength....286

Table 21: Optical depth of gas box for DIAL and scattering case study at the ON wavelength....286

Table 22: LIDAR system configuration for Megascene-Tile4 simulation....289

Table 23: Operational restrictions for MIEV0, BHMIE, and MIEDU....302

Table 24: Comparison of MIEDU and MIEV0 results....305

Table 25: Comparison of MIEDU and BHMIE results....306

Table 26: Comparison of MIEV0 and BHMIE results....306

Table 27: Comparison of values of Q_{ext} in the small particle limit....308

Table 28: Timing comparison for IDL Mie and IDL BHMIE implementations *(m = 10-10i, 65 angles)*....309

Nomenclature

The nomenclature for this dissertation is listed in the table below. In general, the standard conventions in each subject area were followed. The nomenclature attempts to limit the potential for confusion and subscripts were employed for clarification; however, some symbols will have contextual meanings. For instance, k is used for Planck's constant in discussing thermal dynamics or emission and is also used for the wavenumber in the electromagnetic wave equations. These cases were limited as much as possible. The specific context is indicated by the shaded categories within the table.

Symbol	Definition
	General
λ	Wavelength of light
c	Speed of light
∇	Gradient operator
T	Temperature
P	Pressure
Φ	Flux
k	Wavenumber or Planck's constant
h	Boltzmann's constant
	LIDAR
λ_{abs}	DIAL wavelength at a strong absorption feature
λ_{ref}	DIAL reference wavelength in wing of absorption feature
$\xi(\lambda,R)$	LIDAR system function
R	Range
A_r/R^2	Acceptance solid angle of the receiver optics
A_r	Collecting area
$P_L(\lambda)$	Average power in the transmitted pulse at wavelength λ
ΔR	Effective range resolution of LIDAR signal

Symbol	Definition
$C_{B_i}(\lambda)$	Backscattering cross-section at wavelength λ
$N_i(r)$	Number density of scatter species *i* at range *r*
$C_{A_p}(\lambda)$	Particle species absorption cross-section at wavelength λ
$N_p(r)$	Number density of particle absorbing species *p* at range *r*
$C_{A_m}(\lambda)$	Molecular species absorption cross-section at wavelength λ
$N_m(r)$	Number density of molecular absorbing species *m* at range *r*
$\sigma_\beta(\lambda,R)$	Backscattering coefficient at wavelength λ and range *r*
$\sigma_{ext}(\lambda,R)$	Extinction coefficient at wavelength λ and range *r*
τ_L	Laser pulse duration
τ_D	Detector's integration period
$\overline{N}_m$	Averaged molecular number density
$\rho_S(\lambda)$	Backscattering efficiency of the topographic target
R_T	Range to the topographic target
$E(\lambda,R_T)$	Radiative energy received from topographic target at range R_T
$E_L(\lambda)$	Transmitted energy of the laser pulse
SNR	Signal-to-noise ratio
$\left[N(R)\right]_{\min}$	Minimum detectable concentration for aerosol DIAL
$\left[N_{topo}\right]_{\min}$	Minimum detectable concentration for topographic DIAL
c_{min}	Minimum concentration in ppm
N_{atm}	Atmospheric molecular density
$C_m(\lambda)$	Species absorption cross-section at wavelength λ
ω_r	Solid angle subtended by the receiver
$p(\theta)$	Scattering phase function
ρ_L	Angular half-width of transmit laser beam
ρ_T	Angular half-width of receiver
Θ	Mean angular width of scattering phase function main lobe
$\gamma(x)$	Fraction of energy in forward peak of phase function at range x

Symbol	Definition
$p_{\pi n}$	Weighted average of scattering phase function
$P_n(R)$	Received power from range R due to n^{th}-order scattering
$P_t(t)$	Total received power as function of time t
P_l	Legendre associated polynomial
g_l	Legendre associated polynomial coefficient
$\Lambda_l^m(\mu)$	Normalized associated Legendre polynomial
$N_{detected}$	Number of photons detected
N_L	Number of photons in laser pulse
$W(R)$	Transmit beam waist radius at range R
f	Focal length of system
A_D	Area of detector
Scattering and Electromagnetics	
a	Particle diameter
a_{ef}	Effective particle radius
x	Particles size parameter
m	Complex index of refraction
$\mathbf{E}$	Electric field vector
$\mathbf{B}$	Magnetic field vector
ρ	Charge density
ε	Electric permittivity
μ	Magnetic permeability
$\mathbf{j}$	Electric charge
S_1	Perpendicular component of scattered wave amplitude function
S_2	Parallel component of scattered wave amplitude function
a_n	Mie coefficient
b_n	Mie coefficient
π_n	Legrendre associated polynomial
τ_n	Legrendre associated polynomial
ψ_n	Riccati-Bessel function

Symbol	Definition
ζ_n	Riccati-Bessel function
χ_n	Riccati-Bessel function
i_1	Perpendicular scattered irradiance per incident irradiance
i_2	Parallel scattered irradiance per incident irradiance
Q_{ext}	Efficiency factor for extinction
Q_{abs}	Efficiency factor for absorption
Q_{sca}	Efficiency factor for scattering
C_{sca}	Scattering cross-section
C_{abs}	Absorption cross-section
C_{ext}	Extinction cross-section
σ_{sca}^{d}	Differential scattering cross-section
r_n	Recursive Riccatti-Bessel function ratio
A_n	Logarithmic derivative of ψ_n
l_n	Number of lost significant digits for Du's Mie code
σ_{ext}	Extinction coefficient
σ_{sca}	Scattering coefficient
σ_{abs}	Absorption coefficient
ω_0	Single surface albedo
L_λ	Radiance at wavelength λ
c_i	Particle concentration
τ_λ	Optical thickness or depth
N	Number concentration of particles (typically)
g	Asymmetry parameter
c_v	Volumetric concentration of particles
$\Gamma(\ )$	Gamma function
ϑ	Observation angle
ϕ	Observation azimuth angle
ϑ_0	Incident angle

Symbol	Definition
ϕ_0	Incident azimuth angle
$\vec{\Omega}$	Wave propagation vector
θ	Scattering angle
$\vec{n}$	Observation vector
$\vec{r}$	Direction of the light beam
B_0	Internal sources of radiation
$I_{\uparrow}$	Radiant intensity leaving top of plane-parallel layer
$I_{\downarrow}$	Radiant intensity leaving bottom of plane-parallel layer
$I_{\uparrow}^{d}$	Upward diffused light intensity
$I_{\downarrow}^{d}$	Downward diffused light intensity
R	Reflection function
T	Transmission function
R_0^{∞}	Reflection function for semi-infinite layer
I_t	Total intensity
I_{λ}	Radiant intensity at wavelength λ
I_{src}	Internal sources of radiation
I_{em}	Emission sources of radiation
I_{sca}	In-scattered source of radiation
I_0	Initial incident intensity
I_{src}	Internal sources of radiation
$\mathscr{F}_{\vec{\eta}}\{\ \}$	Modified 2-D Fourier transform with respect to incident vector
$\mathscr{F}_{\vec{\rho}}\{\ \}$	Modified 2-D Fourier transform with respect to observation vector
$\vec{F}(\vec{r})$	Flux density vector in direction $\vec{r}$
$w(\vec{r})$	Radiation density in direction $\vec{r}$
γ	Asymptotic attenuation coefficient
q	Scattering inicatrix parameter
$\left[T(\nu)\right]_{\text{homogenous}}$	MTF for a homogenous plane-parallel layer

Symbol	Definition
$\left[T(\nu)\right]_{\text{inhomogenous}}$	MTF for an inhomogenous plane-parallel layer
$I_{\delta}\left(\vec{\tau},\vec{n},u\right)$	Irradiance impulse response to an isotropic point source
E_s	Irradiance from the sun
ρ_{surf}	Reflectance of a surface
Δt	Length of listening window
Photon Mapping	
L_i	In-scattered radiance
$L_{src}\left(x,\vec{n}\right)$	Internal source of radiance within media
L_e	Radiance emitted along the path
d	Distance traveled by a photon prior to the next event
ε_{samp}	Efficiency of the acceptance-rejection method
$L_{i,d}$	In-scattered radiance direct component due to single scattering
$L_{i,i}$	In-scattered radiance indirect portion
L_r	Reflected radiance
f_r	Bidirectional reflectance distribution function (BRDF)
L_p	Radiance through pixel p
t_s	Total frame time
$g\left(x'\right)$	Receiver filter function
$s\left(x',\vec{\omega},t\right)$	Reciever shutter function
Plume Dynamics	
$\vec{u}$	Velocity vector of gas
p	Pressure of gas
g_v	Gravity in the vertical direction
β	Coefficient of thermal expansion
T_0	Initial reference temperature
T_k	Average temperature on the boundary between a gaseous cell and the one above it
λ	Represent both molecular and turbulent diffusion processes
Q	Source strength
t	Time

Symbol	Definition
$\chi(x,y,z)$	Concentration overall
x	Downwind distance
y	Lateral distance from centerline
z	Vertical distance from ground
σ_y	Lateral coefficient of dispersion
σ_z	Vertical coefficient of dispersion
μ	Mean wind speed
h_{eff}	Effective height of stack
h	Height of the centerline of the plume
r_{stack}	Stack radius
v_{ratio}	Emission velocity ratio

Chapter 1

Introduction

For the last decade or so, the remote sensing community has grappled with how to best solve the problem of detecting and analyzing gaseous plumes. Sensor designers and algorithm developers attempt to balance the requirement to determine the makeup, the species type present, the temperature (absolute and relative) within the plume, the particle concentration spatially and temporally, and the rate of release of pollutants or specific chemicals. In general, active measures, such as laser remote sensing with a LIght Detection And Ranging (LIDAR) system, provide a more accurate determination of the concentration of effluents in a plume at fixed wavelengths than passive means (Measures, 1998; Zanzottera, 1990). Within the active sensor regime, the Differential Absorption and Scattering (DAS) or Differential Absorption LIDAR (DIAL) is often the sensor of choice for concentration measurements due to their reputed high accuracy and sensitivity even with a modest design complexity.

Intuitively, researchers suspect that multiple scattering effects from additional constituents as simple as water vapor or soot could impact a DIAL sensor's ability to detect and quantify effluents of interest within a participating medium. For instance, cloud atmospheric inversion algorithms often require the user to intelligently guess or utilize some sort of measurement of how much water vapor is present within the cloud layer. The variability of the results may then be correlated with how accurate the guess is and how much the water vapor varies within the cloud layer. The impact is highly dependent upon the gas constituent of interest. A more complicated situation can arise when examining a variety of different factory stacks, particularly in a third world country where the plumes are typically very "dirty". The potential impact of the multiple scattering in the plume coupled with its very non-stationary nature could be problematic for a DIAL system. Although exploring this problem set with a synthetic data generation tool may be beneficial, modeling these complex scenarios with a high degree of accuracy poses significant challenges. Traditional techniques are not conducive to modeling the multiple scattering and absorption within a non-homogenous, finite volume, such as a plume.

This research presents a new physics-based modeling approach to simulate the multiple scattering and absorption in a medium viewed by a LIDAR sensor, and particularly by a DIAL system. The available tools to simulate LIDAR scenes do not support rigorous atmospheric interactions, participating media, multiple bounce/scattering, thermal and reflective region passive returns, complex scene geometries, moving platform and scanning effects, detailed optical descriptions of materials (e.g., BRDF and scattering models), and time-gated returns. Such requirements were deemed crucial to fully address future research problems and accurately model the observable signatures of gaseous plumes under a variety of complex scene conditions, including multiple scattering.

Developed at the Center for Imaging Science (CIS) at the Rochester Institute of Technology (RIT) in Rochester, NY, the Digital Imaging and Remote Sensing Image Generation (DIRSIG) software is a quantitative first-principle, physics-based synthetic imagery generation model of the imaging chain for specified scenarios. With a 20-year history, DIRSIG is an established scene simulation model for passive multi- and hyperspectral sensing from the visible to long-wave infrared. Leveraging the photon mapping techniques utilized by the computer graphics community, a first-principle-based elastic LIDAR model was incorporated into the passive radiometry framework so that the model calculates arbitrary, time-gated photon counts at the sensor for atmospheric, topographic, and volumetric backscattered returns. In conjunction with recent upgrades to DIRSIG's foundation, this research extended DIRSIG's LIDAR module capability and fidelity beyond the initial proto-type development conducted by Burton in 2002. The LIDAR module now handles a wide variety of complicated scene geometries, diverse surface and participating media optical characteristics, multiple bounce and multiple scattering effects, and a variety of sensor models.

The interest in modeling DIAL sensor engagements involving participating medium, such as gaseous plumes with scattering constituents, presented significant challenges that were overcome using the photon mapping modeling paradigm. Specific approaches are presented to predict sensor-reaching photon counts for a LIDAR system, including the effects of

multiple scattering and absorption within a realistic plume. These approaches are then discussed and benchmarked against analytically predicted results using a non-stationary diffusion approximation. The analytical development and consistency of this new variant of the photon mapping is also presented along with the underlying physics and radiative transfer theory for participating media. Additionally, a LIDAR equation that accounts for the effects of multiple scattering, which forms the foundation for the new modeling approach, is presented in conjunction with a discussion of the importance of accounting for these effects.

Representative datasets generated via DIRSIG for both the improved topographical LIDAR and DIAL system are then shown. Additionally, the results from some interesting phenomenological case studies including standard terrain topography, forest canopy penetration, plume interrogation, and camouflaged hard targets are presented. Finally, some initial conclusions are drawn based upon the modeling efforts and the respective theory about the effects of multiple scattering on DIAL sensor performance.

This dissertation is divided into seven chapters and one appendix. Chapter 2 introduces the primary objectives and some additional desirable goals. Chapter 3 describes the general theory and background material for the entire research effort. The fundamental theory for DAS and DIAL systems, radiative transfer theory for participating medium, photon mapping, and a multiple scattering LIDAR equation are reviewed. Additionally, the foundational theory for modeling plumes and the optical properties of participating medium via Mie theory will be presented. The former sections form the basis for the modeling effort; whereas, the latter sections discuss some enabling theory to generate reasonable data for the simulations. Specific approaches to model the multiple scattering and absorption within the plume will be discussed in Chapter 4, which begins with a discussion of the justification of an active system within the DIRSIG framework and the overall requirements and goals for the LIDAR module. The introduction of the model is then followed by a more detailed description and some practical considerations, such as a practical atmospheric model and reasonable assumptions for the optical properties of water vapor or soot. Then, the verification philosophy and approach are discussed. Chapter 4 ends with a description of some key case studies, both interesting phenomenological case studies and multiple

scattering case studies. Chapter 5 gives the results of the verification efforts, sample results from the case studies, and qualitative results with regards to the importance of modeling the effects of multiple scattering for DIAL concentration measurements of gaseous plumes. Conclusions are then drawn in Chapter 6 including some recommendations for future research. The appendix provides a detailed discussion of the accuracies of the Mie code(s) introduced in Chapter 3, which were used for modeling the plume optical properties.

Chapter 2

Objectives

This chapter provides a general overview of the objectives associated with this research effort. While the scientific endeavor involves a variety of tasks, the overarching objective is the development and verification of a Monte-Carlo photon counting LIDAR model that accurately simulates the multiple scattering and absorption of a laser pulse in a participating medium. To obtain this objective, a series of tasks must be performed to provide a sufficient level of confidence that the simulations are reasonable or physically accurate. The specific tasks deemed necessary are directly tied to the overarching objective and thus are designated as success criteria, as described in Section 2.1 . Additional general research goals were pursued as time and research constraints permitted. Section 2.2 addresses the general research goals and how they tied into the overall scope of work.

2.1 Success Criteria

The specific objectives associated with this research effort are itemized below:

- Develop a set of representative DIAL simulations utilizing the DIRSIG LIDAR sensor module. The intent is to demonstrate the capabilities inherent within the DIRSIG LIDAR module to model a variety of different DIAL scenarios. The operating parameters or system design characteristics which may be used to describe a DIAL payload during an engagement are the transmit power, the pulse width, the transmit wavelength(s), the effective receiver wavelengths and bandwidth, the dwell time, the pulse repetition rate, the duty cycle, the pulse shape, the receiver optics gain, the range resolution, the sampling rate, the detector size, the sensor field-of-view, the detector quantum efficiency, and the laser spot size on the target. The representative set of DIAL simulations will not include the full range of possible operating parameters listed above. Rather, the intent is to generate a reasonable and representative set of collection scenarios that demonstrate how a DIAL sensor might be modeled.

- Develop a firm understanding of the mathematical and theoretical basis, viability, and practical limitations of photon mapping to numerically model multiple scattering and absorption in a dispersive, gaseous participating medium through the following:
  - Explore the analytical development of photon mapping and evaluate consistency with the underlying physics and radiative transfer theory for gaseous media.
  - Verify the accuracy of photon mapping thru analytical means (where tractable) is consistent with the theoretical foundation of scattering, absorption, and radiative transfer theory. The scenarios will be simplified cases for a single layer of dispersive media over a variety of driving parameters. Some of the technical parameters of interest may include:
    - Various scattering phase functions, such as isotropic, anisotropic, Henyey-Greenstein (for water, soot, and aerosols), and Mie generated and importance sampled (for water, soot, and aerosols)
    - Particle size distributions, including homogenous, log-normal, gamma, Junge, and Gaussian
    - Optical thickness ranging from thin to thick
    - Strong, weak, and non-absorbing media
    - Visible and near infrared regimes where thermal self-emission is a factor
  - Substantiate that the photon mapping results of more complex scenes exhibit the characteristic behavior and trends predicted or implied by the established scattering and absorption literature through qualitative assessments where necessary. Exemplar datasets shall be generated that include full complex backgrounds and targets to demonstrate the interactions between the participating medium and a more realistic surrounding environment.
- Develop an understanding of the theoretical basis of light scattering by small particles and demonstrate a practical methodology for generating the critical optical properties of mixed gases required for the propagating photons through the scene and estimating the observed radiance. Specific items to be addressed are:
  - Generating the scattering and absorption cross-sections and the scattering phase functions for a particular gas or aerosol based upon its complex index of refraction.

- Constructing composite scattering phase functions and optical properties for mixed gases based upon an assumed composition and linearity.
- Develop a methodology to invert the scattering phase functions into a random angle generating function that is required for the photon mapping propagation model.

- Develop a set of simulated DIAL datasets with gaseous plumes or voxels suitable to qualitatively confirm whether common scattering constituents, such as water vapor or soot, can significantly degrade a DIAL sensor's ability to accurately detect and measure the concentration level of a particular constituent within the plume.
- Implement an algorithm to detect and measure concentration for DIAL sensor data. The algorithm will be used to augment the qualitative assessments of the impact of plume scattering on the identification and quantification of plume effluents. Additionally, the algorithm will demonstrate the utility of the DIRSIG simulated DIAL dataset(s) and tradeoffs of active versus passive sensor and algorithm combinations against comparable collection scenarios. The intent is not to implement a robust, high-precision algorithm, but rather to estimate the concentration of the constituent of interest based upon something as simple as the band ratios. Additional augmentations will be pursued as time permits.

2.2 Goals

The following goals have been identified for this research effort to help reinforce the value of the basic requirements established in the previous section:

- Extend DIRSIG's LIDAR module capability to model topographic scenarios. While the focus of the research is on DIAL systems, the underlying physics inherently drives a level of fidelity in the modeling that incorporates sufficient capability to model topographic LIDAR sensors.
  - Develop and test a topographic processor with sufficient flexibility to incorporate various detector modes (Geiger-counter, linear, etc…).
  - Conduct phenomenological case studies including standard terrain topography, forest canopy penetration, and camouflaged hard target. The intent is to exercise and

demonstrate capabilities of the DIRSIG LIDAR module to simulate camouflage/canopy penetration and multi-bounce phenomenon.

- Generate a library of scattering phase functions for standard gases and aerosols of interest based upon the published database. As a portion of this goal, the following tasks were considered:
  - Develop a prototype suite of software to directly access the HITRAN database.
  - Develop an interactive tool to view the scattering phase function of interest.
  - Develop an interactive tool to combine multiple scattering phase functions for combinations of well-mixed gases and aerosols based upon relative concentration levels.
  - Develop a database of standard aerosol and gaseous media particle size distribution functions for the purposes of generating scattering phase functions.
- Explore the validity of assumption of linearity when generating the scattering phase functions for mixed gases. Conventionally, the scattering phase function for a voxel is based upon a linear relationship between the relative concentration levels of the gases within that voxel. When the scattering particles have relatively similar optical properties, then the linear assumption is generally deemed acceptable. The primary intent is to explore whether nonlinear combinations should be considered in the future as a research area of interest.

Chapter 3

Background and Theory

This chapter highlights the essential theoretical foundation upon which this research effort is based. The material can be essentially grouped into two categories, the foundation of theory and analysis and practical approaches to modeling. The first three sections of this chapter primarily focus on the first category: governing equations and underlying physics of the problem. Section 3.1 introduces the principles of the DIAL/DAS method, the standard single-scatter LIDAR equation for a DIAL/DAS system, a discussion of typical system parameters, the detection and concentration sensitivity drivers, and a broad comparison with other methods. Section 3.2 initiates the discussion of multiple scattering by developing a LIDAR equation and exploring the potential impacts for a DIAL system. The multiple scatter LIDAR equation presented in Section 3.2 will later be discussed in Chapter 4 as a critical portion of the new modeling methodology. Section 3.3 lays the foundation for describing the interaction of light within a participating medium, such as a gaseous plume. The crux of this section is the general solution to the radiative transfer equation (RTE) for a participating medium. The latter portion of Section 3.3 addresses issues associated with solving the radiative transfer equation for a nonstationary source (such as a mono-directional, pulsed point source) via the diffusion approximation. Chapter 4 will leverage the diffusion approximation and the multiple scattering LIDAR equation as a key analytical verification tool of the accuracy of the DIRSIG LIDAR module. The modeling approach discussed further in Chapter 4 is a variant of photon mapping and is unique. The verification process is critical to ensure both that the implementation and the core algorithms are accurate and robust. As a direct extension of the theoretical development of the radiative transfer equation within a participating medium, Section 3.4 reviews the theoretical, mathematical, and practical implementation of photon mapping for modeling multiple scattering and absorption of light within a dispersive, participating media. Section 3.4 emphasizes the traditional photon mapping approaches that form the enabling paradigm for the DIRSIG LIDAR module; however, the specific implementation details are left to Chapter 4. The last three sections of this chapter discuss the theory and the practical considerations necessary to simulate complex

scenes. Section 3.5 introduces the types of particle size distributions that are relevant to this area of research and the impact of those distributions on the optical properties of the medium. Section 3.6 focuses on the absorption and scattering of arbitrarily-sized small particles. This section introduces the basis for Mie scattering theory and a practical algorithm to physically calculate the necessary optical properties for a particular gas or aerosol based upon its complex index of refraction and particle size distribution function. Rayleigh and non-selective scattering will also be addressed; however, the emphasis will be on Mie scattering theory because the typical particles of interest for this dissertation fall within a regime that requires Mie codes. Section 3.7 briefly addresses modeling of plume dynamics. The section introduces the overall governing equations for modeling the flow of effluent concentrations within a scene and the two plume models fully integrated into DIRSIG, the Gaussian model, and the Blackadar model. The Blackadar plume model is currently the only one that is capable of interacting with DIRSIG's LIDAR module; however, future plans to incorporate higher-fidelity plume models such as QUIC-PLUME are also introduced in Section 3.7.

3.1 DIAL/DAS Systems

A variety of disciplines within the remote sensing community rely upon the ability to efficiently measure the gas or molecular constituents within a path of interest. This is particularly true in monitoring pollution and measuring trace elements within the atmosphere. One of the techniques is the differential absorption LIDAR (DIAL) technique introduced by Schotland (1966). The roots of the DIAL technique are in the remote sensing of atmospheric properties utilizing the absorption and scattering processes of particles and molecular species prior to the invention of the laser. Advances in lasers made over the last 20 years have paved the way for a suite of elegant and useful remote sensing techniques to measure the constituents within a participating medium. For instance, Schotland was measuring water vapor using a simple ruby laser and was then restricted to a limited set of transmit wavelengths. Such restrictions are not as prevalent today due to advances in laser and receiver technology. The continued expansion of LIDAR techniques will rely upon the availability of tunable laser sources to match the absorption lines of various atmospheric gases. The ability to transmit short, coherent pulses of high-intensity energy in a narrow beam and over a very narrow spectral bandwidth is one of the distinct advantages of a laser

in this application. The nature of the laser allows one to employ a set of very powerful optical remote sensing techniques to probe the atmosphere and gaseous volumes, such as plumes or clouds. The DIAL method represents a very selective and sensitive method of measuring those constituents. The purpose of this section is to provide a broad overview of the DIAL technique including the governing equations for DIAL systems and transfer into a top-level discussion of a typical DIAL system design. The latter portion of this section lays the foundation for the basis of how scattering may effect DIAL measurements by covering the detection threshold and sensitivity of the concentration measurements based upon a DIAL approach and the importance of accounting for multiply scattered returns. As part of this discussion, a practical multiple scatter LIDAR equation developed by Eloranta (1972, 1998) will be explored.

3.1.1 Principles of the DIAL Method

The underlying principle of the DIAL method is that the signal attenuation due to a particular molecule in the atmosphere or the participating medium can be used to derive the number density of that molecule along the laser's path. A simple DIAL collection scenario is illustrated in Figure 1. A pair of short pulses at two different wavelengths are transmitted along the same path and the receiver monitors the backscattered LIDAR signal. The return signal is comprised of backscattered returns from the atmosphere, the background, and the participating medium of interest. For the purposes of this illustration, the participating medium is assumed to be a gaseous plume. The wavelength λ_{abs} of one pulse is chosen to coincide with a unique strong absorption feature of the gas of interest and is known as the absorption wavelength. The complementary pulse is transmitted at a reference wavelength λ_{ref} that is detuned slightly from the absorption wavelength and is in the "wing" of the spectral feature. This permits the processor to decouple the absorption of the constituent of interest from the absorption and scattering of other contributors along the path. Essentially, the DIAL sensor receives two return signals similar in form to those shown in Figure 1. Notice the increase in backscatter for the ranges where the plume exists and notice the differences in the returns at each wavelength. In this scenario, the primary scattering mechanism needed to ensure an adequate signal-to-noise ratio (SNR) is assumed to be due to elastic scattering from atmospheric aerosols and particulates. This subset of the DIAL

methods is frequently referred to as "differential absorption and scattering" (DAS). Alternatively, one could employ a strategically placed topographical target or retroreflector to ensure a strong return signal. In some cases, DIAL systems rely upon the underlying surfaces (such as the ground around a gas pipeline) to be the topographic target.

The next stage examines the ratio of the observed power from the reference and absorption pulses. Figure 2a and Figure 2b show an example of a DIAL measurement of a plume with SO_2 published by Measures (1988). The diagrams show the averaged return signals at the absorption and reference wavelengths as described previously in this section. The ratio of the two signals is shown in Figure 2c. Based upon this ratio, the concentration as a function of range was then calculated for each range interval of 50 m (R±25 m) and is shown in Figure 2d. While the DIAL methodology may appear fairly straightforward, the design or modeling of the system can be quite complex. For instance, selection of the wavelengths is strongly influenced by more than the absorption spectrum of the gas of interest. The availability of a laser at that wavelength, the absorption spectrum of other constituents in the atmosphere and participating medium, the scattering nature of the medium, the detector type available, and the range resolution are just a few of the critical factors. Some of the subtleties will become clearer in the next few subsections as the governing equations are introduced and explored.

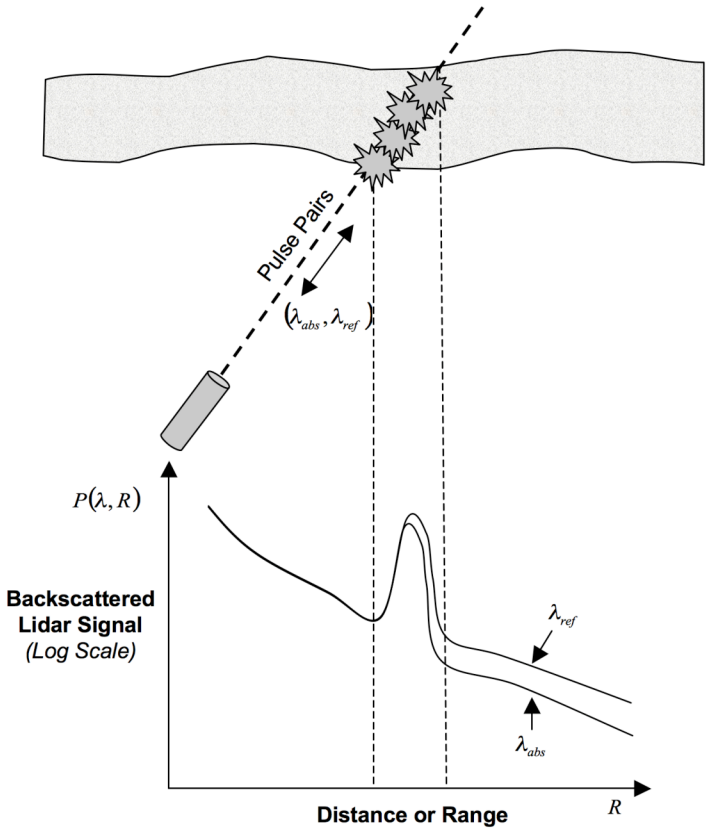


Figure 1: Illustration of DIAL principles

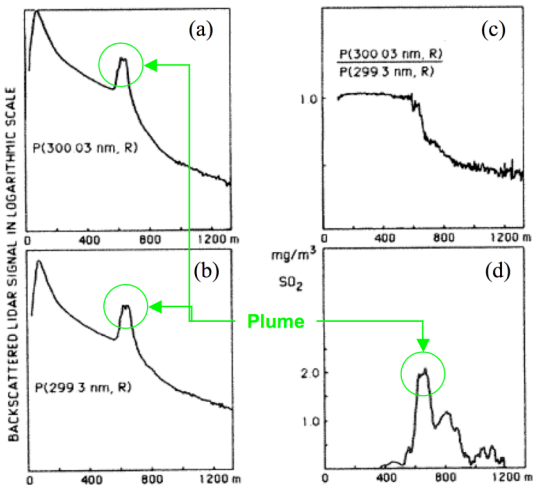


Figure 2: Example of DIAL measurement of SO_2 (Measures, 1988)
(a) Absorption LIDAR signal, (b) Reference LIDAR signal,
(c) DIAL curve, and (d) Calculated concentrations

3.1.2 DIAL LIDAR Equation

The governing equations for the received signal power captured by the DIAL sensor and the associated concentration calculation are derived from a general LIDAR equation for elastic scattering. The derivation of the elastic LIDAR equation from fundamental electromagnetics is well established in literature and additional details can be found in Measures' book (1984). Measures' discussion involves a much more complex and complete form of the LIDAR equation which can be simplified for DIAL applications where only elastic scattering is considered. Stated without proof, the received power from a range R due to elastic backscattered radiation can be written as:

$$P(\lambda,R) = \xi(\lambda,R)\frac{A_r}{R^2}P_L(\lambda)\Delta R\sum_i C_{B_i}(\lambda)N_i(R) \times \exp\left[-2\int_0^R\left[\sum_m C_{A_m}(\lambda)N_m(r)+\sum_p C_{A_p}N_p(r)+\sum_i C_{B_i}N_i(r)\right]dr\right] \quad (1)$$

where $\xi(\lambda,R)$ is a system function determined by the geometric considerations of the receiver optics, the quantum efficiency of the detection system at each wavelength, and the overlap between the transmitted laser beam and the field of view of the receiver; A_r is the area of the entrance pupil; A_r/R^2 is the acceptance solid angle of the receiver optics with a collecting area A_r; $P_L(\lambda)$ is the average power in the transmitted pulse at wavelength λ; ΔR is the effective range resolution of the LIDAR signal; $C_{B_i}(\lambda)$ is the backscattering cross-section at wavelength λ; $N_i(r)$ is the number density of scatter species i at range r; $C_{A_p}(\lambda)$ is the particle species absorption cross-section at wavelength λ; $N_p(r)$ is the number density of particle absorbing species p at range r; $C_{A_m}(\lambda)$ is the molecular species absorption cross-section at wavelength λ; and $N_m(r)$ is the number density of molecular absorbing species m at range r.

Using the definitions for the backscattering (σ_β) and extinction (σ_{ext}) coefficients:

$$\sigma_\beta(\lambda,R) = \sum_i C_{B_i}(\lambda) N_i(R) \tag{2}$$

$$\sigma_{ext}(\lambda,r) = \sum_m C_{A_m}(\lambda) N_m(r) + \sum_p C_{A_p} N_p(r) + \sum_i C_{s_i} N_i(r) \tag{3}$$

and substituting the limit for the effective range resolution, the elastic LIDAR equation may be rewritten as:

$$P(\lambda,R) = \xi(\lambda,R)\frac{A_r}{R^2} P_L(\lambda)\frac{c(\tau_L + \tau_D)}{2}\sigma_\beta(\lambda,R) \times \exp\left[-2\int_0^R \sigma_{ext}(\lambda,r)\, dr\right] \tag{4}$$

where c is the speed of light, τ_L is the laser pulse duration, and τ_D is the integration time of the detector. If the detector's integration time is small in comparison to the pulse duration, then the received power becomes:

$$P(\lambda,R) = \xi(\lambda,R)\frac{A_r}{R^2} P_L(\lambda)\frac{c\tau_L}{2}\sigma_\beta(\lambda,R) \times \exp\left[-2\int_0^R \sigma_{ext}(\lambda,r)\, dr\right] \tag{5}$$

Although not readily apparent, Equation 5 includes the underlying assumption that the multiple scattering effects are minimal. Essentially, the single scattering component is assumed to be the dominant term and the diffuse contribution from multiple scattering is negligible. Although even today most LIDAR techniques are based upon the single scattering approximation, the multiple scattering contributions do represent a source of error in the DIAL calculations and in some cases can be leveraged to extract additional information on the aerosol extinction coefficient and particle sizes (Bissonnette and Roy, 1998). An alternate LIDAR equation that accounts for most of the multiple scattering effects will be addressed in Section 3.2. The potential impact of this assumption on DIAL concentration measurements will also be briefly discussed in Section 3.1.4.

Although some advantages exist for employing more than two wavelengths in a DIAL system, the most common approach is to select only two wavelengths, the absorption and reference wavelengths. As stated previously, the simplest algorithm examines the ratio of the

received power from the two complimentary pulse trains, which can be mathematically expressed as:

$$\frac{P(\lambda_{abs},R)}{P(\lambda_{ref},R)} = \frac{\xi(\lambda_{abs},R)P_L(\lambda_{abs})\sigma_\beta(\lambda_{abs},R)}{\xi(\lambda_{ref},R)P_L(\lambda_{ref})\sigma_\beta(\lambda_{ref},R)} \exp\left[-2\int_0^R \sigma_{ext}(\lambda_{abs},r) - \sigma_{ext}(\lambda_{ref},r)\ dr\right] \tag{6}$$

if the solid angles for the beams and the effective range resolutions at each wavelength are approximately equal. This expression can be further simplified if one assumes that the backscatter for the aerosols and the scattering and absorption for the background constituents are relatively equivalent at the two wavelengths. The ratio of the two powers becomes:

$$\frac{P(\lambda_{abs},R)}{P(\lambda_{ref},R)} = \frac{\xi(\lambda_{abs},R)P_L(\lambda_{abs})}{\xi(\lambda_{ref},R)P_L(\lambda_{ref})} \exp\left[-2\int_0^R \left[\sum_m \left(C_{A_m}(\lambda_{abs}) - C_{A_m}(\lambda_{ref})\right)\ N_m(r)\right] dr\right] \tag{7}$$

If one assumes that one molecular species dominates the differential absorption at the frequencies chosen, then the summation terms cancel in the exponential for all species except that of interest. After applying this assumption and taking the logarithm of both sides, then the expression can be rewritten as:

$$\int_0^R N_m(r)\ dr = \frac{1}{2\left[C_{A_m}(\lambda_{abs}) - C_{A_m}(\lambda_{ref})\right]} \left\{\ln\left[\frac{P(\lambda_{ref},R)}{P(\lambda_{abs},R)}\right] + \ln\left[\frac{\xi(\lambda_{abs},R)P_L(\lambda_{abs})}{\xi(\lambda_{ref},R)P_L(\lambda_{ref})}\right]\right\} \tag{8}$$

After differentiating with respect to the range R, the number density of the absorbing molecules can be expressed as:

$$N_m(R) = \frac{1}{2\left[C_{A_m}(\lambda_{abs}) - C_{A_m}(\lambda_{ref})\right]} \frac{d}{dR}\left[\ln\left[\frac{P(\lambda_{ref},R)}{P(\lambda_{abs},R)}\right] + \ln\left[\frac{\xi(\lambda_{abs},R)P_L(\lambda_{abs})}{\xi(\lambda_{ref},R)P_L(\lambda_{ref})}\right]\right] \tag{9}$$

Then one can find the molecular number density averaged over a range $\Delta R = R_2 - R_1$ by integrating both sides from R_1 to R_2:

$$\int_{R_1}^{R_2} N_m(r)\ dr = \frac{1}{2\left[C_{A_m}(\lambda_{abs}) - C_{A_m}(\lambda_{ref})\right]} \left[\begin{array}{l} \ln\left[\dfrac{P(\lambda_{ref},R_2)P(\lambda_{abs},R_1)}{P(\lambda_{abs},R_2)P(\lambda_{ref},R_1)}\right] \\ + \ln\left[\dfrac{\xi(\lambda_{abs},R_2)\xi(\lambda_{ref},R_1)P_L(\lambda_{abs})}{\xi(\lambda_{ref},R_2)\xi(\lambda_{abs},R_1)P_L(\lambda_{ref})}\right] \end{array} \right] \tag{10}$$

The averaged molecular number density $\left(\overline{N}_m\right)$ then can be written as:

$$\overline{N}_m = \frac{1}{2(R_2 - R_1)\left[C_{A_m}(\lambda_{abs}) - C_{A_m}(\lambda_{ref})\right]} \left[\begin{array}{l} \ln\left[\dfrac{P(\lambda_{ref},R_2)P(\lambda_{abs},R_1)}{P(\lambda_{abs},R_2)P(\lambda_{ref},R_1)}\right] \\ + \ln\left[\dfrac{\xi(\lambda_{abs},R_2)\xi(\lambda_{ref},R_1)P_L(\lambda_{abs})}{\xi(\lambda_{ref},R_2)\xi(\lambda_{abs},R_1)P_L(\lambda_{ref})}\right] \end{array} \right] \tag{11}$$

This expression is often simplified by assuming that the system function for the receiver optics and the average pulse power are similar at the chosen wavelengths. Thus the second logarithmic term is assumed to be negligible and the expression for the averaged molecular number density can be rewritten as:

$$\overline{N}_m = \frac{1}{2(R_2 - R_1)\left[C_{A_m}(\lambda_{abs}) - C_{A_m}(\lambda_{ref})\right]} \ln\left[\frac{P(\lambda_{ref},R_2)P(\lambda_{abs},R_1)}{P(\lambda_{abs},R_2)P(\lambda_{ref},R_1)}\right] \tag{12}$$

One should note that in many operation DIAL systems, this assumption may not be valid and must be compensated for in the processing algorithms.

As alluded to earlier, the detection sensitivity may be improved by employing a topographical scatterer or retro reflecting mirror as the primary scattering mechanism. Similar to the previous case with the aerosol scattering returns, the return signal instantaneous power becomes:

$$P(\lambda,R_T)=\xi(\lambda,R_T)\frac{A_r}{R_T^2}P_L(\lambda)\frac{\rho_S(\lambda)}{\pi} \times\exp\left[-2\int_0^{R_T}\left[\sum_m C_{A_m}(\lambda)N_m(r)+\sum_p C_{A_p}N_p(r)+\sum_i C_{s_i}N_i(r)\right]dr\right] \tag{13}$$

where $\rho_S(\lambda)$ is the backscattering efficiency of the topographic target, R_T is the range to the topographic target, and the other variables are as described previously. For this DIAL approach, the radiative energy received from the topographic target during the detector's integration period is of primary interest and can be expressed as:

$$E(\lambda,R_T)=\xi(\lambda,R_T)\frac{A_r}{R_T^2}E_L(\lambda)\frac{\rho_S(\lambda)}{\pi} \times\exp\left[-2\int_0^{R_T}\left[\sum_m C_{A_m}(\lambda)N_m(r)+\sum_p C_{A_p}N_p(r)+\sum_i C_{s_i}N_i(r)\right]dr\right] \tag{14}$$

where $E(\lambda,R_T)$ is the radiative energy received from the topographic target at distance R_T provided that the integration period of the detector (τ_d) is kept longer than the laser pulse duration (τ_L), and $E_L(\lambda)$ is the transmitted energy of the laser pulse. Using a similar approach to the DAS technique, the average molecular number density can be shown to be:

$$\overline{N}_m=\frac{1}{2R_T\left[C_{A_m}(\lambda_{abs})-C_{A_m}(\lambda_{ref})\right]}\ln\left[\frac{E(\lambda_{ref},R_T)E_L(\lambda_{abs})\rho_S(\lambda_{abs})}{E(\lambda_{abs},R_T)E_L(\lambda_{ref})\rho_S(\lambda_{ref})}\right] \tag{15}$$

Note that the wavelength dependence of reflectivity of the topographic target must be carefully considered for this approach. This is particularly true for DIAL sensors operating in the infrared region (Measures, 1988).

3.1.3 Typical System Configuration

The configuration of the primary hardware components for a typical LIDAR system, including a DIAL sensor, is shown in Figure 3. The setup can be divided into four major partitions: the transmitter, the receiver, the detector, and the processor. This subsection attempts to briefly describe each of the major components and their role in DIAL measurements.

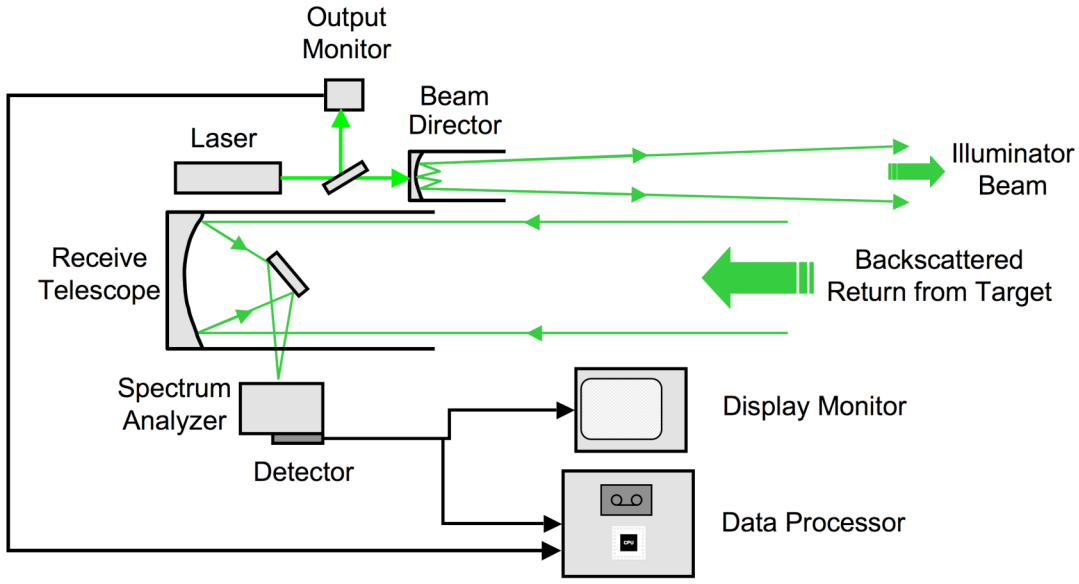


Figure 3: Configuration of typical DIAL system

3.1.3.1 Transmitter

The transmitter is perhaps the most critical component for a DIAL system. The transmitter generates and directs high energy pulses at the prescribed wavelengths through the atmosphere to the target area. The laser has distinct advantages over other light sources in the form of low beam divergence, extremely narrow spectral width, and short intense pulses. Because the background radiance is a significant source of noise for DIAL measurements, the designers prefer to have as small field of view (FOV) as possible. The beam director not only guides the laser beams such that the FOVs of the two transmitted pulses align on the target, but is also used to ensure that the beam is sufficiently well-collimated for transmission through the atmosphere. Thus, the beam divergence is minimized. The narrow spectral width is an inherent feature of lasers, which is advantageous for DIAL measurements because the

narrow spectral width ensures that the energy emitted is only at the wavelength of either the reference or absorption markers.

The pulsing capability of the laser makes it an ideal source for range gating and to maximize increased average power by manipulating the peak transmit power, the pulse duration, and the pulse repetition frequency (PRF). The selection and design of the laser drives the potential performance that can be achieved by the DIAL system. The choice of laser is based upon many factors: desired wavelengths, tunability, output energy, repetition rate, desired duty cycle, and cost. Table 1 lists lasers typically used in LIDAR systems in the 1990s. Although more advanced lasers currently exist, the parameters listed are still consistent with current practical DIAL systems.

The type of laser and wavelength are tightly coupled to the location of the absorption line and reference frequency for the molecular constituent of interest. The next item to consider is the pulse energy. The peak power is a limiting design parameter for each laser, but signal averaging can increase the SNR of the system. However, a high-energy pulse for a few shots is ideal for tracking plumes due to the dynamic nature of plumes. In addition, the signal averaging process must be balanced with the repetition rate and the pulse duration. A faster repetition rate permits additional signal averaging over a fixed time window and thus results in a higher SNR. The laser then must operate at a higher duty cycle, which affects the operational ranges for the system. The PRF is constrained to ensure that each pulse returns from the nominal target range prior to transmission of the next pulse. This requirement limits the range ambiguity between pulses. High-:duty cycle lasers up to continuous wave (CW) can be employed provided that advanced modulation coding techniques are utilized. Such a system is often cost prohibitive and technically complex.

Additionally, one should note that the cost-benefit trade changes depending upon the spectral region of the laser. For instance, a visible DIAL system's SNR is directly proportional to the product of the PRF and the emitted energy. A balance is needed for a visible system. In contrast, the SNR of an IR DIAL system is directly proportional to the emitted energy of the signal because the detector tends to be dominated by detector noise and not shot noise;

therefore, firing just a few shots at high power is a preferred approach. Mixed in with the design trade-space is the pulse duration. Longer pulse durations result in poorer spatial resolution, but an increase in average transmitted power. Once again, the parameters of the transmitter are highly design specific and depend greatly upon the availability of a good laser at the wavelengths of interest.

Table 1: Sample lasers used in LIDAR systems (Zanzotera, 1990)

Type	Wavelength (μm)	Typical Energy (J)	Pulse Duration (μs)	Rep Rate (Hz)
Gas				
CO_2	9-11	0.1-1.0	0.1-2.0	10-50
CO	5-6	0.01-0.05	10	10
HF	2.7-3.0	0.1-0.5	0.1-1.0	1-10
DF	3.7-4	0.1-0.5	0.1-1	1-10
Excimer				
ArF	0.193	0.1	0.01	10-100
KrCl	0.222	0.1	0.01	10-100
KrF	0.249	0.1-0.5	0.01	10-100
XeBr	0.282	0.1	0.01	10-100
XeCl	0.308	0.1-0.5	0.01	10-100
XeF	0.352	0.1	0.01	10-100
Solid State				
Alexandrite	0.71-0.8	0.1-1	0.1-0.2	10
Ruby	0.6943	1	0.02	0.1
Nd:YAG	1.06	0.5-1	0.01	10-30
Nd:YAG x 2	0.532	0.2-0.5	0.01	10-30
Nd:YAG x 3	0.355	0.1-0.2	0.01	10-30
$Co:MgF_2$	1.5-2.3	0.01	0.3	10
Dye Laser				
Visible-NIR	0.4-0.8	0.1-0.01	0.01	10-30
UV	0.2-0.4	0.0001-0.01	0.01	10-30

3.1.3.2 Receiver

The receiver collects the backscattered LIDAR signal, performs some processing, and directs the radiance toward the detector focal plane. The primary optical element of the receiver is the telescope. The receiver telescope is usually a Newtonian, Cassegrainian or Gregorian type with a large parabolic primary mirror. Other configurations are utilized, but most operational DIAL systems are variants of these types. The receiver requires some sort of active or passive alignment system to ensure that the narrow transmit and receive beams overlap properly and maintain that alignment during an engagement. In some instances, a

polarizing filter is added to the optical chain to reduce multiple scattering effects from the background radiation prior to processing by a spectral discriminator or analyzer. The analyzer separates the wavelengths of interest and filters the light to optimize performance for a very narrow bandwidth around those center frequencies.

3.1.3.3 Detector

Two primary modes of detection are used in LIDAR systems: direct detection and heterodyne detection. Direct detection is the simplest and provides a proportional response to the number of photons detected. Heterodyne detection allows one to operate at a lower SNR while maintaining a detection threshold, but is more costly and complex to build. The detector characteristics depend upon the spectral region of interest and are similar to optical detectors used in passive optical remote sensing.

3.1.3.4 Data Processor

After the return signals are recorded, they need to be processed to estimate concentrations based upon the power ratios and the absorption properties of the gas. A processing flow chart of a typical DIAL processor is shown in Figure 4. The core portion of a DIAL processor is fairly straightforward; however, the critical steps are usually in the pre-processing stages before calculating the concentration path length (CPL) and are often design specific.

To begin processing, three classes of datasets are typically required for generating a CPL map: the raw sensor data, the flight data, and the calibration data. The processor requires some general input parameters, which tend to be system or processor specific and often remain the same for different collects. The raw sensor data is the captured linear signal from the detector after the signal has been sent through the A/D converter and formatted into an intelligible form. The flight data includes such items as the platform location for each pulse, the estimated transmit times, the receive windows, the sensor pointing angles, the A/D rate, etc. The calibration data vary based upon the specific system design. The processor leverages the calibration data to adjust for the reference and absorption actual pulse powers, timing, and pulse width.

The first step is to pre-process the raw data and ingest it into a usable format for the processor. In some instances, a form of motion compensation may be applied to the pointing data. The next step is to calibrate each pulse so that the relative transmitted power of the reference and absorption pulses are known or ideally are the same. For most systems, the transmitted power of the pulses can vary from pulse to pulse and is not always the same for the reference and absorption pulse sequence. Although one could calibrate the data, this step is often combined with normalization so that the SNR is maximized during the next few signal processing operations. After calibration, the return signals are filtered to remove the background signal and noise. In some cases, the background estimate is made from a dark image processed through the calibration stage. The challenge is to filter the return signal to remove as much noise as possible without significantly damaging the peak returns. The next step is to use information from the returned pulses to align the absorption and reference signals. Pulse-finding algorithms range from the very simple to highly complicated algorithms depending upon the stability and operational characteristics of the DIAL sensor.

Once aligned, the pulses are integrated and then normalized. A set of pulses at each wavelength may be averaged to obtain the desired concentration sensitivity and inherent SNR of the design. Finally, the CPLs are calculated based upon the integrated power ratio between the absorption and reference returns. The range is then calculated based upon a standard topographical method and a CPL is assigned to that 3-D coordinate. Additionally, a suite of statistics, such as the mean profiles or a time-averaged 3-D concentration map, may be calculated. Because of the narrow FOV, the spatial extent of the maps is limited. Thus the DIAL sensor scan motion must be used to generate a more complete picture, but it also adds complications due to the need for accurate motion compensation and spatial registration of the profiles in the pre-processing and calibration phase.

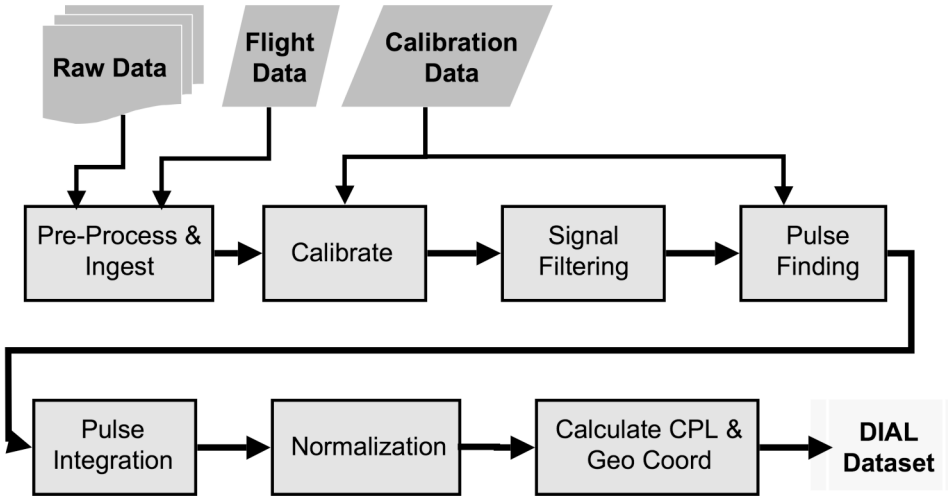


Figure 4: Generalized DIAL processing algorithm

3.1.4 Detection Limit and Concentration Sensitivity

The minimum detection threshold for a DIAL system is often of key interest during system design or when comparing performance. The remote sensing community uses a variety of techniques and measures to determine the detection limit of a DIAL system; however, the primary approach introduced in this subsection is a variant of one presented by Measures (1984). This subsection explores the ability of a dual wavelength-based DIAL system to detect a change in concentration by examining the incremental change in observed energy from either the aerosol return or the topographical target.

3.1.4.1 Detection Limit for Aerosol Return

For a DAS sensor, the incremental change in the observed energy for an aerosol return due to the attenuation by molecular constituent of interest over a range increment of ΔR is:

$$\Delta E^{*} = \Delta E_{abs} - \Delta E_{ref} \tag{16}$$

where the decrease in the signals at each wavelength are:

$$\Delta E_{abs} = E\left(\lambda_{abs}, R\right) - E\left(\lambda_{abs}, R + \Delta R\right) \tag{17}$$

$$\Delta E_{ref} = E\left(\lambda_{ref}, R\right) - E\left(\lambda_{ref}, R + \Delta R\right) \tag{18}$$

If one assumes that the reference signal decreases less than the received signal at the absorption wavelength, then the detection of the overall incremental change should satisfy:

$$E(\lambda_{abs},R) - E(\lambda_{abs},R+\Delta R) > \frac{E(\lambda_{abs},R+\Delta R)}{SNR} \tag{19}$$

where SNR is the signal-to-noise ratio. This requirement essentially states that the incremental change in the signal must be greater than the noise in the signal from the range $R+\Delta R$. Using some simple algebra, the relationship can also be rewritten as:

$$\frac{E(\lambda_{abs},R)}{E(\lambda_{abs},R+\Delta R)} > \left[1+\frac{1}{SNR}\right] \tag{20}$$

The next step is to evaluate the left side of the expression using Equation 5. The received energy at the absorption wavelength is:

$$E(\lambda_{abs},R) = \xi(\lambda_{abs},R)\frac{A_r}{R^2}E_L(\lambda_{abs})\frac{c\tau_D}{2}\sigma_\beta(\lambda_{abs},R)\times\exp\left[-2\int_0^R \sigma_{ext}(\lambda_{abs},r)\,dr\right] \tag{21}$$

If one assumes that the loss in energy over the range interval $(R,R+\Delta R)$ is dominated by the absorption of the molecule of interest, then the left side of Equation 20 becomes:

$$\frac{E(\lambda_{abs},R)}{E(\lambda_{abs},R+\Delta R)} = \frac{(R+\Delta R)^2}{(R)^2}\times\exp\left[2\int_R^{R+\Delta R} C_m(\lambda_{abs})\,N(r)\,dr\right] \tag{22}$$

Assuming that the gas density is relatively constant over the effective range resolution of the sensor such that:

$$\int_R^{R+\Delta R} N(r)\,dr \approx N(R)\,\Delta R \tag{23}$$

then the ratio of energies can be written as:

$$\frac{E(\lambda_{abs},R)}{E(\lambda_{abs},R+\Delta R)} \approx \frac{(R+\Delta R)^2}{(R)^2}\times\exp\left[2C_m(\lambda_{abs})N(R)\Delta R\right] > \left[1+\frac{1}{SNR}\right] \tag{24}$$

After evaluating the logarithm of both sides and manipulating the terms, the minimum detectable concentration for the aerosol scattering DIAL methodology is:

$$\left[N(R)\right]_{\min} = \frac{1}{2C_m(\lambda_{abs})\Delta R} \ln\left[\left(1+\frac{1}{SNR}\right)\left(\frac{R}{R+\Delta R}\right)^2\right] \tag{25}$$

If the effective range resolution of the system is small in comparison to the range of the plume, then the equation for the minimum detectable concentration can be further simplified and expressed as:

$$\left[N(R)\right]_{\min} = \frac{1}{2C_m(\lambda_{abs})\Delta R} \ln\left[\left(1+\frac{1}{\left[SNR\right]_{\min}}\right)\right] \tag{26}$$

Note that the concentration above is expressed in units of m^{-3} and can be converted to parts per million (ppm), using the following conversion:

$$c_{\min} = \frac{N_{\min} \times 10^6}{N_{atm}} \tag{27}$$

where N_{atm} is the atmospheric molecular density and $N_{atm} \approx 2.55 \times 10^{25}$ m^{-3} at standard temperature and pressure.

Equation 26 shows that the minimum detectable concentration is primarily determined by the range resolution of the system, the absorption cross-section of the constituent of interest, and the system SNR. One additional factor is the difference in absorption cross-section. Recall that we assumed that the difference in the reference return signal is negligible due to the increase in concentration of the molecule or particle of interest. If the absorption cross-section at the reference wavelength is similar to that at the absorption wavelength, then the change in the reference return signal is significant.

A more conservative expression for the minimum detectable concentration, which accounts for this factor is (Zanzotera, 1990):

$$\left[N(R)\right]_{\min} = \frac{1}{2\left(C_m(\lambda_{abs}) - C_m\left(\lambda_{ref}\right)\right)\Delta R}\ \frac{2}{\left[SNR\right]_{\min}} \tag{28}$$

For either Equation 26 or 28, the increase in SNR permits a lower detection threshold and greater sensitivity.

Increasing the average transmit power must be balanced with the range resolution. If one increases the average transmit power by extending the transmit pulse length, then the range resolution is decreased. A better approach would be to improve the optical gain, integrating over a series of pulses, or improving detector sensitivity of the system to improve the SNR while maintaining the best possible range resolution. This is one reason that approximately 100 pulses are typically averaged for each return signal in the concentration calculation for highly sensitive DIAL sensors. This discussion is predicated on the absorption cross-sections at the various wavelengths to result in an observable difference.

3.1.4.2 Detection Limit for a Topographic Return

Topographic targets are used to gain greater sensitivity due to a better SNR for low backscatter collections, but sacrifice the range information associated with the concentration measurements. Thus, the detection limit derived previously is not entirely valid; however, the general form and the parameter dependence of the detection limit correlates well with the minimum detection threshold for an aerosol return. Similar to the aerosol return case, the change in energy for a topographic return can be expressed as:

$$\Delta E = E\left(\lambda_{ref}, R_T\right) - E\left(\lambda_{abs}, R_T\right) \tag{29}$$

The change in energy due to absorption by the constituent of interest should be larger than the fluctuations in energy due to the inherent signal noise. This requirement can be expressed as:

$$E\left(\lambda_{ref},R_T\right)-E\left(\lambda_{abs},R_T\right)>\frac{E\left(\lambda_{abs},R_T\right)}{SNR} \tag{30}$$

A viable alternative is to consider the change in energy with respect to the overall signal energy and to require that this ratio be larger than the noise. The result is:

$$\frac{E\left(\lambda_{ref},R_T\right)-E\left(\lambda_{abs},R_T\right)}{E\left(\lambda_{abs},R_T\right)}>\frac{E\left(\lambda_{abs},R_T\right)}{SNR} \tag{31}$$

Equation 31 is more conservative and significantly easier to evaluate. In addition, Equation 31 requires knowledge about the optical path length, which is not always known a priori. Thus we shall continue with the previous requirements, which can be reduced to:

$$\frac{E\left(\lambda_{ref},R_T\right)}{E\left(\lambda_{abs},R_T\right)}>\left[1+\frac{1}{SNR}\right] \tag{32}$$

Note that this is a familiar construct. Using the DIAL equation for the return energy from a topographic target, the left-hand ratio becomes:

$$\frac{E\left(\lambda_{ref},R_T\right)}{E\left(\lambda_{abs},R_T\right)}=\frac{\xi\left(\lambda_{ref},R_T\right)E_L\left(\lambda_{ref}\right)}{\xi\left(\lambda_{abs},R_T\right)E_L\left(\lambda_{abs}\right)}\frac{\rho_S\left(\lambda_{ref}\right)}{\rho_S\left(\lambda_{abs}\right)}\times\exp\left[2\int_0^{R_T}\left[\sigma_{ext}\left(\lambda_{abs},r\right)-\sigma_{ext}\left(\lambda_{ref},r\right)\right]\,dr\right] \tag{33}$$

If one assumes that the system effects, pulse energies, and nominal path attenuation are equivalent, then the equation simplifies to:

$$\frac{E\left(\lambda_{ref},R_T\right)}{E\left(\lambda_{abs},R_T\right)}=\frac{\rho_S\left(\lambda_{ref}\right)}{\rho_S\left(\lambda_{abs}\right)}\times\exp\left[2\left[C_m\left(\lambda_{abs}\right)-C_m\left(\lambda_{ref}\right)\right]\int_0^{R_T}N(r)\,dr\right] \tag{34}$$

If the gas of interest is restricted to a range interval (R_1, R_2), then the molecular concentration $N(r)$ may be considered a constant over the interval (R_1, R_2) and zero elsewhere. Based upon these assumptions, the requirement can be mathematically expressed as:

$$\frac{\rho_S(\lambda_{ref})}{\rho_S(\lambda_{abs})} \times \exp\left[2\left[C_m(\lambda_{abs}) - C_m(\lambda_{ref})\right]\int_0^{R_T} N(r)\,dr\right] > \left[1 + \frac{1}{SNR}\right] \tag{35}$$

Solving for the minimum detectable concentration, the result is:

$$\left[N_{topo}\right]_{\min} = \frac{1}{2(R_2 - R_1)} \frac{1}{\left[C_m(\lambda_{abs}) - C_m(\lambda_{ref})\right]} \left\{\ln\left[1 + \frac{1}{SNR}\right] + \ln\left[\frac{\rho_S(\lambda_{abs})}{\rho_S(\lambda_{ref})}\right]\right\} \tag{36}$$

Note that if the backscatter cross section of the topographic target can be considered constant over the two wavelengths, then that term drops out and the Equation 36 simplifies to:

$$\left[N_{topo}\right]_{\min} = \frac{1}{2(R_2 - R_1)} \frac{1}{\left[C_m(\lambda_{abs}) - C_m(\lambda_{ref})\right]} \ln\left[1 + \frac{1}{SNR}\right] \tag{37}$$

As shown for the aerosol return, the detection limit is driven by the SNR and by the difference in the absorption cross section at the two wavelengths for the molecular constituent of interest. The range resolution dependence in the aerosol case is replaced by the thickness of the plume or participating medium. If the plume is very shallow, then the system detection threshold is high. In contrast, if the participating medium is very thick, like an atmospheric layer or cloud, then the detection threshold is much lower.

3.1.4.3 Concentration Sensitivity and Interfering Constituents

The accuracy of DIAL measurements depends upon a variety of factors. During system design, these factors must be handled carefully and optimized for the intended operational scenario. A comprehensive error analysis for a DIAL system was documented by Measures (1984). The optimization techniques are addressed well in the literature and will not be considered here. While designing a DIAL system, the key factors that determine the potential accuracy are the SNR limits, the absorption properties of the constituent of interest, the spatial, temporal and spectral dependent aspects of the system, and the atmospheric conditions (including multiple scattering effects).

For a DIAL measurement, the SNR is driven by the shot noise of the signal, the background noise, and the dark current. The dark current is a design factor and is not directly affected by scattering media. The signal shot noise is the fluctuation in the detected signal from a statistical mean. It is directly impacted by the spatial and temporal stability of the laser, but also is impacted by the spatial and temporal stability of the atmospheric conditions surrounding the plume. Similarly, the background noise could be increased such that the laser backscattered signal is buried within the background radiation. This is typically counteracted using filters and a narrow field of view. While the SNR could be impacted by the presence of scatterers in the form of additional noise, a well-designed system should not exhibit degraded performance.

As mentioned previously in the detection limit discussion (Section 3.1.4), the absorption cross-sections of the constituents in the plume and path and the degree to which they are accurately known directly impacts the accuracy of the DIAL measurements. Absorption cross sections of atmospheric constituents can be determined with great accuracy in a lab environment; however, many of these molecules do not have strong absorption features in the frequency range of available lasers. Essentially, molecules have vibrational-rotational absorption lines in the infrared (IR) region. Unfortunately, collisions broaden otherwise sharp features of individual molecules and many of the molecules have overlapping features. Thus, DIAL measurements in the IR region present certain challenges, which can be overcome in certain instances. Additional constituents within the plume could theoretically mask the sharp spectral feature such that the differential absorption cross-section between the two wavelengths of interest is greatly reduced. The derivations in this section thus far have relied upon the fact that the molecular constituent of interest is the dominant absorber in the absorption wavelength and that in addition that no other dominant absorber is present at the reference wavelength that would reduce the returned reference signal significantly.

The spatial, temporal, and spectral dependent factors of the DIAL system are generally driven by the as-built design and the operational parameters and are not directly affected by the presence of interfering chemicals. The exceptions are for the backscattering and

extinction factors in the LIDAR equations. Both were considered to be spectrally independent. In other words, they were constant for both wavelengths. This assumption is reasonable provided that the wavelengths are sufficiently close together and that there are no interfering gases. In atmospheric studies, relative humidity has been known to affect the accuracy of DIAL measurements for gases such as CO_2. Water vapor or soot in a plume could have noticeable effects on the accuracy of the pollutant concentration measurements. To counter the effect, multiple wavelengths may be employed by applying much more complicated DIAL algorithms than the simplistic version introduced in this dissertation.

The atmospheric conditions combine multiple scattering and temporal effects. The LIDAR equations presented in this section are predicated upon single scattering events only; however, multiple scattering contributions to the backscattered return are often significant. For a dense plume, the returns from ranges behind the plume that are in fact due to multiple scattering must be accounted for. If not, the concentration measurement will be erroneous. The problem is exacerbated if the scattering cross sections are very large. Bissonnette and Roy (1998) showed that the DIAL ozone concentration inversion could be dramatically affected by the presence of multiple scattering when going from low to high visibility conditions. The resulting errors could be as large as 5% to 60%. They suggested a method to leverage the multiple scattering contributions and improve the computed results. The precise nature of their algorithm is not of primary concern here, but it does demonstrate the importance of accounting for multiple scattering. In theory, using polarization filters can minimize the effect of multiple scattering; however, other design considerations limit the use of this option. In particular, chemicals with a large scattering cross-section could possibly be skewed due to the multiple scattering. Theoretically, if the scattering cross-section for the scattering effluent is nearly constant over the wavelengths of interest, then the DIAL concentration measurements should be only slightly affected. However, there are a few exceptions. First, the temporal fluctuation in the background backscatter in conjunction with the time delay between the reference and absorption pulses may skew the concentration measurement. Secondly, if the substance significantly alters the mean path length of a photon in the participating medium, the concentration path length assessment would be altered. Both of these scenarios are reasonable and thus the effects of multiple scattering should be

included in any model development. The development of a multiple scattering LIDAR equation is explored in the next section, further emphasizes the importance of account for the effects of multiple scattering, and lays the groundwork for the first-principles physics-based LIDAR model that is presented later (Chapter 4).

3.2 Multiple Scattering LIDAR Equation

Many of the underlying principles, theory, and practical considerations for DIAL/DAS systems were just introduced in Section 3.2. In general, the theoretical foundation for LIDAR systems is built upon a single scattered LIDAR equation like Equation 1. The single scattering LIDAR equation encompasses the vast majority of the physics associated with a LIDAR system; however, significant multiple scattering is often present in DIAL/DAS applications. This section attempts to explore two fundamental questions about the effect of multiple scattering on the received LIDAR signal: (1) when is multiple scattering sufficiently significant to be considered? and (2) for a DIAL sensor, how will the system performance degrade in the presence of multiple scattering? To properly discuss these two issues, we shall first develop a practical multiply scattered LIDAR equation that incorporates as many multiple scattering effects as possible. Additionally, one should note that the multiply scattered LIDAR equation presented in this section forms the basis (in conjunction with the photon mapping paradigm) for the DIRSIG LIDAR module participating medium radiance solver.

3.2.1 Key Assumptions

The theory presented in this section was developed by Eloranta (1972, 1998) to enhance the study of size measurements of cloud droplets and particles; however, the principles can be extended to probing plumes with a DIAL system given some constraints and caveats. Before proceeding with the derivation, it is prudent to examine the key assumptions in the development of a multiply scattered LIDAR equation. Since Eloranta was primarily interested in cloud measurements, he restricted the discussion to participating layers dominated by forward scattering. This assumption is reasonable for scattering induced by water vapor or soot in a plume. Eloranta (1972) also shows in his dissertation that the multiply scattered LIDAR return is predominantly composed of photons that were

backscattered via only one large-angle scattering event. The photons may have undergone numerous multiple scatterings; however, these must have been small-angle forward-scattering events to allow photons to reach the receiver aperture. The small-angle forward-scattering events can certainly occur at any time throughout the round trip. This assumption is fairly intuitive, but exhibits the inherent axiom that those returns incident on the receiver are only from backscatter events in the medium. Although these certainly could be included at the cost of some additional complexity, the return from topographic targets and surfaces are not directly considered. Thus, photons returning from the medium must have undergone a large-scale scattering event that redirects them into receiver. The assumption is that if the photons incur a second large-scale redirection, then they will not likely remain within the receiver's field-of-view (FOV).

Based upon the preceding scenario, both the simplified approximation and the general derivation assume that:

- The forward peak of the scattering phase function can be approximated by a Gaussian phase function. In the case of the simplified approximation, this allows one to assume that half of the scattered energy is scattered into a forward diffraction peak. In the general derivation, this significantly simplifies the process of evaluating the redistribution of photons due to scattering events within the layer.
- The backscatter portion of the scattering phase function is assumed to be nearly isotropic in the backscatter direction. This permits direct calculation of the backscattered portion of the energy from a particular range within the medium. If the scattering phase function is generally forward, then this assumption is very reasonable.
- The laser beam is assumed to have a Gaussian spatial distribution with a known divergence angle.
- Multiply scattered photons that return to the receiver aperture have encountered only one large-scale backscattering event.
- Because the photons of interest have undergone only small-angle scattering events, the extra path length traveled by the photons is assumed to be negligible.

Additionally, the photons are not significantly delayed with respect to any singly scattered photons. In many cases, this assumption is reasonable; however, optically thick layers with a fair amount of scattering can induce significant path length differences between the singly and multiply scattered photons.

- The transverse dimension of the receiver FOV in the scattering layer is assumed to be much less than the optical mean free path of photons in the layer. If this is not true, then the derived set of equations overestimates the return signal. This assumption is appropriate for most airborne LIDAR systems; however, space borne systems will likely violate this constraint.

3.2.2 Simplified Approximation of Multiple Scattering

In this subsection, a simplified approximation for the ratio of the contribution of multiple scattered returns and the single scattered photons will be derived based upon the assumptions mentioned previously and upon the fundamental physics involved. The simplified approximation is not strictly valid in many cases, due to some liberties that we shall exercise in this section to simplify the problem; however, as will be shown in the general derivation, this intuitive approach has some validity for wide field-of-view LIDAR systems.

Consider the simplified multiple-scattering scenario described in Figure 5. A laser pulse is transmitted up towards a scattering layer at a distance x_c from the source. The receiver shares the same optical axis as the laser beam, but the receiver FOV is much larger than the transmit beam. Beer's law states that the transmitted power at a distance d within the layer can is:

$$P = P_0 \exp\left[-\sigma_{ext} d\right] \tag{38}$$

where P_0 is the transmitted power, σ_{ext} is the extinction coefficient of the scattering layer, and the penetration depth is $d = ct/2 - x_c$. Technically, not all of the scattered energy is lost. A fraction of the photons are scattered into the forward direction and have a high probability of remaining with the receiver FOV. If we assume that the forward-scattered photons do not incur a significantly delay with respect to the directly transmitted photons, then the primary

impact of those photons is a broadening of the spatial distribution of arriving photons at a particular range.

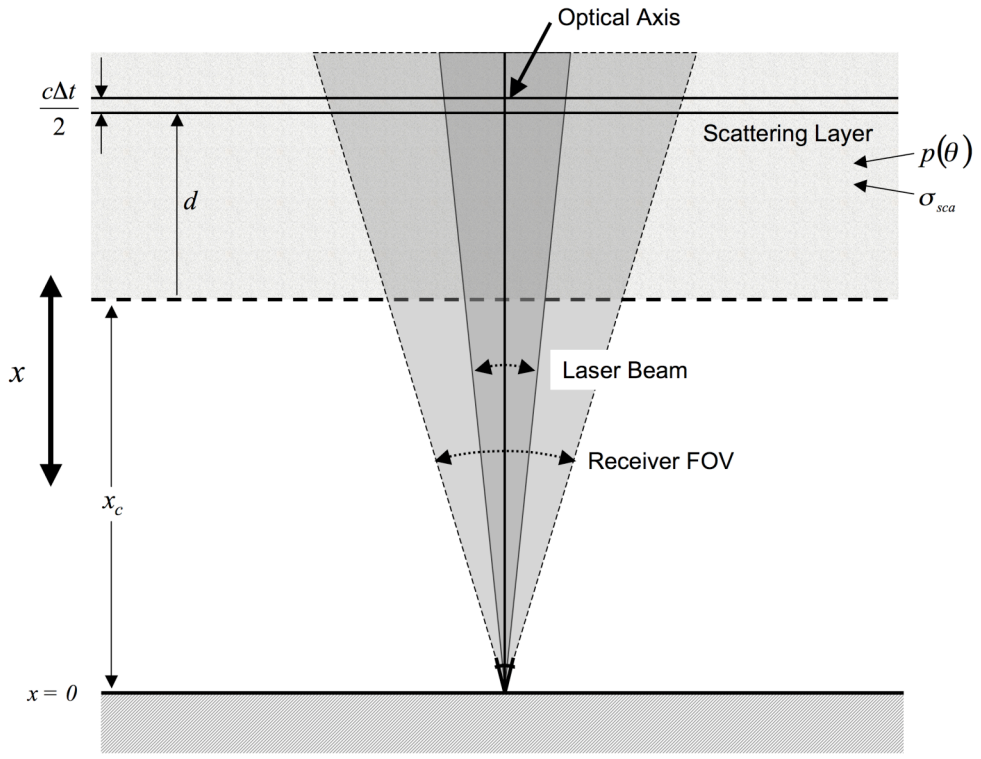


Figure 5: Simplified multiple scattering setup

If the scattering phase function is Gaussian in the forward scattering direction, then approximately half of the scattered energy remains within the diffraction peak and is not truly lost. To accommodate for this fraction of the energy, the power at penetration distance z within the layer can be mathematically expressed as:

$$P = P_0 \exp\left[-\sigma_{ext} d + \frac{\sigma_{sca} d}{2}\right] \tag{39}$$

where σ_{sca} is the scattering coefficient. We shall assume that the backscatter from a particular layer is generally isotropic in the backscatter direction. The result is that the photons are backscattered diffusely, when such an event occurs.

Thus, the power that returns from a particular penetration depth within the layer without any further scattering can be written as:

$$P = P_0 \sigma_{sca} \frac{c \cdot \Delta t}{2} \frac{p(\pi)}{4\pi} \omega_r \exp\left[-2\sigma_{ext} d + \frac{\sigma_{sca} d}{2}\right] \tag{40}$$

where $\sigma_{sca} \frac{p(\pi)}{4\pi}$ is the fraction of the energy that is backscattered per unit length and ω_r is the solid angle subtended by the receiver at that range. However, we have not yet accounted for the photons that are primarily forward scattered during the return trip. If we apply the same adjustment as for the transmit path, then the received power is:

$$\begin{aligned} P_t &= P_0 \sigma_{sca} \frac{c \cdot \Delta t}{2} \frac{p(\pi)}{4\pi} \omega_r \exp\left[-2\sigma_{ext} d + \frac{\sigma_{sca} d}{2} + \frac{\sigma_{sca} d}{2}\right] \\ &= P_0 \sigma_{sca} \frac{c \cdot \Delta t}{2} \frac{p(\pi)}{4\pi} \omega_r \exp\left[-2\sigma_{ext} d\right] \exp\left[\sigma_{sca} d\right] \end{aligned} \tag{41}$$

Then if we expand the last exponential term into a Taylor series, the expression becomes:

$$\begin{aligned} P_t &= P_0 \sigma_{sca} \frac{c \cdot \Delta t}{2} \frac{p(\pi)}{4\pi} \omega_r \exp\left[-2\sigma_{ext} z\right] \left(1 + \sigma_{sca} z + \frac{(\sigma_{sca} d)^2}{2!} + \frac{(\sigma_{sca} d)^3}{3!} + \ldots\right) \\ &= P_1 \left(1 + \sigma_{sca} d + \frac{(\sigma_{sca} d)^2}{2!} + \frac{(\sigma_{sca} d)^3}{3!} + \ldots\right) \end{aligned} \tag{42}$$

where P_1 is the predicted power for single scattering. The additional terms in the series on the right-hand side of the equation could be viewed as contributions from photons undergoing different numbers of scattering events. For instance, the second and third term represent the doubly and the triply scattered photon contribution, respectively the ratio of the multiply scattered and the singly scattered contributions is:

$$\frac{P_N}{P_1} = \frac{(\sigma_{sca} d)^{N-1}}{(N-1)!} \tag{43}$$

where P_N is the Nth-order scattering contribution. Eloranta (1998) denotes that the backscatter approximation made earlier is fairly crude and justifies an adjustment to account for this fact. The ratio of the Nth-order scattering contribution to the single-scatter contribution can be expressed as:

$$\frac{P_N}{P_1} = \frac{\langle p(\pi) \rangle_N}{p(\pi)} \frac{(\sigma_{sca} d)^{N-1}}{(N-1)!} \tag{44}$$

where $\langle p(\pi) \rangle_N$ is the weighted mean of the scattering phase function and can be expressed mathematically as:

$$\langle p(\pi) \rangle_N = 2\pi \int_0^{\pi} M_N(\theta_1) p(\pi - \theta_1) \sin(\theta_1) d\theta_1 \tag{45}$$

where $M_N(\theta_1)$ is the probability that a photon scattered N times is scattered at an angle θ_1 at that point in the layer. Eloranta (1972) points out that these two functions are difficult to calculate in many cases. For the doubly-scattered case, we can use:

$$M_2(\theta) = \begin{cases} \dfrac{p(\theta)}{2\pi \displaystyle\int_0^{\theta_d} p(\theta) \sin\theta \, d\theta} & \text{for } \theta \le \theta_d \\ 0 & \text{otherwise} \end{cases} \tag{46}$$

For photons that are scattered many times, the central-limit theorem shows that the resulting angular distribution of photons is Gaussian and the probability distribution can be expressed as:

$$M_N(\theta) = \frac{1}{K} \exp\left[-\frac{\theta^2}{\langle \theta^2 \rangle_N} \right]$$
$$\text{where} \quad K = 2\pi \int_0^{\theta_d (N-1)} \exp\left[-\frac{\theta^2}{\langle \theta^2 \rangle_N} \right] \sin\theta \, d\theta \tag{47}$$

and $\langle \theta^2 \rangle_N$ is the variance of the scattering angle. The variance of the scattering angle is defined as:

$$\langle \theta^2 \rangle_N = (N-1)\frac{\int_0^{\theta_d} \theta^2 p(\theta)\sin\theta\, d\theta}{\int_0^{\theta_d} p(\theta)\sin\theta\, d\theta} \tag{48}$$

Admittedly, the adjustments for the true nature of the backscatter from the penetration depth observed are complicated, but they can be calculated directly for a known scattering phase function. Equation 44 will be revisited in the next section and shown to emerge from a specific case considered in the generalized model. However, Equation 41 shows that the total power can be expressed as:

$$P_t = P_1 e^{\sigma_{sca} z} \tag{49}$$

where z is the penetration depth within the layer. If the optical depth of the layer due to scattering is approximately 1, then the predicted received power is about 2.7 times longer than the power from the single-scatter LIDAR equation. Although this simplified approximation may overestimate the contribution to multiple scattering in some cases, the discussion clearly indicates that multiply scattered photons cannot be ignored. The next subsection introduces a more rigorous development of a generalized multiply scattered LIDAR equation.

3.2.3 Generalized Multiply Scattered Model

Now let's consider a short duration laser pulse fired into a participating medium. The angular distribution of photons emitted from the laser is assumed to be Gaussian in nature with a known divergence angle. The photons that reach the receiver are assumed to result from a single large-angle scattering event (referred to as "singularly backscattered") from a slab at range $R = ct/2$ and with thickness $c\tau_L/2$.

Based upon the divergence angle, the spatial distribution of photons arriving at the backscattering slab is:

$$dN = \frac{N_t}{\pi\rho_L^2 R^2} \exp\left[-\tau(R)\right] \exp\left[-\frac{\xi^2}{\rho_L^2 R^2}\right] \xi \cdot d\xi \cdot d\psi \tag{50}$$

where dN is the number of photons incident in the incremental area $\xi \cdot d\xi \cdot d\psi$, N_t is the number of photons in the transmitted pulse, R is the range between the laser and the backscatter slab, $2\rho_L$ is the full angular width of the laser beam, $\tau(R) = \int_0^R \sigma_{sca}(x)dx$ is the optical depth at range R, $\sigma_{sca}(x)$ is the scattering cross-section as a function of x, ξ is the radial distance from the laser beam axis measured at the $ct/2$ slab. This distribution is consistent with those observed in the literature.

A scattering layer of thickness dx_1 is introduced at a distance x_1 from the $ct/2$ slab as shown in Figure 6. A photon emitted from the laser that is scattered once at the x_1 layer through a small-angle scattering event will be incident upon the slab at a radial distance of ξ_2 instead of ξ_1. The incident spatial distribution of photons is then directly impacted by the scattering phase function of the x_1 layer. The new spatial distribution of photons can be found by convolving the Gaussian laser beam with a forward-scattering representation of the scattering phase function at x_1.

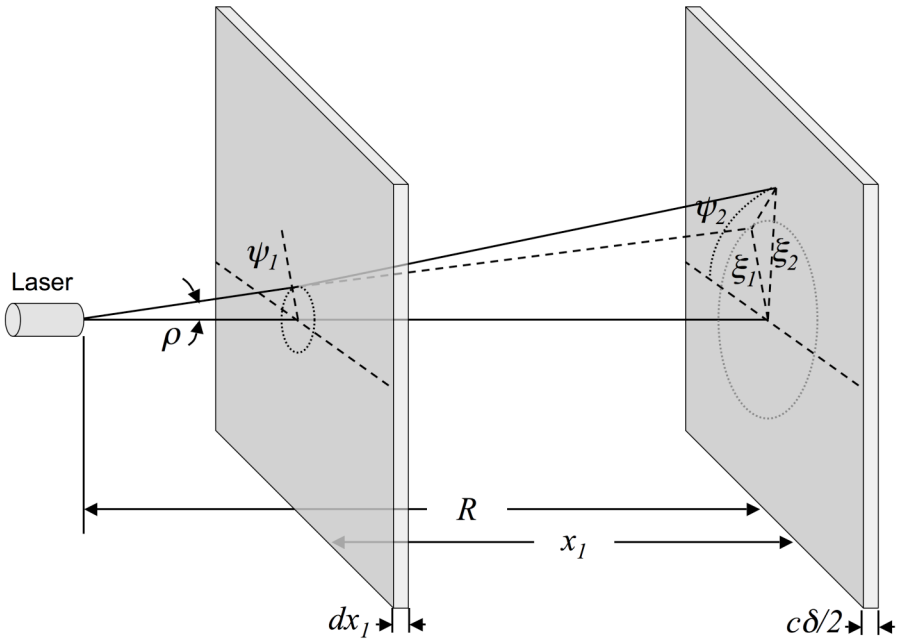


Figure 6: Geometry for a photon emitted by the laser and scattered once at a slab at a distance x_1 from the maximum range R

If the scattering phase function of the layer is predominantly forward-scattered, then a Gaussian approximation can be used to represent the spatial distribution of the small-angle scattering events. The scattering phase function can be approximated as:

$$\frac{p(\theta)}{4\pi} \cong \frac{p_{true}(0)}{4\pi}\exp\left[-\frac{\theta^2}{\Theta_s^2}\right] \qquad \text{where} \quad \Theta_s^2 = \frac{2}{p_{true}(0)} \tag{51}$$

and Θ_s is the angular half-width of the diffraction peak. Although the Gaussian scattering phase function approximation is convenient, it successfully models the peak value and area predicted by diffraction theory:

$$p(0) = p_{true}(0)$$
$$\int_0^{4\pi} \frac{p(\theta)}{4\pi}\, d\Omega = \frac{1}{2} \tag{52}$$

The convenience is due to the fact that an exact computation of the new spatial distribution would require analytical evaluation of a series of complicated joint probabilities. Instead, the new spatial distribution due to the scattering at the x_1 layer is a convolution of two Gaussians which yield a Gaussian distribution. The resulting spatial distribution of photons at range R is:

$$dN = \frac{\gamma(x_1)\ N_t}{\pi\ \rho_l^2 R^2 + \pi\ x_1^2 \Theta^2(x_1)}\ \sigma_{sca}(x_1)\ dx_1 \times \exp[-\tau]\ \exp\left[-\frac{\xi^2}{\rho_l^2 R^2 + x_1^2 \Theta^2(x_1)}\right] \xi \cdot d\xi \cdot d\psi \tag{53}$$

where $\Theta(x_1)$ is the angular half-width of the diffraction peak at x_1, $\gamma(x) = \pi\ \Theta_s^2(x) p(0,x)/4\pi$ is the fraction of energy in the forward peak of the phase function at x.

Additional scatterings can then be considered at distances x_2, x_3, …, x_m between x_1 and the backscattered slab. The spatial distribution of the photons incident upon the incremental area $\xi \cdot d\xi \cdot d\psi$ after m scattering events can be found after performing a multiple set of convolutions in succession and is given by:

$$dN_m = N_t \frac{\prod_{i=0}^{m} \gamma(x_i)\ \sigma_{sca}(x_i)\ dx_i}{\pi\ \rho_l^2 R^2 + \pi \sum_{i=0}^{m} x_i^2\ \Theta^2(x_i)} \times \exp[-\tau]\ \exp\left[-\frac{\xi^2}{\rho_l^2 R^2 + \sum_{i=0}^{m} x_i^2 \Theta^2(x_i)}\right] \xi \cdot d\xi \cdot d\psi \tag{54}$$

One should note that $\gamma(x_0)\sigma_{sca}(x_0)dx_0 = 1$ and $x_0^2\Theta_s^2(x_0) = 0$ were added to account for the photons that are transmitted to the $ct/2$ slab without scattering.

Although Equation 54 accurately describes the spatial distribution of the photons after m scatterings at the specified locations x_1, x_2, …, x_m, the equation does not account for all possible locations at which n scattering events could occur. To accomplish this, one must integrate over all the possible locations; however, integration at this stage would prevent us from using the same Gaussian convolution approach to account for any multiple, small-angle scatterings that might occur on the return trip to the receiver. Thus, we will elect to delay the integration to a later stage.

At this point, a set of critical assumptions must be made. We must assume that the photons arriving at the backscatter slab are identical to those in the non-scattered case except for their spatial distribution. For instance, the photons are assumed to have traveled a similar distance as those which were not yet scattered. This assumption is not entirely valid; however, since the photons under consideration are restricted to have undergone only one small-angle forward scattering, the assumption should not introduce significant error. As noted by Eloranta (1998), the differential difference in the path lengths is:

$$dl - dx = dx\left[\frac{1}{\cos\theta} - 1\right] \approx \frac{\theta^2}{2} dx \tag{55}$$

If the additional path length is incurred in a homogenous portion of the layer with a scattering phase function diffraction peak mean-square width Θ_s, the mean square angle of propagation with respect to the system axis is:

$$\left\langle \theta^2(x) \right\rangle = \sigma_{sca} x \Theta_s^2 \tag{56}$$

Using this relationship and integrating Equation 55, the total path length difference is:

$$l = \sigma_{sca} d^2 \Theta_s^2 \tag{57}$$

where d is the penetration depth. Typically this path length difference is tolerable, but should be evaluated to affirm the validity of this approximation.

Additionally, Eloranta (1998) discusses the issue of whether the multiply scattered photons reach the slab with a different distribution of incident angles than directly transmitted photons. If so, the variation in incident angles directly impacts the amount of backscattered photons from the slab and their spatial distribution at the receiver. One could account for the different distribution of incident angles and turn-around angles at the slab; however, the task would involve evaluating the joint probability of the backscatter angle and the probability of the multiply scattered photon returning to the receiver. In many ways, this unnecessarily complicates the problem. Although the solution proposed by Eloranta (1998) does not fully account for all of the effects, the reduction in complexity is necessary and beneficial. Eloranta (1998) argues that we can assume that the scattering phase function is independent of angle near 180° (the backscattering angle). The result is that incident photons are scattered back to the receiver based upon assuming that the incident angle was 180° regardless of its actual value. To lessen the impact of this assumption, we shall assume that the backscattered phase function shall be calculated based upon a weighted average of the scattering phase function $p(\theta,0)/4\pi$ near the backscatter direction. The weighted average of the scattering phase function is defined as:

$$p_{n\pi}(R) = \frac{1}{n\tau}\int_0^{\infty} p(\pi-\theta,R)\int_{-d}^{d}\frac{1}{\Theta_s^2(x)}\exp\left[-\frac{\theta^2}{n\Theta_s^2(x)}\right]\sigma_{sca}(x)\,dx\,\theta\,d\theta \tag{58}$$

where n is the order of scattering and $2d$ is the distance traveled in the scattering medium for the round trip. Although this is an approximation, Eloranta (1998) argues that this is the best approximation in the limit of large receiver acceptance angles and results in very reasonable results when compared to real-world datasets. A more thorough discussion of the implications is found in Eloranta (1972, 1998).

Now account for the return trip of the photons backscattered by the slab at range R. The geometry is shown in Figure 7. The photons scattered toward the receiver from the volume area $c\delta/2\cdot\xi\cdot d\xi\cdot d\psi$ will be incident on a sphere of radius R centered upon the scattering volume and extending to the entrance of the receiver aperture. If we assume that the backscatter lobe is isotropic, the spatial and angular distribution relative to the radius vector

will be independent of position and independent of the number of scatterings. If we consider a returning photon incident at an angle θ_1 upon a layer x_{m+1} (with a thickness dx_{m+1}) and then scattered so that the angle of incidence upon the receive aperture with respect to the radius vector is θ_2, the differential number of photons incident on the receive aperture per unit time is:

$$\frac{dN_{m+1}}{dt} = dN_m \frac{A_r}{R^2} \frac{p_{\pi m}(0)}{4\pi} \sigma_{sca}(0) \frac{c\delta}{2} \frac{R^2 \, \gamma(x_{m+1}) \, \sigma_{sca}(x_{m+1}) \, dx_{m+1}}{\pi x_{m+1}^2 \Theta^2(x_{m+1})}$$
$$\times \exp[-\tau] \, \exp\left[-\frac{\Theta^2 R^2}{x_{m+1}^2 \Theta^2(x_{m+1})}\right] \theta \cdot d\theta \cdot d\phi \tag{59}$$

where A_r is the area of the receive aperture, θ is the angle between the photon trajectory and the radius vector, and ϕ is the angle measured around the radius vector. Note that we are using the small angle approximation ($\sin\theta \approx \theta$) to relate θ_1 and θ_2 such that $\theta_2 \approx \theta_1(x_{m+1}/R)$.

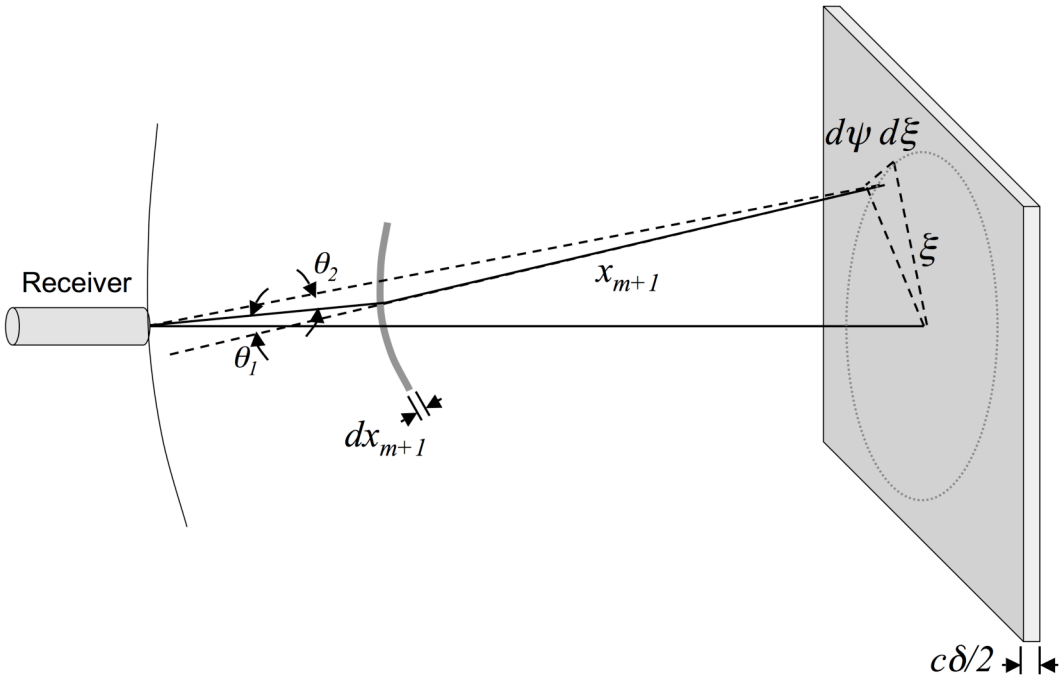


Figure 7: Geometry for a photon returning to the receiver from the area $\xi \, d\xi \, d\psi$

If additional scattering events occur between x_{m+1} and the receiver aperture from layers x_{m+2}, x_{m+3}, …, x_{n-1}, we can then find the angular distribution of photons relative to the radius vector at the spherical surface in front of the receiver aperture by convolving Equation 59 with the

Gaussian phase function approximation at each scattering layer. The resulting relative angular distribution of photons at the receiver can be expressed as:

$$\frac{dN_n}{dt} = dN_m \frac{A_r}{R^2} \frac{p_{\pi m}(0)}{4\pi} \sigma_{sca}(0) \frac{c\delta}{2} \frac{R^2 \prod_{i=m+1}^{n-1} \gamma(x_i)\ \sigma_{sca}(x_i)\ dx_i}{\pi \sum_{i=m+1}^{n-1} x_i^2\ \Theta^2(x_i)}$$
$$\times \exp[-\tau]\ \exp\left[-\frac{\Theta^2 R^2}{\sum_{i=m+1}^{n-1} x_i^2 \Theta^2(x_i)}\right] \theta \cdot d\theta \cdot d\phi \tag{60}$$

To compute the full angular distribution of photons incident on the receiver aperture, we integrate over the illuminated area of the backscatter slab. Fortunately, the integration is fairly straightforward is simply the convolution of two Gaussians and thus easy to evaluate. The resulting angular distribution of photons incident on the receive aperture is:

$$\frac{dN_n}{dt} = N_t \frac{A_r}{R^2} \frac{p_{\pi m}(0)}{4\pi} \sigma_{sca}(0) \frac{c\delta}{2} \frac{R^2 \prod_{i=0}^{n-1} \gamma(x_i)\ \sigma_{sca}(x_i)\ dx_i}{\pi\ \rho_l^2\ R^2 + \pi \sum_{i=0}^{n-1} x_i^2\ \Theta^2(x_i)}$$
$$\times \exp[-2\tau]\ \exp\left[-\frac{\rho^2 R^2}{\rho_l^2 R^2 + \sum_{i=0}^{n-1} x_i^2 \Theta^2(x_i)}\right] \rho \cdot d\rho \cdot d\phi \tag{61}$$

Now if we integrate over the full angular FOV of the receiver $\left(0 \le \rho \le \rho_t; 0 \le \phi \le 2\pi\right)$ to collect all of the photons and then divide by the number of singly scattered photons, we obtain the expression:

$$\frac{dP_n(R)}{P_1(R)} = N_t \frac{A_r}{R^2} \frac{p_{\pi m}(0)}{p(\pi,0)} \left\{1 - \exp\left[-\frac{\rho_t^2}{\rho_l^2}\right]\right\}^{-1} \left\{\prod_{i=1}^{n-1} \gamma(x_i)\ \sigma_{sca}(x_i)\ dx_i\right\} \times \left\{1 - \exp\left[-\frac{\rho_t^2 R^2}{\rho_l^2 R^2 + \sum_{i=0}^{n-1} x_i^2\ \Theta^2(x_i)}\right]\right\} \tag{62}$$

where ρ_t is the angular half-FOV of the receiver. Integration of Equation 62 yields the signal power due to the nth-order scattering divided by the power of single scattered photons that is indicated by the standard LIDAR equation. For simplicity, the coordinate system for the integration can be laid out as shown in Figure 8. The general setup is similar to that already used, but the problem has essentially been "unfolded". The origin has been located at the backscattering slab, which is a distance *R* from the laser and receiver. Therefore photons that are transmitted and eventually backscattered to the receiver go through a thickness of 2*d* in the cloud.

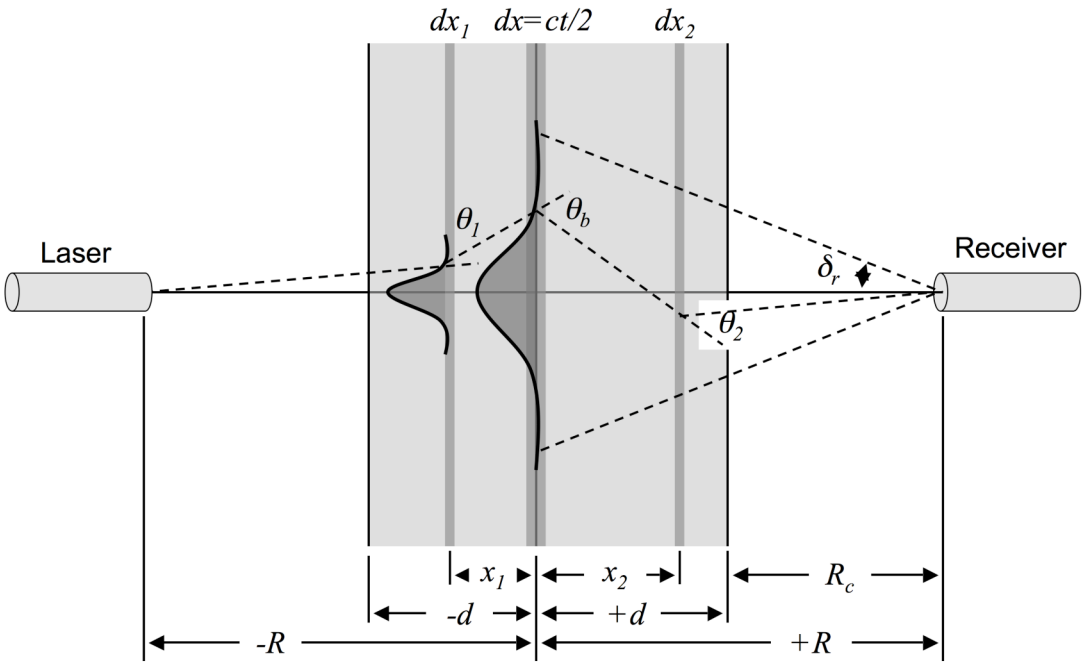


Figure 8: Multiple scattering geometry for a cloud located at a distance R_c from the LIDAR

Given this coordinate system, the resulting expression for the n[th]-order scattering versus single scattered power ratio is:

$$\begin{aligned}\frac{P_n(R)}{P_1(R)} = \frac{p_{\pi n}(R)}{p(\pi,R)}\left\{1-\exp\left[-\frac{\rho_t^2}{\rho_l^2}\right]\right\}^{-1}\int_{-d}^{d}\gamma(x_1)\sigma_{sca}(x_1)\int_{x_1}^{d}\gamma(x_2)\sigma_{sca}(x_2)\\ \times\int_{x_2}^{d}\gamma(x_3)\sigma_{sca}(x_3)\cdots\int_{x_{n-3}}^{d}\gamma(x_{n-2})\sigma_{sca}(x_{n-2})\int_{x_{n-2}}^{d}\gamma(x_{n-1})\sigma_{sca}(x_{n-1})\\ \times\left\{1-\exp\left[-\frac{\rho_t^2R^2}{\rho_l^2R^2+\sum_{i=0}^{n-1}x_i^2\Theta^2(x_i)}\right]\right\}dx_1\,dx_2\,dx_3\cdots dx_{n-1}\end{aligned} \tag{63}$$

The next step is to substitute the approximation of the Gaussian scattering phase function into Equation 63:

$$\begin{aligned}\frac{P_n(R)}{P_1(R)} = \frac{p_{\pi n}(R)}{p(\pi,R)}&\left\{1-\exp\left[-\frac{\rho_t^2}{\rho_l^2}\right]\right\}^{-1}\\ &\times\left\{\frac{\tau^{n-1}}{(n-1)!}-\frac{1}{2^{n-1}}\int_{-d}^{d}\gamma(x_1)\sigma_{sca}(x_1)\int_{x_1}^{d}\gamma(x_2)\sigma_{sca}(x_2)\right.\\ &\times\int_{x_2}^{d}\gamma(x_3)\sigma_{sca}(x_3)\cdots\int_{x_{n-3}}^{d}\gamma(x_{n-2})\sigma_{sca}(x_{n-2})\int_{x_{n-2}}^{d}\gamma(x_{n-1})\sigma_{sca}(x_{n-1})\\ &\times\left.\left\{1-\exp\left[-\frac{\rho_t^2R^2}{\rho_l^2R^2+x_1^2\Theta^2(x_1)+x_2^2\Theta^2(x_2)+\cdots+x_{n-1}^2\Theta^2(x_{n-1})}\right]\right\}dx_1\,dx_2\,dx_3\cdots\,dx_{n-1}\right\}\end{aligned} \tag{64}$$

Although the development could stop here, the expression can be simplified by splitting the integration into two parts, by using symmetry, and by then translating the origin to a more intuitive location. After the first two steps we obtain:

$$\begin{aligned}\frac{P_n(R)}{P_1(R)} = \frac{p_{\pi n}(R)}{p(\pi,R)}&\left\{1-\exp\left[-\frac{\rho_t^2}{\rho_l^2}\right]\right\}^{-1}\\ &\times\left\{\frac{\tau^{n-1}}{(n-1)!}-\int_{-d}^{0}\gamma(x_1)\sigma_{sca}(x_1)\int_{x_1}^{0}\gamma(x_2)\sigma_{sca}(x_2)\cdots\int_{x_{n-3}}^{0}\gamma(x_{n-2})\sigma_{sca}(x_{n-2})\int_{x_{n-2}}^{0}\gamma(x_{n-1})\sigma_{sca}(x_{n-1})\right.\\ &\times\left.\left\{1-\exp\left[-\frac{\rho_t^2R^2}{\rho_l^2R^2+x_1^2\Theta^2(x_1)+x_2^2\Theta^2(x_2)+\cdots+x_{n-1}^2\Theta^2(x_{n-1})}\right]\right\}dx_1\,dx_2\,dx_3\cdots\,dx_{n-1}\right\}\end{aligned} \tag{65}$$

The last step is to move the origin. If we rewrite the equation in terms of distance from the LIDAR by substituting $r=x+R$, then Equation 65 can be rewritten as:

$$\begin{aligned}\frac{P_n(R)}{P_1(R)} = \frac{p_{\pi n}(R)}{p(\pi,R)}&\left\{1-\exp\left[-\frac{\rho_t^2}{\rho_l^2}\right]\right\}^{-1}\\ &\times\left\{\frac{\tau^{n-1}}{(n-1)}-\int_{r_c}^{R}\gamma(x_1)\sigma_{sca}(r_1)\int_{r_1}^{R}\gamma(r_2)\sigma_{sca}(r_2)\cdots\int_{r_{n-3}}^{0}\gamma(r_{n-2})\sigma_{sca}(r_{n-2})\int_{r_{n-2}}^{0}\gamma(r_{n-1})\sigma_{sca}(r_{n-1})\right.\\ &\times\left\{1-\exp\left[-\frac{\rho_t^2R^2}{\rho_l^2R^2+(R-r_1)^2\Theta^2(r_1)+(R-r_2)^2\Theta^2(r_2)+\cdots+(R-r_{n-1})^2\Theta^2(r_{n-1})}\right]\right\}\\ &\left.dr_1\,dr_2\,dr_3\cdots dr_{n-1}\right\}\end{aligned} \tag{66}$$

Equation 66 is the contribution due to the n[th]-order scattering that is absent in the standard singly scattered LIDAR equation. The total power observed can be found by summing Equation 66 for all numbers n of scattered photons and then multiplying by the singly scattered power $P_1(R)$ to obtain:

$$\begin{aligned}P_t(R) = P_1(R)\sum_{n=2}^{\infty}&\left\{\frac{p_{\pi n}(R)}{p(\pi,R)}\left\{1-\exp\left[-\frac{\rho_t^2}{\rho_l^2}\right]\right\}^{-1}\right.\\ &\times\left\{\frac{\tau^{n-1}}{(n-1)!}-\int_{r_c}^{R}\gamma(x_1)\sigma_{sca}(r_1)\int_{r_1}^{R}\gamma(r_2)\sigma_{sca}(r_2)\cdots\int_{r_{n-3}}^{0}\gamma(r_{n-2})\sigma_{sca}(r_{n-2})\int_{r_{n-2}}^{0}\gamma(r_{n-1})\sigma_{sca}(r_{n-1})\right.\\ &\times\left\{1-\exp\left[-\frac{\rho_t^2R^2}{\rho_l^2R^2+(R-r_1)^2\Theta^2(r_1)+(R-r_2)^2\Theta^2(r_2)+\cdots+(R-r_{n-1})^2\Theta^2(r_{n-1})}\right]\right\}\\ &\left.\left.dr_1\,dr_2\,dr_3\cdots\,dr_{n-1}\right\}\right\}\end{aligned} \tag{67}$$

This is a LIDAR equation that accounts for multiple scattering. One must recognize the limitations of the derivation if any of the critical assumptions are violated; however, the expression is very useful in a number of cases.

Although numerical evaluation of Equation 66 is certainly feasible, let's examine a few special cases where the expression can be simplified analytically. First, let's look at a special

case where the FOV is very wide so that all photons scattered by the layer are within the diffraction peak and are collected. In simplified terms, evaluate Equation 66 under the condition that all of the photons that undergo small-angle scatterings are collected. This situation was essentially investigated in Section 3.2.2 as the simplified approximation. Under the wide FOV receiver assumption (WFOV), Equation 66 can be simplified to:

$$\frac{P_n(R)}{P_1(R)} = \frac{p_{\pi n}(R)}{p(\pi,R)} \frac{\tau^{n-1}}{(n-1)!} \tag{68}$$

This is the same expression that we intuitively derived earlier for the simple approximation in Equation 44. Figure 9 shows the power ratio of multiply to singly scattered photons as a function of penetration depth for a cumulus C1 cloud model (Liou and Schotland, 1971; Eloranta, 1972; Kokhanovsky, 2001). The additional contribution made by doubly scattered photons makes when compared to the single scattered photons predicted by the standard LIDAR equation can be very significant. The doubly scattered contribution for a C1 cloud layer begins to impact the signal at very shallow penetration depths. On the other hand, photons scattered three or four times introduce less than 10% error until the penetration depths reach much deeper into the cloud layer (30 m for n=3 and 55 m for n=4). For shallow depths, one could reasonably ignore the 3rd- and 4th-order scattering effects without incurring a great error.

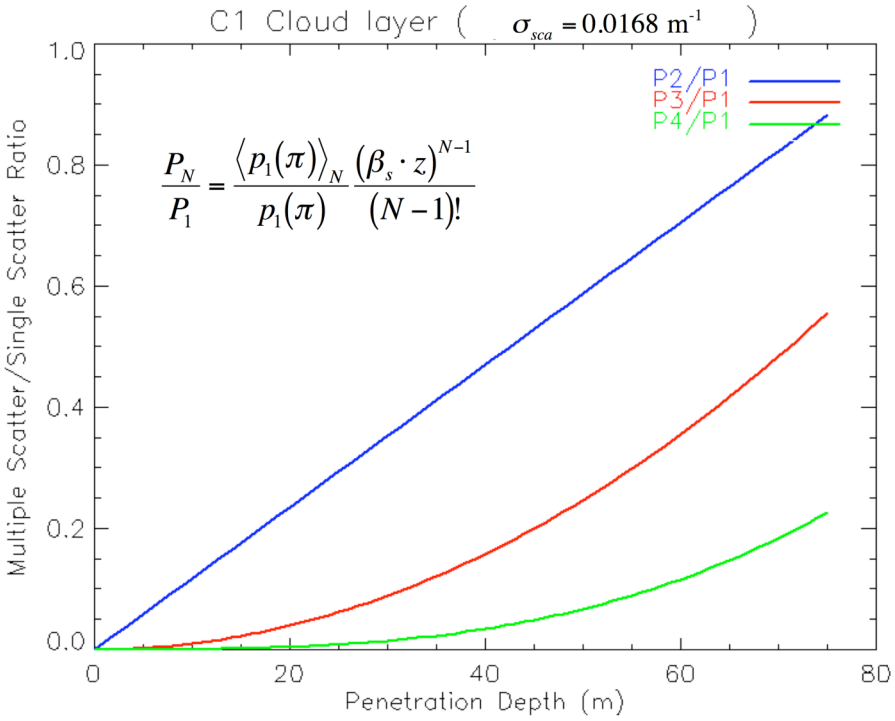


Figure 9: C1 Cloud multiple-to-single scatter power ratio for a WFOV LIDAR at different penetration depths

Another way to explore Equation 68 is to calculate the total power. If all contributions for all orders of multiple scattering are summed, the total received power is:

$$P_t(R) = P_1(R)e^{\tau} \tag{69}$$

For an optical depth of τ=1.0, the total received power is approximately 2.7 times that predicted by the single scatter LIDAR equation. Figure 10 compares the multiply scattered and the singly scattered LIDAR equations for a homogenous layer (similar to a cloud layer) with an extinction coefficient of 0.1 m^{-1}, a scattering albedo of 0.9, and an asymmetry parameter of 0.863. Note that the received power is normalized by the transmit power and receiver aperture area. The photon stream returning from deeper in the layer is significantly underestimated by singly scattered LIDAR equation. The difference is about an order of magnitude at about 30 m penetration depth (200 ns), which corresponds to an optical depth of about $\tau \cong 3.0$.

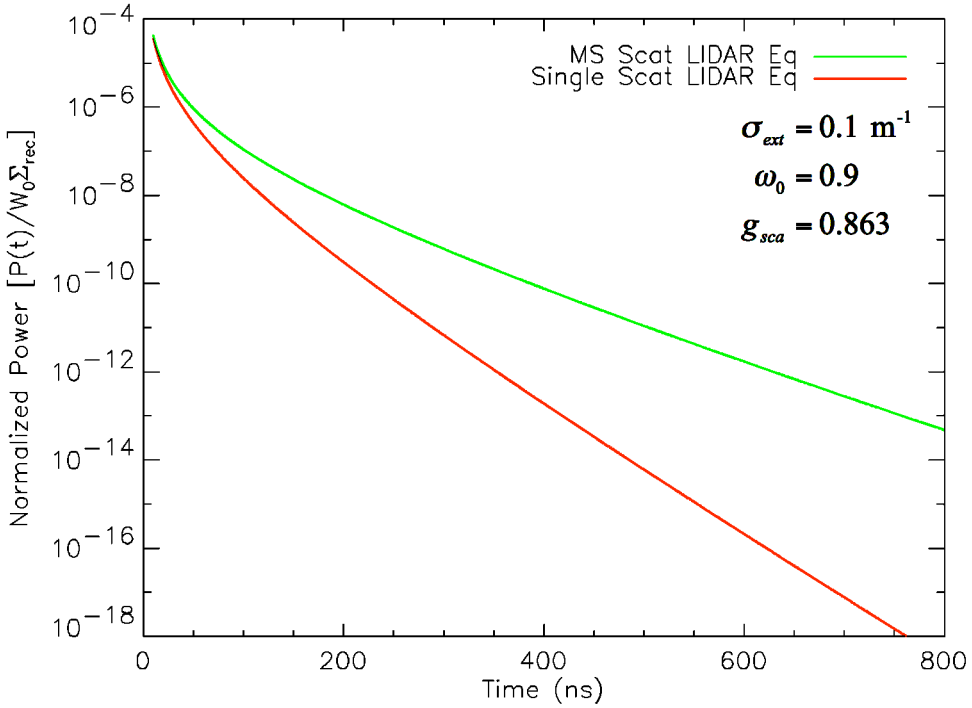


Figure 10: Comparison of multiple scattering and single scattering LIDAR equation

3.2.4 Implications for DIAL Measurements

In Section 3.1.2, Equations 12 and 15 were used to calculate the concentration of a gaseous effluent in a participating medium using the backscattered return or the topographic target return at the reference and absorption wavelengths. The formulation of both equations was based upon the singly scattered LIDAR equation, which we have just shown in the previous section does not entirely account for all of the power observed by the receiver if enough scattering is present. The received power for a return pulse can be significantly larger than anticipated from the single-scattering LIDAR equation. A natural question arises as to whether this will impact results of a processor based upon Equations 12 and 15.

If we assume that the scattering cross-section is approximately constant across the spectral region of interest, then the increase in power at the receiver is approximately the same for both the reference and absorption pulses. Equations 12 and 15 would then not be greatly affected because the ratio between the reference and absorption pulses should remain constant. Although the multiple scattering LIDAR equation may be more accurate for an

individual pulse, the impact to the final concentration measurement should be negligible regardless of the degree of multiple scattering. However, the atmospheric remote sensing community generally acknowledges that multiple scattering can make a difference. One could argue that some error will be introduced due to the variability in the scattering cross-sections at both wavelengths, but this does not account for all observations.

Some necessary assumptions in the derivation of the multiple scattering LIDAR equation are not always valid for real-world scenarios. These discrepancies would result in observable differences for a DIAL system when multiple scattering is present. For instance, we assumed that the path length of a photon that had been scattered for the nth time travels the same distance and arrives at the receiver at the same time as a single scattered photon. If the participating medium is sufficiently thick, this assumption is invalid. The mean distance traveled within the medium can be significantly altered by increasing the scattering cross-section of the layer. If the mean distance is increased, then more absorption will occur and the measured concentration should be higher. Unfortunately, the situation may not be as straightforward when considering that the scattering phase function also changes the distribution of photons to a greater extent as the layer becomes optically thicker. In some instances, the phase function may exhibit less forward scattering as presumed and could theoretically cause photons to turn around and scatter out of the layer prematurely. This could result in an underestimation of the actual concentration because the mean photon path length and distribution within the layer was decreased. If one is going to accurately model the scattering and absorption of photons within a homogenous or non-homogenous medium, then one must somehow relax the restrictions introduced for the derivation of the multiple scattering LIDAR equation.

Another potential impact is due to the temporal variability in the plume itself. The reference and absorption pulse pairs are typically not fired at the same time. They are fired sequentially with a short, but noticeable time delay. If the plume contains significant scattering particles and is active (moving and turbulent), then the observed multiple scattering signature is modified and the DIAL measurements could exhibit significant error. To some degree, the situation may be compensated for using pulse-averaging techniques. This presumes that the

plume variability is wide-sense stationary to some degree over some reasonable time interval. From a modeling perspective, all of the cases mentioned thus far require a robust treatment of multiple scattering effects to support investigation into the impact on DIAL measurements.

3.3 Radiative Transfer in Participating Media

This subsection emphasizes the theoretical basis for propagating light through a participating medium, such as a gas plume or cloud. When electromagnetic radiation interacts with a particle within a participating medium, part of the energy may undergo a change in direction, a loss, or a gain of energy. These processes are commonly referred to as scattering, absorption, or emission. These interactions for a gaseous medium pose significant challenges. First, the scattering, absorption, or emission occurs at every point in space within the participating medium and not only at the system boundaries. As the media changes temperature, concentration, and orientation with time, the events within the gaseous body and the intensity observed outside the gaseous body are constantly shifting and are spatially and temporally correlated. A complete solution of the radiative transfer through a gaseous plume or cloud requires substantial knowledge of the temperature, the local radiation intensity, and physical properties of the gaseous mixture at every instance in the time of interest. In general, the mathematics to describe these physical processes exists; however, the theory is inherently cumbersome and requires simplification to derive any meaningful result.

The theory of radiative transfer, which characterizes light fields traversing through a participating medium, has been studied for years by individuals such as Chandrasekhar (1950), Siegel and Howard (1992), Sobolev (1956, 1972), Ishimaru (1978), and Van de Hulst (1980). The foundation built by these researchers explores solutions to the radiative transfer equation (RTE). Many of the derivations are straightforward if sufficient constraints are applied and limiting assumptions are valid. Generalized solutions of the RTE for real-world situations, such as with a mixed-gas, smoke-stack plume, are not always tractable. One is typically forced to rely on the use of numerical and approximation techniques. In truth, even scenarios which appear at first glance to be trivial can be overly burdensome if you try to analytically evaluate them. Hence, this section shall address some of the commonly used simplifications, some critical terminology and relationships, and derive a RTE that may

adequately represent the real-life physics of laser light propagating through a participating medium such as a factory stack plume. Although the principles and many of the derivations will apply to other scenarios, like fog and rainbows, the specific focus will be upon the theory describing various gas plumes.

3.3.1 Fundamentals and Properties for Participating Medium

As denoted previously, a photon interacts with a particle or molecule through the primary modes of interaction of scattering, absorption, or emission. Within that context, we begin by examining some of the fundamental properties of a participating medium, such as the extinction coefficient, the scattering coefficient, the absorption coefficient, and the scattering phase function.

Consider the change in radiance L_λ at a specific wavelength λ after passing through a small volume dV of participating medium at normal incidence (Figure 11). If any radiance added due to emission is disregarded and the volume is relatively small so that no radiance is scattered into the path of interest, then the change in radiance L_λ can be expressed as:

$$dL_\lambda = -\sigma_{ext} L_\lambda dS \tag{70}$$

where dS is the length of the path through the medium and σ_{ext} is the extinction coefficient. The extinction coefficient σ_{ext} is a physical property of the medium and is dependent upon the wavelength λ, the temperature T, the pressure P, and the material composition denoted by the concentrations c_i. The dependence upon the material composition also includes such properties as the complex indices of refraction, particle size, and particle size distribution. This also indicates that the radiance within the medium and exiting the medium is also a function of these dependencies, which is consistent with intuition.

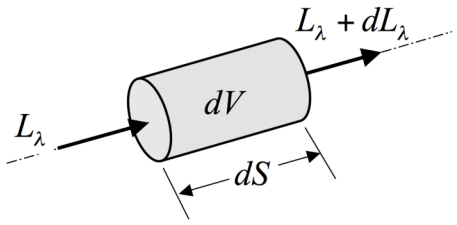


Figure 11: Radiance attenuation through a participating medium of volume dV

Although stated without proof, the extinction coefficient can be viewed as the inverse of the mean penetration distance for a homogeneous medium. If this statement is applied to Equation 70 and integrated over a path length S:

$$\int_{L_\lambda(0)}^{L_\lambda(S)} \frac{dL_\lambda}{L_\lambda} = \int_0^S -\sigma_{ext}(S')dS' \tag{71}$$

where $L_\lambda(0)$ is the incident radiance at the origin of the path, then the result of the integration is:

$$L_\lambda(S) = L_\lambda(0)\exp\left[-\int_0^S \sigma_{ext}(S')dS'\right] \tag{72}$$

This is often known as Bougeur's law, Lambert's law, Bouguer-Lambert law, or Beer's law. Beer's law is somewhat more restrictive and was intended to state the dependence upon the concentration levels. Despite the potential confusion about the law's name, Equation 72 mathematically expresses that the spectral radiance is attenuated exponentially along a path through an absorbing and/or scattering medium where emission and multiple scattering effects are not considered directly. The rate of exponential attenuation is then determined by the integration of the local extinction coefficient over the path length.

The exponential term in Equation 72 is designated the "optical thickness", "depth", or "opacity" of the layer with a thickness *S*. Note that the optical thickness also depends upon the pressure, temperature, material composition, and wavelength and is a function of how these parameters change along the path from 0 to *S*. Bougeuer's law can be restated as:

$$L_\lambda(S) = L_\lambda(0)\exp\left[-\tau_\lambda(S)\right] \tag{73}$$

where $\tau_\lambda(S)$ is the optical thickness. If the medium is homogeneous and at equilibrium such that the temperature and pressure are essentially constant, then one can express the optical depth as:

$$\tau_\lambda(S) = \sigma_{ext,\lambda} S \tag{74}$$

If $\tau_\lambda(S) << 1$, then the volume or layer is designated to be optically thin; however, if $\tau_\lambda(S) >> 1$, then the layer is designated to be optically thick. For the optically thin case, the mean penetration distance is much larger than the physical thickness of the layer; therefore, only a limited amount of extinction occurs and (more importantly) the multiple scattering effects are negligible.

The extinction coefficient σ_{ext} is a physical property of the medium that accounts for the attenuation due to scattering and absorption and can be split into two components, the absorption coefficient σ_{abs} and scattering coefficient σ_{sca}:

$$\sigma_{ext}(\lambda,T,P,c_i) = \sigma_{abs}(\lambda,T,P,c_i) + \sigma_{sca}(\lambda,T,P,c_i) \tag{75}$$

Note that both the scattering and absorption coefficients are also dependent upon the temperature, pressure, wavelength, and material composition. From this point forward, these dependencies will be formally dropped and merely inferred for convenience. The absorption and scattering coefficients can be found using:

$$\sigma_{abs} = N \cdot C_{abs} \tag{76}$$

$$\sigma_{sca} = N \cdot C_{sca} \tag{77}$$

where N is the number concentration of particles, C_{abs} is the absorption cross-section, and C_{sca} is the scattering cross-section. Note that, by construction, the extinction cross-section can also be expressed as:

$$C_{ext} = C_{abs} + C_{sca} \tag{78}$$

such that the extinction coefficient can also be expressed as:

$$\sigma_{ext} = N\left(C_{abs} + C_{sca}\right) \tag{79}$$

If the medium is composed of particles with different sizes, then the mean values of the cross-sections are used in Equation 79. Calculation of the absorption, scattering, and extinction coefficients and cross-sections for different particle sizes and types is addressed in more detail in Section 3.6.

Another important term is the differential scattering cross-section. The scattering coefficient σ_{sca} is defined as the integral of the differential cross-section σ_{sca}^{d}:

$$\sigma_{sca} = \int_0^{2\pi} d\varphi \int_0^{\pi} \sigma_{sca}^{d}(\theta,\varphi)\sin(\theta)d\theta \tag{80}$$

If one assumes that the azimuth-independent local scattering law applies, the expression simplifies to:

$$\sigma_{sca} = 2\pi \int_0^{\pi} \sigma_{sca}^{d}(\theta)\sin(\theta)d\theta \tag{81}$$

The azimuth-independent local scattering assumption is common and reasonable in most cases. Thus, it follows from Equation 81 that:

$$2\pi \int_0^{\pi} \frac{\sigma_{sca}^{d}(\theta)}{\sigma_{sca}} \sin(\theta)d\theta = 1 \tag{82}$$

The central term within the integral of Equation 82 describes the angular distribution of the scattered energy. This distribution is represented by the scattering phase function of a particle or medium, which is defined as:

$$p(\theta) = \frac{4\pi\sigma_{sca}^{d}}{\sigma_{sca}} = \frac{dI_{\lambda}(\theta,\varphi)}{\frac{1}{4\pi}\int_{0}^{4\pi} dI_{\lambda}(\theta,\varphi)d\omega_{s}} \tag{83}$$

where $p(\theta)$ is the scattering phase function which is normalized such that:

$$\frac{1}{2}\int_{0}^{\pi} p(\theta)\sin(\theta)d\theta = 1 \tag{84}$$

The scattering phase function indicates the scattered intensity in a direction specified by θ divided by the intensity that would be scattered in that direction if the scattering was isotropic. Alternatively, the scattering phase function is intuitively interpreted as the probability that a photon is scattered in a direction given that a scattering event occurs. The probabilistic interpretation requires a different normalization for the definition of the scattering phase function. The probability that a photon is scattered into a solid angle $d\Omega$ is equal to $d\Omega/4\pi$. For isotropic scattering, the phase function is uniform:

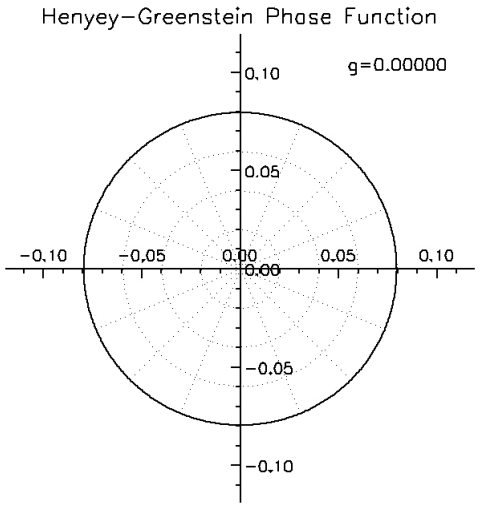
$$p(\theta) = 1 \tag{85}$$

Another commonly used empirical phase function is the Henyey-Greenstein phase function. It is often used to describe scattering in oceans and clouds and can be adjusted by an asymmetry parameter g. The Henyey-Greenstein phase function is defined as:

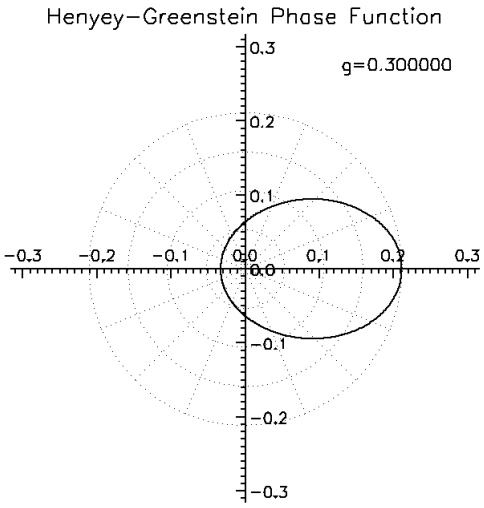
$$p(\theta) = \frac{1-g^{2}}{\left(1+g^{2}-2g\cos\theta\right)^{1.5}} \tag{86}$$

To accommodate more complex scattering phase functions, one can linearly combine different Henyey-Greenstein phase functions to realistically mimic a naturally occurring phase function. Figure 12 illustrates the effect of the asymmetry parameter g on the probabilistic version of the Henyey-Greenstein function. For many applications, this

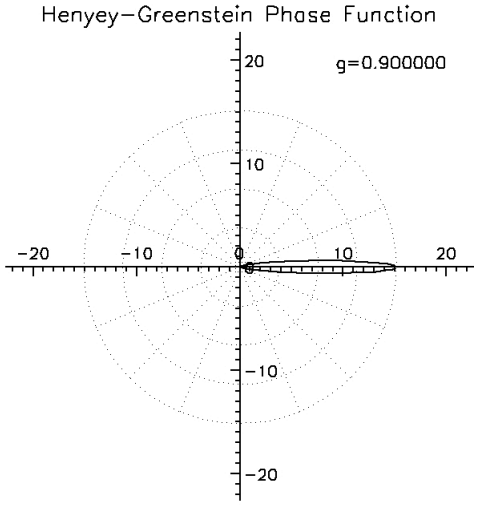
empirical phase function is adequate; however, one can also leverage Mie scattering theory to find the scattering phase function as is discussed in Section 3.6. A sample plot of a scattering phase function for C1 cloud model water droplets is shown in Figure 13. The phase function is shown for an effective particle diameter of 6 μm at λ=650 nm.



(a) g = 0.0



(b) g = 0.3



(c) g = 0.9

Figure 12: Henyey-Greenstein phase functions for *g*=0, 0.3, and 0.9

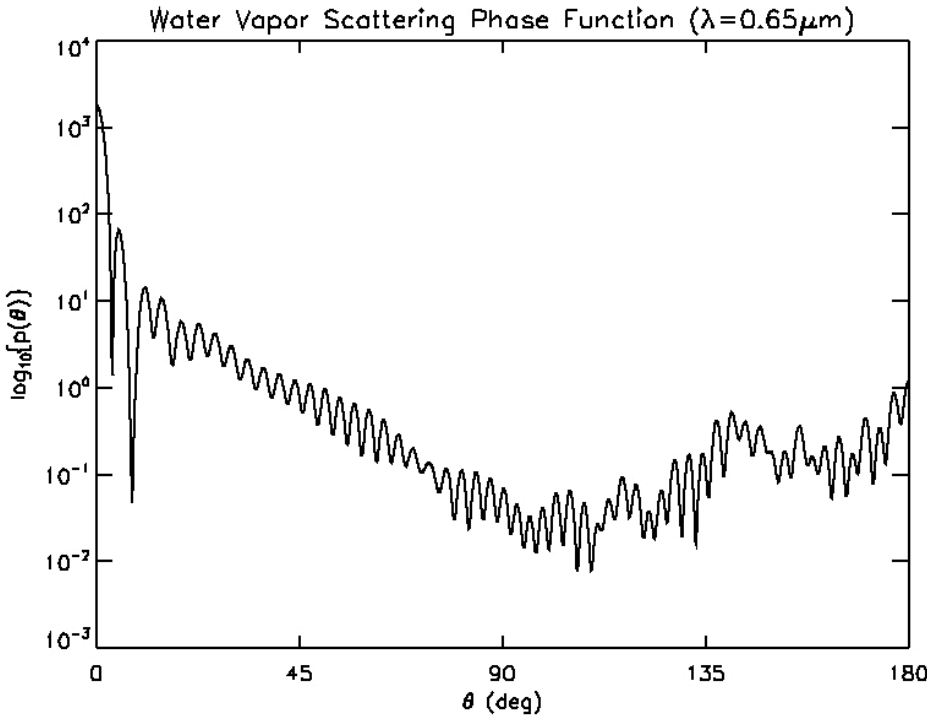


Figure 13: Scattering phase function for water using Mie theory
(log scale, λ=650 nm, m=1.33, a_{eff}=6 μm)

For a significant number of derivations and analytical approximations, the scattering phase function must be expanded into something that can be integrated or at least estimated. One common method is to expand using Legendre polynomials:

$$p(\theta) = \sum_{l=0}^{\infty} g_l P_l(\cos\theta) \tag{87}$$

The coefficients of this expansion are:

$$g_l = \frac{2l+1}{2} \int_0^{\pi} p(\theta) P_l(\cos\theta) \sin\theta \cdot d\theta \tag{88}$$

where the first five Legendre polynomials are:

$$\begin{aligned} P_0(\mu) &= 1 \\ P_1(\mu) &= \mu \\ P_2(\mu) &= \frac{3\mu^2 - 1}{2} \\ P_3(\mu) &= \frac{5\mu^3 - 3\mu}{2} \\ P_4(\mu) &= \frac{35\mu^4 - 30\mu^2 + 3}{8} \end{aligned} \tag{89}$$

where $\mu = \cos\theta$ in this case. One should note that the second expansion coefficient (l=1) is usually referred to as the asymmetry parameter and indicates the degree of forward or isotropic scattering.

3.3.2 Radiative Transfer Equation

The basic concepts and definitions were introduced for absorption and scattering in a participating medium in the previous subsection. Now let's employ those basic concepts and develop a governing equation of transfer for radiation as it travels through a dispersive, participating medium. The derivation in this subsection is most appropriate for media with low volumetric concentrations of scatterers (c_v< 0.01-0.1). Fortunately, almost all natural media and most plumes are characterized by extremely low values of volumetric concentration. For instance, c_v is in the range of 10^{-11} to 10^{-7} for water clouds and is 0.3 to 0.4 for snow and soil (Kokhanovsky, 2001). Closely packed media require that the correlation of the particles be accounted for and the RTE is much more complicated.

Consider light propagating within an absorbing, emitting, and scattering medium traveling in the direction $\vec{\Omega} = (\vartheta, \phi)$, as shown in Figure 14. In the absence of absorbing, emitting, or scattering events, the radiance will be considered to be constant. For now, the localized portion of the medium under consideration is assumed to be homogenous. If linearity is assumed, the change in intensity after traversing the thickness dS is:

$$dI_\lambda = -\sigma_{ext} I_\lambda dS + I_{em} dS \tag{90}$$

where σ_{ext} is the extinction coefficient as described earlier and I_{em} is the radiant intensity emitted into the observation path per unit distance. Although this equation does not account for nonlinear effects, the approximation is appropriate for a localized area. The emission component can be broken down into two portions:

$$I_{em} = I_{src} + I_{sca} \tag{91}$$

where I_{src} is due to internal sources of radiation inside a medium and I_{sca} is the radiant intensity due to the photons scattered from other directions into the direction $\vec{\Omega} = (\vartheta, \phi)$. If only elastic scattering is considered and the medium is in local equilibrium, then the emission contribution can be assumed to be characterized as black body radiation. Thus, the internal sources of radiation can be written using the Planck equation:

$$I_{src}(T) = \sigma_{abs}\left(\frac{2h\upsilon^3}{c^2}\frac{1}{e^{h\upsilon/kT}-1}\right) \tag{92}$$

where σ_{abs} is the absorption coefficient, υ is the frequency, c is the speed of light, T is the temperature, h is the Boltzmann constant, and k is the Planck constant. If one is considering the visible or ultraviolet region, then the internal source function is typically presumed to be zero; however, if the system is operating in a thermal region then the internal source function must be accounted for. The intensity that is scattered into the observation direction $\vec{\Omega} = (\vartheta, \phi)$ from all of the other directions $\vec{\Omega}' = (\vartheta', \phi')$ can be found using (Chandrasekhar, 1950):

$$I_{sca}(\Omega) = \int_{4\pi} \sigma_{sca}^{d}(\Omega, \Omega') I(\Omega') d\Omega' \tag{93}$$

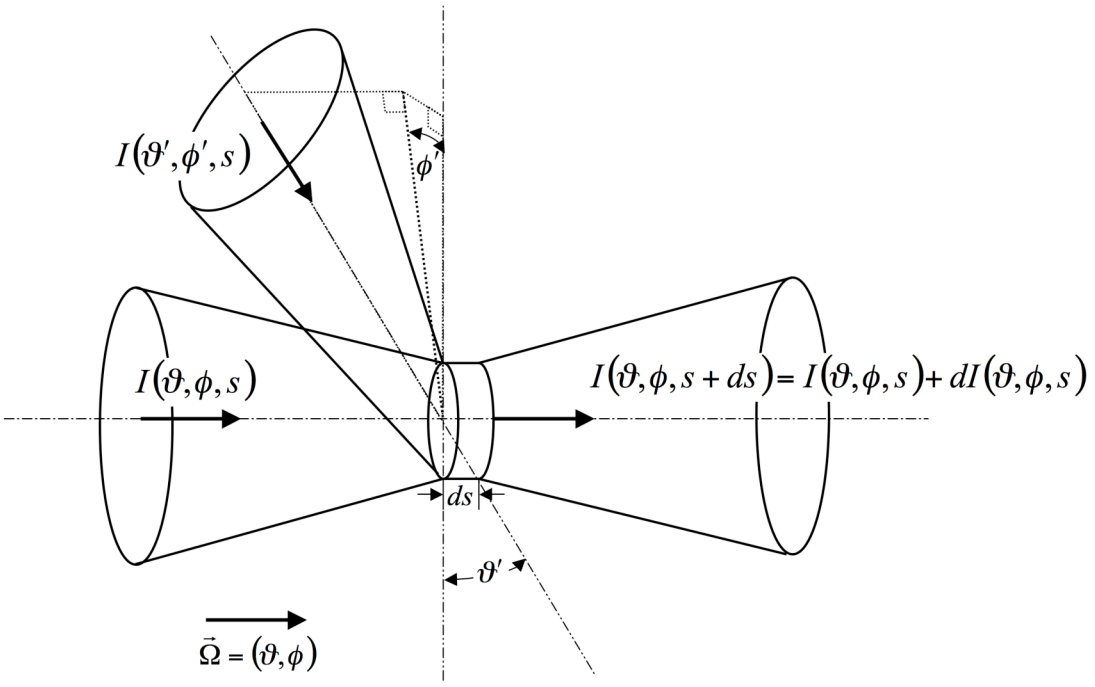


Figure 14: Scattering into direction $\vec{\Omega}$ through distance *dS* in a participating medium

Therefore, the RTE can be written as:

$$\frac{dI(\vartheta,\phi)}{dS} = -\sigma_{ext} I(\vartheta,\phi) + \int_0^{2\pi} d\phi' \int_0^{2\pi} d\vartheta' \sin\vartheta' \sigma_{sca}^{d}(\vartheta,\vartheta',\phi,\phi') I(\vartheta',\phi') + I_{src}(\vartheta,\phi,T) \tag{94}$$

For dispersive media, one can use Equation 83 for the definition of the scattering phase function and rewrite the RTE as:

$$\frac{dI(\vartheta,\phi)}{dS} = -\sigma_{ext} I(\vartheta,\phi) + \frac{\sigma_{sca}}{4\pi} \int_0^{2\pi} d\phi' \int_0^{\pi} d\vartheta' \sin\vartheta' p(\cos\theta) I(\vartheta',\phi') + I_{src}(\vartheta,\phi,T) \tag{95}$$

where θ is the scattering angle and is defined as:

$$\theta = \cos^{-1}\left(\cos\vartheta\cos\vartheta_o + \sin\vartheta\sin\vartheta_o\cos(\phi-\phi_o)\right) \tag{96}$$

where (ϑ_o,ϕ_o) and (ϑ,ϕ) defines the angle of incidence and the observation angle in 3-D space respectively. If one examines the plane defined by $\phi-\phi_o=0$, then the scattering angle θ is merely:

$$\theta = \vartheta - \vartheta_o \quad \text{if } \phi=\phi_o \tag{97}$$

The scattering angle is then the difference between the observation and incident angle. The RTE divided by the extinction coefficient and we obtain:

$$\sigma_{ext}^{-1}\frac{dI(\vartheta,\phi)}{dS} = -I(\vartheta,\phi) + \frac{\omega_0}{4\pi}\int_0^{2\pi} d\phi' \int_0^{\pi} d\vartheta' \sin\vartheta' p(\cos\theta) I(\vartheta',\phi') + \sigma_{ext}^{-1} I_{src}(\vartheta,\phi,T) \tag{98}$$

where ω_0 is the single scattering albedo and can be expressed as:

$$\omega_0 = \frac{\sigma_{sca}}{\sigma_{sca} + \sigma_{abs}} \tag{99}$$

One should note that many texts do not introduce the single scattering albedo term, but rather leave the RTE in terms of the scattering and extinction coefficient; however, ω_0 property is commonly used in the remote sensing community and is included here for that reason. Additionally, one should note that the polarization effects have not been directly addressed thus far in the RTE derivation. For an isotropic medium, the polarization effects reduce to a scalar. If the medium is not isotropic, then one must revert to the vector form of the RTE, which will be introduced shortly to account for the polarization effects.

Now if the medium is assumed to be homogenous over the distance *dS*, then the change in optical depth can be written as a constant:

$$d\tau = \sigma_{ext} dS \tag{100}$$

and the RTE equation becomes:

$$\frac{dI(\vartheta,\phi)}{d\tau} = -I(\vartheta,\phi) + \frac{\omega_0}{4\pi}\int_0^{2\pi} d\phi' \int_0^{\pi} d\vartheta' \sin\vartheta' p(\cos\theta) I(\vartheta',\phi') + \sigma_{ext}^{-1} I_{src}(\vartheta,\phi,T) \tag{101}$$

As intended, Equation 101 accounts for the localized change in intensity as the radiation travels through a dispersive participating medium excluding non-elastic effects.

A more complete and generalized vector form of the RTE is:

$$\sigma_{ext}^{-1}(\vec{n}\nabla)I_t(\vec{r},\vec{n}) = -I_t(\vec{r},\vec{n}) + \frac{\omega_0}{4\pi}\int_{4\pi} p(\vec{n},\vec{n}')I_t(\vec{r},\vec{n}')d\Omega' + B_0(\vec{r},\vec{n}) \tag{102}$$

where $\vec{r}$ is the observation point vector, $\vec{n}$ determines the direction of the beam with intensity I_t, ∇ is the gradient operator, and $B_0(\vec{r},\vec{n})$ describes the internal sources of radiation. The internal sources of radiation may include sources such as fluorescence, but is often limited to self-emission for simplicity. Note that Equation 98 can be derived from Equation 102 where:

$$(\vec{n}\nabla)I_t(\vec{r},\vec{n}) \equiv \frac{dI_t(\vec{r},\vec{n})}{dS} \tag{103}$$

if $B_0(\vec{r},\vec{n}) \to 0$. This is the most general form of the RTE and can be used in a variety of situations. It is the basis of many numerical techniques, including photon mapping, used to evaluate complex gaseous media.

3.3.3 Radiative Transfer Equation for a Plane-Parallel Gaseous Layer

The RTE for a plane-parallel gaseous layer is the most widely used approach for evaluating even more complex geometries. In the previous subsection, the RTE equation was derived for the medium case and then generalized into a vectorized equation. The layer of dispersive medium has thickness τ_0 and is assumed to be infinitely wide and deep. The top and bottom form parallel planes, and the top boundary is illuminated at every point by a unidirectional beam. The general geometry for the situation is shown in Figure 15 and follows the general conventions established in the preceding derivation of the RTE. Note that although the observation point is currently indicated to be below the layer, the derivation will examine observation points within the medium as well.

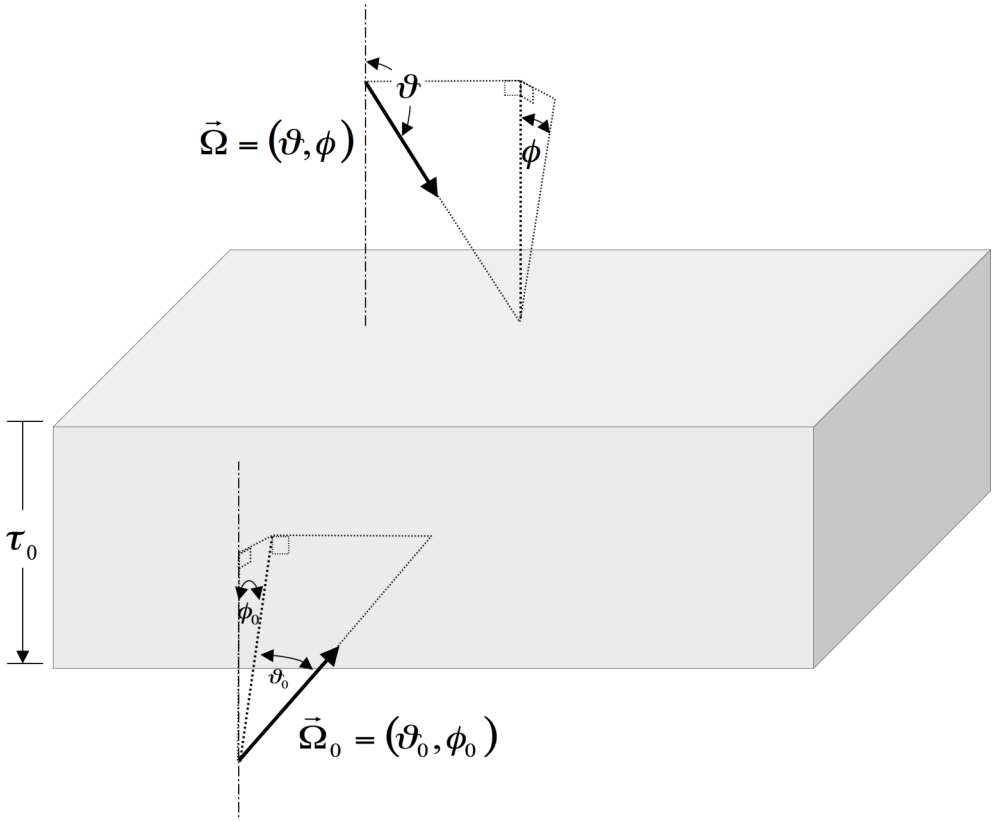


Figure 15: Geometrical construct for RTE of plane-parallel layer

Although presented without formal derivation, the RTE can be written as:

$$\cos\vartheta \frac{dI(\tau,\vartheta,\vartheta_0,\varphi)}{d\tau} = -I(\tau,\vartheta,\vartheta_0,\phi) + B(\tau,\vartheta,\vartheta_0,\phi) \tag{104}$$

where

$$B(\tau,\vartheta,\vartheta_0,\phi) = \frac{\omega_0}{4\pi}\int_0^{2\pi} d\phi' \int_0^{\pi} I(\tau,\vartheta',\vartheta_0,\phi') p(\theta') \sin(\vartheta') d\vartheta' + \frac{\omega_0 I_0}{4} p(\theta) e^{-\tau/\cos\vartheta_0} \tag{105}$$

is the source function, τ is the optical thickness of the layer, ϑ is the incidence angle, ϑ_0 is the observation angle, ϕ is the azimuth of the observed radiation, ω_0 is the single scattering albedo, $p(\theta)$ is the phase function, $I(\tau,\vartheta,\vartheta_0,\phi)$ is the diffused intensity at the optical thickness in the direction (ϑ,ϕ), and πI_0 is the net flux per unit area normal to the incident

light beam. Note that the emission is ignored and that the scattering angle for this setup is defined as:

$$\cos\theta' = \cos\vartheta\cos\vartheta_o + \sin\vartheta\sin\vartheta_o\cos(\phi - \phi_o) \tag{106}$$

$$\cos\theta = \cos\vartheta\cos\vartheta_o + \sin\vartheta\sin\vartheta_o\cos\phi \tag{107}$$

where the angles are as described previously and shown in Figure 15. Equation 104 is more restrictive than Equation 102 because it only accounts for the diffuse component of the radiant intensity. The total intensity I_t including the direct contribution is:

$$I_t(\tau,\vartheta,\vartheta_0,\phi) = -I(\tau,\vartheta,\vartheta_0,\phi) + \pi I_0 \exp\left[-\frac{\tau}{\cos\vartheta_0}\right]\delta(\Omega - \Omega_0) \tag{108}$$

where $\delta(\Omega)$ is the dirac-delta function.

It is reasonable to assume that diffused radiation does not enter a scattering layer at the boundaries specified by $\tau = 0$ or $\tau = \tau_0$. Based upon this assumption, a set of boundary conditions can be established such that:

$$I(0,\vartheta,\vartheta_0,\phi) = 0 \text{ at } \vartheta < \frac{\pi}{2} \tag{109}$$

$$I(\tau_0,\vartheta,\vartheta_0,\phi) = 0 \text{ at } \vartheta > \frac{\pi}{2} \tag{110}$$

Then one can solve the differential equation presented in Equation 104. The result is:

$$I(\tau,\vartheta,\vartheta_0,\phi) = \frac{e^{-\tau/\cos\vartheta}}{\cos\vartheta}\int_0^{\tau} B(\kappa',\vartheta,\vartheta_0,\phi)e^{-\tau'/\cos\vartheta}d\tau' \text{ at } \cos\vartheta > 0 \tag{111}$$

and

$$I(\tau,\vartheta,\vartheta_0,\phi) = \frac{e^{-\tau/\cos\vartheta}}{\cos\vartheta}\int_{\tau_0}^{\tau} B(\tau',\vartheta,\vartheta_0,\phi)e^{-\tau'/\cos\vartheta}d\tau' \text{ at } \cos\vartheta < 0 \tag{112}$$

In many derivations, authors elect to simplify the notation by substituting the following variables into the RTE equation:

$$\eta = \cos\vartheta \text{ and } \xi = \cos\vartheta_0 \tag{113}$$

Based upon the geometry and the definitions, the scattering angle is:

$$\theta = \cos^{-1}\left((-1)^l|\eta\xi| + \sqrt{\left(1-\eta^2\right)\left(1-\xi^2\right)}\cos\phi\right) \tag{114}$$

where l=1 for reflected cases and l=2 for transmitted cases. If the source function $B(\tau,\vartheta,\vartheta_0,\phi)$ is known, Equations 111 and 112 can be used to find the intensity for any depth within or outside the layer. Essentially, Equation 111 is the upward radiation and Equation 112 is the downward radiation in the layer.

The real interest is focused on the radiant intensity coming out of the layer from the top or the bottom. Equations 111 and 112 define the intensity for those situations as:

$$I_{\uparrow}(0,\vartheta,\vartheta_0,\phi) = -\frac{1}{\cos\vartheta}\int_0^{\tau_0} B(\tau',\vartheta,\vartheta_0,\phi)e^{-\tau'/\cos\vartheta}d\tau' \text{ at } \cos\vartheta < 0 \tag{115}$$

$$I_{\downarrow}(\kappa_0,\vartheta,\vartheta_0,\phi) = -\frac{e^{-\kappa_0/\cos\vartheta}}{\cos\vartheta}\int_0^{\kappa_0} B(\kappa',\vartheta,\vartheta_0,\phi)e^{-\kappa'/\cos\vartheta}d\kappa' \text{ at } \cos\vartheta > 0 \tag{116}$$

Once again, the issue is whether the source function is truly known. In most cases, the source function is not analytically known. Using Equations 105, 111, and 112, the integral to find the source function is:

$$\begin{aligned} B(\tau,\vartheta,\vartheta_0,\phi) = \frac{\omega_0}{4\pi}\int_0^{2\pi} d\phi' \Bigg\{ & \int_0^1 p(\theta')d(\cos\theta')\int_0^{\kappa}\frac{B(\tau',\vartheta,\vartheta_0,\phi)}{\cos\vartheta}e^{-\tau'/\cos\vartheta}d\tau' \\ & -\int_{-1}^0 p(\theta')d(\cos\theta')\int_{\tau}^{\tau_0}\frac{B(\tau',\vartheta,\vartheta_0,\phi)}{\cos\vartheta}e^{-(\tau'-\tau)/\cos\vartheta}d\tau' \Bigg\} + \frac{I_0\omega_0}{4}p(\theta)e^{-\tau/\cos\vartheta_0} \end{aligned} \tag{117}$$

Unfortunately, this integral cannot be solved analytically, but a number of numerical methods may be used to solve the set of equations to find the source function $B(\kappa,\vartheta,\vartheta_0,\phi)$.

3.3.3.1 Thin Layers

While the source function can be difficult to determine analytically in many cases, $B(\tau,\vartheta,\vartheta_0,\phi)$ can be found from Equation 105 for an optically thin layer. Essentially, if the layer is thin enough, then the multiple scattering contributions are negligible and the dominant term is from the singly scattered photons. Based upon this assumption, the source function is:

$$B(\tau,\vartheta,\vartheta_0,\phi)=\frac{I_0\omega_0}{4}p(\theta)e^{-\tau/\cos\vartheta_0} \tag{118}$$

By substituting Equation 118 into Equations 115 and 116 and assuming that the layer is homogenous, the upward and downward radiant intensity are found:

$$I_{\uparrow}^{d}=\frac{I_0\omega_0\cos\vartheta_0}{4(\cos\vartheta+\cos\vartheta_0)}\left\{1-\exp\left[-\tau_0\left(\frac{1}{\cos\vartheta}+\frac{1}{\cos\vartheta_0}\right)\right]\right\}p(\theta) \tag{119}$$

$$I_{\downarrow}^{d}=\frac{I_0\omega_0\cos\vartheta_0}{4(\cos\vartheta-\cos\vartheta_0)}\left\{\exp\left[-\frac{\tau_0}{\cos\vartheta}\right]-\exp\left[\frac{\tau_0}{\cos\vartheta_0}\right]\right\}p(\theta)\ \text{ at }\ \cos\vartheta\neq\cos\vartheta_0 \tag{120}$$

$$I_{\downarrow}^{d}=\frac{I_0\omega_0\tau_0}{4\cos\vartheta}\exp\left[-\frac{\tau_0}{\cos\vartheta}\right]p(\theta)\ \text{ at }\ \cos\vartheta=\cos\vartheta_0 \tag{121}$$

where $I_{\uparrow}^{d}$ and $I_{\downarrow}^{d}$ are the downward and upward diffused light intensity. The reflection and transmission functions are a common way to characterize the scattering of a gaseous layer. The reflection function is the ratio between the upward diffused light intensity and the normal light intensity component such that:

$$R=\frac{I_{\uparrow}^{d}}{\cos\vartheta_0 I_0} \tag{122}$$

The transmission function is the ratio between the downward diffused light intensity leaving the medium and the normal light intensity entering the medium such that:

$$T = \frac{I_{\downarrow}^{d}}{\cos\vartheta_0 I_0} \tag{123}$$

Substituting in the expressions for $I_{\uparrow}^{d}$ and $I_{\downarrow}^{d}$ the reflection and transmission functions become:

$$R = \frac{\omega_0 p(\theta)}{4(\cos\vartheta + \cos\vartheta_0)}\left\{1 - \exp\left[-\tau_0\left(\frac{1}{\cos\vartheta} + \frac{1}{\cos\vartheta_0}\right)\right]\right\} \tag{124}$$

and

$$T = \frac{\omega_0 p(\theta)}{4(\cos\vartheta - \cos\vartheta_0)}\left\{\exp\left[-\frac{\tau_0}{\cos\vartheta}\right] - \exp\left[\frac{\tau_0}{\cos\vartheta_0}\right]\right\} \tag{125}$$

where θ is defined according to Equation 114.

Now, consider a few simple cases. Although these equations were derived for a thin layer, if the layer thickness goes to infinity ($\tau_0 \to \infty$), then the transmission function goes to zero and the reflection function becomes:

$$R = \frac{\omega_0 p(\theta)}{4(\cos\vartheta + \cos\vartheta_0)} \tag{126}$$

Equation 126 can be used to calculate the single scattering contribution to the reflectance function for a very thick layer. A few useful observations can be made from this equation. First, the amount of reflected energy is directly proportional to the albedo term. If the absorption dominates $(\omega_0 \to 0)$, then less energy is reflected from the layer. Secondly, for an isotropically scattering phase medium, as the incidence and observation angle increase, the amount of reflected radiation is greater.

3.3.3.2 Thick, Homogenous Non-absorbing Layer

If the layer is optically thin, then the contribution from multiple scattering is minimal; however, the contribution is non-trivial for optically thick layers and an alternate RTE is necessary. In this subsection, the reflection function for a thick, homogenous non-absorbing medium is introduced. Specifically, we shall examine a model that was derived for use with cloud layers. Stated without proof, the reflection function is (Kokhanovsky, 2001):

$$R_{\infty}^{0} = \alpha\left(\frac{1}{2} + \frac{\left|\cos\vartheta\cos\vartheta_0\right|}{\left|\cos\vartheta\right| + \left|\cos\vartheta_0\right|}\right) + \beta\frac{p(\theta)}{4\left(\left|\cos\vartheta\right| + \left|\cos\vartheta_0\right|\right)} \tag{127}$$

where α and β are unknown constants. The first term of the equation represents the multiple scattering contributions, while the second is proportional to the amount from single scattering. Note the similarity for the second term with Equation 126. The value for the unknown constants is often obtained from experimental data. For instance, liquid water clouds exhibit characteristics such that the constants are (Kokhanovsky, 2001):

$$\begin{aligned} \alpha &= 1 \\ \beta &= 8 - 4.5e^{-5(\pi-\theta)} - 5e^{-5\left(\theta^{*}-\theta\right)} \end{aligned} \tag{128}$$

where θ is the scattering angle and θ^{*} is the rainbow angle in radians (θ^{*}=2.4 in the visible).

For isotropic scattering, both constants are equal to unity:

$$\alpha = \beta = 1 \tag{129}$$

Models of the reflection and transmission function of clouds using the equations and parametric coefficients have been found to be very consistent with real-world datasets (Kokhanovsky, 2001). Figure 16 is a sample plot of the predicted reflectance values using Kokhanovsky's cloud approximation. The effective optical depths of the curves range from 10-70. The surface albedo r_s was set to 0. Mie theory was used to predict the optical characteristics of the cloud layer based upon a gamma particle size distribution with the effective mean particle size of 6 μm and a coefficient of variance equal to $1/\sqrt{7}$. The solar angle was set at 45°. This approximation is fairly accurate for optically thick media, but it

does tend to overestimate the reflection functions for optically thin clouds. Kokhanovsky (2001) claims that the error is less than 15% in the visible and near infrared region for reasonable optical depths. In general, many researchers use this approach to derive empirical models for specific scenarios. The problem is that the solutions are highly specialized and do not adequately describe general cases, such as a scattering and absorbing layer with a "medium" optical thickness.

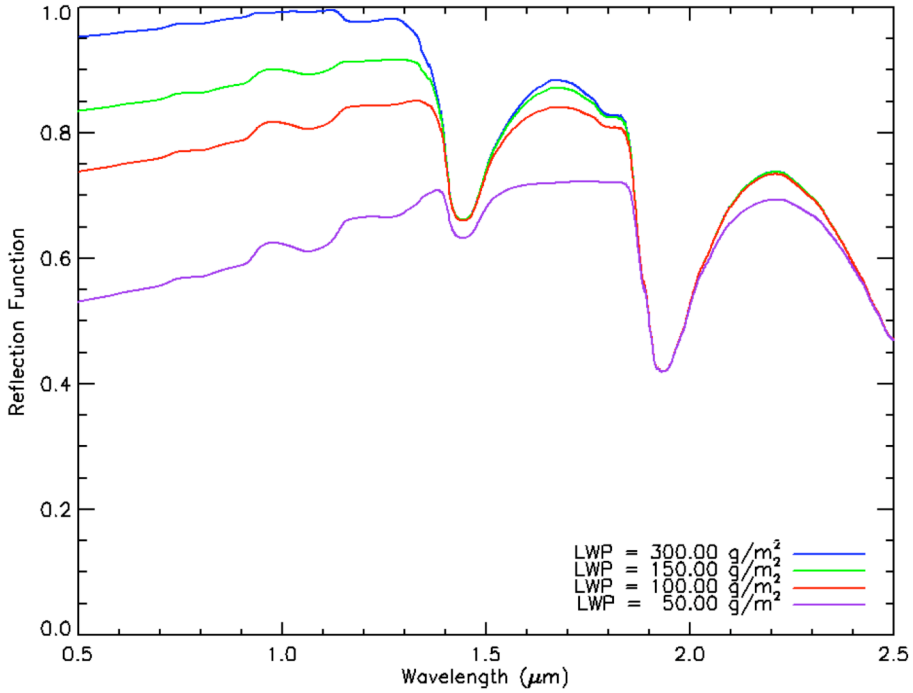


Figure 16: Reflection function of a water cloud with different liquid water paths (a_{eff}=6 μm, μ=1, μ_0=0.707, r_s=0)

3.3.4 General Solutions and Approximations for Plane-Parallel Layers

The focus of the previous section was upon optically thin layers. Ideally, one would like to be able to analytically evaluate the reflection and transmission functions or the upward and downward observed radiance for optical layers of any size. Unfortunately, this is not always feasible. Solutions for thick layers under a very limiting set of conditions do exist in the literature; however, many of the solutions require numerical integration or Monte Carlo techniques to evaluate the final expression. For now, we examine a few of the key approximations and their basic premises. There are four common approaches to evaluating

the radiative transfer equation for plane-parallel participating media: the diffusion approximation, the small angle approximation, the small angle diffusion approximation, and the discrete ordinate approximation. An expanded discussion is included for the diffusion and discrete ordinate approximations because of their relevance for this research effort and for evaluating multiple scattering effects.

3.3.4.1 Diffusion Approximation

The diffusion approximation (DA) is based upon techniques first applied in neuron transfer theory (Kokhanovsky, 2001). Many of the other approximations are only valid when the volume density of the medium is considerably small, less than 0.1%. In contrast, the diffusion approximation is best suited for cases where the volume density is >> 1%. The underlying assumption for the diffusion approximation is that the diffuse intensity is scattered by a large number of particles such that its angular distribution is almost uniform. In truth, this cannot be the case. If the angular distribution were constant, then the flux would be zero and no net power would propagate through the medium. Thus, the angular distribution of the diffuse intensity is assumed to be skewed slightly so that it has more magnitude in the direction of the net flux flow than in the reverse direction. Then one can proceed to simplify the governing equations and evaluate important asymptotic cases. The diffusion approximation is most relevant for considering isotropic sources; however, the equations can be modified to account for a mono-directional and non-stationary sources, such as a collimated or divergent pulsed laser beam. Significant complications are encountered due to the effects of surface boundaries and the corresponding assumptions generally restrict the accuracy of the diffusion approximation to photons deep within a scattering layer. The next few paragraphs will introduce a way of developing the diffusion approximation. There are multiple derivation paths throughout the literature. This one is primarily based upon the work by Zege, Ivanonv, and Katsev (1991), but also leverages the work by Ishimaru (1978) and Kokhanovksy (2001). One should refer to all three for a more complete derivation and additional applications of the diffusion approximation for radiative transfer theory.

First, let's start with the generalized vector form of the RTE which we introduced earlier that can be written as:

$$\sigma_{ext}^{-1}(\vec{n}\nabla)I_t(\vec{r},\vec{n}) = -I_t(\vec{r},\vec{n}) + \frac{\omega_0}{4\pi}\int_{4\pi} p(\vec{n},\vec{n}')I_t(\vec{r},\vec{n}')d\Omega' + B_0(\vec{r},\vec{n}) \tag{130}$$

where $\vec{r}$ is the observation point vector, $\vec{n}$ determines the direction of the beam with intensity I_t, ∇ is the gradient operator, and $B_0(\vec{r},\vec{n})$ describes the internal sources of radiation. If we move the extinction coefficient to the right-hand side and integrate the RTE over all $\vec{n}$ directions, the result is:

$$\nabla \cdot \vec{F}(\vec{r}) = -\sigma_{abs} w(\vec{r}) + B_{00}(\vec{r}) \tag{131}$$

where $\vec{F}(\vec{r})$ is the flux density vector, $w(\vec{r})$ is the radiation density, and B_{00} is the zeroth moment of the source function, which is defined as:

$$B_{00}(\vec{r}) = \int\int_{4\pi} B_0(\vec{r},\vec{n})d\vec{n} \tag{132}$$

Equation 131 relates the flux density vector to the radiation density within the medium. We shall use this equation later to formulate the diffusion approximation, but we need to first develop another set of equations to allow us to find an expression that relates the source function and the radiation density function. If both sides of Equation 130 are multiplied $\vec{n}$ and integrated with respect to the solid angle, the resulting equation is:

$$\int\int_{4\pi} \vec{n}(\vec{n}\nabla)I_t(\vec{r},\vec{n})d\vec{n} = -\sigma_{ext}(1-\omega_0 g)\vec{F}(\vec{r}) + \vec{B}_{01}(\vec{r}) \tag{133}$$

where

$$\vec{B}_{01}(\vec{r}) = \int\int_{4\pi} \vec{n}B_0(\vec{r},\vec{n})d\vec{n} \tag{134}$$

and is the first moment of the source function. The first portion of the integral was simplified using the definition of the asymmetry parameter, g, so that:

$$\frac{1}{4\pi}\int\int_{4\pi} p(\vec{n},\vec{n}')\vec{n}'d\vec{n}' = g\vec{n} \tag{135}$$

According to classical diffusion theory, the scattered light radiance for weakly anisotropic thick layers can be represented as (Zege, et al., 1991):

$$I_t(\vec{r},\vec{n}) = \frac{1}{4\pi}\left\{w(\vec{r}) + 3\left[\vec{F}(\vec{r})\cdot\vec{n}\right]\right\} \tag{136}$$

If we combine Equations 133 and 136, then:

$$\int\int_{4\pi} \vec{n}(\vec{n}\nabla) I_t(\vec{r},\vec{n}) d\vec{n} = \frac{1}{3}\nabla w(\vec{r}) \tag{137}$$

From Equation 133 and 137, we can infer another relationship between the radiation density and the flux. The flux density vector can be expressed as:

$$\vec{F}(\vec{r}) = \frac{1}{3\sigma_{ext}(1-g\omega_0)}\left\{\nabla w(\vec{r}) - 3\vec{B}_{01}(\vec{r})\right\} \tag{138}$$

which is known as Fick's law (Zege, et al., 1991). Based upon Equations 131 and 138, we can then find the direct relationship that we have been seeking between the radiation density and the moments of the source function. If we substitute Equation 138 into Equation 131 and express the optical coordinates to be in terms of optical depth, we get the well-known diffusion equation:

$$\Delta_\tau w(\vec{\tau}) - \gamma^2 w(\vec{\tau}) = G(\vec{\tau}) \tag{139}$$

where the γ is the asymptotic attenuation coefficient and $G(\vec{\tau})$ is an expression based upon the angular moments of the source function:

$$\begin{aligned} \gamma^2 &= 3(1-\omega_0)(1-g\omega_0) \\ G(\vec{\tau}) &= -\frac{3(1-g\omega_0)}{\sigma_{ext}} B_{00}(\vec{r}) + \frac{3}{\sigma_{ext}}\nabla_{\vec{\tau}}\vec{B}_{01}(\vec{r}) \end{aligned} \tag{140}$$

One should note that one of the most difficult issues to deal with when solving the diffusion equation is establishing the boundary conditions. This is one of the reasons that the diffusion approximation is not very accurate near the surface boundaries of a semi-infinite layer.

One common use of the diffusion approximation is to find the radiation density for an isotropic-unit point source lying at the top surface boundary of a semi-infinite medium $\left(P_0 = 1;\ \tau = \tau';\ \rho = 0\right)$. For simplicity, we shall rely upon the axial symmetry of the scenario and use a cylindrical coordinate system. Using the definition for $G\left(\vec{\tau}\right)$ and an isotropic-unit point source:

$$G\left(\rho,\tau\right) = -\frac{\sigma_{ext}^2}{q}\delta\left(\tau - \tau'\right)\frac{\delta\left(\rho\right)}{2\pi\rho} \tag{141}$$

where ρ is the radial component for the cylindrical coordinate system and q is the scattering indicatrix parameter (also called the scatter phase function parameter) which is defined as:

$$q = \frac{1}{3\left(1-g\right)} \tag{142}$$

We now impose a set of reflection conditions at the layer boundaries by introducing different extrapolated lengths for the upper (d_1) and the lower (d_2) boundaries of the layers where:

$$\begin{aligned} w\left(\rho,\tau = -d_1\right) &= 0 \\ w\left(\rho,\tau = \tau_0 + d_2\right) &= 0 \end{aligned} \tag{143}$$

This assumption basically states that the radiation is zero at some distance outside the layer boundaries.

Based upon these boundary conditions and Equations 139 and 141, the resulting radiation density is:

$$w\left(\rho,\tau,\tau_0,\tau'\right) = \frac{\sigma_{ext}^2}{4\pi q}\left\{\frac{\exp\left[-\gamma\alpha_{04}\right]}{\alpha_{04}} - \frac{\exp\left[-\gamma\alpha_{03}\right]}{\alpha_{03}} - \sum_{k=1}^{\infty}\sum_{i=1}^{4}\left(-1\right)^{i+1}\frac{\exp\left[-\gamma\alpha_{ki}\right]}{\alpha_{ki}}\right\} \tag{144}$$

where

$$\begin{aligned} \alpha_{ki} &= \sqrt{\beta_{ki}^2 + \rho^2} & \beta_{k1} &= 2kb_1 - a_1 \\ a_2 &= \tau - \tau' & \beta_{k2} &= 2kb_1 - a_2 \\ a_1 &= \tau + \tau' + 2d_1 & \beta_{k3} &= 2kb_1 + a_1 \\ b_1 &= \tau_0 + d_1 + d_2 & \beta_{k4} &= 2kb_1 + a_2 \end{aligned} \tag{145}$$

As noted by Zege, et al., (1991), the structure of Equation 144 can be interpreted intuitively. Figure 17 illustrates the geometry for conceptual, virtual sources in a diffusion approximation of an isotropic point source in a semi-infinite medium for an observation point *M*. Ignoring the scalar, the first term in Equation 144 is the solution for an isotropic point source in an infinite medium. The second term acts like a sink located above the upper boundary. Combined, these two terms provide a solution for a semi-infinite medium. The third term adjusts for the finite thickness of the layer. If the layer is semi-infinite $\left(\tau_0 \to \infty\right)$, then the radiation density is simply:

$$w\left(\rho, \tau, \tau_0 \to \infty, \tau'\right) = \frac{\sigma_{ext}^2}{4\pi q}\left\{\frac{\exp\left[-\gamma\alpha_{04}\right]}{\alpha_{04}} - \frac{\exp\left[-\gamma\alpha_{03}\right]}{\alpha_{03}}\right\} \tag{146}$$

Later, we shall revisit the solution for an isotropic point source presented here to eventually derive an approximation for a pulsed monodirectional, point source. The latter will provide a good benchmark for the backscattered returns deep within a layer of the DIRSIG LIDAR model.

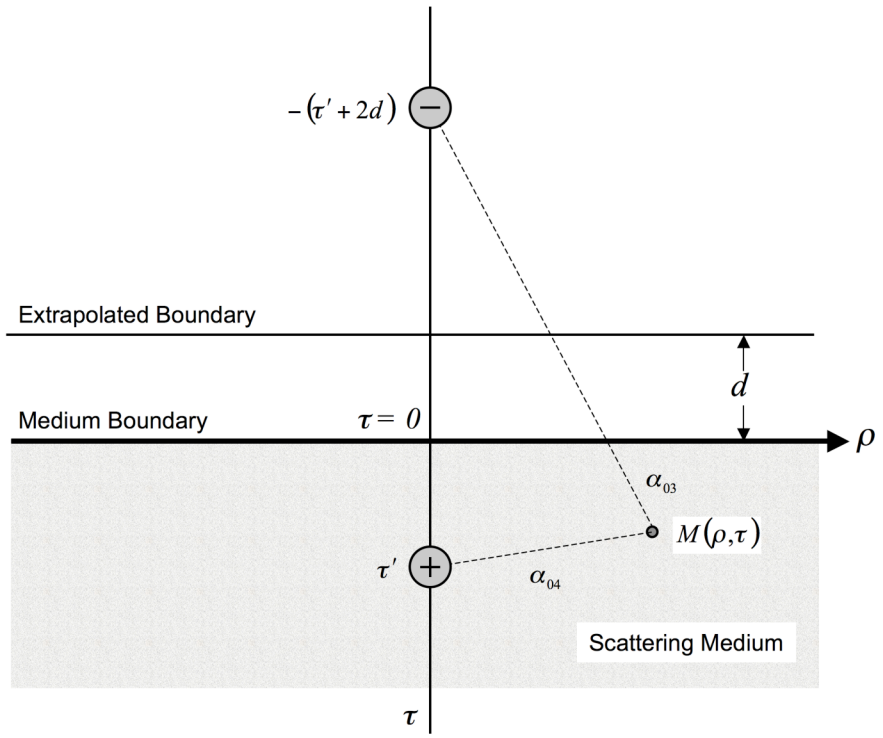


Figure 17: Geometry for virtual sources in a diffusion approximation of an isotropic point source in a semi-infinite medium for an observation point *M*

3.3.4.2 Small Angle Approximation

The small angle approximation (SAA) assumes that the light scattered by the particles in the medium is largely restricted to a small angle in the forward direction. This assumption is most valid if the particle size is much greater than the wavelength under consideration; however, the small angle approximation can be applied in more general cases if the medium is dominated by highly anisotropically scattering and is illuminated by directional localized sources. The SAA forms the foundation for deriving the optical transfer functions of scattering media and for radiative transfer theory of multiple scattering by moving particles. Along with the benefits, the SAA carries two primary restrictions. First, it cannot be applied to optically thick media or used to describe the temporal deformation of a pulse signal propagating through a participating medium. Secondly, calculation of the results for the SAA requires the capability to evaluate multidimensional Fourier transforms. The latter restriction is of less concern today and is also one of the attractions for many researchers.

For instance, using the SAA, the radiance can be mathematically described as (Zege, et al., 1991):

$$I(z,\vec{r},\vec{n}) = \mathscr{F}_{\vec{\rho}}^{-1}\left\{\mathscr{F}_{\vec{\eta}}^{-1}\left\{\begin{array}{l}\mathscr{F}_{\vec{\rho}}\left\{\mathscr{F}_{\vec{\eta}}\left\{I_0(0,\vec{r},\vec{n})\right\}\right\} \\ \times\exp\left[-\int_0^z \sigma_{ext}\left(1-\frac{1}{4\pi}\mathscr{F}_{\vec{\eta}}\left\{p(\vec{n})\right\} * \delta\left(\vec{\rho}(z-z')\right)dz'\right)\right]\end{array}\right\}\right\} \tag{147}$$

where $I_0(0,\vec{r},\vec{n})$ is the incident radiance at the boundary and the modified multidimensional Fourier transforms are:

$$\begin{aligned}\mathscr{F}_{\vec{\eta}}\left\{f(z,\vec{r},\vec{n})\right\} &= \iint f(z,\vec{r},\vec{n})\exp\left[i\vec{n}\cdot\vec{\eta}\right]d\vec{n} \\ \mathscr{F}_{\vec{\rho}}\left\{f(z,\vec{r},\vec{n})\right\} &= \iint f(z,\vec{r},\vec{n})\exp\left[i\vec{r}\cdot\vec{\rho}\right]d\vec{r}\end{aligned} \tag{148}$$

For an isotropically radiating point source located at the surface boundary, the modulation transfer function (MTF) for an inhomogeneous layer can be found to be (Zege, et al., 1991):

$$\left[T(\nu)\right]_{\text{inhomogenous}} = \exp\left[\int_0^{z_0}\sigma_{ext}(z')\left[1-p\left(\nu(z_0-z'),z'\right)\right]dz'\right] \tag{149}$$

If one then considers a plane-parallel layer that is homogenous, the MTF simplifies to (Zege, et al., 1991):

$$\left[T(\nu)\right]_{\text{homogenous}} = \exp\left[-\sigma_{ext}z_0 + \int_0^{z_0}\sigma_{ext}p(\nu z')dz'\right] \tag{150}$$

The SAA approach was considered as a potential solution for analytically tractable cases that can be used as a reliable benchmark for the accuracy of the photon mapping algorithm; however, the diffusion approximation and the multiple scattering LIDAR equation were selected to form the baseline of the verification process.

3.3.4.3 Small-Angle Diffusion Approximation

The small angle diffusion approximation (SADA) is a combination of the DA and the SAA. Essentially, the optical characteristics of the participating media are assumed to be

characterized by forward scattering and the angular radiance distribution is described by smooth functions. The degree of smoothness is restricted such that the variance of the angular radiance distribution must be greater than the phase function variance. Because of the angular radiance distribution requirements, the SADA is not valid for weakly or strongly absorbing media; however, the optical depth does not directly restrict the SADA. Therefore, the SADA complements both the SAA and DA methods and generates results that both overlap and bridge the gap between the other approximations.

3.3.4.4 Discrete Ordinate Approximation

Another approach is the discrete ordinate approximation (DOA), which calculates the complicated integral in the governing radiative transfer equation by first removing the azimuth dependence, then introducing a set of Fourier series, and finally converting the integrals to quadrature sums. The quadrature sums transform the integro-differential equation into a system of ordinary differential equations that can be solved using standard linear algebra. The DOA approach published by Stamnes and Dale (1981) is the core of the Fortran code developed in 1988 called DISORT, which is the gold standard for radiative transfer codes for vertically inhomogeneous layered media in the remote sensing community. DISORT is the underlying code embedded in larger atmospheric models such as MODTRAN for the purpose of calculating multiple scattering effects. The implementations of DOA and DISORT are designed to calculate the radiative transfer for a set of stacked plane-parallel scattering, absorbing, and emitting media with a lower surface boundary that has a specific bidirectional reflectivity function and that is illuminated by a parallel beam or diffuse radiance. One can then calculate the diffuse and direct radiance anywhere within the described media.

Equations 104 and 105 are the radiative transfer equations for a plane-parallel layer. They are repeated below for ease of reference:

$$\cos\vartheta \frac{dI(\tau,\vartheta,\vartheta_0,\varphi)}{d\tau} = -I(\tau,\vartheta,\vartheta_0,\phi) + B(\tau,\vartheta,\vartheta_0,\phi) \tag{151}$$

where

$$B(\tau,\vartheta,\vartheta_0,\phi) = \frac{\omega_0}{4\pi}\int_0^{2\pi} d\phi' \int_0^{\pi} I(\tau,\vartheta',\vartheta_0,\phi') p(\theta') \sin(\vartheta') d\vartheta' + Q(\tau,\vartheta,\vartheta_0,\phi) \tag{152}$$

is the source function, τ is the optical thickness of the layer, ϑ is the incidence angle, ϑ_0 is the observation angle, ϕ is the azimuth of the observed radiation, ω_0 is the single scattering albedo, $p(\theta)$ is the phase function, $I(\tau,\vartheta,\vartheta_0,\phi)$ is the diffused intensity at the optical thickness in the direction (ϑ,ϕ), and $Q(\tau,\vartheta,\vartheta_0,\phi)$ is the external source function. The external source function includes the incident beam and the thermal contribution of the layer(s) and can be written as:

$$Q(\tau,\vartheta,\vartheta_0,\phi) = \frac{\omega_0 I_0}{4} p(\theta) e^{-\tau/\cos\vartheta_0} + \{1-\omega_0(\tau)\} I_{src}(\tau,T,\vartheta,\phi) \tag{153}$$

where $\pi\ I_0$is the net flux per unit area normal to the incident light beam and $I_{src}(\tau,T,\vartheta,\phi)$ is typically Planck's blackbody equation. The azimuthal ϕ dependence is then removed through two modifications. First, the scattering phase function is written as a series of $2M$ Legendre polynomials such that:

$$P(\tau,\cos\Theta) = \sum_{l=0}^{2M-1} (2l+1) g_l(\tau) P_l(\cos\Theta) \tag{154}$$

where the expansion coefficients are given by:

$$g_l(\tau) = \frac{1}{2}\int_{-1}^{+1} P_l(\cos\Theta) p(\cos\Theta) d(\cos\Theta) \tag{155}$$

Note that the expansion assumes that the scattering phase function depends only on the angle between the incident and scattered beams. This assumption is very reasonable. The second stage transforms the scattering phase function and the intensity into a Fourier cosine series. The expanded scattering phase function then becomes:

$$P(\tau,\cos\Theta) = \sum_{l=0}^{2M-1} (2l+1) g_l(\tau) \cdot \left\{ P_l(\mu) P_l(\mu') + 2\sum_{m=1}^{l} \Lambda_l^m(\mu) \Lambda_l^m(\mu') \cos m(\phi-\phi_m) \right\} \tag{156}$$

where $\mu = \cos\vartheta$ and $\Lambda_l^m(\mu)$ is the normalized associated Legendre polynomial defined by:

$$\Lambda_l^m(\mu) = \sqrt{\frac{(l-m)!}{(l+m)!}} P_l^m(\mu) \tag{157}$$

where $P_l^m(\mu)$ is the associated Legendre polynomial.

The azimuth dependence is removed by a Fourier cosine series expansion:

$$I(\tau,\mu,\phi) = \sum_{m=0}^{2N-1} I^m(\tau,\mu)\cos m(\phi - \phi_0) \tag{158}$$

Substituting Equations 156 and 158 into Equations 104 and 105, the RTE is split into 2*M* different equations such that:

$$\mu \frac{dI^m(\tau,\mu)}{d\tau} = -I^m(\tau,\mu) + S^m(\tau,\mu) \quad \text{for } m = \{0,1,...,2M-1\} \tag{159}$$

where the internal source function becomes:

$$S^m(\tau,\mu) = \int_{-1}^{1} D_m(\tau,\mu,\mu') I^m(\tau,\mu') d\mu' + Q^m(\tau,\mu) \tag{160}$$

and the additional terms are:

$$\begin{aligned} D_m(\tau,\mu,\mu') &= \frac{\omega(\tau)}{2} \sum_{l=m}^{2m-1} (2l+1) g_l(\tau) \Lambda_l^m(\mu) \Lambda_l^m(\mu') \\ Q_m(\tau,\mu) &= X_0^m(\tau,\mu) e^{-\tau/\cos\vartheta_0} + \delta_{m0}\{1-\omega_0(\tau)\} I_{src}(\tau,T,\vartheta,\phi) \\ X_0^m(\tau,\eta) &= \frac{\omega(\tau) I_0}{4\pi}(2-\delta_{m0}) \sum_{l}^{2M-1} (-1)^{l+m} (2l+1) g_l(\tau) \Lambda_l^m(\eta) \Lambda_l^m(\eta_0) \\ \delta_{m0} &= \begin{cases} 1 & \text{if } m = 0 \\ 0 & \text{otherwise} \end{cases} \end{aligned} \tag{161}$$

The next step is to convert this set of equations to a form that can be calculated numerically. If you examine the internal source function, the integral is formed appropriately so that we

can replace the integrals with Gaussian quadratures. This generates a system of ordinary differential equations where:

$$\mu_i \frac{dI^m(\tau,\mu_i)}{d\tau} = -I^m(\tau,\mu_i) + S^m(\tau,\mu_i) \quad \text{for } i = \{\pm 1, \pm 2, ..., \pm N\} \tag{162}$$

$$S^m(\tau,\mu_i) = \sum_{\substack{j=-N \\ j\neq 0}}^{N} w_j D_m(\tau,\mu_i,\mu_j) I^m(\tau,\mu_j) d\mu' + Q^m(\tau,\mu_i) \tag{163}$$

where μ_i and w_i are the quadrature points and weights respectively. Each of the $2N$ equations is often referred to by the community as a "stream". If we presume that the atmosphere or our system of participating layers can be divided into L homogeneous layers, then for any particular layer we can rewrite Equation 162 in matrix form as:

$$\begin{bmatrix} \frac{d\mathbf{I}^+}{d\tau} \\ \frac{d\mathbf{I}^-}{d\tau} \end{bmatrix} = \begin{bmatrix} -\alpha & -\beta \\ \beta & \alpha \end{bmatrix} \begin{bmatrix} \mathbf{I}^+ \\ \mathbf{I}^- \end{bmatrix} + \begin{bmatrix} \tilde{\mathbf{Q}}^+ \\ \tilde{\mathbf{Q}}^- \end{bmatrix} \tag{164}$$

where the associated matrices are:

$$\begin{aligned}
\mathbf{I}^{\pm} &= \{I^m(\tau,\pm\eta_i)\} && i = 1,2,...,N \\
\tilde{\mathbf{Q}}^{\pm} &= \mathbf{M}^{-1}\mathbf{Q}^{\pm} && \\
\mathbf{Q}^{\pm} &= \{Q^m(\tau,\pm\eta_i)\} && i = 1,2,...,N \\
\mathbf{M} &= \{\eta_i \delta_{ij}\} && i,j = 1,2,...,N \\
\alpha &= \mathbf{M}^{-1}(\mathbf{D}^+\mathbf{W} - \mathbf{1}) && \\
\beta &= \mathbf{M}^{-1}\mathbf{D}^-\mathbf{W} && \\
\mathbf{W} &= \{w_i \delta_{ij}\} && i,j = 1,2,...,N \\
\mathbf{D}^+ &= \{D^m(\eta_i,\eta_j)\} = \{D^m(-\eta_i,-\eta_j)\} && i,j = 1,2,...,N \\
\mathbf{D}^- &= \{D^m(-\eta_i,\eta_j)\} = \{D^m(\eta_i,-\eta_j)\} && i,j = 1,2,...,N \\
\mathbf{1} &= \{\delta_{ij}\} && i,j = 1,2,...,N
\end{aligned} \tag{165}$$

Equation 164 now represents a linear system of coupled differential equations that can be solved using common linear algebra techniques. In general, DISORT attempts to first find

the homogenous and then the particular solutions based upon the internal source function. The resulting answer is then the sum of the two solutions. A thorough discussion and derivation for the DISORT algorithm is presented in the DISORT Documentation of Methodology (Stamnes, et al., 2000).

If one is considering plane-parallel layers illuminated by an infinitely wide plane wave, discrete-order radiative transfer codes like DISORT are very valuable. For instance, the assumptions are generally valid for analyzing the passive reflection functions for a cloud layer. Figure 18 shows DISORT's predictions for the nadir reflection function of a cloud with an optical depth of 30 that is illuminated by the sun at 45° and for a ground albedo as indicated by the values of r_s. The optical properties were generated based upon a gamma distribution via Du's Mie code, which is discussed in Section 3.6. At longer wavelengths, the bulk returns are from backscatter of the layer and the impact of the ground albedo is minimal. In contrast, the ground albedo differences for r_s=0.5 to 0.9 results in a 10% increase in the apparent reflectance of the cloud in the visible region. Figure 19 is a companion plot that compares Kokhanovksy's cloud approximation (Equation 127) and DISORT for this specific cloud layer scenario. Notice that the approximation is a reasonable fit to the more accurate DISORT calculations; however, this is not always the case. Both Figure 18 and Figure 19 show the reflection function as a function of wavelength. Another instructive scenario is to examine the change of the reflection function at a particular wavelength with respect to optical depth. Figure 20 compares the cloud approximation and DISORT for cloud layers of varying thicknesses. The reflection function is plotted at a wavelength of 2130 nm and a solar angle of 60°. Once again, the two solutions are very similar for optical depths greater than 1. Although we have demonstrated that similar results can be achieved using reasonable approximations, radiative transfer codes such as DISORT are significantly more robust and accurate over a wider range of input parameters. This is because the RTE is calculated numerically as opposed to making restrictive assumptions to reduce it to a manageable form. Naturally, the accuracy of discrete ordinate radiative transfer codes depend upon the number of streams and Fourier cosine terms that one employs.

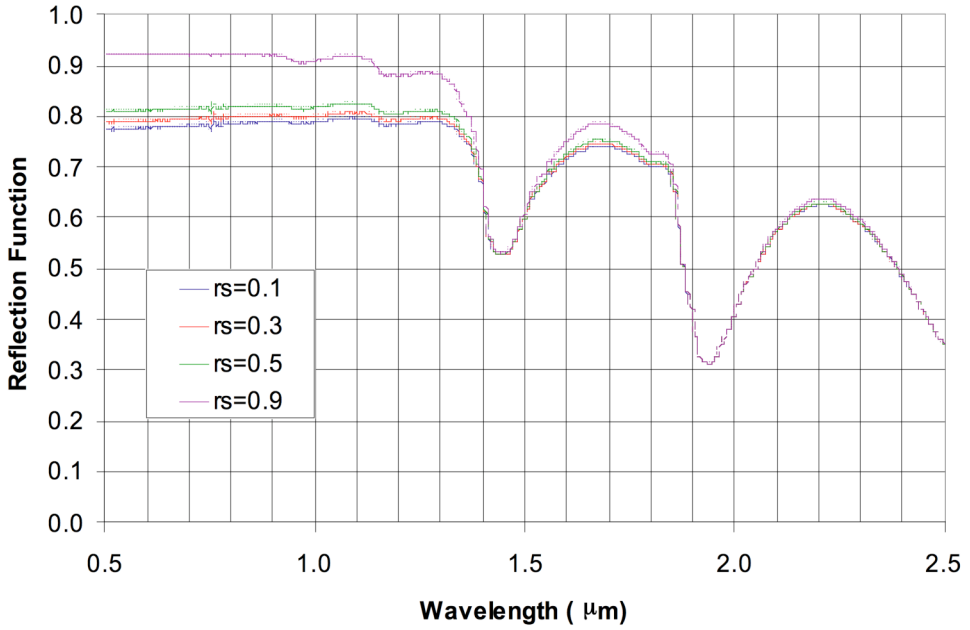


Figure 18: Reflection function of water clouds at τ=30, μ=1, μ_0=0.707, a_{eff}=6 μm for different ground albedos

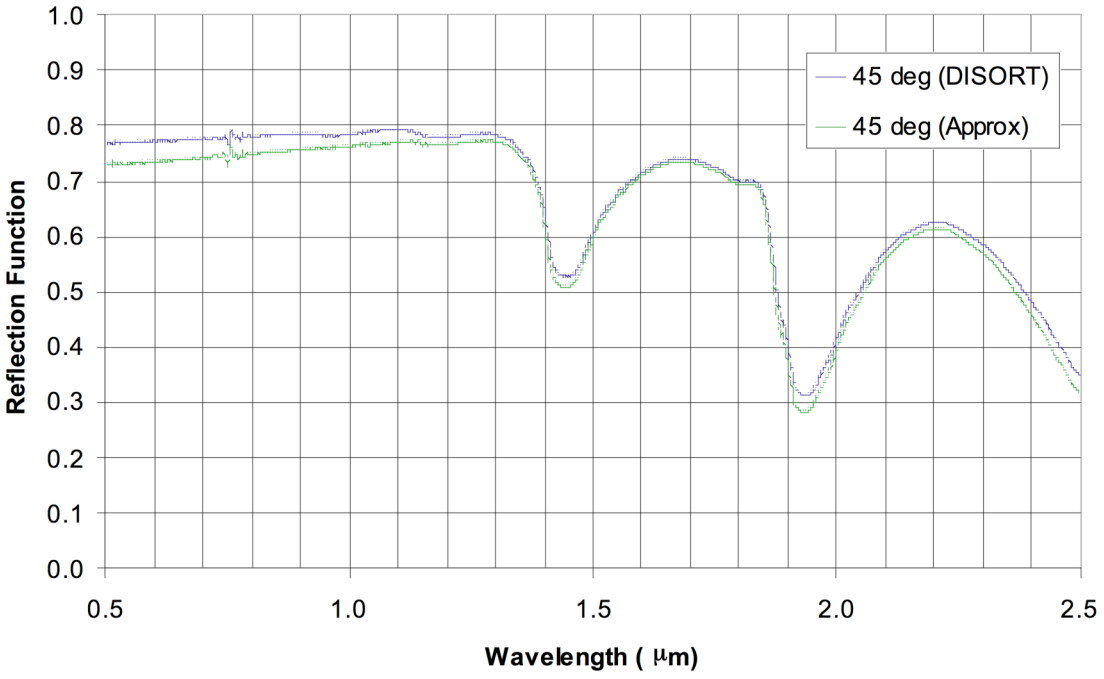


Figure 19: Reflection function of water clouds from DISORT and Kokhanvosky's cloud approximation (Equation 127) (τ=30, μ=1, μ_0=0.707, a_{eff}=6 μm)

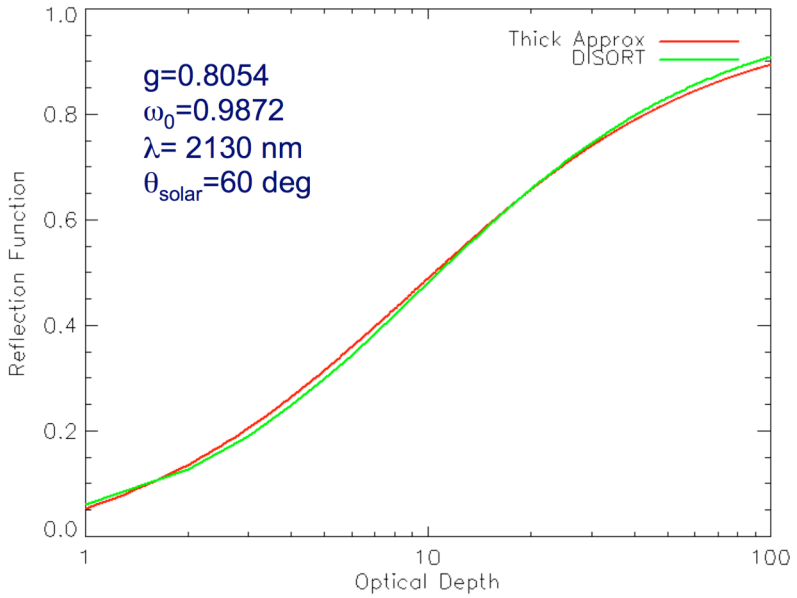


Figure 20: Reflection function of water clouds from DISORT and Kokhanvosky's cloud approximation (Equation 127)

3.3.4.5 Approximation Applicability Diagram

Figure 21 is a conventional applicability diagram for a particular medium with an asymmetry parameter of 0.9. The curve AB bounds where the SAA is valid and the curve EF bounds where the DA is valid. The DOA is not restricted to a specific case for this example and is therefore not directly represented on the chart. Such a diagram is often used to guide selection of an appropriate method to calculate the reflection or transmission functions for the participating medium. As stated previously, the supporting theory for these approximations is not presented in this dissertation. The method of discrete ordinates was not included in this applicability diagram, because the derivation is theoretically applicable over a wide range of parameters depending upon the number of streams and quadrature weights that one employs to solve for the diffuse flux or intensity. For the purposes of verification of the scattering contributions, we shall primarily consider a range of optical depths from thin to thick with a high scattering albedo (low absorption). The DIRSIG LIDAR model is designed to be similar to DISORT in that the module is applicable in all of the situations described in the applicability diagram (presuming you shoot enough photons into the scene).

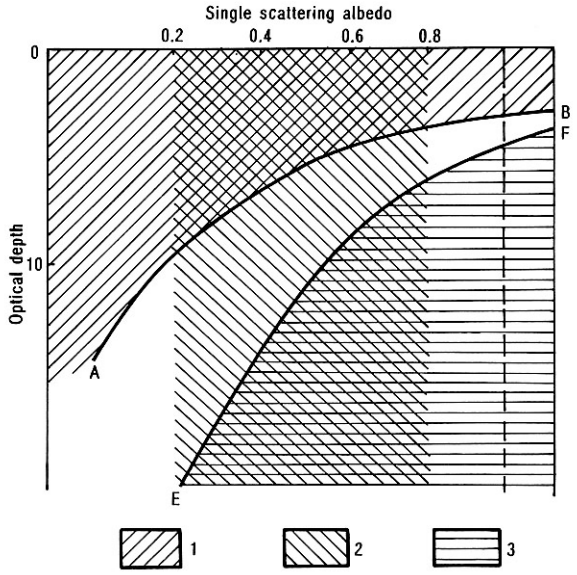


Fig. 4.12. Applicability domains of approximation methods: (1) small-angle approximation; (2) small-angle diffusion approximation; (3) diffusion approxmation

Figure 21: Applicability domains of approximation methods (Zege, et al., 1991)

3.3.4.6 Non-stationary Diffusion Approximation

Thus far, we have only considered RTE for stationary sources. The sources illuminate the participating media for an infinite amount of time such that the light field reaches steady state. The assumption is not valid for pulsed sources, such as lasers. In this subsection, we will discuss the general process of deriving a nonstationary solution from a stationary solution and then eventually converge to an expression for a monodirectional-pulsed point source. The latter mathematical relationship will then be evaluated using the backscatter noise (BSN) approximation to find the received power from deep within a scattering layer when illuminated by a narrow laser pulse.

The nonstationary RTE can be mathematically expressed as:

$$\left\{\frac{\partial}{\partial u}+\left(\vec{n}\nabla\right)+\sigma_{ext}\right\}I\left(\vec{r},\vec{n}\right)=\frac{\omega_0}{4\pi}\int_{4\pi}p\left(\vec{n},\vec{n}'\right)I\left(\vec{\tau},\vec{n}',u\right)\vec{n}'+B'\left(\vec{\tau},\vec{n},u\right) \tag{166}$$

where $u = \sigma_{sca} ct$ is a dimensionless parameter. To solve this equation, one first finds the impulse response of the medium $I_\delta(\vec{\tau},\vec{n},u)$ when the medium is excited by the source function:

$$B'(\vec{\tau},\vec{n},u) = B'(\vec{\tau},\vec{n})\ \delta(u) \tag{167}$$

Once the impulse response of the medium is known, the radiance for a different source can be found by integrating the source function with the impulse response using the equation:

$$I(\vec{\tau},\vec{n},u) = \int_0^\infty I_\delta(\tau,\vec{n},u')I_0(u-u')du' \tag{168}$$

and the alternative source function is expressed as:

$$B'(\vec{\tau},\vec{n},u) = B'(\vec{\tau},\vec{n},u)I_0(u) \tag{169}$$

$I_\delta(\vec{\tau},\vec{n},u)$ may be considered to be the Green's function of the nonstationary transfer equation. Another common description is the propagating pulse spread function or the photon time-of-arrival fluctuations or the photon path distribution function. All of these descriptions refer to the physical reality of the fluctuations of the photon time-of-arrival at a particular point in space. If one can find $I_\delta(\vec{\tau},\vec{n},u)$ for a weakly or non-absorbing media, then the impulse response can be adjusted to account for the true absorption of the media. One such relationship is:

$$I_\delta(\vec{\tau},\vec{n},u,\omega_0) = \omega_0 e^{-(1-\omega_0)u} I_\delta(\omega_0\vec{\tau},\vec{n},\omega_0 u,\omega_0 = 1) \tag{170}$$

To find the impulse response, we need to utilize the Laplace transform in conjunction with the stationary solution. First, the Laplace transform of the impulse response is defined as:

$$I_\delta(\vec{\tau},\vec{n},p) = \int_0^\infty I_\delta(\vec{\tau},\vec{n},u,)e^{-pu}du \tag{171}$$

We can find the Laplace transform of the impulse response $I_\delta(\vec{\tau},\vec{n},p)$ by making the following substitutions to the corresponding stationary solution $I(\vec{\tau},\vec{n})$:

$$\begin{aligned} \tau &\rightarrow \tau(1+p) \\ \sigma_{ext} &\rightarrow \sigma_{ext}(1+p) \\ \omega_0 &\rightarrow \frac{\omega_0}{(1+p)} \end{aligned} \tag{172}$$

where p is the Laplacian space coordinate. Then we take the Laplace transform of the nonstationary RTE (Equation 166) and insert $I_\delta(\vec{\tau},\vec{n},p)$ into the resulting equation. The final step is to take the inverse Laplace transform to obtain a solution for the nonstationary RTE. Unfortunately, the solution is not generally applicable over a wide range of *u*. The asymptotic solutions where u >> 1 or <<1, however, are very useful.

Take a specific example of a monodirectional-pulsed point source for a semi-infinite layer that is optically thick and has strong scattering characteristics. For a diffuse point source located at the coordinate $(\rho = 0,\tau')$, we found earlier that the radiation density is:

$$w(\rho,\tau,\tau_0) = \frac{\sigma_{ext}^2}{4\pi q}\left\{\frac{\exp\left[-\gamma\sqrt{(\tau-\tau')^2+\rho^2}\right]}{\sqrt{(\tau-\tau')^2+\rho^2}} - \frac{\exp\left[-\gamma\sqrt{(\tau+\tau'+2d_1)^2+\rho^2}\right]}{\sqrt{(\tau+\tau'+2d_1)^2+\rho^2}}\right\} \tag{173}$$

If we then make the substitutions in Equation 172 and take the inverse Laplace transform for $\omega_0 = 1$ and *u*>>1, the radiation density becomes:

$$w(\rho,\tau,\tau',u) = \frac{\sigma_{ext}^2 \exp\left[-\frac{\rho^2}{4qu}\right]}{8\pi^{1/2}(qu)^{3/2}}\left\{\exp\left[-\frac{(\tau-\tau')^2}{4qu}\right] - \exp\left[-\frac{(\tau+\tau'+2d_1)^2}{4qu}\right]\right\} \tag{174}$$

This is Green's function for the boundary-value problem presented. After applying Equation 168 to adjust for a monodirectional point source and examining the region where $u \to \infty$, the asymptotic solution for a semi-infinite medium illuminated by a monodirectional-pulsed point source located at the upper medium boundary is:

$$w(\vec{\tau},u) = \frac{5\sigma_{ext}^2(\tau+2q)}{8(\pi q)^{3/2}u^{5/2}}\exp\left[-\frac{\rho^2}{4qu}\right] \tag{175}$$

Although we now have an expression for the radiation density including its fluctuations with respect to time, we would like to be able to predict the received power at the aperture as a function of time. While there are a number of ways to proceed, we shall invoke the backscatter noise (BSN) approximation that assumes that the receiver and source axis are parallel. The receiver FOV is assumed to be much larger than the transmitter beam. If these conditions are met, then the backscattered power as a function of range *r* is:

$$P(r) = \frac{P_0\sigma_{sca}p(\pi)\Sigma_{rec}\Omega_{rec}}{2\pi}\int_0^\infty S(2r,z,\Omega_s=\Omega_{rec},\Sigma_s=4\Sigma_{rec},u)dz \tag{176}$$

where P_0 is the source power, Σ_{rec} is the receive aperture area, *z* is the physical depth, Ω_{rec} is solid angle or the receiver, Ω_s is the solid angle of the transmit beam, and Σ_s is the cross-section of the transmit beam. To evaluate this integral, we first have to find the irradiance using the radiation density solution found earlier. Stated without proof, the specific irradiances S_1 and S_2 can be found using (Zege, et al., 1991):

$$S_i(\tau_x,\tau_y,\tau) = \frac{1}{4\pi P_0}\left[w(\tau_x,\tau_y,\tau) + (-1)^i 2q\frac{dw(\tau_x,\tau_y,\tau)}{d\tau} - (-1)^i 2q\frac{B_{01}(\tau_x,\tau_y,\tau)}{\sigma_{ext}}\right] \tag{177}$$

Therefore, the specific irradiances for a monodirectional-pulsed point source are:

$$S_i(\vec{\tau},u) = \frac{5\sigma_{ext}^2}{32(\pi q)^{3/2}u^{5/2}}\exp\left[-\frac{\rho^2}{4qu}\right]\left(\tau+2q+(-1)^i 2q\right) \tag{178}$$

If we now evaluate the BSN approximation for a pulsed source and receiver located at τ=0, the backscattered power is:

$$P(u) = \frac{5\sigma_{ext}^2 W_0 \Sigma_{rec} Q}{8\pi^{5/2} q^{1/2} u^{5/2}} \exp\left[-\frac{\rho^2}{4qu}\right] \quad \text{as} \quad u \to \infty \tag{179}$$

where W_0 is the pulse energy and Q is similar to the geometrical form factor in the LIDAR equation. Note that for a collimated source and an irradiance receiver results in Q=π. Technically, the solution above is valid only for non-absorbing media. If we apply equation 170 to adjust for an absorbing medium and convert back to real time units, then the received backscattered power is approximately:

$$P(t) \cong \frac{5\sigma_{sca}^3 W_0 \Sigma_{rec} Q}{8\pi^{5/2} q^{1/2} \left(\sigma_{sca} ct\right)^{5/2}} \exp\left[-\sigma_{abs} ct\right] \text{ as } t \to \infty \tag{180}$$

A comparison of the normalized power observed from a laser pulse for this approximation, the multiple scatter LIDAR equation, and the single scatter LIDAR equation is shown in Figure 22. The scattering layer has an extinction coefficient of 0.1 m^{-1} and a scattering albedo of 0.9. The asymmetry parameter was 0.863 and the incident beam was collimated. As expected, the diffusion approximation significantly underestimates the received power from ranges near the boundary edge. The single scatter scattering and multiple scattering equations provide a much better estimate. The multiple scattering LIDAR equation and the diffusion approximation are equal at about 600 ns (τ=18). If the diffusion approximation holds asymptotically, then the modeled LIDAR returns should transition at about that optical depth for this scenario. One of the interesting questions is why the multiple scattering LIDAR equation underestimates the backscattered return from deep within the layers. This is likely due to a variety of factors, but is heavily correlated to the assumptions made for the multiple scattering LIDAR equation. For instance, the mean path length of multiply scattered photons begins to differ greatly from that of singly scattered photons as one proceeds deeper into the layer; therefore, the temporal distribution and the spatial distribution of the photons at large optical depths are affected. Additionally, the diffusion approximation makes allowances for photons to undergo multiple large scattering events. Lastly, the photons were assumed to be normal to the plane where they backscatter for convenience in the multiple scattering LIDAR

equation derivation. Intuitively, we know that this is cannot be true deep within a highly-scattering medium. The distribution of incident angles may be wider which could result in a higher backscatter. Regardless, the diffusion approximation offers a reasonable benchmark for model verification of multiple scattering deep within a layer.

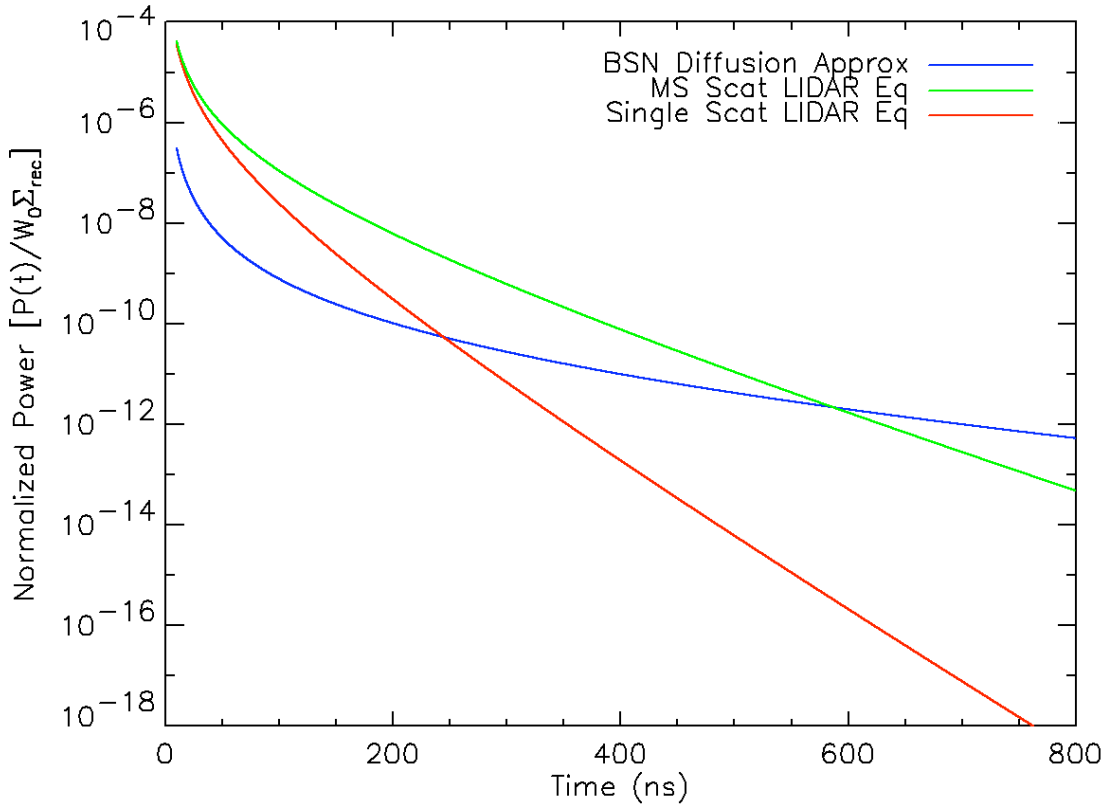


Figure 22: Predicted backscattered return from a laser pulse for (1) BSN diffusion approximation, (2) Multiple scatter LIDAR equation, and (3) Single scatter LIDAR equation

3.4 Photon mapping

Photon mapping is fundamentally based upon bidirectional Monte Carlo ray tracing and uses what are referred to as photon maps to increase the computational efficiency over traditional approaches. Jensen (1996), who is the recognized father of photon mapping, synthesized a suite of stochastic ray tracing methods together with a method for using records of what occurred during the ray traces to estimate the actual radiance received by the sensor. Although the techniques themselves were not unique, the combined approach was and is being utilized heavily within the computer graphics community. Initially, researchers focused

on the direct illumination component, which cannot adequately address multiple scattering. As introduced earlier in this dissertation, this approximation is valid for an optically thin medium; however, the approach breaks down for denser media. Brute force tracing the additional rays required to accommodate the multiple scattering effects is computationally prohibitive for complex scenes with objects such as clouds or plumes. This is where photon mapping may be very valuable.

Photon mapping essentially runs in two phases. The first stage, called photon tracing, traces a series of rays through the scene and records the interactions in a surface or volume photon map. The second stage, called rendering, casts rays to calculate the direct illumination component and incorporates the information within the photon maps to calculate the in-scattered radiance and surface caustics. Because the principles of photon tracing are rooted in the physics of how light propagates and interacts with matter, including gases and aerosols, photon mapping should be able to adequately address multiple scattering effects within a plume. Additionally, the use of a volume photon map and a statistical method to accurately estimate the radiance enables photon mapping to handle multiple scattering in a nonhomogenous participating medium. One is not restricted to representing the plume as a set of homogenous parallel-plane layers. Because the volume photon maps record the particular direction of scattering for each event, one is not limited to isotropic scattering phase functions. Instead, any scattering phase function that can be inverted or importance sampled can be used. The Monte-Carlo ray tracing roots of photon mapping also decouples the geometric limitations of a complex scene from the problem. In essence, anything that can be ray-traced can be simulated using photon mapping. Thus items such as clouds, fog, and plumes can have complex boundaries and shapes, anisotropic scatterers, and arbitrary particle size distributions. The one caveat is that non-stationary sources can pose significant challenges for traditional photon mapping methodologies. In general, photon mapping presumes that the source is at least somewhat wide-sense stationary about the simulation time. The sources are not restricted to a particular orientation, shape, or irradiance pattern; however, they are assumed to have been relatively constant for the time interval of interest. Thus a variation of photon mapping is necessary to handle the temporal nature of multiple scattering for a LIDAR pulse. The traditional approach to time-dependent photon mapping

will be discussed at the end of this section and the modeling approach adopted for this research effort will be discussed further in Chapter 4. For now, we examine the fundamental principles of traditional photon mapping and radiative transfer theory.

This section reviews the governing equation for radiative transfer in a participating medium in the context of photon mapping, briefly reviews the basic principles of the photon mapping approach, discusses the traditional radiance estimation for a volume of participating media, and provides sample results from the computer graphics community to showcase the potential. The implementation details of photon mapping are not directly addressed in this section. For more information with regards to photon mapping, particularly for surfaces and "standard scenes", one should consult Jensen's book on photon mapping (2001). Additional materials are continuously being published within the computer graphics community and are an excellent place to review specific aspects not directly addressed here. As stated previously, the specific implementation and modifications necessary to model a LIDAR pulse in a participating medium are addressed in more detail in Chapter 4.

3.4.1 Governing Radiative Transfer Equations for Photon Mapping

The governing equation for radiative transfer in a participating medium was derived thoroughly in Section 3.3 and the general vectorized form of the RTE was mathematically expressed as:

$$\sigma_{ext}^{-1}(\vec{n}\nabla)L(\vec{r},\vec{n}) = -L(\vec{r},\vec{n}) + \frac{\omega_0}{4\pi}\int_{4\pi} p(\vec{n},\vec{n}')L_i(\vec{r},\vec{n}')d\Omega' + B_0(\vec{r},\vec{n}) \tag{181}$$

where $\vec{r}$ is the observation point vector, $\vec{n}$ determines the direction of the beam with radiance L, $B_0(\vec{r},\vec{n})$ describes the internal sources of radiation, and L_i is the in-scattered radiance from a particular direction. This equation is repeated in this section merely for reference. To review the underlying theory, the reader is referred to Section 3.3. The vectorized form of the RTE for a participating medium is the most flexible and applicable for the scenario under consideration. For photon mapping, let's consider an observation vector along the x-axis. This is a reasonable assumption since one is primarily concerned with the incremental change in radiance along a cast ray. Although the equation has a spectral

component to it, the spectral effects shall not be directly addressed in this section. Unfortunately, one might need to account for the spectral effects on a case by case basis or based upon a parametric empirical model. For now, the light shall be assumed to be of one wavelength, which is reasonable for the DIAL systems under consideration. When rewritten under these conditions and with the extinction coefficient moved to the other side of the equation, the RTE becomes:

$$(\vec{n}\nabla)L(x,\vec{n}) = -\sigma_{ext}(x)L(x,\vec{n}) + \frac{\sigma_{sca}(x)}{4\pi}\int_{4\pi} p(\vec{n},\vec{n}')L_i(x,\vec{n}')d\Omega' + L_{src}(x,\vec{n}) \tag{182}$$

where the emission term $L_{src}(x,\vec{n})$ is:

$$L_{src}(x,\vec{n}) = \sigma_{abs}(x)L_e(x,\vec{n}) \tag{183}$$

where σ_{abs} is the absorption cross-section and L_e is the radiance emitted along the path.

Equation 183 is valid under the assumption of self-emission. Essentially, the change in radiance is due to the difference between the loss in scattered radiance and the gain by in-scattered radiance and internal sources of radiation. Although the internal sources of radiation will be carried throughout this derivation, the emission term is not currently modeled within the DIRSIG LIDAR module using the photon mapping architecture. The passive and emissive terms are incorporated using traditional radiance solvers built-in to DIRSIG that operate in conjunction with photon mapping in the enhanced model. The derivation below is a more thorough treatment but is not as computationally efficient for simulating LIDAR returns. When combined the previous equations yield:

$$\frac{dL(x,\vec{n})}{dx} = -\sigma_{ext}(x)L(x,\vec{n}) + \frac{\sigma_{sca}(x)}{4\pi}\int_{4\pi} p(\vec{n},\vec{n}')L_i(x,\vec{n}')d\Omega' + \sigma_{abs}(x)L_e(x,\vec{n}) \tag{184}$$

The first step in solving this differential equation is to define a function, which calculates the optical depth from a point along the cast ray s_1 to another point along the same ray s_2. The function is:

$$\tau(s_1,s_2) = \int_{s_1}^{s_2} \sigma_{ext}(s')ds' \tag{185}$$

Let's consider the solution of the differential equation along the straight path from x_0 to x. If one multiplies both sides of Equation 184 by an exponential with the optical depth function defined above as the input term, then the RTE becomes:

$$e^{\tau(x_0,x)}\left(\frac{dL(x,\vec{n})}{dx}+\sigma_{ext}L(x,\vec{n})\right)=e^{\tau(x_0,x)}B(x,\vec{n}) \tag{186}$$

where $B(x,\vec{n})$ is defined for convenience as:

$$B(x,\vec{n})=\frac{\sigma_{sca}(x)}{4\pi}\int_{4\pi}p(\vec{n},\vec{n}')L_i(x,\vec{n}')d\Omega'+\sigma_{abs}(x)L_e(x,\vec{n}) \tag{187}$$

The optical depth exponential term was chosen because the derivative with respect to x of the radiance, L, times the optical depth exponential term is:

$$\begin{aligned}\frac{d}{dx}\left[L(x,\vec{n})e^{\tau(x_0,x)}\right]&=\frac{d\kappa}{dx}e^{\tau(x_0,x)}L(x,\vec{n})+\frac{dL(x,\vec{n})}{dx}e^{\tau(x_0,x)}\\&=\sigma_{ext}(x)e^{\tau(x_0,x)}L(x,\vec{n})+\frac{dL(x,\vec{n})}{dx}e^{\tau(x_0,x)}\end{aligned} \tag{188}$$

Substituting Equation 188 into Equation 186 and integrating over a small, straight path from x_0 to x results in:

$$d\left[L(x,\vec{n})e^{\tau(x_0,x)}\right]\Big|_{x_0}^{x}=\int_{x_0}^{x}e^{\tau(x_0,x')}B(x',\vec{n})dx' \tag{189}$$

which can be evaluated on the left-hand side and rearranged such that:

$$L(x,\vec{n})=L(x_0,\vec{n})e^{-\tau(x_0,x)}+\int_{x_0}^{x}e^{-\tau(x',x)}B(x',\vec{n})dx' \tag{190}$$

One should note that when the exponential attenuation term on the left-hand side is transferred to the right side of the equation that one uses the relationship:

$$\int_{x_0}^{x'}\sigma_{ext}(s')ds'-\int_{x_0}^{x}\sigma_{ext}(s')ds'=-\int_{x'}^{x}\sigma_{ext}(s')ds' \tag{191}$$

When expanded the solution of the RTE equation becomes:

$$L(x,\vec{n}) = L(x_0,\vec{n})e^{\tau(x_0,x)} + \int_{x_0}^{x} e^{-\tau(x',x)} \frac{\sigma_{sca}(x')}{4\pi} \int_{4\pi} p(x',\vec{n},\vec{n}')L_i(x',\vec{n}')d\Omega' dx' + \int_{x_0}^{x} e^{-\tau(x',x)}\sigma_{abs}(x')L_e(x',\vec{n})dx' \quad (192)$$

Equation 192 can be interpreted physically as the radiance at x along the cast ray to be comprised of three terms (illustrated in Figure 23). The first term is the direct illumination at x_0 attenuated exponentially by the optical depth. The second and third terms are due to the in-scattering and emission along the path from x_0 to x reduced along the way by the optical path difference between each point between x_0 and x.

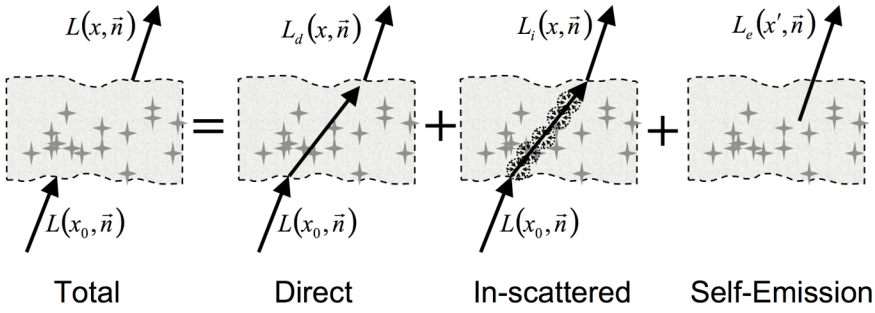


Figure 23: Illustration of key terms in radiance calculation for a participating medium

Equation 192 can be simplified if the media is presumed to be homogenous or scatters isotropically. Thus far, the assumptions are broader than those made when considering homogenous, plane-parallel layers in the previous section and encompass many more cases of interest for interrogating plumes. Solving Equation 192 directly is not feasible under most conditions; however, one can iteratively calculate the radiance along a cast ray if one has a feasible methodology to estimate the in-scattered radiance as the ray passes through a participating medium. The statistical casting of rays and recording of events into a volume photon map enables the estimation of the multiple scattering and emission terms along a path within the map. Equation 192 is the underlying equation for the iterative equations presented

in this section for simulating light propagating through a participating medium with photon mapping.

3.4.2 Photon Mapping Concept

As indicated previously, the traditional photon mapping concept is comprised of two basic phases, photon tracing and rendering. The first phase, photon tracing, casts photons from the light sources into the scene and traces them. As they propagate through the scene, the photons will interact with the surfaces or volumes of participating medium and a record of the events are stored in the photon map(s). For surfaces, all hits upon a nonspecular surface are stored. The effective result is that each surface has a distribution of photons spread over them. Typically, one utilizes multiple photon maps to account for the caustic and indirect illumination effects. For participating media, events such as absorption and scattering are recorded in a separate photon map to be used in the rendering phase to account for the in-scattered radiance. Based upon the physics of the physical process involved, all of the interactions are simulated using a Monte-Carlo technique called Russian roulette[1] (Szirmay-Kalos, 2003; Jensen, 2001). Figure 24 illustrates the Monte-Carlo ray tracing performed during the photon tracing phase. After completing the ray tracing, one has a set of photon maps that describes the events that occurred during the tracing stage such as is represented in Figure 25. The second phase, illustrated in Figure 26, renders the scene by calculating the direct illumination using traditional ray tracing approaches and the indirect and multiple scattering effects using the information stored in the photon maps. The key to this phase is the radiance estimation for the surfaces and participating volumes that will be discussed shortly. Combined with the photon maps, the direct illumination calculations provide an adequate representation of the observed scene radiance, presuming that a statistically significant number of photons are cast and traced in the initial phase.

[1] Russian roulette solves the infinite-dimensional integration that utilizes randomization and importance sampling. The technique is routinely used in Monte-Carlo and quasi-Monte-Carlo random walk ray tracing and numerical methods. A thorough discussion is available in Szirmay-Kalos (1998) and Jensen (2001).

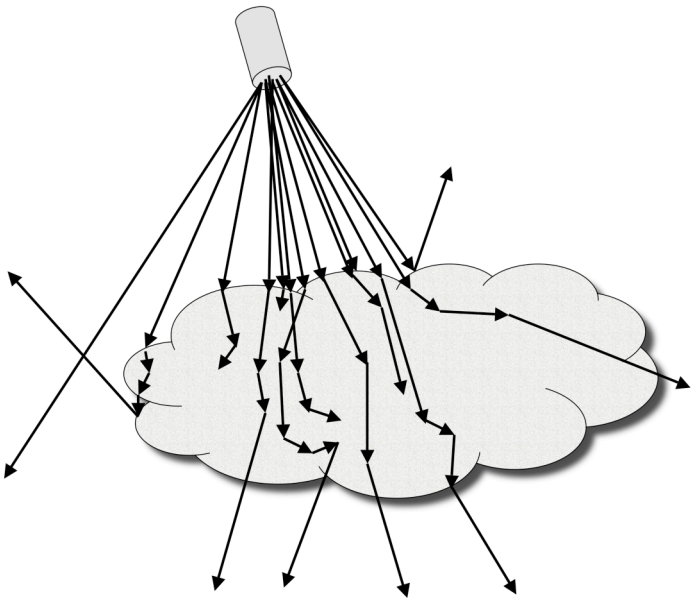


Figure 24: Pass 1 - Photon tracing

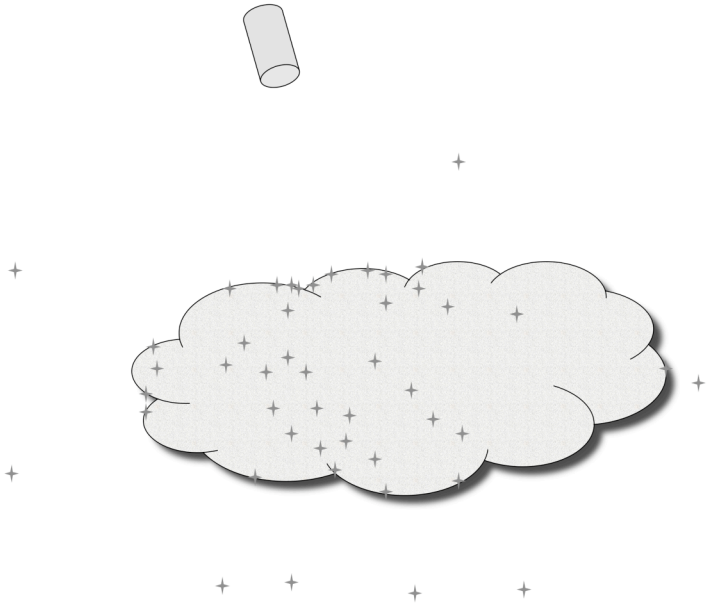


Figure 25: Pass 1 - Recorded photon map

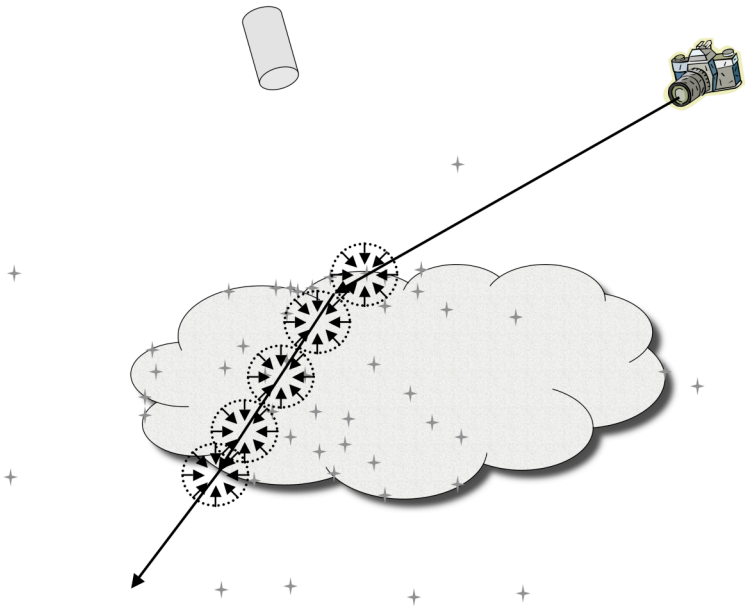


Figure 26: Pass 2 - Rendering

3.4.3 Photon Tracing (Phase 1)

When considering a scene without participating medium such as gases or aerosols, photon interactions are primarily limited to surfaces. At the surfaces, the photons may be absorbed or reflected. Russian roulette is used to determine the nature of the event because it is a probabilistic sampling technique that allows one to reduce the computational requirements for photon tracing. In the case of reflection for a surface that has both a specular and diffuse reflectance, Russian roulette is once again employed to determine whether the photon will count towards the specular or diffuse cases. If specular scattering is selected, then the direction is determined from the geometry and the tracing continues. If diffuse scattering is selected, then the photon is stored within the photon map and another photon is emitted from the source. Alternatively, one could importance sample a BRDF model to determine the reflected direction and stop only when an absorption event is recorded. The latter method is what was selected for the LIDAR model described in Chapter 4.

When a photon passes through the boundary of a participating medium such as a gaseous plume, the photon interacts with the particles or molecules by being scattered or absorbed. Naturally, this ignores the emitting of new photons and can be accommodated by creating a

separate internal source function that emits photons that are subsequently traced. The mean distance that a photon will travel in the medium before an absorption or scattering event occurs is inversely proportional to the extinction coefficient. The cumulative distribution of the probability of a photon interacting with a participating medium at position x is:

$$\begin{aligned} F(x) &= 1-\kappa(x_0,x) \\ &= 1-\exp\left[-\int_{x_0}^{x}\sigma_{ext}(x')dx'\right] \end{aligned} \tag{193}$$

where x_0 is the previous position of the photon. Importance sampling this distribution results in the following formula:

$$d = -\frac{\log\xi}{\sigma_{ext}} \tag{194}$$

where $\xi \in [0,1]$ is a uniformly distributed random number and d is the distance traveled by the photon prior to the next event. This relationship can then be used to determine the next location of an event within a participating medium. Special cases must be considered for thin media or when the photon leaves the media; however, the relationship above defines the general case. Given that an event occurred, Russian roulette is then leveraged to determine whether the photon was scattered or absorbed. The probability that a photon is scattered given an event occurred is proportional to the scattering albedo and can be mathematically expressed as:

$$\begin{aligned} \text{Prob}\{\text{photon is scattered}|\text{event occurred}\} &= \frac{\sigma_{sca}}{\sigma_{sca}+\sigma_{abs}} \\ &= \omega_0 \end{aligned} \tag{195}$$

In a practical implementation, one randomly picks a number from a uniform distribution from [0,1] and uses the rule:

$$\text{Given } \xi \in [0,1] \rightarrow \begin{cases} \text{Event : Photon is scattered} & \xi \le \omega_0 \\ \text{Event : Photon is absorbed} & \xi > \omega_0 \end{cases} \tag{196}$$

where $\xi \in [0,1]$ is a uniformly distributed random number. Whenever a photon interacts with the medium, it is stored in the volume photon map, which is separate from the other photon maps.

If a photon is scattered, the new direction of the photon is determined based upon the scattering phase function. The Henyey-Greenstein phase function is often used to characterize the medium because it is easily invertible and can be generated using a simple uniformly distributed random number generator. The new pseudorandom generated angle for the scattered photon can be calculated as:

$$\theta = \cos^{-1}\left(\frac{1}{|2g|}\left(1+g^2-\left(\frac{1-g^2}{1-g+2g\xi}\right)^2\right)\right) \tag{197}$$

$\xi \in [0,1]$ is a uniformly distributed random number. The azimuth rotation ϕ is then presumed to be uniformly distributed and is generated using a random number generator.

Alternatively, many scattering phase functions cannot be directly inverted and the approximation using the Henyey-Greenstein function may not be desirable. In this case, one can importance sample the scattering phase function using the acceptance/rejection method. The acceptance/rejection method is based upon von Neumann's theorem. If the probability distribution function of interest, $f(x)$, can be written such that:

$$f(x) = c\ g(x)\ h(x) \tag{198}$$

where $h(x)$ is an arbitrary probability distribution function, c is a constant > 1, and $g(x)$ is a correction function < 1, then:

$$f(x) \le c \cdot h(x) \tag{199}$$

Based upon this statement, the new scattering angle for an arbitrary scattering phase function can be determined by the following steps:

(1) Find a and b such that $f(x) = 0$ when $x \notin (a,b)$.

(2) Find a constant c such that $1 > c \ge (b-a) \cdot f(x)$.

(3) Sample x uniformly over the interval (a,b).

(4) Sample y uniformly over the interval $\left(0,\frac{c}{b-a}\right)$.

(5) Evaluate $f(x)$.

a. If $y \le f(x)$, then accept x.

b. If $y > f(x)$, then reject x and go back to step (3).

The functions involved are illustrated in Figure 27.

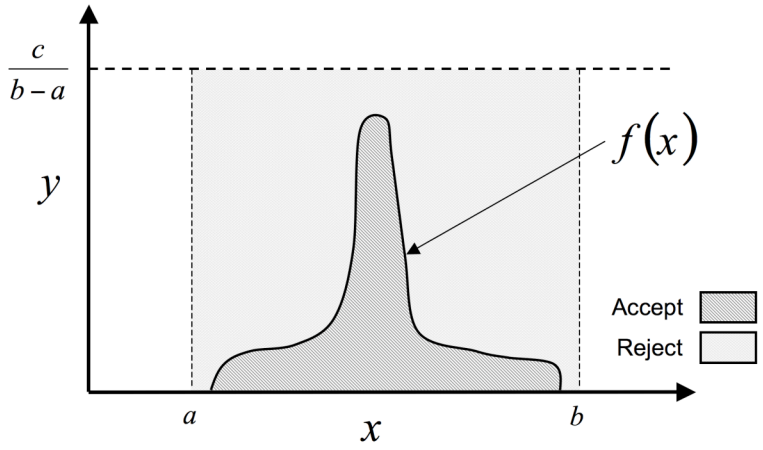


Figure 27: Importance sampling of *f*(*x*) with uniform distributions

This method can be very inefficient and the computational time can increase exponentially. The efficiency of the acceptance rejection method is defined as:

$$\varepsilon_{samp} = \frac{\int f(x)dx}{\int c \cdot h(x)dx} \tag{200}$$

Essentially, the efficiency is driven by the ratio of the areas of the two functions. An alternative is to find a different *h*(*x*) to reduce the number of excess iterations, such as one illustrated in Figure 28. Thus one might be able to use an invertible function such as the Henyey-Greenstein phase function to importance sample a more complex function without incurring too great of a computational burden.

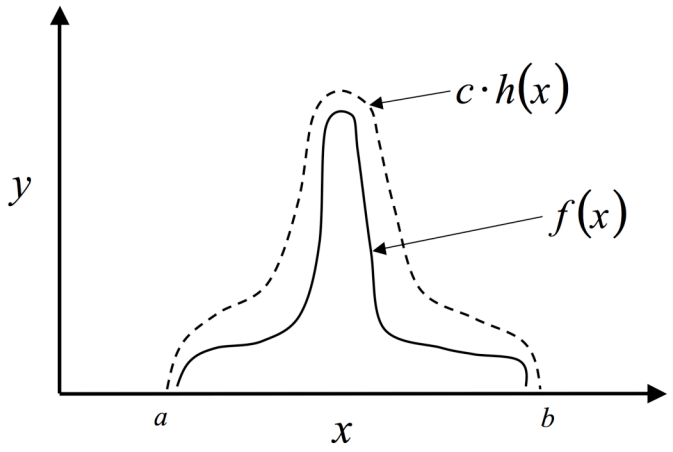


Figure 28: Importance sampling of $f(x)$ with distribution $h(x)$

3.4.4 Rendering in Participating Medium (Phase 2)

The second phase of photon mapping involves using ray tracing to calculate the direct illumination and using the photon mapping information to factor in the additional terms in the radiative transfer equation. The two most important aspects of this phase are the volume and surface radiance estimate.

3.4.4.1 Volume Radiance Estimate

The volume radiance estimate provides a way to account for the in-scattered radiance L_i within a medium. For many simulations, this is the most troublesome calculation. Let's begin by examining the relationship between the scattered flux and the radiance at any point within the participating medium, which is:

$$L_{sca}(x,\vec{n}) = \frac{d^2\Phi(x,\vec{n})}{\sigma_{sca}(x)d\vec{n}dV} \tag{201}$$

where Φ is the flux and dV is the volume. The in-scattered radiance can then be expressed as:

$$\begin{aligned} L_i(x,\vec{n}) &= \int_{\Omega} f(x,\vec{n}',\vec{n}) L(x,\vec{n}') d\vec{n}' \\ &= \int_{\Omega} f(x,\vec{n}',\vec{n}) \frac{d^2\Phi(x,\vec{n}')}{\sigma(x) d\vec{n}' dV} d\vec{n}' \\ &= \frac{1}{\sigma_{ext}(x)} \int_{\Omega} f(x,\vec{n}',\vec{n}) \frac{d^2\Phi(x,\vec{n}')}{dV} \\ &\approx \frac{1}{\sigma_{ext}(x)} \sum_{p=1}^{n} f(x,\vec{n}'_p,\vec{n}) \frac{\Delta\Phi_p(x,\vec{n}'_p)}{\frac{4}{3}\pi r^3} \end{aligned} \tag{202}$$

where $f(x,\vec{n}',\vec{n})$ is a valid probability distribution for the scattering phase function, $\vec{n}'$ is the in-scattered radiance vector, and r is the radius of the smallest sphere containing at least n nearest photons. This is essentially a nth nearest neighbor estimate and is illustrated in Figure 29. The sphere is expanded until it contains at least n nearest photons so that a reasonable estimate of the local photon density can be obtained. Then the in-scattered radiance can be calculated based upon the local photon density estimate and the normalized version of the scattering phase function using Equation 202. Note that the exponential attenuation term was dropped from within the integral because the integration step is assumed to be small enough that the in-scattered contribution along the path from x to $x+dx$ is negligible. Calculating the in-scattered contribution at each point along the path presumably accounts for the dominant contributors. This assumption should not introduce significant error provided that the step size is small enough such that the gradient of the radiance is not very great.

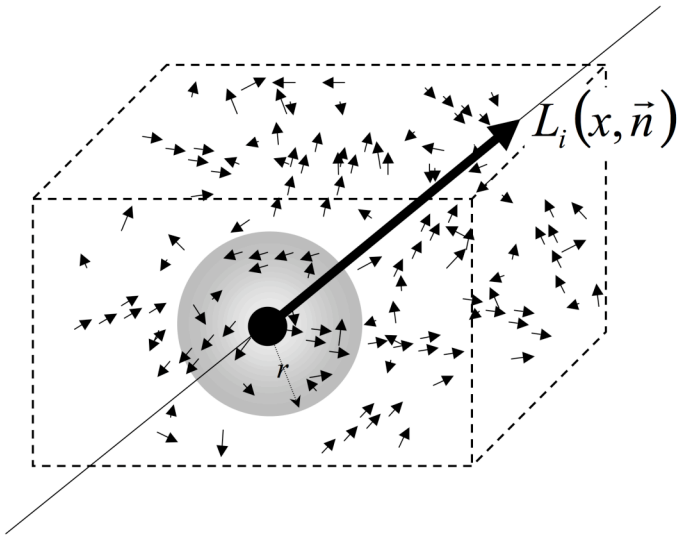


Figure 29: Photon mapping volume radiance estimate

As mentioned previously, the direct portion of the radiance is calculated using an adaptive ray marching approach described by Jensen (2001). The radiance is iteratively computed at points along the ray as the ray traverses the participating medium. At each step, the emitted and in-scattered radiance is approximated using the equation:

$$L_i(x,\vec{n}) = L_{i,d}(x,\vec{n}) + \omega_0 L_{i,i}(x,\vec{n}) \tag{203}$$

where $L_{i,d}$ is the direct component due to single scattering computed by the ray marching and $L_{i,i}$ is the indirect portion of the in-scattered radiance which is computed using:

$$L_{i,i}(x,\vec{n}) \approx \frac{1}{\sigma_{ext}(x)} \sum_{p=1}^{n} f(x,\vec{n}'_p,\vec{n}) \frac{\Delta\Phi_p(x,\vec{n}'_p)}{\frac{4}{3}\pi r^3} \tag{204}$$

The indirect contribution is calculated using all of the photons in the photon map including those that were absorbed; therefore, the scattering albedo term is necessary to adjust the indirect contribution to the overall in-scattered radiance. The emission contribution is computed based upon the local temperature using Planck's blackbody equation or upon a defined source function. The latter would be employed to simulate the effects of a fire.

With these approximations, the radiance at points x_k along a ray in the direction $\vec{n}$ is computed iteratively as shown in Figure 30 using:

$$\begin{aligned} L(x_k,\vec{n}) &= \sigma_{abs}(x_k)L_e(x_k,\vec{n})\Delta x_k \\ &+\sigma_{sca}(x_k)L_i(x_k,\vec{n})\Delta x_k \\ &+e^{-\sigma_{ext}(x_k)\Delta x_k}L(x_{k-1},\vec{n}) \end{aligned} \tag{205}$$

where $\Delta x_k = |x_k - x_{k-1}|$ is the step size, and x_0 is the nearest intersection point of the ray with a surface or backside of the volume. The adaptive portion of the ray marching algorithm randomly selects a step size and then divides the step size in half or by some predetermined amount if the radiance along the ray significantly differs over adjacent points. In addition, a random jittering technique is used to set the final step size. These features reduce the jittering and aliasing effects associated with a fixed step size when marching through rays.

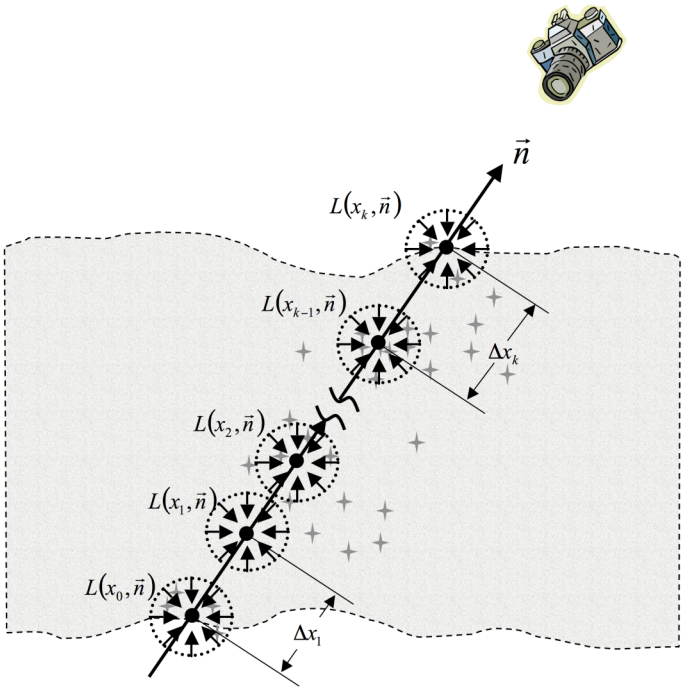


Figure 30: Adaptive ray tracing calculation of radiance at points x_k

3.4.4.2 Surface Radiance Estimate

Similar to the volume estimate, the surface estimate (illustrated in Figure 31) attempts to infer the radiance at any point on a surface based upon the photon density in the photon map near that point. The primary difference is that the photons only exist on the surface areas instead of a volume. The rendering algorithm finds the smallest distance on the surface that contains *n* photons and uses the area to estimate the reflected radiance as:

$$L_r\left(x,\vec{n}\right) \approx \sum_{p=1}^{n} f_r\left(x,\vec{n}'_p,\vec{n}\right)\frac{\Delta\Phi_p\left(x,\vec{n}'_p\right)}{\pi r^2} \tag{206}$$

where f_r is the bidirectional reflectance distribution function and r is the distance to the nth nearest photon. The approach is commonly visualized as expanding a sphere centered at *x* until it contains *n* photons and then calculating the projected area that the sphere encompasses on the surface as shown in Figure 31. Because the primary focus is on using photon mapping with the participating medium, the details for handling surfaces is not completely covered here. For additional details on traditional photon mapping, one should consult the details in Jensen (2001). Chapter 4 will discuss the modifications that were made to the surface radiance estimate to enhance DIRSIG's LIDAR module.

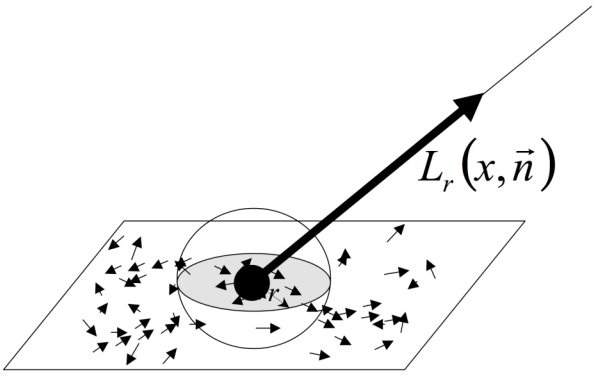


Figure 31: Photon mapping surface radiance estimate

3.4.5 Sample Results

The computer graphics community has consistently demonstrated that photon mapping generates more visually appealing results than traditional ray tracing approaches when

rendering scenes with participating medium. This subsection contains a handful of relevant sample images that demonstrate the viability of the photon mapping approach for these situations. For more examples, one could review the computer graphics publications on rendering smoke and clouds listed at the end of the proposal.

The first set of images shown in Figure 33 is of a simple cloud. The cloud was generated using a distribution function to generate 10 blobs and turbulent noise. The medium is nonhomogenous and the scattering phase function is very anisotropic. The top image is a simulation using the single scattering approximation only. The bottom image was generated using photon mapping to account for the multiple scattering effects within the cloud. The bottom image was rendered using only ~10,000 photons and could be improved by casting more photons; however, the image is obviously brighter and more realistic. The increase in radiance towards the center of the cloud is largely due to the multiple scattering effects.

Figure 33 is a more complex scene with clouds above a mountain landscape. The image is actually a snapshot from a movie sequence that Jensen created of the clouds forming and moving over a representation of Little Matterhorn. A large number of photons were cast for this rendering and demonstrate the possibility of using photon mapping to account for the multiple scattering effects due to clouds. The radiometric accuracy of the simulation is not known, but the scene is certainly visually appealing.

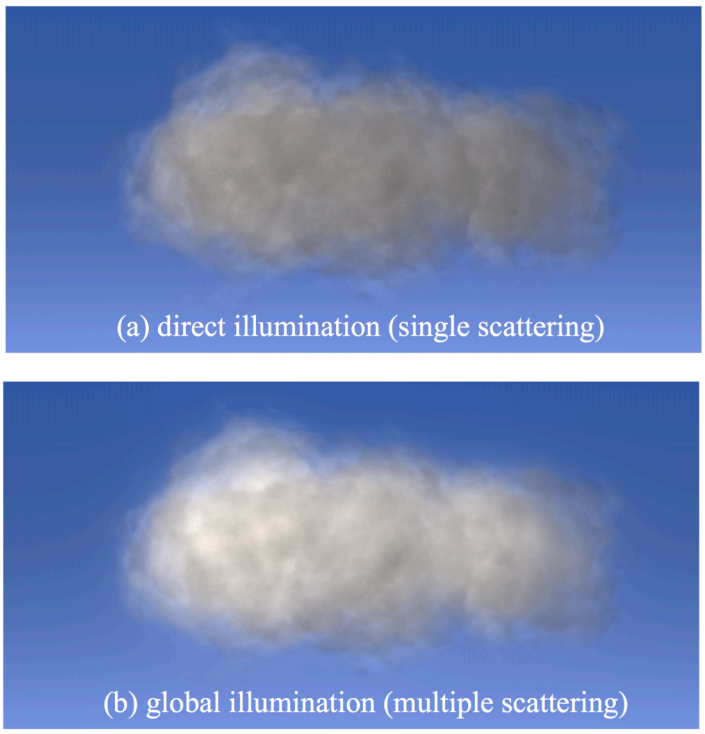


Figure 32: Photon mapping simulation of a non-homogeneous cloud (Jensen and Christensen, 1998)



Figure 33: “Little Fluffy Clouds” over mountain landscape
(Jensen 2001)

Another impressive image is of sunlight scattering through a stained glass window into a dusty room (shown in Figure 34). According to Jensen and Christensen (1998), the scattering phase function used was Schlick’s approximation of a murky Mie scattering phase function. The purpose was to demonstrate the scattering of light off of dust particles. This is applicable to plumes that contain soot and other dust particles, particularly when the concentration levels are fairly low and the plume is optically thin. The stained glass added a spectral component to the demonstration and the streaming light source is different than previous sources that simulated a more diffuse source.



Figure 34: Dusty room illuminated by sunlight through a stained glass window (Jensen and Christensen, 1998)

The final set of images are of smoke plumes rising in a small scene (Figure 35). The primary purpose of the images was to demonstrate that the fluid dynamics modeling Fedkiw, Stam, and Jensen employed in conjunction with photon mapping could render a realistic smoke plume. The smoke plume appears natural because it has a proper amount of swirling and also because the solver correctly handles how the smoke would interact with the boundary surface of objects immersed in the smoke. The theory indicates that photon mapping should be able to handle the multiple scattering and absorption in a participating environment and the examples shown in this subsection are additional evidence towards that conclusion. However, the crucial temporal issues and the casting of a sufficient number of photons in order to generate reasonable estimates of the in-scattered radiance contribution are still challenging.

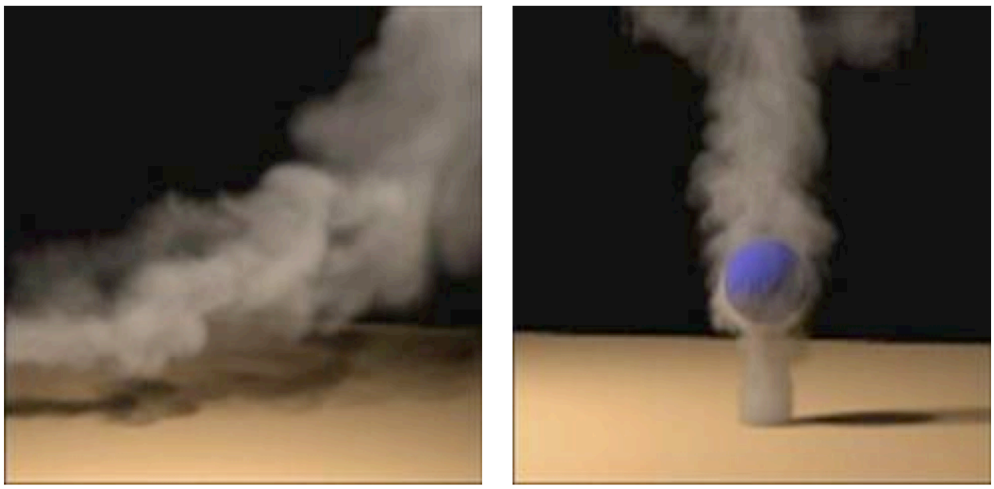


Figure 35: Photon mapping rendering of smoke
(Fedkiw, Stam, and Jensen, 2001)

3.4.6 Time-dependent Photon Mapping

In 2001, Cammarano and Jensen introduced an approach to account for the time-dependence of motion within the scene. The primary interest was in simulating motion blur due to moving objects within the scene. They decided to augment traditional photon mapping using super-temporal-sampling techniques. Cammarano and Jensen rejected analytical, geometric distortion, and post-processing methods because they were too restrictive and did not offer the robustness and flexibility for generating complex scenes. The critical modifications to traditional photon mapping were (1) adding time to the photon event map records, (2) casting a set number of photons at each time sampling interval, and (3) modify the photon radiance estimate to generate a temporal estimate leveraging the recorded event times. The first modification is fairly straightforward and is one which we will adopt for our modeling efforts described in Chapter 4. During the Monte Carlo tracing phase, photon bundles are cast into the scene and events are recorded into a photon map. When an event occurs, one simply adds the time of the event to the photon map record. To generate a representative temporal and spatial sampling of the photons within a scene, Cammarano and Jensen shot a set of photon bundles from the source at a specific rate. This is the second modification. The intent was to cast the same number of bundles into the scene for a variety of different times so that the temporal aspect of the light distribution was accounted for. This modification is essentially similar to generating a set of temporal spaced photon maps and then combining them into

one large photon map structure. Because one is tracking time, the sorting of the photon map was converted to a searchable 4-D data structure. Finally, the radiance estimate is now a function of time. The third major modification involves deriving a new radiance estimate based upon the information within the 4-D photon map. The temporal radiance through a specific pixel *p* can be expressed as:

$$L_p = \int_{t_s} \int_{A_d} L(x', \vec{\omega}, t)\ s(x', \vec{\omega}, t)\ g(x')\ dA_D(x')\ dt \tag{207}$$

where L_p is the radiance through pixel *p*, t_s is the total frame time, A_D is the area of the pixel, $g(x')$ is the filter function, $s(x', \vec{\omega}, t)$ is the shutter function for each pixel, and $L(x', \vec{\omega}, t)$ is the radiance through location x' on the image plane in the direction of the observer at time *t*. The challenge is to find an expression to describe $L(x', \vec{\omega}, t)$, the radiance at a specific location and time. If we consider the first surface intersection, then the observed radiance leaving the surface as a function of time is:

$$L(x, \vec{\omega}, t) = L_e(x, \vec{\omega}, t) + \int_{\Omega} f_r(x, \vec{\omega}', \vec{\omega}, t) L_i(x, \vec{\omega}, t)(\vec{\omega}' \cdot \vec{n}, t) d\vec{\omega}' \tag{208}$$

where L_e is the emitted radiance, f_r is the surface BRDF, L_i is the incident radiance in the direction $\vec{\omega}'$ at time *t*. Using a similar approach to Section 3.4.4, we can approximate the reflected radiance from a surface based upon the local photon density as:

$$L_r(x, \vec{\omega}, t) \approx \frac{1}{\pi\ r^2 \cdot \Delta t} \sum_{p=1}^{n_p} f_r(x', \vec{\omega}', \vec{\omega}, t) Q_p \tag{209}$$

where L_r is the reflected radiance, *r* is the smallest radius of a sphere which contains n_p photons within a nearest time frame Δt, and Q_p is the value of the nearest n_p photon bundles. Note that the search criteria has been altered to encompass time as well. The photon bundles within a specific time interval are then gathered and the local temporal density is calculated. This is done for all of the sampling intervals of interest. The propagation of the radiance estimate back to the sensor is then completed in the traditional manner.

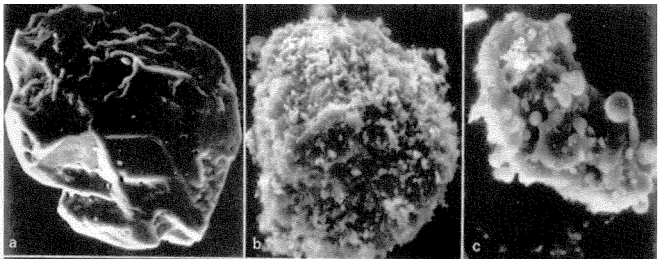
Although we will also add the time information to the photon event map, the super-sampling approach selected by Cammarano and Jensen is too computationally expensive for an arbitrary time-gated LIDAR simulation. The pulse durations are very short and the sampling required is orders of magnitude greater than what Cammarano and Jensen were considering at the time. We would need to shoot a very large number of photons to get a decent temporal and spatial distribution of photon bundles. Otherwise the estimate would not be accurate. Instead, we shall adopt a blend of an analytical technique and this approach. Implementation details are discussed further in Chapter 4. In general terms, we will (1) trace the photon bundles through the scene, (2) record the event information including time into the photon map, (3) parametrically spread each bundle temporally based upon the pulse shape and duration, and (4) accumulate each photon bundle at the sensor. One should note that this introduces some complexity and computational burden during the rendering phase, but the benefits far outweigh shooting enough photons within the scene to get an adequate temporal and spatial photon density.

3.5 Particles and Polydiverse Media

The focus of this section is to examine the characteristics of the participating medium that drive the characterization of light in a scattering and absorbing medium. The particles in the scattering medium are generally described by six characteristics: concentration, shape, orientation, size, structure, and chemical composition. The complexity of describing a gaseous elementary volume is exacerbated by the fact that particles of different sizes, shapes, structures, and chemical compositions can simultaneously exist. While the scattering theory can handle many different variations on these parameters for a single particle, the real world is dominated by a mixture of these individual particles. Given this fact, the local optical statistics of an elementary volume are often described by a statistical averaging over various representative particles. The final portion of this section will address how to calculate the localized statistical properties of the particles for a given particle size distribution.

For simplicity, one can assume that the particles are uniform, isotropic spheres. This assumption is often employed as a 1st-order approximation for selected atmospheric aerosols, water droplets, and ice crystals. Particles of different shapes can generally be approximated

as a summation of smaller spherical particles. Figure 1 shows pictures of irregular shaped particles including fly ash. For the purposes of this research, the assumption is that the particles are uniform, isotropic spheres.



(a) quartz (b) activated charcoal (c) fly ash

Figure 36: Photographs of typical irregular terrestrial particles (Kokhansky, 2001)

Media comprised of uniform, isotropic spheres are then defined by complex index of refraction, $m = n + i\chi$, which is determined by the chemical composition and by the number concentration of particles, *N*. The volumetric concentration of particles, C_v, is defined as:

$$C_v = N\langle V \rangle \tag{210}$$

where $\langle V \rangle$ is the average volume of particles in a unit volume of a medium. For spherical particles, the average volume of particles in a unit volume of medium is:

$$\langle V \rangle = \frac{4\pi}{3}\int_0^\infty a^3 f(a)da \tag{211}$$

where *a* is the radius of a particles and *f(a)* is the normalized particle size distribution (PSD). As with any probability distribution, the PSD is normalized such that:

$$\int_0^\infty f(a)da = 1 \tag{212}$$

The mean particle size is defined as:

$$\langle a \rangle = \int_0^\infty af(a)da \tag{213}$$

However, the mean particle size is not typically used to represent the media if the properties are known only for a few radii. Instead one uses the effective radius which is expressed as:

$$a_{ef} = \frac{\int_0^\infty a^3 f(a) da}{\int_0^\infty a^2 f(a) da} \tag{214}$$

All of these characteristics depend upon the PSD for the particulate of interest. The most common PSD functions used for atmospheric research are the Junge, Gamma, and Log-normal distributions. The Junge PSD was introduced in 1963 in connection with atmospheric aerosols and is commonly used today because of its simplicity. The Junge distribution can mathematically be expressed as:

$$f(a) = \begin{cases} ka^{-\upsilon} & a \in [a_1, a_2] \\ 0 & a \notin [a_1, a_2] \end{cases} \tag{215}$$

where a is the radius of a particles, k is a constant, the interval from a_1 to a_2 defines the interval over which the PSD is valid, and υ depends upon the type of aerosol. Typically, the input parameters must be found using empirical data and curve fitting the results.

Another common PSD is the gamma distribution. Figure 37 shows a gamma distribution with the input parameters μ=6 and a_0=4 μm. The gamma distribution can be defined as:

$$f(a) = \begin{cases} \dfrac{\mu^{\mu+1} a^{\mu}}{a_0^{\mu+1}\Gamma(\mu+1)} \exp\left[-\mu \dfrac{a}{a_0}\right] & a \geq 0 \\ 0 & \text{elsewhere} \end{cases} \tag{216}$$

where μ+1 is the shape parameter, a_0/μ is the location parameter, and $\Gamma(\ )$ is the standard gamma function which is defined as:

$$\Gamma(x) = \int_0^\infty e^{-\alpha} \alpha^{x-1} d\alpha \tag{217}$$

Some typical parameters for common dispersive media are recorded in Table 2.

As indicated in Table 2, the log-normal distribution is also used to describe disperse media. The table shows some standard parameters for different particles when using the log-normal distribution which can be defined as:

$$f(a) = \begin{cases} \dfrac{1}{\sqrt{2\pi}\sigma a}\exp\left[-\dfrac{\ln^2(a/a_m)}{2\sigma^2}\right] & a \geq 0 \\ 0 & \text{elsewhere} \end{cases} \tag{218}$$

where σ is the shape parameter and a_m is the scale parameter. Figure 37 is a plot of a log-normal distribution such that the coefficient of variance is the 0.38, which is the same as the gamma distribution on the same plot.

Table 2: Particle size distributions of selected disperse media
(Kokhanovsky, 2001)

Disperse Medium	PSD	a_{eff} (μm)	Δ
Cloud C1	Gamma ($\mu=6$, $a_0=4\mu m$)	6	0.38
Stratospheric aerosol	Gamma ($\mu=2$, $a_0=0.1\mu m$)	0.25	0.58
Water soluble aerosol	Log-normal ($\sigma=1.09527$, $a_m=0.05\mu m$)	0.1	1.52
Dust aerosol	Log-normal ($\sigma=1.09527$, $a_m=0.5\mu m$)	10.0	1.52
Soot aerosol	Log-normal ($\sigma=0.69317$, $a_m=0.0118\mu m$)	0.04	0.79
Oceanic aerosol	Log-normal ($\sigma=0.92028$, $a_m=0.3\mu m$)	2.5	1.15

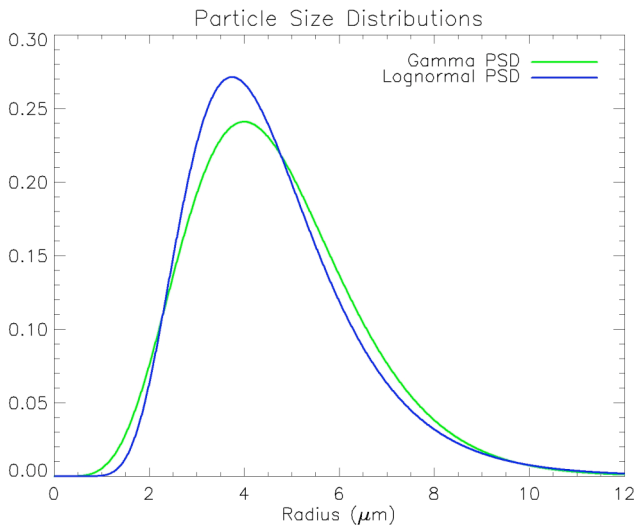


Figure 37: Gamma and Log-normal particle PSDs
(a_{eff}=6 μm and coefficient of variance Δ=0.38)

If one knows the PSD for a medium and the individual properties for each particle size, then the localized statistical average of the optical characteristics for the particles can be calculated. For instance, the extinction and scattering coefficient is calculated using the following equations:

$$\sigma_{ext} = N\int_0^\infty \pi a^2 C_{ext} f(a) da \tag{219}$$

$$\sigma_{sca} = N\int_0^\infty \pi a^2 C_{sca} f(a) da \tag{220}$$

where C_{sca} is the average scattering cross-section and C_{ext} is the average extinction cross-section which is the sum of the average scattering and absorption cross-sections.

Similarly, the scattering phase function for a medium with different particles sizes can be calculated using:

$$p(\theta) = \frac{2\pi N\int_0^\infty (i_1 + i_2) f(a) da}{k^2 \sigma_{sca}} \tag{221}$$

where i_1 and i_2 are the scattered irradiance per unit incident irradiance for the perpendicular and parallel components respectively and $k = 2\pi / \lambda$. The key is that one must be able to use particle scattering theory to predict the properties for each particle size within the distribution. Additionally, one needs to know or estimate the particle size distribution within the localized medium.

3.6 Scattering Theory for Spheres of Arbitrary Size (Mie Theory)

This section introduces the fundamental components of Mie scattering theory and then discusses a robust implementation algorithm. The primary interest is driven by the requirement to calculate the necessary optical properties of a particular gaseous effluent or aerosol based upon its complex index of refraction and particle size distribution. While one could examine Rayleigh-Gans approximations for small particles or scalar diffraction theory for large particles with respect to the wavelength of light, Mie theory stems from a rigorous derivation of scattering for spheres of an arbitrary size and encompasses the accepted approximations. The challenge with Mie theory is in implementing a calculation algorithm that is stable over the very small and very large regimes. Historically, stable Mie calculations also tend to be computationally intense. Hence the research community routinely leverages Rayleigh-Gans theory for small particles where the absolute value of the index of refraction, m, times the particles size parameter x is much less than 1 ($|mx| << 1$). For many of the wavelengths of interest in this research, the nominal particle size of a factory stack consituent leads to particle size parameters which are not small enough to invoke the Rayleigh-Gans scattering theory. The particle size parameter is inversely proportional to the wavelength and is defined as:

$$x = \frac{2\pi a}{\lambda} \tag{222}$$

where a is the particle's effective diameter and λ is the wavelength of light. Specifically, water vapor and soot are also typically in the middle regime between "small" and "large" particles. Thus, Mie scattering theory was selected for the generation of the required optical properties of the gaseous medium.

A thorough treatment of Mie theory is beyond the scope of this effort. For a more formal treatment, the reader is encouraged to review van de Hulst (1957) or Bohren and Huffman (1983). Both contain detailed derivations and explore scattering theory for various particles sizes and shapes. The general nomenclature introduced by van de Hulst will be adopted throughout this section with some adaptation when addressing practical Mie scattering calculation algorithms. After introducing Mie scattering theory and a robust algorithm, the section will finish by examining some of the preliminary results obtained and some practical considerations.

3.6.1 Mie Formulation

Let's consider investigating the scattering of an incident plane wave by a homogenous sphere. For simplicity, the outside medium is a vacuum with m_2=1 and the material of the sphere has an index of refraction, m. The incident radiation is linearly polarized and is traveling in the positive z-axis direction such that the x-axis is in the plane of electric vibration (as shown in Figure 38). The origin of the coordinate space is set to be at the center of the sphere. The problem is to find a closed form solution that describes the electromagnetic wave fields inside and outside the sphere.

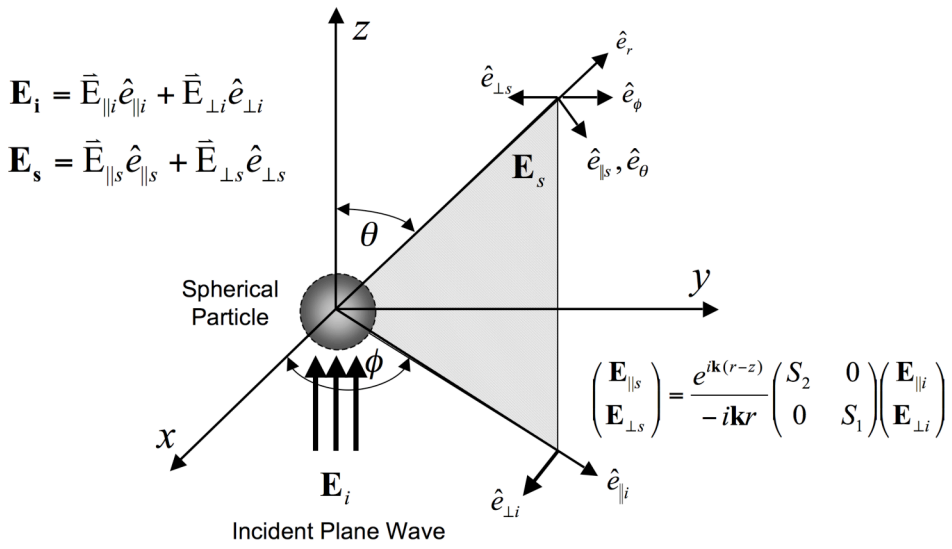


Figure 38: Geometry of incident and scattered fields for spherical particle and plane wave

As with most theoretical optics problem sets, the starting place is Maxwell's equations and a set of appropriate boundary conditions. Maxwell's general equations are:

$$\nabla \times \mathbf{E} = \frac{\partial \mathbf{B}}{\partial t} \tag{223}$$

$$\nabla \times \mathbf{B} = \mu \mathbf{j} + \varepsilon\mu \frac{\partial \mathbf{E}}{\partial t} \tag{224}$$

$$\nabla \cdot \mathbf{E} = \frac{\rho}{\varepsilon} \tag{225}$$

$$\nabla \cdot \mathbf{B} = 0 \tag{226}$$

where **E** is the electric field, **B** is the magnetic field, ρ is the charge density, ε is the electric permittivity, μ is the magnetic permeability, and **j** is the electric charge. Applying the appropriate boundary conditions, one can then work through the mathematics and find a solution set for inside and outside of the sphere. The result is an expression for an outgoing spherical wave with amplitude that is dependent upon the direction.

Although shown here without proof, the amplitude functions for the perpendicular and parallel components can be mathemaically written as:

$$S_1(\theta) = \sum_{n=1}^{\infty} \frac{2n+1}{n(n+1)} \left[a_n \pi_n(\cos\theta) + b_n \tau_n(\cos\theta) \right] \tag{227}$$

$$S_2(\theta) = \sum_{n=1}^{\infty} \frac{2n+1}{n(n+1)} \left[b_n \pi_n(\cos\theta) + a_n \tau_n(\cos\theta) \right] \tag{228}$$

where a_n and b_n are known as the Mie coefficients and π_n and τ_n are associated Legrendre polynomials. The special functions, π_n and τ_n, for the Mie scattering formulation are defined as:

$$\pi_n(\cos\theta) = \frac{dP_n(\cos\theta)}{d\ \cos\theta} \tag{229}$$

$$\tau_n(\cos\theta) = \cos\theta\ \pi_n(\cos\theta) - \sin\theta \frac{d\pi_n(\cos\theta)}{d\ \cos\theta} \tag{230}$$

where $P_n(\cos\theta)$ is a Legendre polynomial. Figure 39 is a polar plot of the first six realizations of π_n that would be used to calculate S_1 or S_2. A similar set of graphs for τ_n is shown in Figure 40. Both special functions are introduced into the Mie scattering theory derivation as general solutions of the scalar wave equation associated with Maxwell's equations.

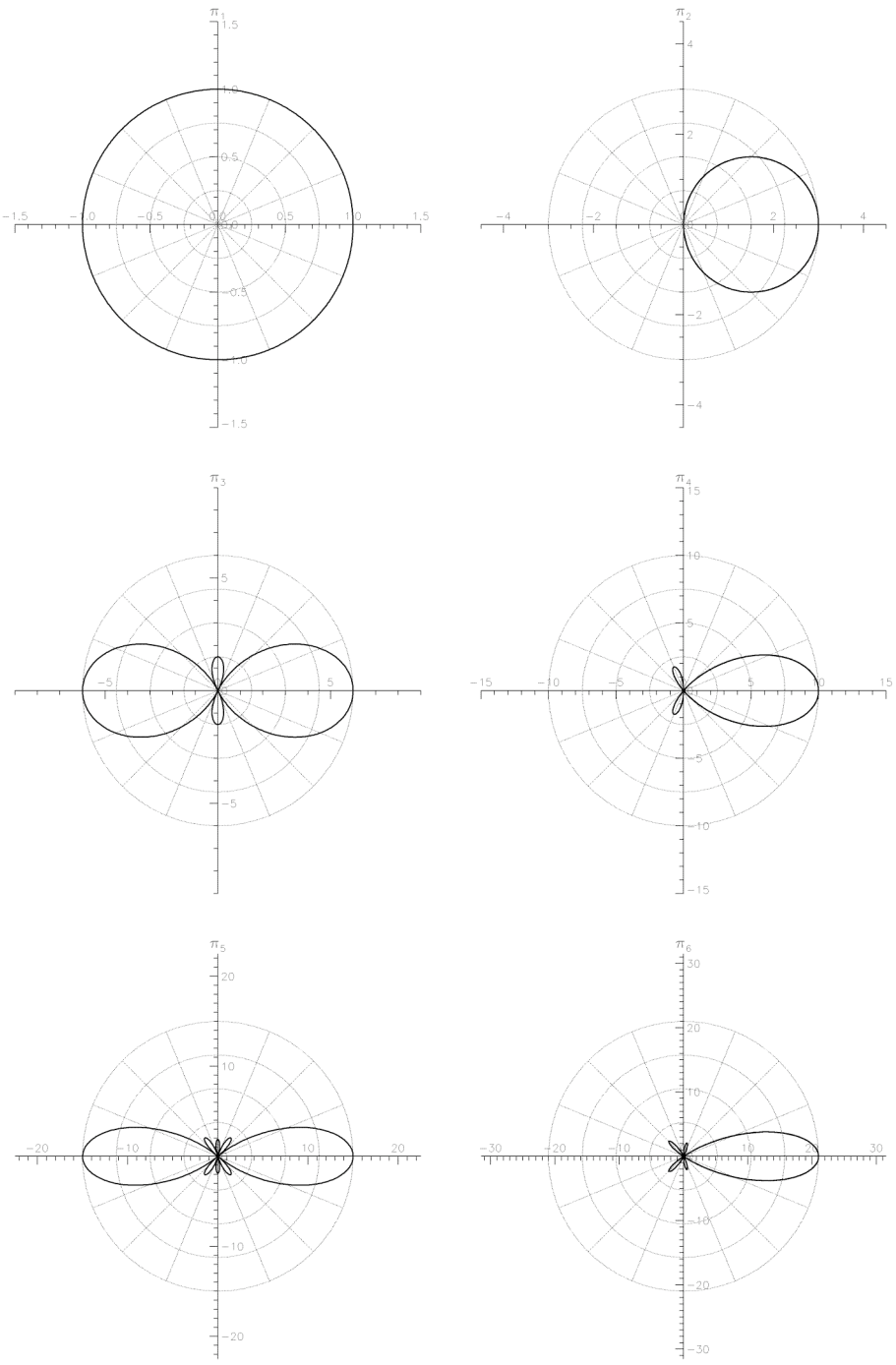


Figure 39: Polar plots of first six angle-dependent functions for π_n

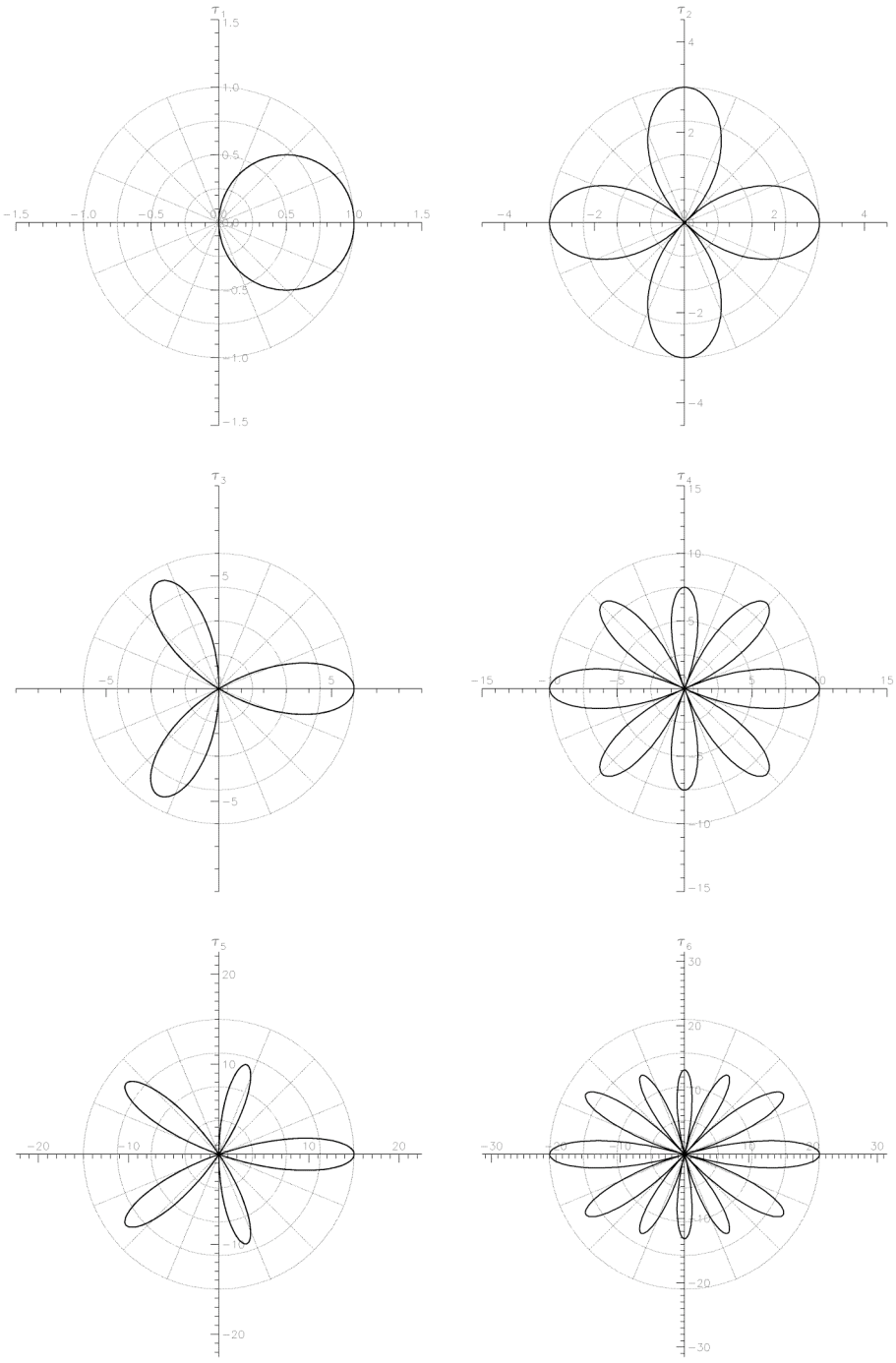


Figure 40: Polar plots of first six angle-dependent functions for $\boldsymbol{\tau}_n$

The Mie coefficients, a_n and b_n, are parts of the solution to the applied boundary conditions and constraints. In particular, they are introduced as a result of requiring the waves inside or outside of the sphere at the sphere boundary ($r=a$) to be equal. The notation was then simplified by introducing this new set of functions which differ from spherical Bessel functions by a factor of the argument. The Mie coefficients may be expressed as:

$$a_n = \frac{\psi_n'(mx)\ \psi_n(x) - m\psi_n(mx)\ \psi_n'(x)}{\psi_n'(mx)\ \zeta_n(x) - m\psi_n(mx)\ \zeta_n'(x)} \tag{231}$$

$$b_n = \frac{m\psi_n'(mx)\ \psi_n(x) - \psi_n(mx)\ \psi_n'(x)}{m\psi_n'(mx)\ \zeta_n(x) - \psi_n(mx)\ \zeta_n'(x)} \tag{232}$$

where the special functions ψ_n and ζ_n are a subset of the Riccatti-Bessel functions which are defined as:

$$\psi_n(z) = \sqrt{\frac{\pi\ z}{2}} J_{n+1/2}(z) \tag{233}$$

$$\chi_n(z) = \sqrt{\frac{\pi\ z}{2}} Y_{n+1/2} \tag{234}$$

$$\begin{aligned} \zeta_n(z) &= \sqrt{\frac{\pi\ z}{2}} H^{(2)}_{n+1/2}(z) \\ &= \sqrt{\frac{\pi\ z}{2}} \left(J_{n+1/2} + iY_{n+1/2}\right) \end{aligned} \tag{235}$$

where $J_{n+1/2}$ is a spherical Bessel function of the first kind, $Y_{n+1/2}$ is a spherical Bessel function of the second kind, and $H^{(2)}_{n+1/2}$ is also a spherical Bessel function. This notation was first introduced by Debye in 1909 and is the predominant notation. For calculation, one often introduces the relationship between the Riccati-Bessel functions which is:

$$\zeta_n(z) = \psi_n(z) + i\chi_n(z) \tag{236}$$

The critical spherical Bessel functions of the first and second kind are shown in Figure 41 for the first few values of n. The derivatives of these functions are denoted by the primes in Equations 231 and 232.

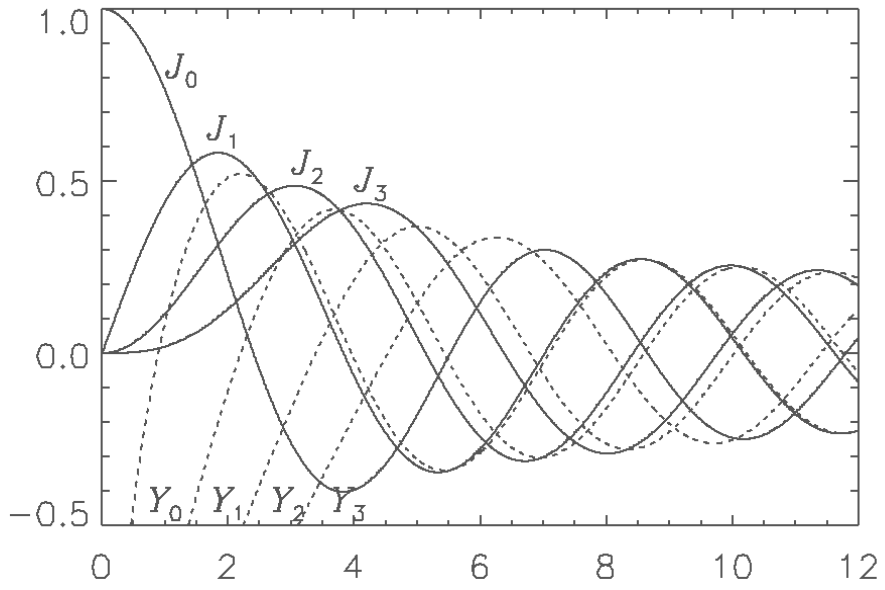


Figure 41: Spherical Bessel functions of the first (J_n) and second (Y_n) kind for $n = \{0,1,2,3\}$

The actual calculation of the coefficients and polynomials will be addressed shortly in Section 3.6.2; however, for now consider the optical properties of interest that can be gleaned from the amplitude functions. The scattered irradiance per unit incident irradiance for the perpendicular and parallel components is respectively:

$$i_1 = \left|S_1(\theta)\right|^2 \quad \text{and} \quad i_2 = \left|S_2(\theta)\right|^2 \tag{237}$$

While these expressions do not provide the scattered irradiance by the particles because they do not depend upon the incident irradiance I_0, they are routinely used to calculate the optical properties of the scattering particle. The actual scattered irradiance is:

$$I = \frac{I_0(i_1 + i_2)}{2k^2r^2} \tag{238}$$

where r is the distance from the particle and $k = 2\pi/\lambda$. Although the incident wave was linearly polarized, the scattered light may or may not be depending upon the particle. The degree of polarization of the scattered light is expressed as:

$$\frac{(i_1 - i_2)}{(i_1 + i_2)} \tag{239}$$

While the scattered irradiance can be important, the most critical parameters for modeling the multiple scattering and absorption effects are the extinction efficiency, the scattering efficiency, the absorption efficiency, and the scattering phase function. The efficiency factor for extinction (Q_{ext}) may be determined based upon the value of the amplitude functions at θ=0. Both $S_1(0)$ and $S_2(0)$ are equal for a homogenous spherical particle and may be mathematically written as:

$$S_1(0) = S_2(0) = \frac{1}{2}\sum_{n=1}^{\infty}(2n+1)(a_n + b_n) \tag{240}$$

Therefore, the efficiency factor for extinction (Q_{ext}) can be calculated as:

$$\begin{aligned} Q_{ext} &= \frac{4}{x^2}\mathrm{Re}\{S(0)\} \\ &= \frac{2}{x^2}\sum_{n=1}^{\infty}(2n+1)\mathrm{Re}\{a_n + b_n\} \end{aligned} \tag{241}$$

where x is the particle size parameter. This indicates that Q_{ext} is independent of the polarization of the incident wave. Evaluating the cross sections over the entire scattering pattern, Debye showed that the scattering efficiency Q_{sca} can be written in terms of the Mie coefficients as:

$$Q_{sca} = \frac{2}{x^2}\sum_{n=1}^{\infty}(2n+1)\left(|a_n|^2 + |b_n|^2\right) \tag{242}$$

Because of the conservation of energy, the absorption efficiency can then be easily found using the relationship:

$$Q_{abs} = Q_{ext} - Q_{sca} \tag{243}$$

The scattering phase function, which as described previously, is the scattered irradiance in direction divided by the irradiance that would be scattered in that direction if the scattering were isotropic is one of the other optical properties of interest. The scattering phase function can be mathematically expressed as:

$$\begin{aligned} p(\theta) &= \frac{2\pi(i_1 + i_2)}{k^2 C_{sca}} \\ &= \frac{2\pi\left(\left|S_1^2\right| + \left|S_2^2\right|\right)}{k^2 C_{sca}} \\ &= \frac{2\left(\left|S_1^2\right| + \left|S_2^2\right|\right)}{k^2 a^2 Q_{sca}} \end{aligned} \tag{244}$$

Combined with the extinction, absorption, and scattering efficiency parameters, the phase function forms the primary optical properties required to model the multiple scattering and absorption within a gaseous plume.

3.6.2 Practical Mie Calculations

Putting the Mie theory presented in the previous section into practice can be quite challenging. Although Mie theory has been around for a very long time (early 1900s), the computational history of Mie theory really only began recently, in the 1960s. Still, Mie codes were used only in limited cases because they were time consuming and we now know that they were not all that accurate. In the 1960s, the calculations were restricted to particle size parameters ($x=2\pi a/\lambda$) between 1 and 100. With the introduction of Dave's 1968 and 1969 papers, much larger size parameters were considered up to about 1000. The principle algorithms established by Dave in those papers still form the foundation of most Mie codes today. The bulk of the alterations to those Dave's algorithms are centered on expanding the range of particle size parameters over which the algorithm is stable or reducing the iterations and computational cycles necessary for convergence. For most cases, the primary differences lie in tweaks to take advantage of memory and computational precision of today's computers. In addition, the commonality of vectorized computations has permitted greater accuracy and operational size parameter range than previously thought possible.

Two of the research community work-horse Mie codes are Wiscombe's MIEV0 code and the simplistic Bohren and Huffman (BHMIE) code. MIEV0 was a direct outcome of an extensive study published by Wiscombe in 1980. Wiscombe studied the variety of algorithms and variants that had emerged and developed the foundation for MIEV0. BHMIE was developed by Bohren and Huffman (1998) to augment their text on absorption and scattering of light.
The primary algorithm discussed in this section is another variant that was first published by de Rooij and van der Stap (1984) and is based upon some concepts rooted in van de Hulst's (1957) discussion of the Riccatti-Bessel functions. This subsection shall discuss the fundamental instability and overflow problems associated with Mie scattering codes and the traditional approaches to circumvent those issues. Then the subsection will introduce a new algorithm published by Du (2004) that was used as the workhorse Mie code for this research effort. A more detailed discussion of the accuracy of these Mie codes will follow in a subsequent subsection.

The first step is to determine the number of iterations required for the summations in the amplitude equations to achieve an acceptable accuracy. The optimum decision point is highly dependent upon the wavelength and the complex index of refraction. Instead of establishing an elaborate methodology, one typically follows the community standard where:

$$N_{stop} = x + 4x^{1/3} + 2 \tag{245}$$

This cutoff is not entirely analytically defensible, but is supported by empirical data and by the communities experience at large.

Calculation of the angular functions π_n and τ_n is relatively straightforward. They both are stable and can be calculated using an upwards recurrence relationship as long as at least double precision mathematics is used. π_n is calculated using the following initial conditions and recursive relationship:

$$\begin{aligned}
\pi_0(\cos\theta) &= 0 \\
\pi_1(\cos\theta) &= 1 \\
\pi_2(\cos\theta) &= 3\cos\theta \\
\pi_{n+1}(\cos\theta) &= \cos\theta \cdot \pi_n(\cos\theta) \cdot \left(\frac{2n+1}{n}\right) - \pi_{n-1}(\cos\theta) \cdot \left(\frac{n+1}{n}\right)
\end{aligned} \tag{246}$$

Similarly, τ_n is calculated using the following initial conditions and recursive relationship based upon the values calculated for π_n :

$$\begin{aligned}
\tau_0(\cos\theta) &= 0 \\
\tau_1(\cos\theta) &= \cos\theta \\
\tau_2(\cos\theta) &= 3\cos 2\theta \\
\tau_n(\cos\theta) &= n \cdot \left(\cos\theta \cdot \pi_n(\cos\theta) - \pi_{n-1}(\cos\theta)\right) - \pi_{n-1}
\end{aligned} \tag{247}$$

In contrast, the calculation of the Riccatti-Bessel functions can be problematic. If the argument, *mx*, has a very large imaginary component, then both $\psi_0(mx)$ and $\zeta_0(mx)$ will overflow even if one uses double precision. This limitation prevents the application to larger particles sizes. To alleviate this problem, the logarithmic derivative of $\psi_n(mx)$ is introduced. This logarithmic derivative is often written as:

$$\begin{aligned}
A_n(mx) &\equiv \frac{d\left[\log\left(\psi_n(mx)\right)\right]}{d(mx)} \\
&= \frac{\psi_n'(mx)}{\psi_n(mx)}
\end{aligned} \tag{248}$$

and is very well behaved over a large range of *mx* from the Rayleigh limit to very large particles with an imaginary components as large as 100,000.

When $A_n(mx)$ is substituted into Equations 231 and 232, the Mie coefficients are then reduced to:

$$a_n = \frac{\left[A_n(mx)/m + n/x\right]\psi_n(x) - \psi_{n-1}(x)}{\left[A_n(mx)/m + n/x\right]\zeta_n(x) - \zeta_{n-1}(x)} \tag{249}$$

$$b_n = \frac{\left[A_n(mx)\cdot m + n/x\right]\psi_n(x) - \psi_{n-1}(x)}{\left[A_n(mx)\cdot m + n/x\right]\zeta_n(x) - \zeta_{n-1}(x)} \tag{250}$$

Although this approach does allow for consideration of larger particles sizes, the calculation of $A_n(mx)$ is non-trivial. A variety of methods have been developed, but they all essentially use the upward recurrence of $A_n(mx)$ where feasible and rely on the downward recurrence of $A_n(mx)$ when necessary because it is always stable. Additionally, most Mie codes either warn the user or use an alternative method of calculation for $A_n(mx)$ when $mx \to 0$. Wiscombe's MIEV0 code for instance actually uses a power series expansion for smaller particles. Since an alternative will be presented to actually calculating $A_n(mx)$, the algorithms will not be presented here and the reader is referred to the open literature or to Bohren and Huffman (1997).

To avoid the complicated algorithms and separate treatment for small particles, the algorithm published by Du (2004) establishes a ratio of the Riccatti-Bessel functions which allows one to avoid the calculation of $A_n(mx)$. The ratio is defined as:

$$r_n(mx) \equiv \frac{\psi_{n-1}(mx)}{\psi_n(mx)} \tag{251}$$

Equations 231 and 232 are then expressed as:

$$a_n = \frac{\left[r_n(mx)/m + n\left(1-1/m^2\right)/x\right]\psi_n(x) - \psi_{n-1}(x)}{\left[r_n(mx)/m + n\left(1-1/m^2\right)/x\right]\zeta_n(x) - \zeta_{n-1}(x)} \tag{252}$$

$$b_n = \frac{r_n(mx)m\psi_n(x) - \psi_{n-1}(x)}{r_n(mx)m\zeta_n(x) - \zeta_{n-1}(x)} \tag{253}$$

Although not required for calculating the results, the associated identity for $A_n(mx)$ can be written in terms of the ratio $r_n(mx)$ as:

$$A_n(mx) = r_n(mx) - \frac{n}{mx} \tag{254}$$

This concept is not revolutionary and has been theoretically discussed by a variety of respected experts in the field of scattering. In fact, the idea of the ratio of Riccatti-Bessel functions and more complicated ratios are commonly invoked to solve the problem of multilayered spheres (Du, 2004). The ratio, $r_n(mx)$, can be calculated using either upward or downward recursive means and exhibits similar stability as the underlying Riccatti-Bessel functions. Both sets of functions are stable when calculated with the downward recurrence presuming that the starting iteration is sufficiently large so that the answer converges correctly. Unfortunately, the downward recurrence relationships are extremely inefficient and at times can cost thousands of unnecessary iterations (Du, 2004). Du suggests that one can estimate the number of significant digits lost when using the upwards recurrence and then determine based upon the desired accuracy which recursive relationship to invoke.

Prior to discussing Du's "rule of thumb", let's examine the recursive relationships for the Riccatti-Bessel functions and for the associated ratio. The first Riccatti-Bessel function, $\psi_n(mx)$, can be calculated using the following initialization values and upwards recursive relationship:

$$\begin{aligned}
\psi_{-1}(z) &= \cos(z) \\
\psi_0(z) &= \sin(z) \\
\psi_1(z) &= \frac{\sin(z)}{z} - \cos(z) \\
\psi_{n+1}(z) &= (2n+1)\psi_n(z)/z - \psi_{n-1}(z)
\end{aligned} \tag{255}$$

Similarly, the imaginary component of $\xi_n(mx)$ can be calculated using the upwards recurrence relationship:

$$\begin{aligned}\chi_0(z) &= \cos(z) \\ \chi_1(z) &= \frac{\cos(z)}{z} + \sin(z) \\ \chi_{n+1}(z) &= (2n+1)\chi_n(z)/z - \chi_{n-1}(z)\end{aligned} \tag{256}$$

where $z=mx$ for the Mie coefficient calculations. Alternatively, the Riccati-Bessel functions can be calculated using the downward recurrence:

$$\begin{aligned}\psi_{N^*}(z) &= 0.0 + 0.0i \\ \psi_{N^*-1}(z) &= 1.0 + 0.0i \\ \psi_{n-1}(z) &= (2n+1)\psi_n(z)/z - \psi_{n+1}(z)\end{aligned} \tag{257}$$

$$\begin{aligned}\chi_0(z) &= \cos(z) \\ \chi_1(z) &= \frac{\cos(z)}{z} + \sin(z) \\ \chi_{n+1}(z) &= (2n+1)\chi_n(z)/z - \chi_{n-1}(z)\end{aligned} \tag{258}$$

where N^* is large enough to make the downward recurrence converge at the cutoff order N_{stop}. Du suggests that one method of determining N^* is to start with:

$$N^* = \mathrm{MAX}\left\{4|mx|^{\frac{1}{3}},\ 5\right\} \tag{259}$$

and to leverage his "rule of thumb" for calculating the number of lost significant digits to incrementally increase N^* to find the minimum necessary to meet the convergence criteria. is also appropriate and produces consistent results.

Additionally, the defined ratio, $r_n(mx)$, can be calculated using a Taylor series, an upwards recurrence, or a downwards recurrence. The general properties and behavior of $r_n(mx)$ follow the properties of $\psi_n(mx)$; therefore, when one should utilize the downwards recurrence is at the same decision point.

The upwards recurrence of $r_n(mx)$ can be calculated using:

$$\begin{aligned} r_0(z) &= \cot(z) \\ r_{n+1}(z) &= \left[\frac{2n+1}{z} - r_n(z)\right]^{-1} \end{aligned} \tag{260}$$

One of the caveats is that many default implementations of cot(z) may not suitable when mx has a large imaginary component. Instead one can implement a more direct calculation of the cot(z) using the formula:

$$\cot(z) = \frac{i + \tan\left[\mathrm{Re}\{z\}\right] - \exp\left[-2\,\mathrm{Im}\{z\}\tan\left[\mathrm{Re}\{z\}\right] + i\exp\left[-2\,\mathrm{Im}\{z\}\right]\right]}{-1 + i\tan\left[\mathrm{Re}\{z\}\right] + i\exp\left[-2\,\mathrm{Im}\{z\}\tan\left[\mathrm{Re}\{z\}\right] + \exp\left[-2\,\mathrm{Im}\{z\}\right]\right]} \tag{261}$$

and the complex division in the above equation can be calculated using double precision operators and the equation:

$$\frac{a+bi}{c+di} = \frac{ac+bd}{c^2+d^2} + \frac{bc-ad}{c^2+d^2}\,i \tag{262}$$

The downward recurrence of $r_n(mx)$ can be expressed mathematically as:

$$\begin{aligned} r_{N*}(z) &= \frac{2N*+1}{z} \\ r_n(z) &= \frac{2n+1}{z} - \frac{1}{r_{n+1}} \end{aligned} \tag{263}$$

where N* is sufficiently large to converge at N_{stop} and is set to obtain the desired precision.

How does one decide when to use the upward or downward recurrence and where to set N*? Du states that it is possible to estimate the number of significant digits lost when using either technique. He observes that the complex function $\psi_n(mx)$ is monotonically decreasing and that whenever it becomes one order smaller then the most significant digit is lost. This implies that if the modulus or absolute value of $\psi_n(mx)$ decreases by l orders compared with $\psi_0(mx)$ then $\psi_n(mx)$ will have l less significant digits. The Kapteyn inequality (Du 2004) provides the upper bound for the modulus of the complex function $J_n(z)$ and is in the limit approximately on the same order as $\psi_n(mx)$.

The inequality states that:

$$\left|J_n(z)\right| \le \left|\frac{z\exp\left[\left(1-\frac{z^2}{n^2}\right)^{1/2}\right]}{n\left(1+\left(1-\frac{z^2}{n^2}\right)^{1/2}\right)}\right|^n \approx \psi_n(z) \tag{264}$$

In addition, the moduli for the upward recurrence starting values are approximately:

$$\left|\psi_{-1}\right| \cong \left|\psi_0\right| \cong \frac{1}{2}\exp\left[\left|\mathrm{Im}(mx)\right|\right] \tag{265}$$

Combined with the Kapteyn inequality stated in Equation 264, the approximate number of lost significant digits, $l_n(mx)$, can be found using the following "rule of thumb":

$$l_n(z) \approx \frac{1}{\ln(10)}\left[\left|\mathrm{Im}\{z\}\right| - \ln(2) - n\left(\mathrm{Re}\left\{\ln\left(\frac{z}{n}\right)+\left(1-\frac{z^2}{n^2}\right)^{1/2}-\ln\left(1+\left(1-\frac{z^2}{n^2}\right)^{1/2}\right)\right\}\right)\right] \tag{266}$$

One calculates the anticipated number of lost significant digits using the upwards recurrence relationships and if the number is greater than desired thenn the downwards recurrence methods are invoked. For instance, the value of $l_{75}(100+100i)$ is approximately 5.93. The calculation indicates that 6 most significant digits were lost after recurring from N=0 to N=75. When using single precision, one only has about 2 most significant digits left which can lead to erroneous results; therefore, the downward recurrence would be advisable. In order to calculate the downward recurrence, one must first find an appropriate value for N*. Using Equation 259 as a starting point, one can incrementally increase N* and determine the actual number of significant digits. Stated here without proof, this is done by calculating:

$$l_{N^*}(mx) - l_{N^*-1}(mx) \tag{267}$$

which is approximately the number of significant digits for a downward recurrence of the Riccatti-Bessel functions and associated ratio (Du, 2004). Thus if the number of significant digits is too small, then N* is incremented again. This process is repeated until the desired number of significant digits is achieved. The starting point designated in equation 259 was

chosen to reduce the number of incremental updates required to get to reasonable N^* while not overshooting.

3.6.3 Performance and Accuracy

Once the component functions have been found, then the Mie coefficients (a_n and b_n), the amplitude functions, the scattering phase functions, and the efficiency factors can be calculated. The advantages of Du's algorithm are that it is simple, accurate, and robust for a variety of situations. The algorithm was tested thoroughly by Du over a wide range of refractive indices and particle sizes. For this research effort, I coded an IDL implementation of Du's algorithm (denoted MIEDU) and ran a battery of stressing test cases to verify the accuracy of the Mie code performance. Appendix A contains a detailed description of the sources of errors in Mie codes, potential pitfalls, some of the differences between the Mie codes mentioned thus far, and the resulting accuracy of the codes. The benchmark code written by Wiscombe (MIEV0) is an industry standard and uses a variety of different algorithms to calculate the necessary parameters depending upon the particle size and distribution. An IDL implementation of Bohren and Huffman's Mie code (BHMIE) was also included in the comparison. A summary of the overall operational restrictions and accuracies for the various Mie codes presented (MIEV0, BHMIE, and MIEDU) are shown in Table 3 below:

Table 3: Operational restrictions for MIEV0, BHMIE, and MIEDU

	Size Parameter (um)	Indices of Refraction		Accuracy
MIEV0	0.02 < x < 20,000	1 < Re{m} < 9	0 < Imag{m} < 10	>6
IDL BHMIE	1 < x < 1,000	1 < Re{m} < 2.5	0 < Imag{m} < 2	5 to 6
IDL MIEDU	0.02 < x < 20,000	1 < Re{m} < 9	0 < Imag{m} < 10	dialable up to 14

Smaller particles can pose significant challenges for some Mie codes; however, all three of these codes operate admirably within this range. As a demonstration of the performance for smaller particles where the Rayleigh approximation is valid, the amplitude functions for a very small particle with an index of refraction of 1.77 and a particle size parameter of ~0.05 were calculated. The normalized results are shown in Figure 42. The behavior for the unpolarized, perpendicular, and parallel amplitude functions are consistent with scattering behavior in the Rayleigh scattering regime. Table 4, Table 5, and Table 6 show a comparison of the results from the three different Mie codes (BHMIE, MIEV0, and MIEDU). Note that

any disagreements, however small, are highlighted in red. Du's algorithm performed as advertised and is in good agreement for these stressing cases with the industry standard, MIEV0. BHMIE did not achieve the same accuracy over the entire range of input parameters, but performed admirably within its published input parameter range.

Overall, all of the Mie codes evaluated have demonstrated a very high degree of accuracy for the calculating the scattering and absorption properties of a spherical particle over a very wide range of input parameters. The precision and accuracy for Du's algorithm is also truly deterministic and could be increased if necessary or reduced for improved computational efficiency. Any of the Mie codes explored in this subsection are more than adequate for generating optical properties of plume constituents such as water vapor or soot.

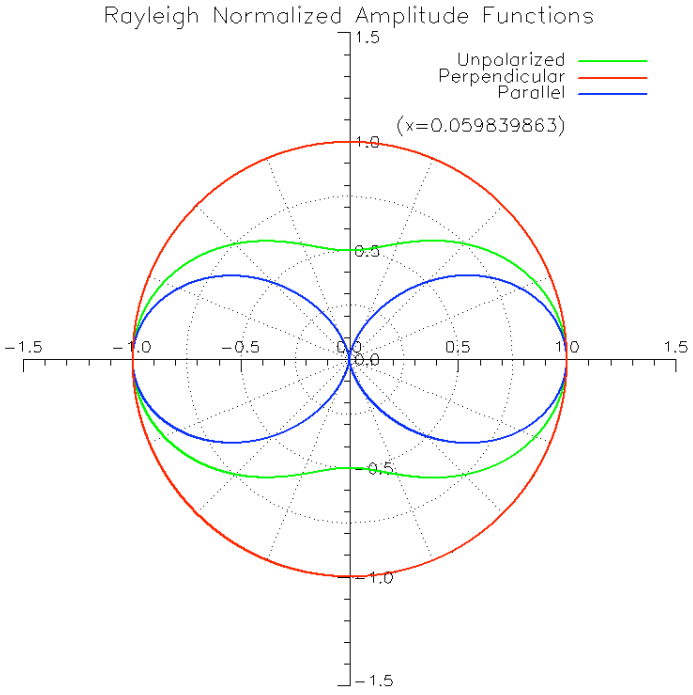


Figure 42: Normalized Rayleigh scattering amplitude functions

Table 4: Comparison of MIEDU and MIEV0 results

			IDL version of Du's Algorithm				Wiscombe's MIEV0 (FORTRAN)			
Re{m}	Imag{m}	x	Qext	Qsca	Qabs	gsca	Qext	Qsca	Qabs	gsca
0.75		0.099	7.41786E-06	7.41786E-06	0.00000E+00	0.001448	7.41786E-06	7.41786E-06	0.00000E+00	0.001448
0.75		0.101	8.03354E-06	8.03354E-06	0.00000E+00	0.001507	8.03354E-06	8.03354E-06	0.00000E+00	0.001507
0.75		10	2.23226E+00	2.23226E+00	0.00000E+00	0.896473	2.23227E+00	2.23227E+00	0.00000E+00	0.896473
0.75		1000	1.99791E+00	1.99791E+00	0.00000E+00	0.845093	1.99791E+00	1.99791E+00	0.00000E+00	0.844944
1.33	-1.0E-05	1	9.39520E-02	9.39233E-02	2.86810E-05	0.184517	9.39520E-02	9.39230E-02	2.90000E-05	0.184517
1.33	-1.0E-05	100	2.10132E+00	2.09659E+00	4.72690E-03	0.868961	2.10132E+00	2.09659E+00	4.72700E-03	0.868959
1.33	-1.0E-05	10000	2.00409E+00	1.72386E+00	2.80232E-01	0.907784	2.00409E+00	1.72386E+00	2.80232E-01	0.907840
1.50	-1.0E+00	0.055	1.01491E-01	1.13169E-05	1.01480E-01	0.000491	1.01491E-01	1.10000E-05	1.01480E-01	0.000491
1.50	-1.0E+00	0.056	1.03347E-01	1.21631E-05	1.03335E-01	0.000509	1.03347E-01	1.20000E-05	1.03335E-01	0.000509
1.50	-1.0E+00	1	2.33632E+00	6.63454E-01	1.67287E+00	0.192136	2.33632E+00	6.63454E-01	1.67287E+00	0.192136
1.50	-1.0E+00	100	2.09750E+00	1.28370E+00	8.13805E-01	0.850252	2.09750E+00	1.28370E+00	8.13805E-01	0.850252
1.50	-1.0E+00	10000	2.00437E+00	1.23657E+00	7.67793E-01	0.846272	2.00437E+00	1.23657E+00	7.67793E-01	0.846310
10.00	-1.0E+01	1	2.53299E+00	2.04941E+00	4.83588E-01	-0.110664	2.53299E+00	2.04941E+00	4.83588E-01	-0.110664
10.00	-1.0E+01	100	2.07112E+00	1.83679E+00	2.34339E-01	0.556215	2.07112E+00	1.83679E+00	2.34339E-01	0.556215
10.00	-1.0E+01	10000	2.00591E+00	1.79539E+00	2.10521E-01	0.548191	2.00591E+00	1.79539E+00	2.10521E-01	0.548194

Table 5: Comparison of MIEDU and BHMIE results

			Wiscombe's MIEV0 (FORTRAN)				IDL version of Bohren/Huffman Algorithm			
Re{m}	Imag{m}	x	Qext	Qsca	Qabs	gsca	Qext	Qsca	Qabs	gsca
0.75		0.099	7.41786E-06	7.41786E-06	0.00000E+00	0.001448	7.41786E-06	7.41786E-06	0.00000E+00	0.001448
0.75		0.101	8.03354E-06	8.03354E-06	0.00000E+00	0.001507	8.03354E-06	8.03354E-06	0.00000E+00	0.001507
0.75		10	2.23227E+00	2.23227E+00	0.00000E+00	0.896473	2.23226E+00	2.23226E+00	0.00000E+00	0.896473
0.75		1000	1.99791E+00	1.99791E+00	0.00000E+00	0.844944	1.99791E+00	1.99791E+00	0.00000E+00	0.844944
1.33	-1.0E-05	1	9.39520E-02	9.39230E-02	2.90000E-05	0.184517	2.02490E+00	2.02490E+00	0.00000E+00	0.184517
1.33	-1.0E-05	100	2.10132E+00	2.09659E+00	4.72700E-03	0.868959	2.15784E+00	2.15335E+00	4.49140E-03	0.859799
1.33	-1.0E-05	10000	2.00409E+00	1.72386E+00	2.80232E-01	0.907840	2.00436E+00	1.93166E+00	7.26961E-02	0.887362
1.50	-1.0E+00	0.055	1.01491E-01	1.10000E-05	1.01480E-01	0.000491	1.01491E-01	1.13169E-05	1.01480E-01	0.000491
1.50	-1.0E+00	0.056	1.03347E-01	1.20000E-05	1.03335E-01	0.000509	1.03347E-01	1.21631E-05	1.03335E-01	0.000509
1.50	-1.0E+00	1	2.33632E+00	6.63454E-01	1.67287E+00	0.192136	2.33632E+00	6.63454E-01	1.67287E+00	0.192136
1.50	-1.0E+00	100	2.09750E+00	1.28370E+00	8.13805E-01	0.850252	2.09750E+00	1.28370E+00	8.13805E-01	0.850252
1.50	-1.0E+00	10000	2.00437E+00	1.23657E+00	7.67793E-01	0.846310	2.00437E+00	1.23657E+00	7.67793E-01	0.846310
10.00	-1.0E+01	1	2.53299E+00	2.04941E+00	4.83588E-01	-0.110664	2.53299E+00	2.04941E+00	4.83588E-01	-0.110664
10.00	-1.0E+01	100	2.07112E+00	1.83679E+00	2.34339E-01	0.556215	2.07116E+00	1.83683E+00	2.34327E-01	0.556209
10.00	-1.0E+01	10000	2.00591E+00	1.79539E+00	2.10521E-01	0.548194	2.00591E+00	1.79539E+00	2.10521E-01	0.548194

Table 6: Comparison of MIEV0 and BHMIE results

			IDL version of Du's Algorithm				IDL version of Bohren/Huffman Algorithm			
Re{m}	Imag{m}	x	Qext	Qsca	Qabs	gsca	Qext	Qsca	Qabs	gsca
0.75		0.099	7.41786E-06	7.41786E-06	0.00000E+00	0.001448	7.41786E-06	7.41786E-06	0.00000E+00	0.001448
0.75		0.101	8.03354E-06	8.03354E-06	0.00000E+00	0.001507	8.03354E-06	8.03354E-06	0.00000E+00	0.001507
0.75		10	2.23226E+00	2.23226E+00	0.00000E+00	0.896473	2.23226E+00	2.23226E+00	0.00000E+00	0.896473
0.75		1000	1.99791E+00	1.99791E+00	0.00000E+00	0.845093	1.99791E+00	1.99791E+00	0.00000E+00	0.844944
1.33	-1.0E-05	1	9.39520E-02	9.39233E-02	2.86810E-05	0.184517	2.02490E+00	2.02490E+00	0.00000E+00	0.184517
1.33	-1.0E-05	100	2.10132E+00	2.09659E+00	4.72690E-03	0.868961	2.15784E+00	2.15335E+00	4.49140E-03	0.859799
1.33	-1.0E-05	10000	2.00409E+00	1.72386E+00	2.80232E-01	0.907784	2.02447E+00	2.01513E+00	9.33560E-03	0.883624
1.50	-1.0E+00	0.055	1.01491E-01	1.13169E-05	1.01480E-01	0.000491	1.01491E-01	1.13169E-05	1.01480E-01	0.000491
1.50	-1.0E+00	0.056	1.03347E-01	1.21631E-05	1.03335E-01	0.000509	1.03347E-01	1.21631E-05	1.03335E-01	0.000509
1.50	-1.0E+00	1	2.33632E+00	6.63454E-01	1.67287E+00	0.192136	2.33632E+00	6.63454E-01	1.67287E+00	0.192136
1.50	-1.0E+00	100	2.09750E+00	1.28370E+00	8.13805E-01	0.850252	2.09750E+00	1.28370E+00	8.13805E-01	0.850252
1.50	-1.0E+00	10000	2.00437E+00	1.23657E+00	7.67793E-01	0.846272	2.00437E+00	1.23657E+00	7.67793E-01	0.846310
10.00	-1.0E+01	1	2.53299E+00	2.04941E+00	4.83588E-01	-0.110664	2.53299E+00	2.04941E+00	4.83588E-01	-0.110664
10.00	-1.0E+01	100	2.07112E+00	1.83679E+00	2.34339E-01	0.556215	2.07116E+00	1.83683E+00	2.34327E-01	0.556209
10.00	-1.0E+01	10000	2.00591E+00	1.79539E+00	2.10521E-01	0.548191	2.00591E+00	1.79539E+00	2.10521E-01	0.548194

3.7 Plume Dynamics Modeling

The fundamental theory associated with modeling the dynamics and dispersion of gaseous plumes is well established in the literature. The modeling of turbulence and turbulent diffusion from discrete sources has been for the last century and continues to be a vast topic for ongoing research. The focus of this dissertation is not on modeling the dynamics of the plume itself, but on the interaction of light with the plume; therefore, for the purposes of this disseration, only a brief summary of the key relationships for the plume models utilized will

be provided. The primary purpose of the plume dynamics models for this research effort was to produce a gas makeup, species, temperature, concentration levels, and velocity, time-sequenced truth map to be used by DIRSIG for the LIDAR simulations. One should consult Blackadar (1997) or the Quick Urban & Industrial Complex Plume Model (QUIC-PLUME) documentation (Williams, et al., 2004) for additional theoretical development as appropriate. Additionally, one might consider reviewing Kuo's (1997) and Bishop's (2001) thesis regarding early plume modeling within the DIRSIG framework.

Modeling the dynamic nature of a gaseous plume is a very complex task. The task involves considering molecular and macro-scale motion, eddies, and energy transfer. Each localized area within the plume is dependent upon the nature and action of the surrounding particles or environments. The impact of a simple motion change in a particles ripples throughout the plume to some degree. Additionally, one must consider the effects of drag, convection, diffusion, the changing pressure gradient, and buoyant forces simultaneously on a very small time scale. Although each of these forces is related to familiar properties such as the velocity vector field, the pressure, the temperature and the kinematic viscoscity of the gases involved, solving the problem for even the simplest realistic cases is not trivial. Much of the work in this area and in the general field of fluid dynamics for the last few decades has been dedicated to finding techniques, algorithms, and numerically based analytical tools for predicting the behavior of a wide range of fluid flows. The compressibility or ability to be deformed significantly complicates this problem for gases over fluids such as water. The best models utilize intricate and computationally intense computational fluid dynamic (CFD) techniques. Even with the increase in computing power, a full-blown CFD model can take days to weeks to run for even a basic scene. In response, the research community initially adopted simpler models, such as the JPL Gaussian plume model. Although not rigorously true, the Gaussian model predicts the behavior of the factory stack plumes adequately for many applications and is based upon a set of statistical assumptions and a simple diffusion transport model. The Gaussian model was incorporated into DIRSIG in the late 1990s and is the current standard for many research efforts. In parallel, higher fidelity models that require much less computer time than a typical CFD run were also pursued. While many exist today, the Los Alamos National Lab QUIC-PLUME is the plume model that was selected to be

incorporated into DIRSIG. QUIC-PLUME was designed to handle the complex flows and dispersion of airborne contaminants released in an urban environment with the constraint that the predictions must be obtained quickly. While ranging from fairly straightforward to extremely complex, the analytical and numerical plume models essentially all attempt to solve a single set of governing equations, the Navier-Stokes equations, with respect to the time interval of interest. Unfortunately, the integration of QUIC-PLUME into DIRSIG has not yet been completed. As an alternative, a simple voxelized plume model based upon a model described in Blackadar's book on turbulence and diffusion (1997) was incorporated into DIRSIG. The Blackadar plume model offers a more realistic puff model of a plume than the Gaussian plume model, but is certainly less accurate or robust than the QUIC-PLUME model.

3.7.1 Governing Equations (Navier-Stokes Equations)

Before getting into the various aspects of the plume models, let us first consider a fluid that is at rest. At the localized level, the pressure exerts itself equally in all directions and is the only stress on the fluid. When a fluid is in motion, then the stress due to the pressure is not the only component present. Based upon the second law of thermodynamics, one typically removes the pressure term from the field and the remainder denotes the viscous stress. Although the gradient of the viscous stress is small, the effect is prominent when considering the dissipation of a fluid. The difficulty lies in determining how to find the viscous stress contribution.

Now consider the motion of a fluid in the neighborhood of any selected point. The localized motion can decompose into some fundamental invariants. For a two-dimensional (2-D) case shown in Figure 43, the simple shear motion can be decomposed into four components. Note that the last component, divergence, is not shown in the figure. Essentially the motion in the local neighborhood is comprised of a uniform velocity known as translation, a rotation of the particle, and a stretching and squeezing of the particle or fluid. When expressed in three dimensions, translation causes the volume of fluid to move in a specific direction as a whole, the vorticity (previously referred in 2-D as rigid rotation) causes it to rotate around a local

axis, divergence causes the volume to expand at an equal rate in all directions, and pure deformation causes the shape to change.

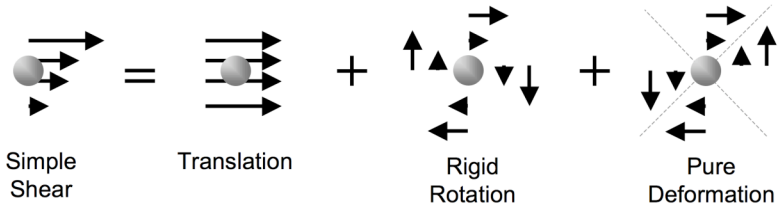


Figure 43: Decomposition of a simple shear flow into fundamental invariants

In 1845, Stokes (and Navier to some degree 20 years earlier) proposed that the viscous stress was proportional to the rate of pure deformation of the fluid motion. Based upon this proposition, the decomposition of the motion into the fundamental invariants, and the second law of thermodynamics, Stokes surmised that the governing equations for a turbulent fluid (or gas) can be mathematically expressed as:

$$\frac{\partial \vec{u}}{\partial t} = \underbrace{\nu \nabla \cdot \left(\nabla \vec{u}\right)}_{\text{Drag}} - \underbrace{\left(\vec{u} \cdot \nabla\right)\vec{u}}_{\text{Convection}} - \underbrace{\nabla p}_{\text{Pressure Gradient}} - \underbrace{\beta \vec{g}_v \left(T_0 - T_k\right)}_{\text{Buoyant Forces}} \tag{268}$$

$$\frac{\partial T}{\partial t} = \underbrace{\lambda \nabla \cdot \left(\nabla T\right)}_{\text{Diffusion}} - \underbrace{\nabla \cdot T\vec{u}}_{\text{Convection}} \tag{269}$$

$$\nabla \cdot \vec{u} = 0 \quad \textit{Navier-Stokes Constraint Equation (Conserves mass)} \tag{270}$$

where ∇ is the gradient operator, $\vec{u}$ is the velocity vector of the gas, p is the pressure of the gas, g_v is the gravity in the vertical direction, β is the coefficient of thermal expansion, T_0 is the initial reference temperature, and T_k is the average temperature on the boundary between a gaseous cell and the one above it, and λ is chosen to represent both molecular and turbulent diffusion processes in the gas. It is this set of governing equations that form the foundation of fluid dynamics with respect to gaseous plumes. While simple in appearance, solving the Navier-Stokes equations for even the simplest situation is non-trivial.

3.7.2 JPL Gaussian Plume Model

The JPL Gaussian plume model was originally designed to model gas plumes released from factory stacks by the U.S. Environmental Protection Agency (EPA) (Bishop, 2001). The model was then modified by Kaman Corp and the Jet Propulsion Laboratory (JPL) and incorporated into DIRSIG in 1997. The JPL Gaussian plume model is a standard Gaussian plume model based on the Brigg's equation for plume dynamics (Bishop, 2001). While not rigorously accurate, the model is consistent with empirical results observed downwind of factory stacks and is very straightforward. The fundamental premise is that the concentration downwind can be found as a function of three independent probability distribution functions whose means are distributed about the plumes centerline such that:

$$\chi(x,y,z) = Q \cdot F(x)G(y)H(z) \tag{271}$$

where Q is the source strength expressed as the emission rate per unit of time. In truth, the distribution functions are correlated and not independent. For simplicity, let's initially fix the plume's centerline to be the height of the release point. The situation is depicted in Figure 44, where the plume is approximated by successive point sources. The concentration in the x-direction can be expressed as:

$$F(x) = \frac{1}{\bar{u}dt} \tag{272}$$

where $\bar{u}$ is the mean wind velocity and $\bar{u}dt$ is the width of the slab of interest. When one examines the concentration between two vertical slabs at $x = \bar{u}t$ over a very small distance $\bar{u}dt$ as $dt \to 0$, then to a reasonable assumption the distribution in the x direction is uniform over that slab.

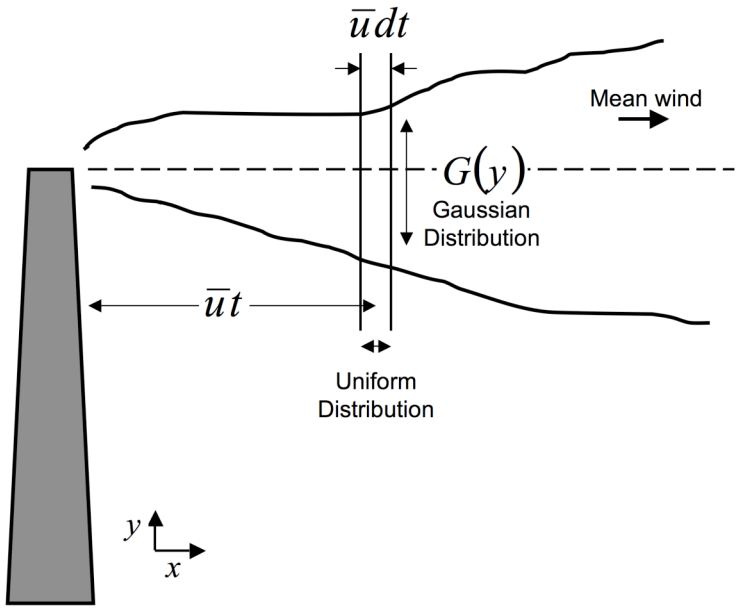


Figure 44: Gaussian plume approximated by successive point sources

The overall concentration can then be expressed as:

$$\chi(x,y,z) = \frac{Q}{\bar{u}} G(y) H(z) \tag{273}$$

Intuitively, the notion that the concentration of pollutant everywhere is proportional to the emission rate and inversely proportional to the wind speed is appropriate. The next step is to find the forms and parameters of *G(y)* and *H(z)*. When one solves Fick's equations (Blackadar, 1997) using K-theory or some other means, the concentration of gases or aerosols from the plume centerline downwind is found to be Gaussian distributions. The concentration can be mathematically expressed as:

$$\chi = \frac{Q}{2\pi\sigma_y\sigma_z\mu} \exp\left[-\frac{y^2}{2\sigma_y^2}\right] \exp\left[-\frac{z^2}{2\sigma_z^2}\right] \tag{274}$$

where x is the downwind distance, y is the lateral distance from the centerline, z is the vertical distance from the ground, Q is the source intensity (mass released per unit time), μ is the mean wind speed, and σ_y and σ_z are the lateral and vertical coefficients of dispersion respectively. Note that this formulation assumes that the height of the source is at $z = 0$.

When one takes into account the effective height of the stack, h_{eff}, then the concentration becomes:

$$\chi = \frac{Q}{2\pi\sigma_y\sigma_z\mu}\exp\left[-\frac{y^2}{2\sigma_y^2}\right]\exp\left[-\frac{\left(h_{eff}-z\right)^2}{2\sigma_z^2}\right] \tag{275}$$

Obviously, this equation is only valid for $z > 0$. One could choose to assume that the particles that touch the ground are absorbed or one could assume that all of the particles are reflected from the surface. If the latter were true, then the concentration levels indicated in Equation 275 would be too low. For that reason, regulatory agencies and most researchers simply reflect the subsurface plume back into plume above the ground. This is illustrated in Figure 45. Thus the concentration at any point above or at the surface is:

$$\chi = \frac{Q}{2\pi\sigma_y\sigma_z\mu}\exp\left[-\frac{y^2}{2\sigma_y^2}\right]\left(\exp\left[-\frac{\left(z-h\right)^2}{2\sigma_z^2}\right]+\exp\left[-\frac{\left(z+h\right)^2}{2\sigma_z^2}\right]\right) \tag{276}$$

where h is the height of the centerline of the plume and is usually found from Briggs equations, which will be discussed later in this section. The true concentration probably lies somewhere between Equation 275 and 276.

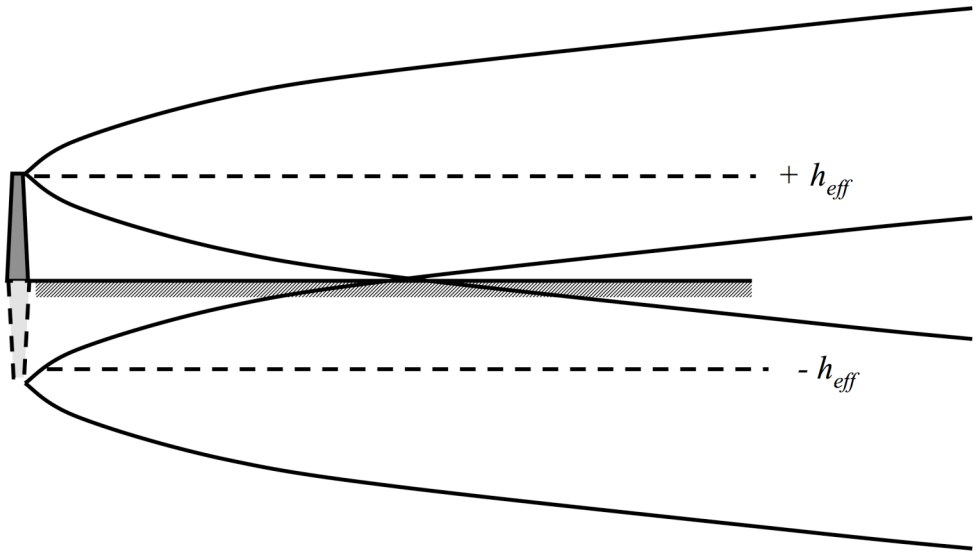


Figure 45: Reflected plume created by use of a virtual source at z=-h_{eff}

Thus far, the plume centerline has been assumed to be at the same height as the source release. As noted earlier, the plume centerline can be found based upon the comprehensive theory of plume rise developed by Briggs (Blackadar, 1997). In a neutral atmosphere, the Briggs equation assumes a buoyant rise of the plume. For a neutrally buoyant effluent, the plume height is:

$$h = h_{eff} + 3x^{1/3}\left(\frac{r_{stack}v_{ratio}^2}{v_{ratio}+3}\right)^{2/3} \tag{277}$$

Where h_{eff} is the effective stack height, r_{stack} is the stack radius, x is the downwind distance, and v_{ratio} is the emission velocity ratio which is defined as the vertical emission velocity divided by the wind velocity. Alternative forms can be used to find the plume centerline depending upon the level of information that one has about the heat emitted from the stack and surrounding environment and the detailed wind vector fields. The model implemented into DIRSIG incorporates one of these variations based upon some statistics about how a plume centerline wanders. A sample ACAD drawing of a Gaussian plume with multiple regions defined and a "wander" is shown in Figure 46.

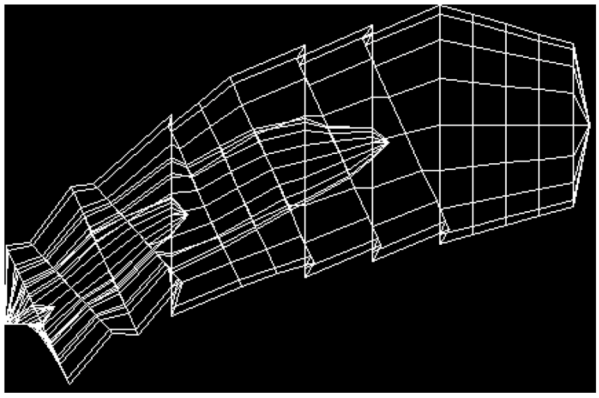


Figure 46: ACAD of JPL "Wander" Gaussian Plume Model

Although many of the parameters in Equations 275 and 276 are straightforward, the values for σ_y and σ_z must often be derived by fitting curves to empirical to measurements. Additionally, the form of Equations 275 and 276 do not readily indicate that σ_y and σ_z are functions of x. The most widely accepted method of determining σ_y and σ_z is to use a set of diagrams based upon the work of Pasquill and Gifford (Blackadar, 1997). The diagrams are

based upon a simple classification scheme attributed to Pasquill shown in Table 7. Using the guidance based upon the generalized scene conditions in Table 8 and diagrams similar to those shown in Figure 47, one can then determine the values for σ_y and σ_z. The diagrams are typically based upon measurements of tracers released above a smooth terrain. Although this method is very simple, the potential for error is great. The largest source of error is in estimating the stability based upon measurements for a smooth terrain. Additionally, this method does not account for all of the turbulent effects within a plume, such as fanning. Another factor to consider is that the model does not handle the complex turbulent motion or turbulent diffusion present in an urban environment. The assumption is that the plume essentially transverses without interruption or dramatic change in the wind velocity field. Despite these caveats, the approach is commonly accepted and deemed adequate. As such, the JPL Gaussian plume model is still the primary workhorse plume model for many researchers.

Table 7: Pasquill Stability Classes

Letter	Class
A	Extremely unstable
B	Moderately unstable
C	Slightly unstable
D	Neutral
E	Slightly stable
F	Moderately stable

Table 8: Pasquill Stability Types Guidance

	Daytime Insolation			Night-time	
Surface wind speed (m/s)	Strong	Moderate	Slight	Thin overcast (≥ 4/8)	Cloudiness (≥ 3/8)
< 2	A	A-B	B		
2	A-B	B	C	E	F
4	B	B-C	C	D	E
6	C	C-D	D	D	D
> 6	C	D	D	D	D

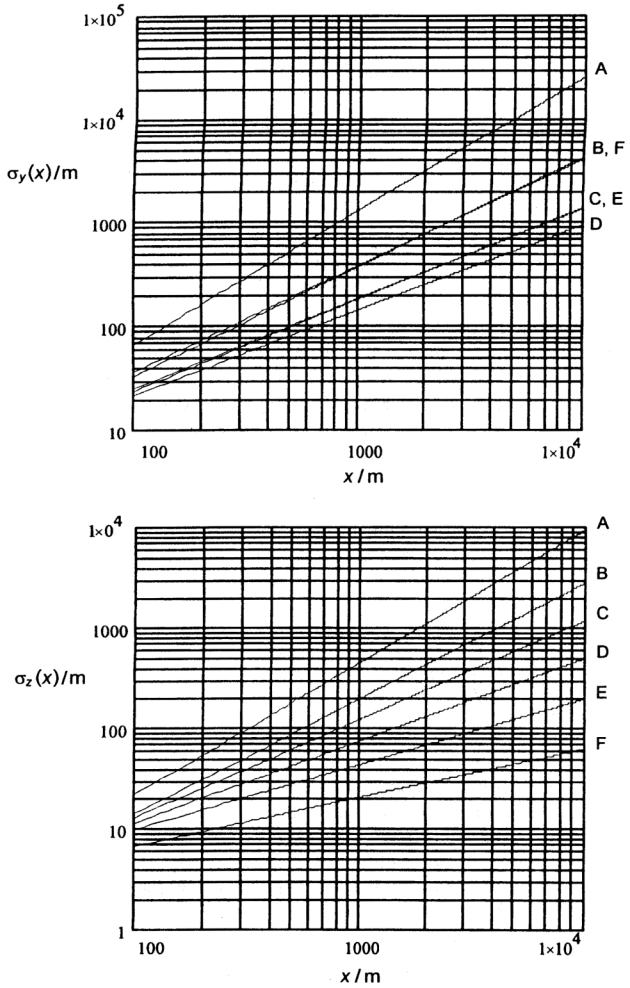


Figure 47: Gaussian plume model diagrams for σ_y and σ_z for release heights of 100m over rough terrain (Blackadar, 1997)

3.7.3 LANL QUIC-PLUME Model

It is possible to create a more accurate simulation of how a plume will disperse without making the restrictive assumptions of homogeneity and stationarity as was done for the Gaussian plume model. The approach is to issue particles sequentially from the source and stochastically conform to the Navier-Stokes equations over a very small time. The motion of each particle is assumed to be independent from the influence of the other particles over that small time scale, but is primarily driven by physics-based statistics. Often the particles undergo a drunkard's walk, which is defined as being a random walk where the particle "remembers" the previous motion to some degree. One such model is Los Alamos National Lab's (LANL's) Quick Urban & Industrial Complex (QUIC) dispersion modeling system of which QUIC-PLUME is the primary dispersion model (Williams, et al., 2004). The other primary modules essentially determine the wind velocity vector field, particularly around buildings. QUIC was designed to model the dispersion of airborne contaminants released near buildings where the results must be computed quickly (Williams, et al., 2004). Currently, the QUIC-PLUME model is being assimilated into DIRSIG as an optional model and is anticipated to be operational within the near future. QUIC-PLUME is a Lagrangian dispersion model that uses a Langevin random-walk approach based upon the mean and the turbulent wind fields. The code attempts to account for the inhomogeneity of the flow around buildings and updates rotation terms to account for the lateral and vertical motion gradients in the turbulence parameters. Figure 48 and Figure 49 are renderings of a sample QUIC-PLUME simulation that appears in the literature (Williams, et al., 2004). The simulation is of a smoke release in the West Village area of New York City and demonstrates QUIC-PLUME's ability to model dispersion in urban environments. While the computer graphics rendering was not intended to be radiometrically accurate, the concentration variations and the small fluxuations between time-steps and within the plume structure are still evident. This is most evident in the close-ups shown in Figure 49. For either the detailed derivation or implementation guide, one should review both of the LANL QUIC-PLUME references (Williams, et al., 2004).

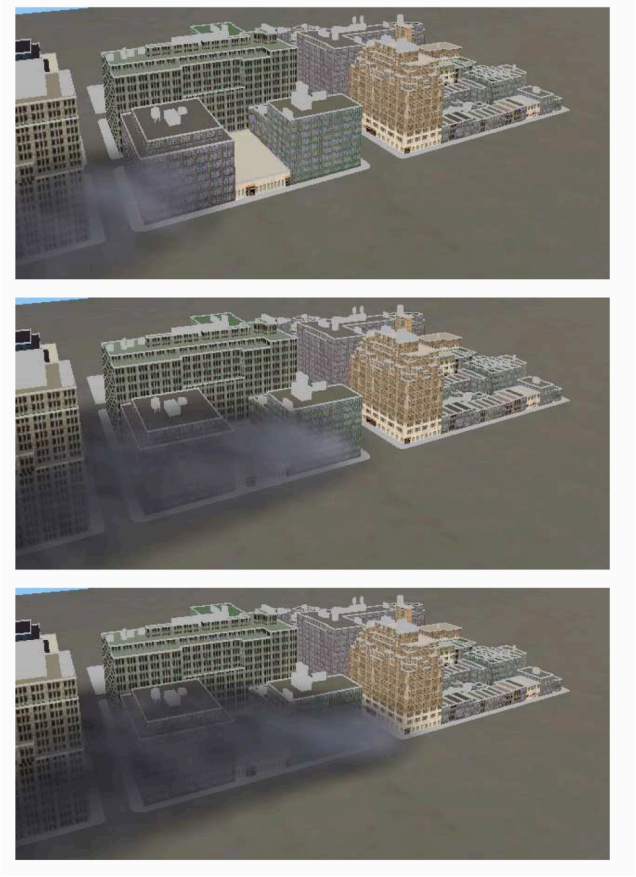


Figure 48: Rendered snapshots of a QUIC-PLUME simulation of a release in West Villiage area of New York City (Qui, et al., 1997)

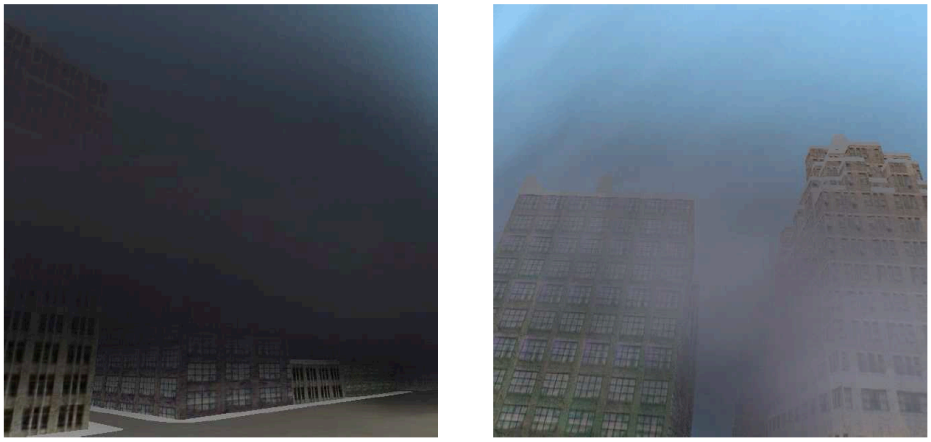


Figure 49: Rendered close-up views for a QUIC-PLUME simulation of a release in West Villiage area of New York City (Qui, et al., 1997)

3.7.4 Blackadar Plume Model

The Blackadar plume model was recently incorporated into DIRSIG primarily as an interface test-bed for more advanced voxelized or puff-based plume models. The Blackadar plume model is based upon the fundamental turbulence and diffusion theory introduced in Blackadar's book, Turbulence and Diffusion in the Atmosphere (1997). Because Blackadar's intent was to create a simplified, particle-based plume model that users could utilize to explore the effects of various environmental parameters or the plume's fundamental characteristics, the model accurately represents the fundamental physics and behaviors of plumes. However, the plume model has not been validated and should be used with caution.

As stated above, the Blackadar plume model is a particle-based model. The general flow diagram is shown in Figure 50. Small particles are created at the defined release point within the user-defined stack diameter with known material properties, a concentration, exit velocity, and a dispersion coefficient. The particles are released individually and then move based upon a drunkard's walk random process and the simulation parameters, such as the wind velocity. Between time increments, the particle essentially remembers a portion of its previous velocity and the model uses that information to predict the new velocity vector. The rate of memory loss for each particle is defined by the Lagrangian time scale, which is a function of the stability classes described in Table 7 and Table 8. At the moment, DIRSIG has the stability class hardwired to Pasquill's moderate stability class. Note that the particle's initial velocity is determined by a suite of different factors including the mean wind velocity, the particle mass, the emission rate, and the variability in the emission rate. The latter attribute is also intimately linked with the chosen stability class. Blackadar's plume model incorporates the buoyant (rise and fall) tendencies of the plume based upon Brigg's equation (Equation 277) which was the basis of the plume center-line for the Gaussian plume model. As the particles traverse the simulation space, the mass of the each particle remains the same, but the size, and thus the volume, is expanded using the assigned puff dispersion coefficient. The effect is shown in Figure 51 which is a DIRSIG height truth map of a Blackadar plume. The small particles grow in size as they drift downwind. Thus, the concentration is effectively diluted. Additionally, the temperature profile of the particles is dependent upon the stack release temperature, the ambient air temperature, and the dispersion coefficient.

Adjustments to the temperature are made for each time-step; however, the law of conservation of energy is not strictly enforced by design to reduce the complexity of the calculations. One should not confuse the puff dispersion coefficient with the plume dispersion coefficient. The plume dispersion coefficient impacts where the puffs go and how quickly they spread apart. Plume dispersion is primarily affected by large eddies and turbulence. The puff dispersion coefficient describes how the individual puffs dilute and are influenced by very small eddies. Finally, the Blackadar plume model deals with collisions with solid surfaces in a very straightforward manner. If the particles hit a surface, then the deposition probability defined by the user determines statistically whether that particle is deposited or "bounces" off of the surface. The Blackadar plume model does not account for the changes in wind velocity through an array of buildings, such as QUIC-PLUME. For a more complete treatment of collisions, plume models need to have some knowledge of the wind velocity and acceleration vector fields to accurately predict a particle's likely behavior. Unfortunately, this added complexity incurs a significant computational penalty. Overall, the Blackadar plume model is an excellent representation of a particle-based plume model which offers an added degree of realism for the temporal movement over the standard Gaussian plume model. At the same time, some basic assumptions and limitations are imposed for the sake of simplicity and computational speed.

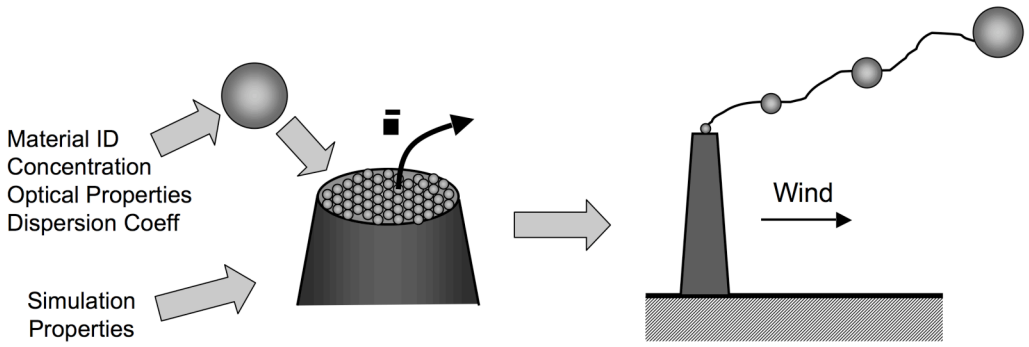


Figure 50: Conceptual diagram for DIRSIG's Blackadar plume model

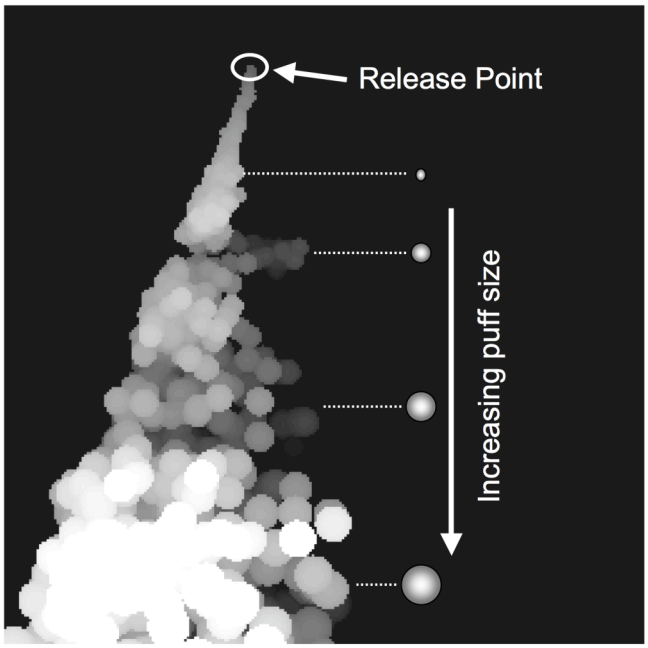


Figure 51: Annotated DIRSIG truth map image of a Blackadar plume

3.8 Summary

This chapter forms the theoretical and analytical foundation for this research effort. We have reviewed the principles of the DIAL/DAS method and discussed some of the potential impacts that multiple scattering may have upon a DIAL sensor's concentration sensitivity and accuracy. In addition, we derived a multiple scattering LIDAR equation which accounts for most of the multiple scattering effects in a strongly forward scattering medium in Section 3.2. Section 3.2 also stressed the importance of accounting for multiple scattering effects for optically thick and "medium" scattering layers. As note previously in this chapter, the modeling approach infused into the DIRSIG framework is based upon this multiple scattering LIDAR equation in conjunction with the core photon mapping principles discussed in Section 3.4. Although one could employ the multiple scattering LIDAR equation for some instances, plumes are not semi-infinite or always predominantly forward scattering in nature. Section 3.3 went through the underlying physics of radiative transfer theory and common approximations for the RTE, including a useful derivation of the BSN diffusion approximation for a monodirectional-pulsed point source. Chapter 4 will leverage the diffusion approximation and the multiple scattering LIDAR equation as a key analytical

verification tool for the scattering portion of the LIDAR model. As a direct extension of the theoretical development of the radiative transfer equation within a plume, Section 3.4 discussed the theoretical, mathematical, and practical implementation of photon mapping for modeling multiple scattering and absorption of light within a dispersive, participating media. The emphasis for Section 3.4 was on the traditional photon mapping approaches which form the enabling paradigm for the DIRSIG LIDAR module; however, the specific implementation details and new adaptations were left to Chapter 4. The last three sections of this chapter then shifted to discuss the theory and practical considerations necessary to simulate complex scenes. Section 3.5 introduced the types of particle size distributions that are relevant to this area of research and the impact of those distributions on the optical properties of the medium. Section 3.6 focused on the absorption and scattering of arbitrarily-sized small particles. This section introduced the basis for Mie scattering theory and a practical algorithm to physically calculate the necessary optical properties for a particular gas or aerosol based upon its complex index of refraction and particle size distribution function. Rayleigh and non-selective scattering was also addressed; however, the emphasis was on Mie scattering because the typical particles of interest for this dissertation fall within this regime. The final section, Section 3.7, addressed plume dynamics modeling very briefly. The section introduced the overall governing equations for modeling the flow of effluent concentrations within a scene and the two plume models fully integrated into DIRSIG, the Gaussian model and the Blackadar model. The Blackadar model is currently the only plume model which is capable of interacting with the DIRSIG LIDAR module; however, future plans are also mentioned in Section 3.7 with regards to the incorporation of higher fidelity plume models, such as QUIC-PLUME.

Chapter 4

Approach

The core of this research effort and this chapter is the development and verification of a physics-based modeling approach to simulate the multiple scattering and absorption in a participating medium for a LIDAR sensor, particularly for a DIAL system. The chapter begins by introducing the current first-principles, physics-based elastic LIDAR model. After reviewing the historical development, motivation, and potential requirements for the LIDAR model in Section 4.1, the specific requirements, innovations, and numerical approaches are presented in Section 4.2. These innovations and numerical approaches enable the DIRSIG LIDAR module to support rigorous atmospheric interactions, participating media, multiple bounce/scattering, thermal and reflective region passive returns, complex scene geometries, moving platform and scanning effects, detailed material optical descriptions (BRDF and scattering models) and time-gated returns. Section 4.3 then discusses some practical implementation considerations, such as generating the optical parameters, photon density requirements, the benefits of multiple photon maps, and utilizing the Blackadar plume model. In addition, the chapter discusses the verification methodology and a series of phenomenological case studies designed to investigate the viability and accuracy of the model in Sections 4.4 and 4.5 respectively. The phenomenological case studies provide crucial insight into the model performance for realistic collection scenarios. Section 4.6 discusses the simplified approach crafted to demonstrate the potential effects of multiple scattering on DIAL concentration measurements and the construction of an exemplar DIAL dataset using the water treatment plant in Megascene 1 and the Blackadar plume model.

4.1 Model History

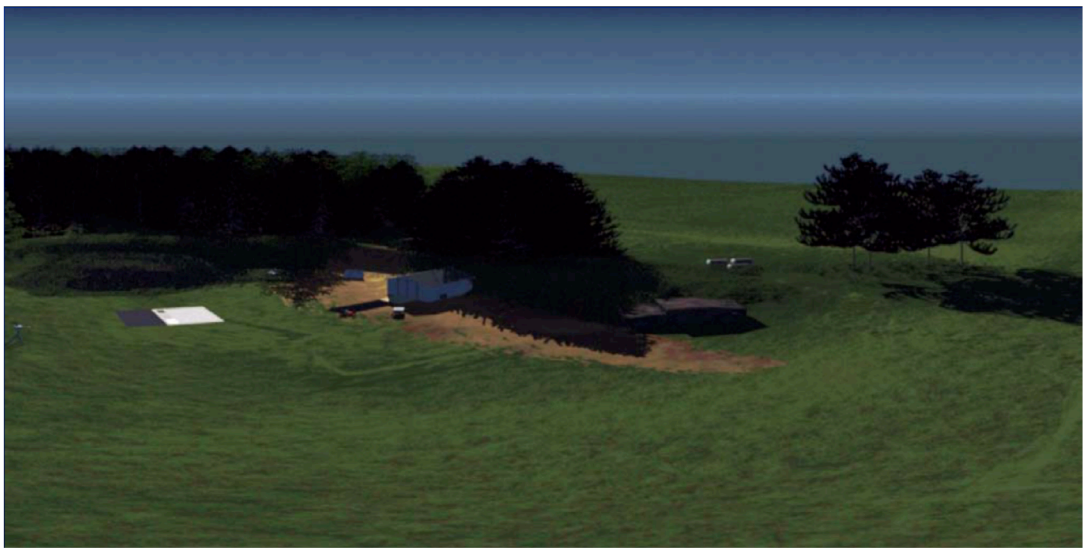
The initial development of the Digital Imaging and Remote Sensing Image Generation (DIRSIG) model began at the Rochester Institute of Technology (RIT) in the late 1980's as a 3D simulation environment for predicting images that would be produced in the thermal infrared systems. Since that time, the model has been expanded to cover the 0.35 to 20.0 μm region of the spectrum. DIRSIG is employed throughout the research community as a tool to aid in the evaluation of sensor designs and to produce imagery for algorithm testing

purposes. The model is designed to produce passive broad-band, multi-spectral, and hyper-spectral imagery through the integration of a suite of first-principles, physic-based radiation propagation modules. These object-oriented modules address tasks ranging from bi-directional reflectance distribution function (BRDF) predictions of a surface, to instruments on agile platforms (Schott, etal., 1999). In addition to the myriad of DIRSIG-specific objects that have been created, a suite of interface objects leverage externally developed components that are the modeling workhorses for the mulit- and hyper- spectral community. Some of these models include atmospheric codes such as MODTRAN (Berk, et al., 1989) and FASCODE, as well as the thermal model, THERM (DCS Corporation, 1990). Key components of the model and some aspects of the model's overall performance have been gauged by several validation efforts over the past decade (Mason, et al., 1994; Brown, etal., 1996).

4.1.1 Historical Modeling Approach

The modeling philosophy that has driven DIRSIG model development over the years is one that favors first-principles radiation transfer mechanisms over statistical or empirical modeling approaches. Most statistical or empirical models have been derived from specific data sets that feature specific conditions. The fit of empirical models to the respective original data may be exceptional, but depending on the underlying approach, the model may not be applicable for a different time of day, for a different season, for a different sensor, etc. Such models may have a high degree of accuracy for specific cases, but very little flexibility for modeling alternative scenarios. These same limitations may also be applicable to some classes of statistically based models. In contrast, the historical DIRSIG approach is to model as many physically based interactions as possible by utilizing model inputs that predominantly consist of geometric, optical, and thermodynamic inputs. The underlying radiative transfer model then interacts with this combined geometric and optical scene model to predict the radiational flux into a given direction for a specific set of collection conditions. Although this approach may not model a specific data set as accurately as an empirical or statistical model that is derived from imagery, this modeling approach has a higher degree of flexibility by allowing the user to change the imaging conditions, scene conditions, etc.

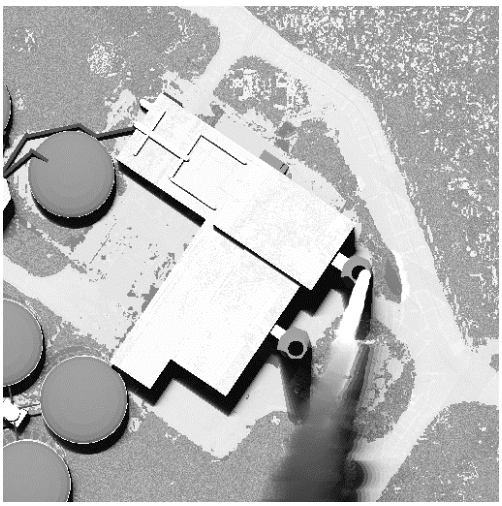
The general approach of mating high fidelity geometric models with high fidelity optical and thermodynamic models prevails throughout the DIRSIG model and carries over to the LIDAR model. Some empirically and statistically driven models appear in the lower levels of the overall model, but the higher level modeling capabilities are driven from the integration of a myriad of lower level representations. Historically, researchers have found this modeling architecture capable of reproducing specifically sought phenomenology as well as unexpected collateral phenomenology that might not be realized using other techniques (Ientilucci and Brown, 2003). The images in Figure 52 visually illustrate some of the spatial and spectral fidelity resulting from the modeling approach and the vast optical properties database used by the DIRSIG model. As stressed earlier, this modeling philosophy pervades the DIRSIG LIDAR model approach.



(a) DIRSIG RGB image of a portion of RIT's campus
also known as Microscene (Barcomb, 2004)



(b) RGB DIRSIG image of a urban residential scene



(c) MWIR DIRSIG image of CH_4 plume

Figure 52: Representative DIRSIG passive images

4.1.2 Active System Justification

Until 2002, the DIRSIG model was focused on simulating passive multi- and hyper-spectral sensing systems in the visible through thermal infrared regions. At that time, the ability to perform trade studies between passive and active laser systems required the use of separate modeling packages that used different geometric, optical, and thermodynamic descriptions. In addition, the available LIDAR scene simulation tools did not offer many of the key requirements considered necessary for in-depth trade studies and algorithm development. The LIDAR model must appropriately support rigorous atmospheric interactions, participating mediums, multiple bounce/scattering, thermal and reflective region passive returns, complex scene geometries, moving platform and scanning effects, detailed material optical descriptions (BRDF and scattering models), and arbitrary time-gated returns. The additional benefits of an integrated active LIDAR and passive multi- and hyper-spectral passive simulation environment that leverages a unified set of model inputs and underlying radiation propagation models were deemed significant. This type of simulation tool allows users to simulate active and passive sensors using the same scenes and scenarios. Thus researchers can evaluate alternative passive versus active approaches to specific problems and explore the potential benefit of data fusion between the two imaging paradigms.

Additionally, the rigorous and robust treatment of elastic LIDAR interactions would permit us to investigate issues such as the potential effects of scattering within a plume on DIAL concentration measurements and eventually research mitigation techniques using both active and passive data sets.

4.1.3 Prototype DIRSIG LIDAR Model

A prototype of this combined simulation environment was completed by Burton (2002). In general, Burton's challenge was to model the returned fluxes from the scene as a function of time with respect to the shooting of the source laser for topographic targets. The research objectives were to investigate potential development options and to implement a rudimentary elastic LIDAR model for topographic targets. The prototype model was limited, but did demonstrate the fundamental physics and the potential of an integrated LIDAR model within the DIRSIG architecture. Figure 53 shows the simulated time slices of the returned intensity from a single pulse fired at a T-72 tank on a flat plate using the prototype LIDAR model. The next two subsections describe the general modeling approach and limitations of the prototype LIDAR model. These limitations and a requirement for a more robust and rigorous model drove the design decisions for the improved and expanded DIRSIG LIDAR module presented and verified in this dissertation.

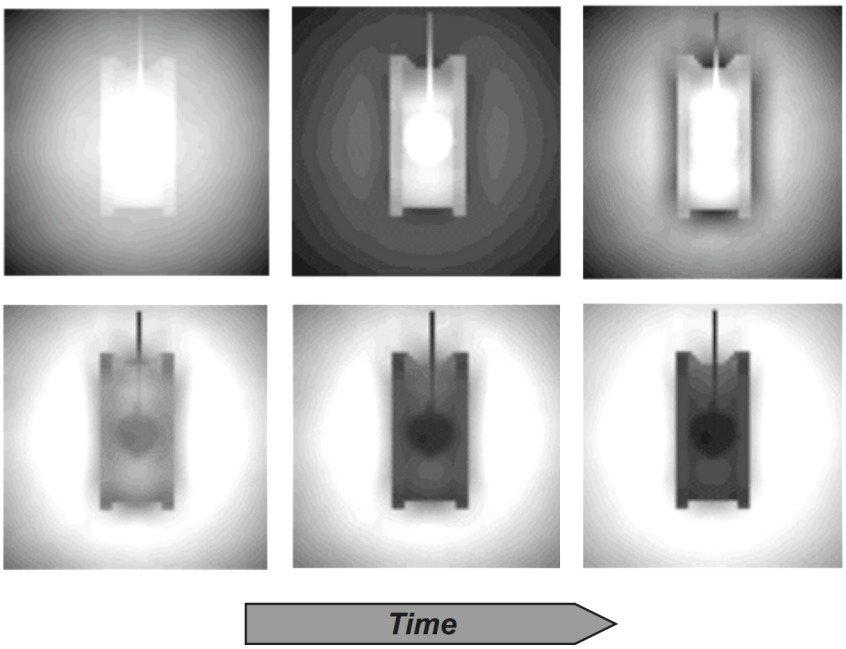


Figure 53: Prototype DIRSIG LIDAR module time slices for a T-72 tank (Burton, 2002)

4.1.3.1 Description

The core foundation of Burton's prototype LIDAR model is the standard, single scattering LIDAR equation presented in Chapter 3 previously and is included below for convenience. The detected return signal power from a single pulse is:

$$P(\lambda,R)=\xi(\lambda,R)\frac{A_r}{R^2}P_L(\lambda)\frac{c\tau_L}{2}\sigma_\beta(\lambda,R)\times\exp\left[-2\int_0^R\sigma_{ext}(\lambda,r)dr\right] \tag{278}$$

where $\xi(\lambda,R)$ is a system function determined by the geometric considerations of the receiver optics, the quantum efficiency of the detection system at each wavelength, and the overlap between the transmitted laser beam and the field of view of the receiver; A_r is the area of the entrance pupil; A_r/R^2 is the acceptance solid angle of the receiver optics with a collecting area A_r; $P_L(\lambda)$ is the average power in the transmitted pulse at wavelength λ; *c* is the speed of light; τ_L is the pulse width; ;$\sigma_\beta(\lambda,R)$ is the backscattering cross-section at wavelength λ and range *R*; and $\sigma_\beta(\lambda,R)$ is the extinction cross-section at wavelength λ and range *r*. The elastic LIDAR equation does not include multiple scattering effects, but at the

time, the scattering requirement had not yet been considered tractable. The most challenging aspect was the calculation of the geometric form factor at each range. The photon mapping concept of using two passes, a forward ray tracing followed by a reverse ray tracing using a recorded event data structure, afforded a practical approach to account for the geometrical form factor even in a complex scene. However, a full photon mapping implementation or even a true variant was not used, and thus, the full benefits of photon mapping were not realized.

Figure 54 is a simplified illustration of the modeling approach for the prototype model. The prototype LIDAR model first loads the scene and the LIDAR system characteristics. A set of parallel plane layers were then defined based upon the receive window and desired sampling. The primary purpose of these range planes was to accrue information to calculate the atmospheric backscatter and the geometric form factor for each range sample from the atmosphere. Effectively, these planes defined the range bins for the received signal and were assumed to be larger than the transmit pulse width. The 2D range planes were required to be perpendicular to the transmitter, the receiver, and the scene-wide xy-plane. Bi-static configurations were permitted, but only under the constraint that the FOVs were parallel. The prototype model did permit alternate geometries for the receiver; however, the temporal and radiometric characteristics of the results would not be accurate. Due to these restrictions, the transmitter and receiver were effectively required to be pointing nadir. Additionally, the platform and instrument motion necessary to model a scanning system were not supported.

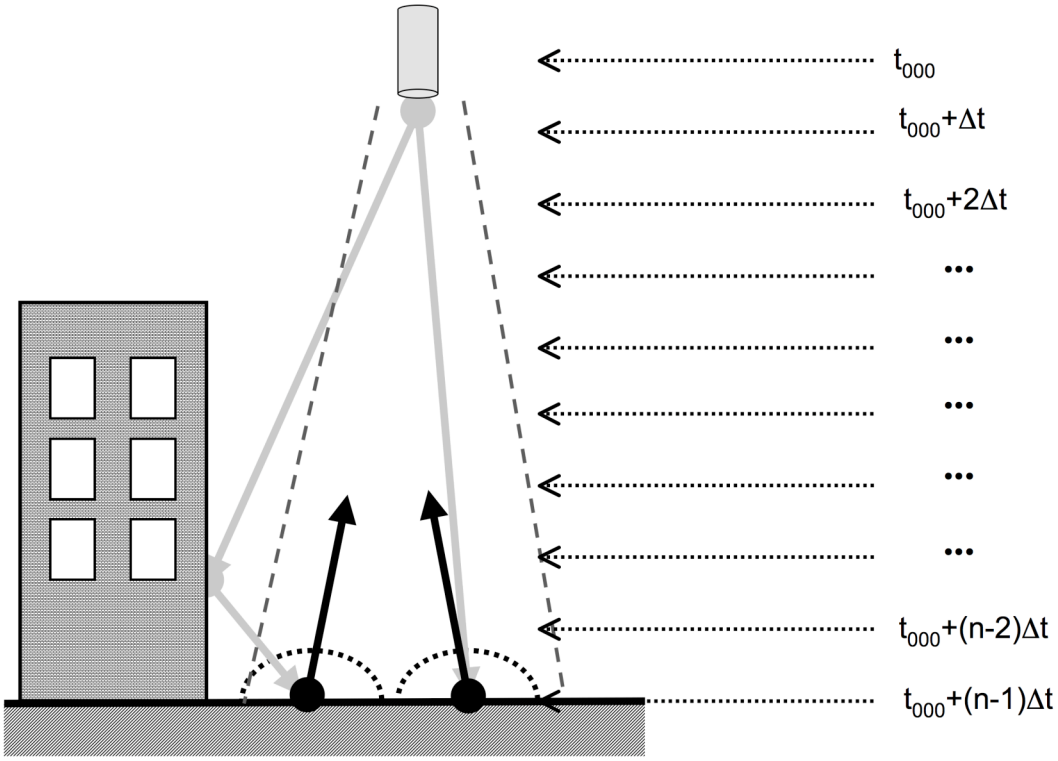


Figure 54: Illustration of the prototype DIRSIG LIDAR model approach in 2002

Once the range planes were setup, a set of randomly generated photon bundles were shot into the scene for each layer. The power from the laser pulse was divided equally into a preset number of photon bundles. For each photon bundle, the starting location and path vector were generated based upon a random Gaussian spatial distribution, the beam divergence, and the predicted effects of turbulence. The importance sampling algorithm that was used to generate the random transmit vectors was maintained and enhanced in the current DIRSIG LIDAR model. This approach easily permits modeling of alternative transmit spatial distributions and turbulence effects. The forward ray tracing vectors were cast into the scene until they hit the first range plane and the event was recorded. This would proceed until the predetermined number of photon bundles had been traced to the first range plane. Then the model would proceed to do the same procedure for each range plane. Unfortunately, this approach is very computationally inefficient.

For instance, if you had 100 range bins and wanted 50,000 photon bundles to be cast. The prototype would first cast 50,000 photon bundles until they intersected the first range bin. Then the model would proceed and shoot another 50,000 to the second range bin after removing the first range bin from consideration. This process would repeat until all of the parallel plane layers were complete. At each intersection for the layer under consideration, the localized peak power was calculated and recorded. The photon bundles were not randomly walked through the scene and did not deviate from the initial assigned vector. In addition, each bundle ended up with representing a different power. Thus, the implementation was not a true representation of the photon mapping paradigm and was not guaranteed to converge to the true photon distribution at those ranges.

For surfaces, random photon bundles were cast from the transmitter using the same importance sampling algorithm and traced until they hit a specific scene element. The localized incident power of the bundle was then recorded based a fixed atmospheric coefficient. If scene element is the first surface that the bundle hit, then the ray would be automatically reflected with a power due to the reflectance of a Lambertian surface. The BRDF function was not incorporated at this point, but such a modification could have been accommodated. If the photon bundle had already been reflected once, then it was automatically absorbed. In essence, the model only permitted one bounce (and actually forced bounces), but this could have been relaxed. Additionally, the entire process is not truly Monte Carlo based and is more parametric in nature. Thus the statistical accuracy of the approach does not guarantee radiometric accuracy for many situations.

To calculate the received power at the detector(s), rays from each detector element with a corresponding FOV were cast into the scene until they hit a surface. The localized power at the surface was then gathered based upon the events recorded at that surface. The time information of each of the recorded surface events was used to bin the power of each bundle into one of the range bins. The sampling was assumed to be coarser than the actual transmit pulse duration, thus the received power was merely added to the nearest range bin. The received power at the sensor from the intersected surface was calculated using the elastic LIDAR equation. Because of the use of forward and reverse ray tracing, the geometric form

factor was inherently already accounted for. The atmospheric backscatter term was calculated based upon the collected photon bundles within the FOV of the receiver for each pre-defined range plane. The atmospheric optical properties were hard-coded and could not be adjusted by the user. After adding the surface and atmospheric returns, fully developed speckle was incorporated statistically based upon user-defined inputs.

4.1.3.2 Prototype Limitations and the Path Forward

Before we proceed and discuss some of the important limitations of the prototype LIDAR model that were overcome by the new modeling approach presented in this dissertation, I must stress that the prototype played a very important role. The prototype model development established the viability of incorporating a LIDAR model into the DIRSIG framework and defined specific challenges that would need to be mastered. In addition, the concept behind photon mapping was introduced during the prototype development cycle. The power and flexibility of photon mapping was not really leveraged at the time. Eventually our understanding of photon mapping matured and now our arbitrary time-gated variant is the backbone of the current DIRSIG LIDAR model. The next few paragraphs walk through some of the challenges brought to light by the prototype LIDAR model development and briefly address the approach to solving those issues.

The first challenge was to convert to a true Monte Carlo modeling approach. The primary reason is to ensure that the approach accurately models the time-gated returns in the statistical sense. To accomplish the conversion, the surface processes and eventually the volume ray tracing were updated to utilize the local optical properties in a random, statistically appropriate manner. This would ensure that if enough bundles were cast into the scene, then the simulation results would be fairly accurate in an absolute sense. For surfaces, this would also permit an accurate representation of multiple bounce phenomenon for such scenarios as tree canopy or camouflage penetration. In addition, the prototype model assumed that the surfaces were Lambertian, and the material's BRDF function should be used if available. The roadmap forward also indicated that we would want the hooks in place to permit polarized BRDF functions and the capability to simulate polarmetric LIDAR

systems. To do so, the surface interactions needed to be dictated by Russian roulette techniques based upon some type of user-defined input.

Volume interactions, particularly scattering, were not supported in the prototype in any way. This included atmospheric returns from different atmospheres (mid-latitude summer versus sub-artic winter). Devising a means to access and randomly walk through volumes would be necessary to explore the returns from participating media, such as water or gaseous plumes. To support gaseous plume research, the DIRSIG LIDAR module should involve a rigorous treatment of scattering within a medium due to the considerable complexity involved. This had not been done before. The bulk optical property descriptions and ray tracing functions existed prior to the addition of the LIDAR capabilities, but their interfaces were enhanced for the new LIDAR model to facilitate efficient implementation of the photon mapping subsystem. Kuo (1997) researched simulating scattering in plumes, but the techniques were not deemed appropriate for modeling scattering for nonstationary LIDAR pulses traveling through a non-homogenous medium.

At least three major inter-related issues drove the dramatic re-architecture of the LIDAR modeling approach to a more faithful representation of photon mapping. The first was computational complexity and memory requirements. The original prototype was very memory intensive due to the 2D parallel-plane range arrays and took approximately 45 minutes per pulse to run. Simulating a nominal run with 1,000 pulses on a single dedicated Sun Blade 1000 workstation would have required about a month or so. This was deemed to be cumbersome and did not even factor in the computational cost growth with the added complexity of volume interactions.

The second issue was that the range gating was still fairly coarse in the prototype. Ideally, the model would handle an arbitrary sampled receive window that might have a very high sampling rate. To accommodate this requirement, the temporal distribution, as well as the spatial distribution, would need to be more carefully managed. The solution was to utilize the 3D kd-tree photon map structure. The kd-tree was augmented to keep track of the time that events occurred, but maintained the advantage of rapid sorting and retrieval of photon events

during the collection process. This approach also accommodates more complex geometry and removed the constraints upon the location or relative geometry between the transmitter and receiver. Because the precise location of the events are stored in the photon map, the time that photons are scattered or reflected back to the sensor can be more accurately constructed. Arbitrary time-gated returns are now possible.

The third issue is closely coupled with the Monte Carlo requirement. The prototype model predetermined how many photon bundles would be cast into the scene and then tracked the power for each bundle. Not only does this approach consume more memory than necessary, but the user is required to estimate how many photon bundles will be necessary to obtain the desired photon density throughout the scene. For topographic applications, this approach is fairly reasonable. The effective photon density is somewhat predictable and is well correlated to the number of photon bundles cast. The variability can be accounted for by casting slightly more photon bundles than deemed necessary to ensure performance. However, when a participating media is introduced, the photon density becomes less predictable and ideally should be treated differently than for surfaces. The photon event density within the plume determines the accuracy of the simulated return, but varies greatly depending upon the optical parameters of the volume and the geometry. To ensure that the plume is sufficiently sampled to estimate the flux, the process must be driven by the required photon density or number of events within the associated photon map. Thus, the LIDAR architecture had to be overhauled. As I stated earlier, this is less of an issue for simulating a topographical LIDAR, but it is non-trivial for more complex scenarios, such as a DIAL simulation when scattering is present.

4.2 DIRSIG LIDAR Module (New and Improved)

Although the emphasis in this dissertation is on modeling the multiple scattering and absorption for a LIDAR pulse within a gaseous plume, broader LIDAR modeling requirements were always under consideration and drove many of the implementation decisions. As stated previously in this chapter, the DIRSIG LIDAR module was designed to support rigorous atmospheric interactions, participating media, multiple bounce/scattering, thermal and reflective region passive returns, complex scene geometries, moving platform

and scanning effects, detailed material optical descriptions (BRDF and scattering models) and time-gated returns. This is a challenging set of requirements. Table 9 is an expanded list of the critical DIRSIG LIDAR modeling requirements set, the prototype capabilities, and the current development status. The foundation for some items such as fully developed speckle and turbulence were carried forward from the prototype model developed by Burton (2002). Others were inherited from the DIRSIG architecture, particularly the passive and thermal returns, the detector/sensor effects, complex scenes and properties, and moving platform and scanning effects. The latter capabilities did require varying degrees of integration effort, but significantly enhance the LIDAR module's capabilities. The remaining modeling requirements represent the focus of most of the research effort involved with this dissertation.

The most stressing requirement was certainly the multiple scattering effects and devising a methodology to verify, at least to a reasonable degree, the validity of the model's predictions. The next few subsections provide a broad overview of the current DIRSIG LIDAR model, the numerical approaches adopted, and some new innovations using the photon mapping paradigm. One should note that the requirements for inelastic interactions, polarametric returns, and partially developed speckle are not addressed in the model yet; however, the design enables the future integration of those capabilities into the model.

Before we begin the discussion of the modeling approach, let's take a look at a simple comparative example that demonstrates just how far the model has progressed over the last few years. Brown and Blevins (2005) published some initial results and a general description of the DIRSIG LIDAR model for topographic applications. The model has continued to progress so that it now handles volume scattering and absorption accurately. Figure 55 is a passive, monochromatic DIRSIG image of a T-72 tank on a flat plate. This setup is similar to the one shown for the prototype model in Figure 53. Figure 56 is a series of sample output slices from the current DIRSIG LIDAR model. The temporal sampling rate was set to achieve a range resolution less than 0.03 m (approximately 1.2 inches) whereas the nominal range resolution of the system was approximately 0.15 m. The sample intensity slices were extracted from the output LIDAR pulse cube and show the high degree of fidelity available. In particular, notice the multiple bounce photons in the bottom row, middle image. The

photons appear to have bounced off the turret, hit the body of the tank, and then returned to the sensor. We shall see later in the Chapter 5 that if the user supplies a model with sufficient spatial fidelity, even the few photons "lost" in the high grass may be observed. For now, let's proceed and discuss the modeling approach for the current DIRSIG LIDAR module.

Table 9: DIRSIG LIDAR modeling requirements and development status

Driving Requirement	Prototype Capability	New Capability	Verified	Future Capability
Complex Scenes & Properties	✓	✓	✓	
Monostatic & Bistatic	(limited)	✓	✓	
Topographic/Surface Returns	✓	✓	✓	
Aerosol Returns	(limited)	✓	✓	
Participating Medium Returns		✓	✓	
Rigorous Atmospheric Interactions		✓	✓	
Support BRDF and Scattering Models		✓	✓	
Elastic Interactions	✓	✓	✓	
Inelastic Interactions		(framework)		✓
Polarametric Returns		(framework)		✓
Thermal & Refective Passive Returns		✓	✓	
Fully Developed Speckle	✓	✓	✓	
Partially Developed Speckle		(framework)		✓
Atmospheric Turbulence Effects	✓	✓	✓	
Multiple Bounce Effects	(limited)	✓	✓	
Multiple Scattering Effects		✓	✓	
Arbitrary Signal Gating	(limited)	✓	✓	
Detector/Sensor Effects	(limited)	✓	✓	
Moving Platform & Scanning Effects		✓	✓	

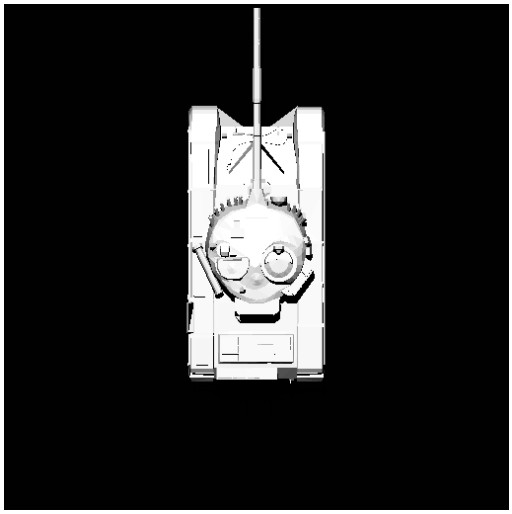


Figure 55: DIRSIG passive simulation of a T-72 tank on a flat plate (λ=768 nm)

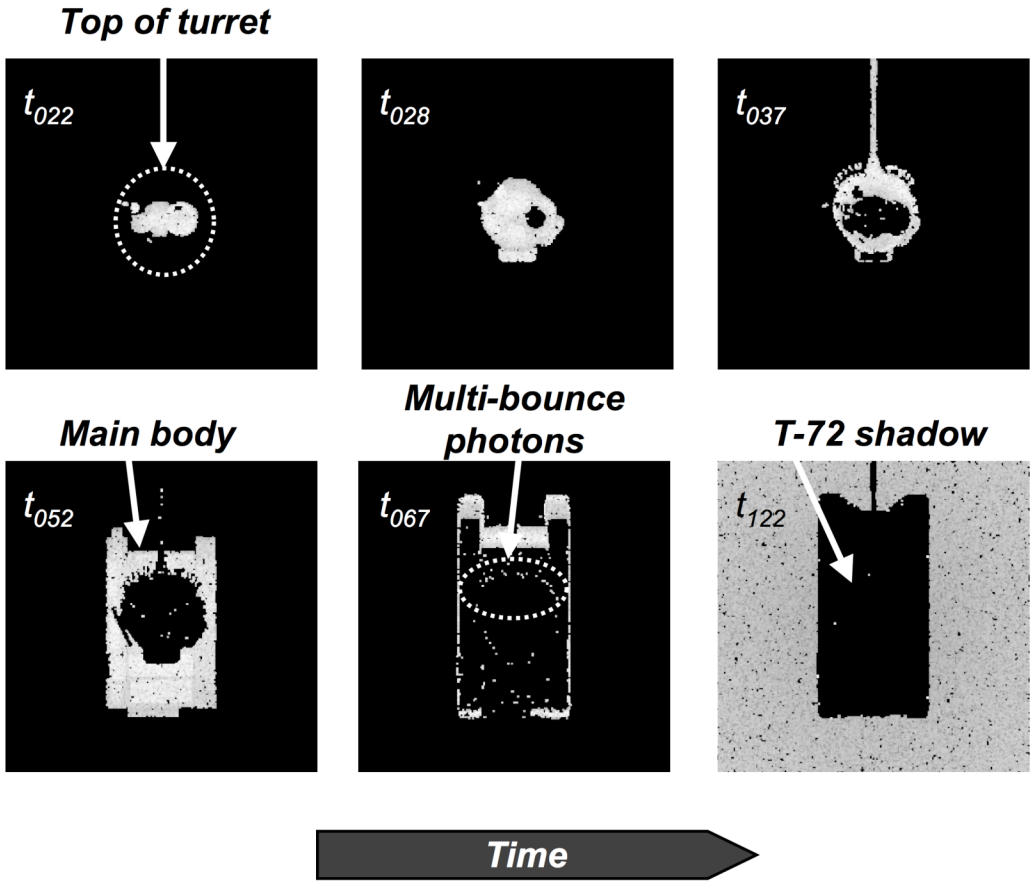


Figure 56: DIRSIG LIDAR module time slices for a T-72 tank on a flat plate

4.2.1 Numerical Modeling Approach

The addition of an active, laser radar capability to the DIRSIG model was accomplished by the addition of a suite of new objects to the existing radiometry framework. As indicated earlier, the specific challenges of this imaging model were largely driven by the requirement to predict the received photon counts as a function of space and time. The photon flux arriving at a LIDAR system often approaches discrete photon events due to the low amount of backscattered radiation and can prove difficult for many traditional Monte-Carlo ray tracing techniques. Additionally, the temporal structure of these returns is driven and highly correlated with the spatial structure of the scene and the total travel time of the arriving photons accrued during multiple bounce and scattering events within the scene. Analytical, statistical, and existing passive radiometry solvers were found insufficient in many instances, particularly for low flux situations.

The new approach that was identified leverages the modeling technique called photon mapping that was discussed in Chapter 3. One of the reasons that this technique was selected was because photon mapping has been demonstrated to be applicable to traditional solid geometry reflective illumination and scattering and absorption by participating mediums, particularly in multiple bounce and multiple scattering cases. For the purpose of LIDAR applications, some modifications to the basic photon mapping treatment were made, including the tracking of the total travel time and a literal photon counting process.

Once the core photon mapping architecture was put into place within the DIRSIG software architecture, we began to develop the augmentations that would be necessary to produce the temporal returns from laser pulse with a complex scene. The modifications to the photon mapping treatment were devised based upon close examination of the underlying physics of the light interactions with both volumetric and surface elements and the standard RTEs. In parallel, the development of the verification methodologies included exploring the multiple scattering LIDAR equation developed by Eloranta (1972, 1998) that was derived in Chapter 3. The basic construction and derivation of the multiple scattering LIDAR equation directly paralleled the current modeling approach for the DIRSIG model. The beauty of the realization was that the limiting constraints and assumptions that Eloranta was forced to

make so that the analytical solution was tractable could be lifted if the photon mapping paradigm was modified slightly.

As introduced in Chapter 3, the total power P_t observed as a function of range R from a LIDAR pulse fired into a semi-infinite, forward scattering medium is:

$$\begin{aligned} P_t(R) = P_1(R)\sum_{n=2}^{\infty}\Bigg\{ & \frac{p_{\pi m}(R)}{p(\pi,R)}\left\{1-\exp\left[-\frac{\rho_t^2}{\rho_l^2}\right]\right\}^{-1} \\ & \times\Bigg\{\frac{\tau^{n-1}}{(n-1)!}-\int_{r_c}^{R}\gamma(x_1)\sigma_{sca}(r_1)\int_{r_1}^{R}\gamma(r_2)\sigma_{sca}(r_2)\cdots\int_{r_{n-3}}^{0}\gamma(r_{n-2})\sigma_{sca}(r_{n-2})\int_{r_{n-2}}^{0}\gamma(r_{n-1})\sigma_{sca}(r_{n-1}) \\ & \times\Bigg\{1-\exp\left[-\frac{\rho_t^2R^2}{\rho_l^2R^2+(R-r_1)^2\Theta^2(r_1)+(R-r_2)^2\Theta^2(r_2)+\cdots+(R-r_{n-1})^2\Theta^2(r_{n-1})}\right]\Bigg\} \\ & dr_1\,dr_2\,dr_3\cdots\,dr_{n-1}\Bigg\}\Bigg\} \end{aligned} \tag{279}$$

where P_1 is the return power predicted by the elastic LIDAR equation, $p_{\pi m}(R)$ is the weighted average of the scattering phase function at range R, $p(\pi,R)$ is the scattering phase function at range R for a backscatter angle of π, ρ_t is the angular half-width of the receiver, ρ_l is the angular half-width of the transmit beam, τ is the optical depth, γ is the fraction of energy in the forward peak of the scattering phase function, and σ_{sca} is the scattering coefficient.

While this equation was derived only for a semi-infinite scattering medium, let's examine the general approach implicitly embedded in the formulation. First, the latter half of the complex integral represents the successive convolutions of photons from the laser with the front lobe of the scattering phase function. Effectively, this portion of the equation is calculating the temporal and spatial distribution of the flux (or photons) due to beam divergence and scattering. The expression in the middle line could be viewed as calculating the relative power at each of those locations weighted by the probability of scattering in that location. The spatial and temporal distribution of the photons are weighted by how much power they

each represent and how much of that power is scattered. The backscattered photon stream is then calculated by the weighted average of the backscatter lobe of the scattering phase function, $p_{\pi n}(R)/p(\pi,R)$. This provides us with the power from each location within the scene. Those powers are then integrated and propagated back through the receiver to the detector elements.

The more generalized LIDAR model that is presented in this dissertation parallels this basic approach. The photon mapping paradigm and the source model attempt to first generate a sufficient estimation of the temporal and spatial distribution of photons within the scene. The photon distribution is not just due to scattering and absorption, but also includes surface interactions including multiple bounces in complex scenes, such as forest canopies. This is done during the forward propagation or tracing stage of photon mapping. The photon map or maps generated represent the temporal and spatial distribution of photons. Each photon bundle within the map represents a specific portion of the power from the transmit pulse that reached that location within the scene. The fraction of the power that is scattered or reflected at each of these event locations is calculated using the local optical properties of the volume or surface element. Because the photon map records the event location and the incident angle, the actual BRDF or scattering phase function can then be applied to calculate the backscattered return for each event in the photon map. We are not limited to using the averaged backscattered component or to assuming Gaussian, forward scattering only. In fact, we can importance sample real-world BRDF or scattering phase function data if available in the DIRSIG optical properties library. Lastly, we can sum up all of those contributions, apply the appropriate optical transfer functions for the receiver, and sample the received signal according to the user-defined inputs. Traditional photon mapping utilizes density estimations that are carefully back-traced to sensor; however, this variant is more akin to a photon counting process and permits us to generate a high fidelity, time-gated return signal for very complex scenes, including scenes involving scattering media. Since the total travel time for each recorded event was added to the photon map data structure, the photon map represents the temporal distribution of flux in the form of the impulse response of the scene. If linearity is assumed, then the full temporal distribution can be obtained by convolving the back-propagated signal with the transmitted pulse waveform. The next few subsections dive into

more of the details of this modeling approach: source and sensor modeling, modified photon mapping approach, passive and thermal contributions, atmospheric backscatter modeling, instrument and platform modeling, and the generalized modeling process.

4.2.2 Source and Sensor Modeling

Implementation of the laser source and sensor models entailed the development of a new software source object and modifications to the built-in sensor objects. The first new object was a flexible source model that supports directional characteristics and the spatial, spectral, and temporal distribution of source photons. In the current implementation, the system is modeled in a monochromatic mode at the peak wavelength of the source. The temporal shape of the pulse is stored parametrically in each photon bundle rather than shooting photons as a function of time. If linearity is assumed, then this approach is reasonable. The pointing and spatial distribution of the source is numerically modeled based on either Gaussian or top-hat spatial distributions; however, the hooks were put into place to support importance sampling of other spatial distributions so that one could opt to model specific systems or modes more accurately. The transmitter coordinate system is nearly arbitrary and is defined relative to the scene and/or to the detector positioning and pointing geometries. This allows the user to model most co-axial and bi-static systems, including the platform and scanning motion.

A robust and flexible suite of sensor software objects was already available within DIRSIG and were directly incorporated into the DIRSIG LIDAR model. The available sensor model permits the user to specify very complex focal plane arrays or configurations of detectors in addition to a host of additional functions such as point spread functions, spectral responses, etc. The key DIRSIG input parameters for a LIDAR simulation, including the source and sensor characteristics, are illustrated in Figure 57. In future upgrades, the LIDAR model will likely expand to include spectral characteristics of the photon bundles and then the full spectral capabilities inherent in the sensor model will be become more crucial. For now, the source and sensor parameters shown in Figure 57 are adequate to generate synthetic LIDAR data sets for most elastic, incoherent LIDAR systems.

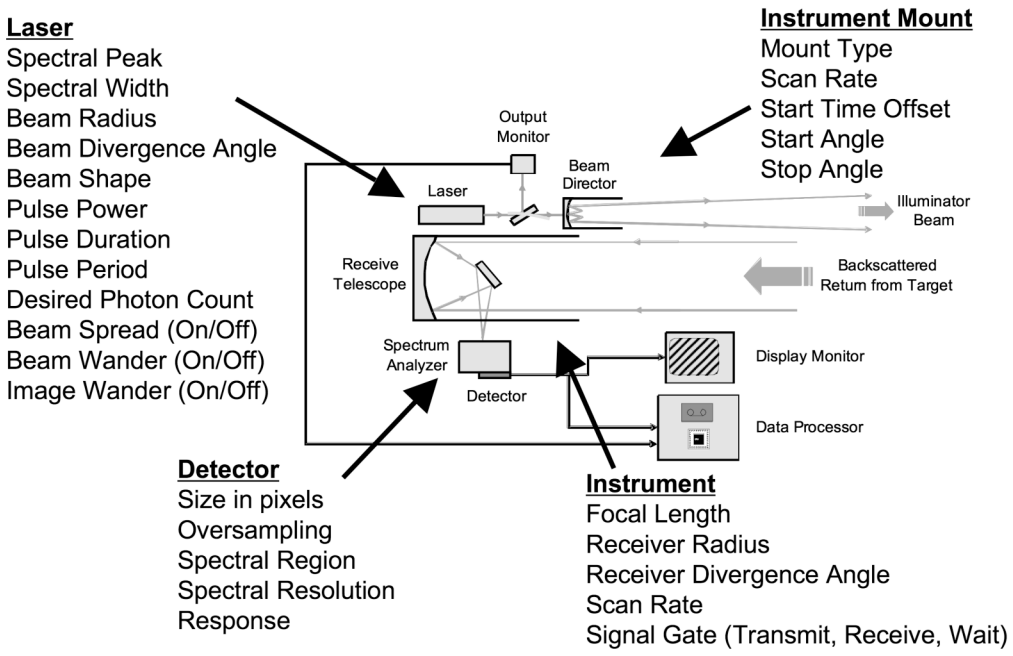


Figure 57: Key DIRSIG LIDAR source and sensor model inputs

4.2.3 Modified Photon Mapping

The photon mapping approach is the enabling paradigm for this modeling effort. As discussed in Chapter 3, photon mapping is a hybrid of traditional forward and backward Monte-Carlo ray tracing techniques. In this two-pass method, source photons are shot from a source into the scene using forward ray tracing during the first pass and then collected using a backward ray tracing during the second pass. The collection/rendering process utilizes the events recorded in during the first pass to calculate the sensor reaching radiance. The bulk of the modifications to the photon mapping approach for modeling a LIDAR system were to the collection/rendering phase; however, the total travel time tracking system was added to the forward propagation stage.

4.2.3.1 Forward Propagation – Tracing

During the first pass, a modeled photon is cast into the scene from the source and performs a pseudo-random walk through the scene based upon the local optical properties. The photon shooting function leverages the generic ray tracing support that already existed within the DIRSIG model. The ray tracer interacts with scene elements that have material specific

properties. Each material has a set of surface optical properties and an optional set of bulk or medium properties. The surface properties include a spectral reflectance and/or emissivity property. The currently supported BRDF models include importance-based sampling functions to support forward and backward Monte-Carlo ray tracing. The bulk properties include spectral extinction, absorption, and scattering coefficient models. When a volume scattering is modeled, a scattering phase function object is configured to describe the directional nature of the scattering. The scattering phase function objects also support importance-based sampling functions for the forward and backward Monte-Carlo ray tracing. Currently, the default convention for the scattering phase function is to use the Henyey-Greenstein model and the user-supplied asymmetry parameter of the specified material. However, software hooks were put into place to support importance-based sampling of arbitrarily complex scattering phase function data.

At the location of each interaction, information regarding the event is stored into a fast 3D data structure, referred to as a photon map. In some instances, a user may specify the use of multiple maps based upon material types. This is very useful for scenes involving elements requiring a high photon density, such as scattering media. The typical information stored is the location, incident direction, and event type. A critical addition for the LIDAR model was the total travel time. The time field accrues as the ray is traced throughout the scene; therefore, the additional time accrued due to multiple bounce/scattering events are accounted for and are used for time gating during the second pass. The modeled photon is then followed until it is absorbed somewhere in the scene or by the atmospheric boundary. This photon casting process is repeated until a specified number of interaction events have been recorded in the photon map(s) or until a user-defined maximum number of modeled photons have been cast. All of the transmitter spatial, spectral, and temporal characteristics are incorporated into the forward ray casting process to ensure the proper temporal and spatial distribution of photon events is generated.

From an absolute radiometry perspective, each modeled photon represents a “photon bundle” emitted from the source. Similar to traditional photon mapping, the variance of the estimated received photon stream is intimately linked to the number of photon bundles cast into the

scene. The number cast must be sufficient to obtain a statistically significant number of events throughout the FOV of the sensor. Depending upon the angular extent of the beam, the FOV of the sensor and the spatial detail of the scene, approximately 50,000 to 1,000,000 photon bundles must be utilized in the photon mapping process to create reliable statistics for topographic returns. For volume scattering returns, this number may need to be higher depending on the absorption and scattering coefficients and the spatial extent of the participating volumes. In some high scattering cases, I have utilized up to 2.5 million photon bundles.

The final result of the tracing phase is a spatial and temporal distribution representation of the photons throughout the scene in a readily accessible data structure. For demonstration purposes only, Figure 58 was generated to show a sample what a side-profile of a 3D photon map looks like for a scattering medium. A pulsed plane wave was shot through a very high, generally forward, scattering layer with a 100% absorbing plate as a backdrop. The high scattering coefficient was selected so that the scattering paths of the photons and the pseudo random-walk nature of the process could be easily shown. While the scattering is primarily in the forward direction, the spreading of the beam and the random walk of some stray photons due to multiple scattering is readily evident. This photon map would then be used in the second pass/phase to calculate the backscattered return form the scattering layer.

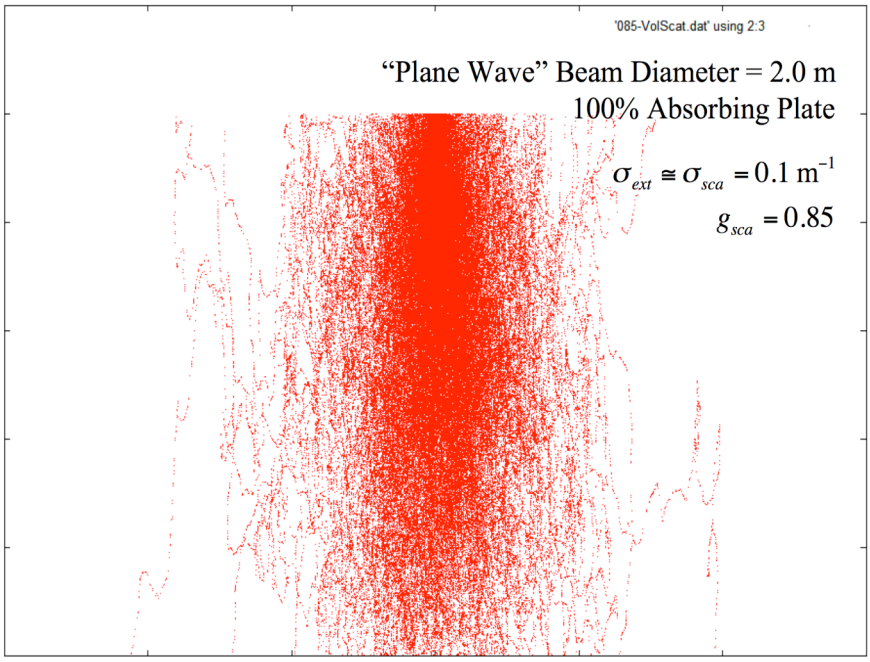


Figure 58: Sample volume scattering photon map profile

4.2.3.2 Backward Propagation – Rendering

The second pass or backward propagation/rendering phase is driven by a "capture method" object within the system that directs how the outputs for the detectors on how the focal plane are computed. The capture method calls a series of radiometry solvers including the passive, emissive, and LIDAR-specific modules. Each radiometry solver encapsulates an approach to predict the energy reflected, scattered, and emitted by a surface or volume. These solvers utilize the material specific and bulk optical properties to predict their results and propagate the energy back to the sensor. One or more of the radiometry solvers can be assigned to each element in the scene. To support the active LIDAR returns, a new radiometry solver was created to compute the returns from a scene surface or volume by using the optical properties and the photon map to estimate the number of incident photons at the element's point in space. Unlike the existing radiometry solvers that would place the final result in a time-independent result object, the LIDAR-specific radiometry solver places the result into a time-gated result object. The time gating process is governed by a user-defined signal gate consisting of a start, stop, and delta time.

Rays are cast from the image plane into the scene and the radiometry solver compiles a "hit list" with all of the interactions with scene elements. This hit list is then sorted and the appropriate radiometry solvers are run for each scene element (both passive and active). The LIDAR specific capture method then forward propagates the energy to the focal plane and then writes the arriving photon counts to the output file. The focal point of discussion for the rest of this subsection is the LIDAR radiometry solver that uses the recorded photon map from the tracing stage to determine the temporal signature returning from a particular scene element.

Figure 59 through Figure 63 illustrate the general process that the LIDAR capture method and radiometry solver cycles through for each individual detector element. The initial recorded photon map (see Figure 59) contains the temporal and spatial distribution information for the photon bundles. Each bundle within a specified photon map has the same power and each entry in 3D kd-tree data structure has a location, time-of-arrival, and incident angle. Figure 59 is a cartoon of a volume photon map that we shall use for demonstration purposes. The scene is a simple gaseous layer covering a reflecting plate. The photon events recorded on the surface are not shown for convenience.

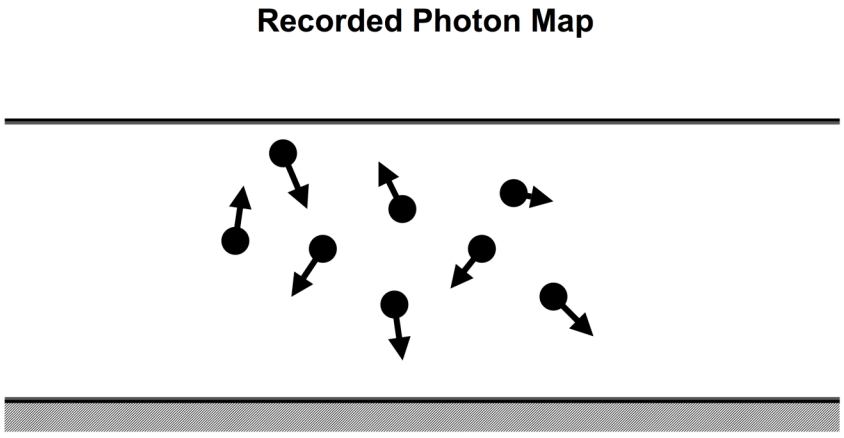


Figure 59: Initial recorded photon map after forward ray tracing

The capture method turns over a sorted hit list, the detector element vector, and detector element FOV. The LIDAR radiometry solver then projects the detector element FOV into the scene and filters the photon map to eliminate contributions from regions outside the FOV.

Figure 60 illustrates this process. The number of hits in the hit list is two for this situation, one for the surface and one for the volume element. The LIDAR radiometry solver will handle the solution for each of these elements slightly different. Traditional photon mapping would employ radiance estimation techniques based upon localized densities on the surface or with the volume element. However, to accommodate the temporal aspects of a LIDAR simulation, we elected to adopt more of a photon counting approach introduced in Chapter 3.

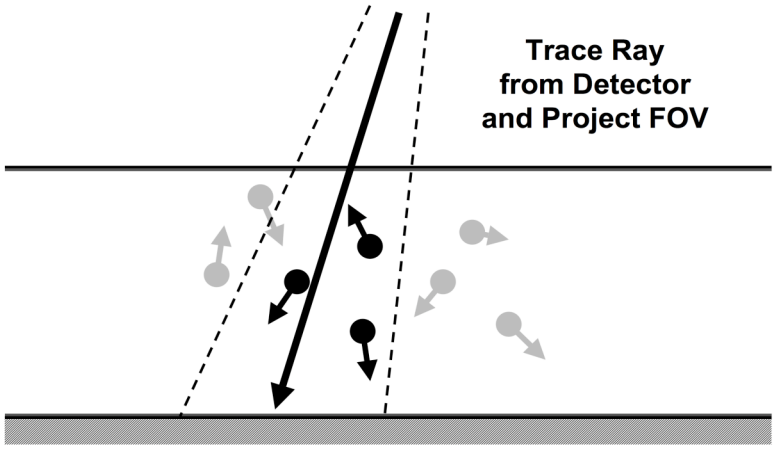


Figure 60: Collection Step 1 – Trace ray from detector and project FOV

For surfaces, the photon map is searched for all photon events that are within the detector's footprint. The local reflectance property and the BRDF for each event are applied to calculate the number of photons that are reflected back to the sensor in the direction of the detector element. A parallel process is shown in Figure 61 for a volume element. As shown in Figure 61, the LIDAR radiometry solver applies the probability of scattering and the scattering phase function to each and every volume event within the detector element FOV based upon the recorded incident angle. The result is that we now have an estimate of the number of photons at specific times within the detector element FOV.

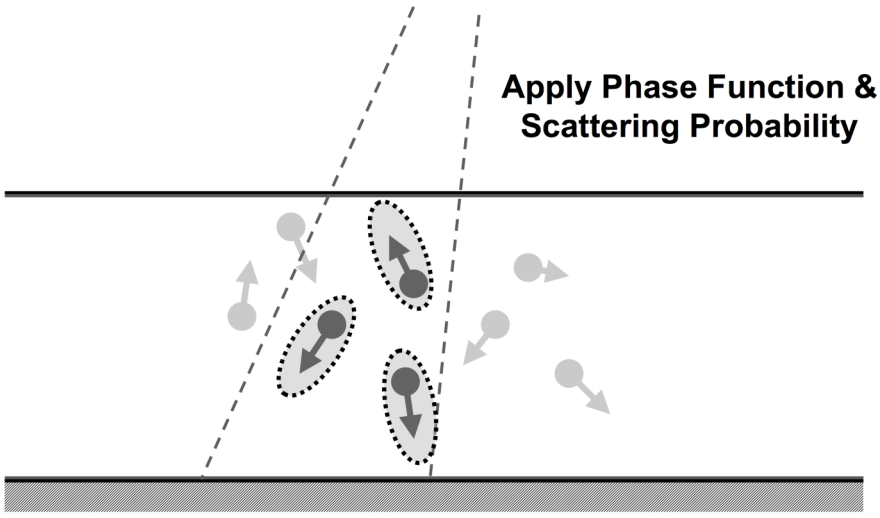


Figure 61: Collection Step 2 – Apply phase function and scattering probability

The final step is to forward propagate the energy back to the focal plane, convolve with the transmit pulse shape to temporally spread each photon bundle, range gate the received signal, and sample according to the user-defined inputs. This is illustrated in Figure 62. The convolution operation technically is applied to each individual photon event propagated back to the focal plane; however, if the process is assumed to be linear, the distinction is merely a matter of implementation. This process can be mathematically expressed as:

$$\Phi_{total} = \left[\Phi_{surface} e^{-\tau_0} GAUS\left[\frac{t - t_0}{\tau_d} \right] + \sum_{n \in \{\text{bundles in FOV}\}} \Phi_n \sigma_{sca} p(\theta_n) e^{-\tau_n} GAUS\left[\frac{t - t_n}{\tau_d} \right] \right] RECT\left[\frac{t - n_p T}{\tau_{rw}} \right] \quad (280)$$

where Φ_{total} is the temporal photon stream, $\Phi_{surface}$ is the photon stream from the surface, τ_0 is the optical path length from the surface to the focal plane, τ_d is the pulse duration, t_0 is the accrued time of arrival at the focal plane, σ_{sca} is the scattering coefficient, $p(\theta)$ is the scattering phase function of the nth photon in the map, τ_n is the accrued time of arrival at the focal plane for the nth photon in the volume photon map, τ_{rw} is the width of the receive window, n_p is the pulse number, and T is the pulse transmit period.

Figure 63 shows the return from a range-gated pulse that is sampled. The 2.5 nsec wide pulse was fired at a flat plate at 1200 m. It was range gated and then sampled 0.1 nsec spacing. The smooth curve is the analog signal and the stepped-response is the digitally sampled signal.

This is far more than would be required for simulating most LIDAR systems; however, it demonstrates the rigorous nature and flexibility of this modified modeling approach to support more detailed external detector models. Users may use external detector models to incorporate design specific detector characteristics, such as dark current, blooming, fill factor, probability of detection, etc.

The final responsibilities of the capture method are to run the appropriate passive, thermal, and atmospheric backscatter radiometry solvers and write the arriving photon counts and auxiliary data to the designated output file. The next few subsections will briefly address these three radiometry solvers and some of the assumptions that are made in the current model.

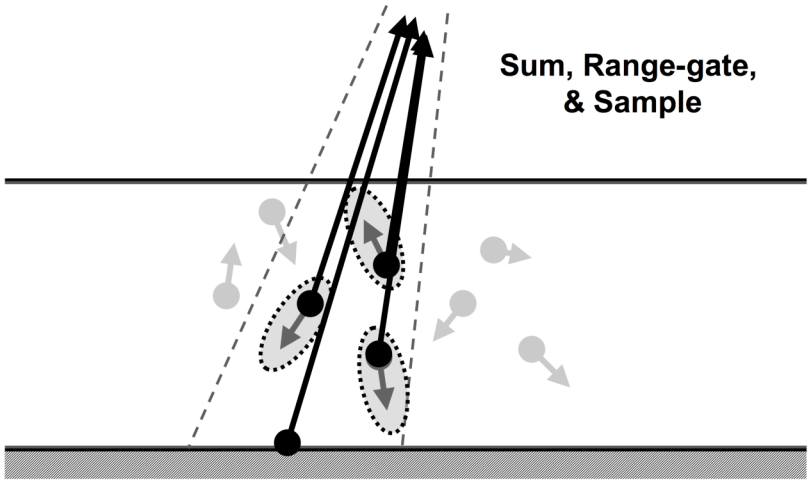


Figure 62: Collection Step 3 – Sum, range-gate, and sample photon stream

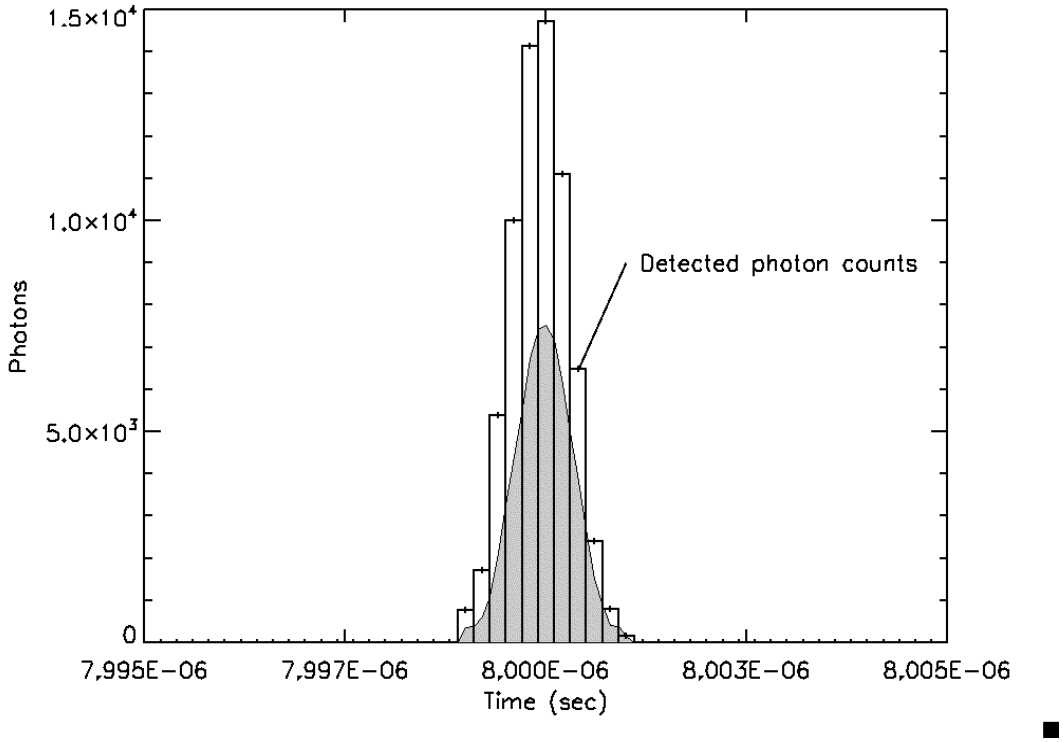


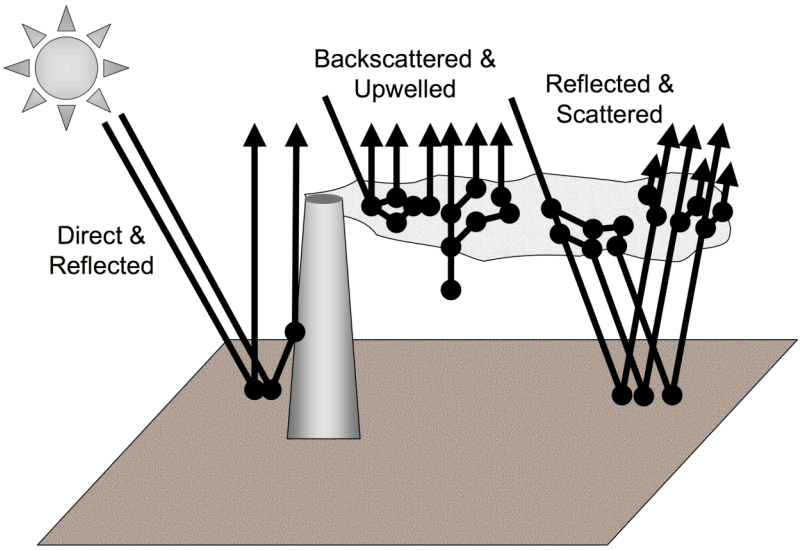
Figure 63: Range-gated and sampled backscattered pulse

4.2.4 Passive and Thermal Contributions

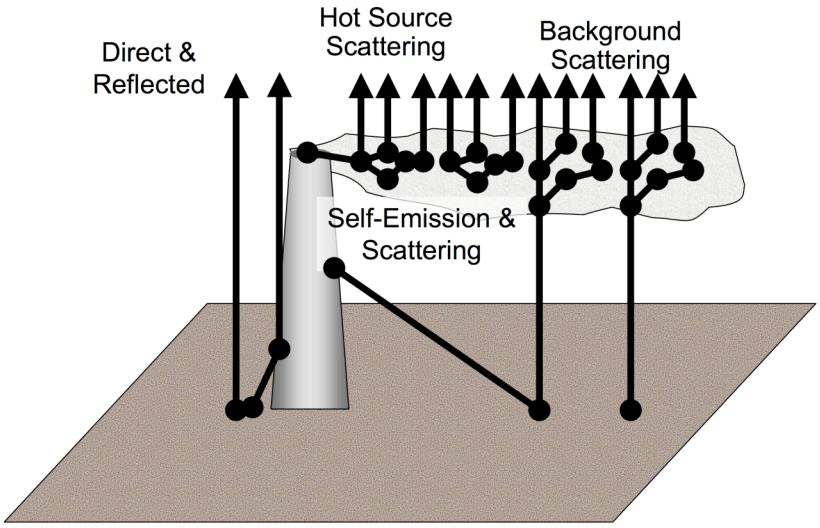
As indicated in the previous subsection, the capture method may also call a variety of different radiometry solvers based upon which ones are assigned to a specific scene element. One of the requirements for this modeling effort was to ensure that the passive and thermal components were adequately captured. Because the LIDAR model was built within the DIRSIG framework, the capture method has direct access to the radiometry solvers that are the backbone of the DIRSIG passive and thermal model. As mentioned earlier in this chapter, the passive portion of the DIRSIG module has been validated and provides an inherent capability to the LIDAR model that is often missing in many research LIDAR scene simulation tools. The passive radiometery solvers already existed in the DIRSIG framework and were updated to work in concert with the LIDAR-specific radiometry solver and capture method. The options with the various passive radiometry solvers to disable the thermal model or the texture maps were maintained for user convenience and flexibility.

Figure 64 illustrates the physical processes for the solar and emissive contributions in a typical scene with a plume. The primary components for the solar terms are the direct and reflected solar flux, the upwelled radiance, and the solar radiance that is reflected and scattered. As illustrated in Figure 65a, the DIRSIG radiometry solvers currently account for the majority of these terms, with the exception of the effects of volume scattering by the reflected or direct solar radiance. The emissive contributions in the LIDAR model (Figure 65b) are limited to primarily the direct and upwelled radiance. The scattering effects and the reflections off of scene elements for the self-emitted radiance are not directly addressed. The hot source scattering from the stack can be significant and could be added as another source object in the future. The baseline passive radiometry solvers do not readily handle the effects of multiple scattering; however, future research efforts may overcome this capability and the current passive radiometry solvers accurately predict the dominant contributions for a LIDAR return signal.

The total passive contribution is highly dependent upon the receive window and the sampling rate. They are assumed to be wide-sense-stationary with respect to the receive window and are linearly added to the LIDAR return signal. The additional received power is also greatly dependent upon the specified time, day, location, viewing geometry, and atmosphere. All of these aspects were already built into the passive side of the DIRSIG and were directly leveraged. Additionally, the user can turn off any of the radiometry solvers so that the solar and emissive terms are in effect zero. This option may limit the complications associated with interpreting the results of a particular case study where the solar and emissive terms are not as relevant. In contrast, the passive contributions are not trivial even when collecting at night. The thermal aspects will be discussed in Chapter 5; however, an example of the difference between the solar contributions at midnight versus noon on a spring collect in Rochester, NY is shown Figure 66. The simulation is setup so that a single pulse is fired at a flat Lambertian plate and the entire beam is collected by the receiver. The results are then plotted for different plate reflectances. The validity of these results will be discussed further in Chapter 5.

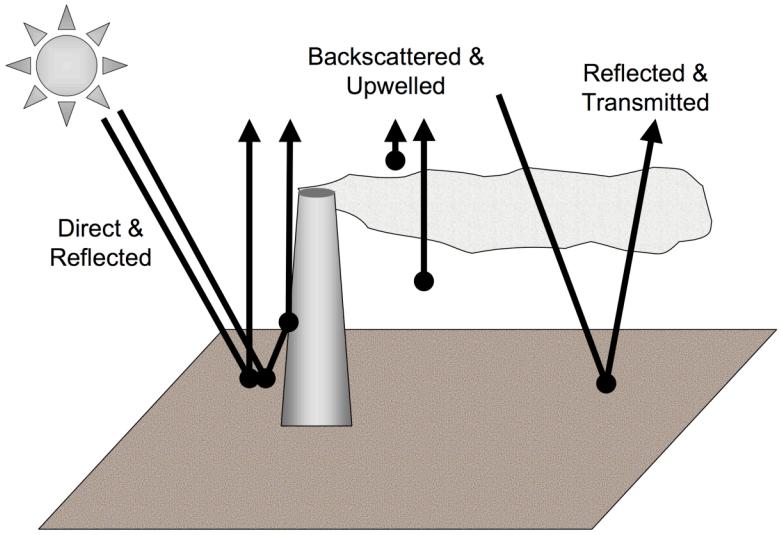


Solar contributions

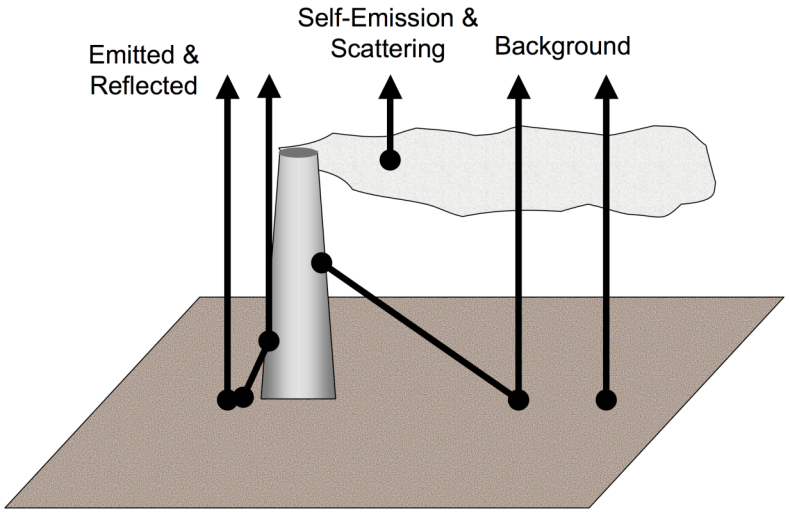


(b) Emissive contributions

Figure 64: General passive contributions for the LIDAR return signal



(a) Solar contributions



(b) Emissive contributions

Figure 65: Passive contributions to the LIDAR return signal modeled in DIRSIG

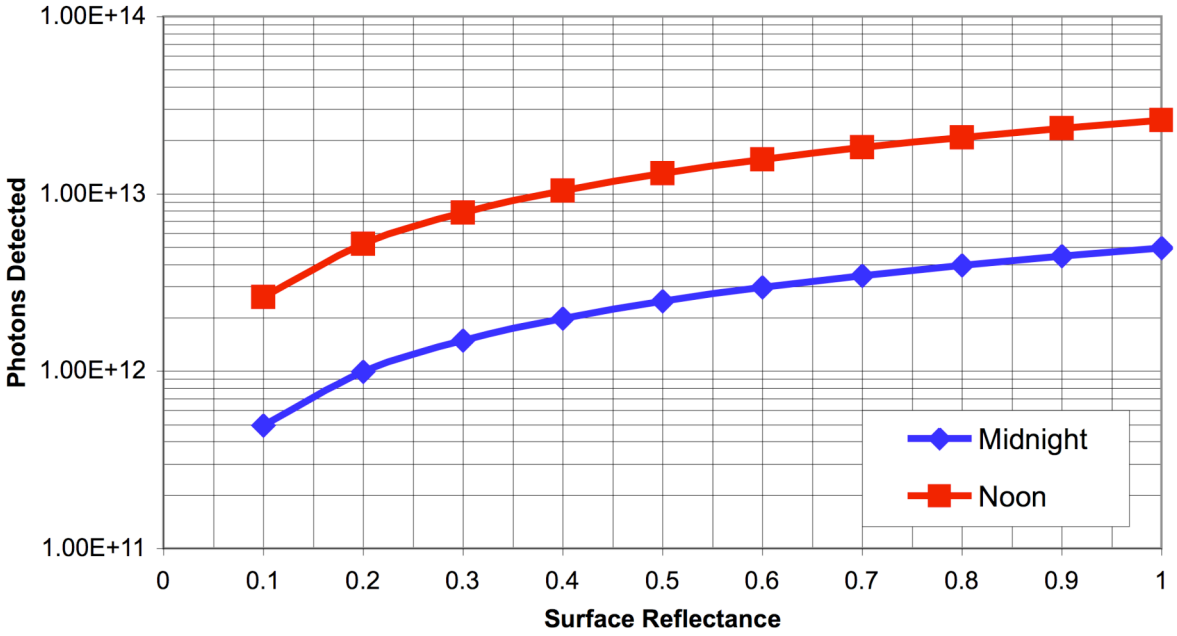


Figure 66: DIRSIG simulation of passive solar contribution for a pulse fired a Lambertian plate with different reflectances (mid-latitude summer atmosphere; Rochester, NY)

4.2.5 Backscattered Atmospheric Returns

In the current LIDAR model, the atmosphere is assumed to be spatially uniform as a function of position and altitude, which may not be accurate for some real-world applications. The horizontal and vertical structure of the atmosphere results in different absorption and scattering characteristics as a function of location. Ideally, robust atmospheric optical models like MODTRAN and FASCODE would drive both the extinction and scattering optical properties of the atmosphere. DIRSIG currently uses the extinction coefficients extracted from the existing MODTRAN and FASCODE derived tables. However, extraction of the vertically structured scattering coefficients and phase functions from MODTRAN (FASCODE does not support scattering) would require custom modifications to the MODTRAN code. As an alternative, the user can create their own scene elements with user-defined extinction and scattering properties to replace the atmosphere if this level of control is critical. Additionally, the user could then determine if photon mapping was used for a specific layer, such as a cloud or fog layer, or if the default atmospheric radiance solver was called.

Under most conditions, the extinction and backscatter coefficients of the atmosphere are extremely small, which means that the probability of absorption and scattering events within the atmosphere is very low. For example, the scattering coefficient for a dry atmosphere might be $1x10^{-5}$ m^{-1}, which means that you would need to shoot 10^5 photons into a 1-meter long box of atmosphere to witness one scattering event. Many systems are attempting to resolve vertical resolutions of a fraction of a meter and from an altitude of several thousand meters, which implies that you would need to model 10^{10} photons within each spatial detector element in order to get one scattering event within each numerical contribution element. To achieve robust statistics, this number would be ideally several orders larger.

To use the numerical approach utilized by the photon mapping technique, the number of photons that would need to be shot into the atmosphere to create a statistically accurate representation of the scattering events would be many orders of magnitude larger than the number of photons needed to model the topographic returns. To avoid the problems of predicting the atmospheric returns numerically, the atmospheric returns from the model are currently modeled analytically using the formulation proposed by Measures (1984):

$$P(\lambda_L,R) = P_L \frac{c\tau_L}{2}\frac{A_r}{R^2}\xi(\lambda_L)\xi(R)\beta(\lambda_L,R)\exp\left[-2\int_0^R \sigma_{ext}(\lambda_L,r)dr\right] \tag{281}$$

which was discussed in Chapter 3. For most of the LIDAR systems modeled to date, the atmospherically scattered photon returns amount to only a few photons accumulated over the entire path length, which is far below the detection level of the modeled systems; however, if these approaches are used to model a significantly longer path length or an optically thicker atmosphere (containing fog), then these numbers will grow to be large enough for consideration by the detection model.

4.2.6 Instrument and Platform

Most operational LIDAR systems, including DIAL systems, utilize some method of relative scanning to increase the spatial coverage of the system. The changes in viewing geometry during the scanning process and the location, orientation, and stability of the instrument

platform can affect the final data products, particularly for airborne systems. For example, the ability to resolve a specific object in a topographic data product derived from a dataset might be dependant on the angle from which it is illuminated. For a DIAL sensor, the measured concentration path length of a gaseous volume is also very dependent upon the relative geometry. The overall accuracy of a derived product might also depend upon the overall stability of the platform and knowledge of the platform's position. The DIRSIG framework has a flexible platform model that allows the platform to be positioned and oriented as a function of time. Furthermore, the instrument can be pointed with respect to the platform either statically or dynamically using one of the available instrument mount objects. For instance, these mount objects support temporal scanning using basic sinusoidal across-track scanning as a function of a user-defined scan rate. Another available option is for the user to provide a detailed platform position description file. The description file enables the user to define very complex platform and scanning geometries. The latter approach is very useful for defining custom collection scenarios, such as an extended-dwell, spotlight-imaging mode. The detailed information associated for each pulse is included in the DIRSIG LIDAR output pulse cube(s) and could be used to support pointing accuracy and knowledge sensitivity studies. This level of fidelity and sophistication already existed within the DIRSIG framework and was one of the inherent benefits of incorporating a robust LIDAR module into DIRSIG.

4.2.7 Generalized Modeling Process

With the basic components of the model now described, the overall modeling process can now be summarized. A modeling run consists of the user specifying the scene to be modeled, the instrument and instrument mount description, the source description, the platform positioning data, and a set of tasks that describe the time windows over which the data is to be generated. The data generation process begins by walking through each user-defined task according to a time step that is usually driven by the source pulse repetition rate. During each time step, the platform and instrument mount positions and orientations are computed for the current time, the source is fired and fills the photon map(s), the focal plane is captured which collects the photons and propagates them to the sensor, and the focal plane reaching photon

counts are written to the output file. This cycle repeats for each time in the task window and for each task in the list.

The final product of the DIRSIG tool is a 3D cube consisting of the photon counts as a function of two horizontal spatial dimensions and one temporal dimension (Figure 67). The LIDAR data cube is typically ingested by an external focal plane model to handle instrument specific detection schemes (e.g. linear mode versus Gieger mode), noise sources, etc. In these situations, the data cube should be generated with a significant amount of over sampling in the spatial and temporal dimensions to allow for spatial and temporal integration by the external sensor model. Further external processing of the resulting modeled raw instrument outputs can be used to create final data products, such as topographic maps, concentration path length maps, etc.

For the purposes of the DIAL case studies, the detector/sensor modeling process was simplified a great deal to avoid introducing sensor specific artifacts and over-complicating the process. For instance, neither noise nor pointing inaccuracies were introduced into the datasets and result in unique grid patterns in the topographic products. The processing algorithms used for both the topographic and DIAL simulations were fairly straightforward and did not use any advanced processing algorithms, such as co-coincidence processing; however, the output of the DIRSIG LIDAR module certainly does not prohibit such options for future investigations.

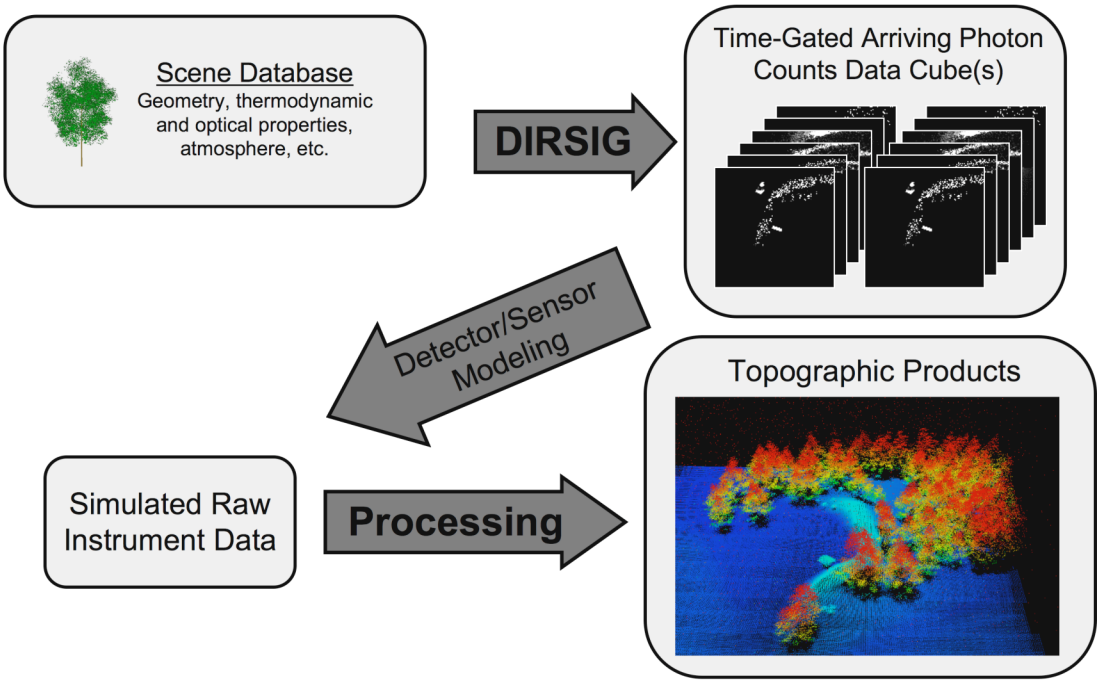


Figure 67: Conceptual end-to-end DIRSIG LIDAR simulation process flow

4.2.8 Practical Implementation Issues

With every modeling approach, some practical implementation concerns and issues must be considered. The DIRSIG LIDAR model is no different. Two of the most important considerations that drive the accuracy of the simulated datasets are establishing the desirable photon map density and calculating the optical parameters of the participating media or scene objects. The next few subsections briefly present the selected approach for these two critical factors and discuss some general guidelines when setting up LIDAR simulations in DIRSIG.

4.2.8.1 Multiple Photon Maps and Required Photon Density

Traditional photon mapping implementations typically use two photon maps when dealing with volumes or participating media, a global and a volume map. Each map uses slightly different estimation techniques and often has different sample density requirements due to the nature of the scene elements. Complex pheonmena, such as multiple bounces or multiple scattering, require very large numbers of photon bundles to ensure adequate statistical sampling. Simpler scenarios, such as a direct bounce or double bounces, require fewer Monte

Carlo traces and thus require less memory or computational time. Recording the photon events into multiple different maps affords the flexibility of increasing the sample density for complex portions of the scene while not adding unnecessary computations or memory allocations for the rest of the scene. Traditional photon mapping rarely uses more than two photon maps due to the increased complexity during the rendering phase; however, the computational and memory reduction due to multiple maps for the temporal return from a LIDAR pulse is very beneficial because the required photon density may vary significantly across the scene. Thus, the DIRSIG LIDAR model was built with the capability to specify and assign a large number of photon maps. Theoretically, every material in the scene could have a separate photon map. This would not be an efficient use of resources or memory; however, the flexibility was added to provide the user with more influence over the resulting photon density within a scene.

As with traditional photon mapping, the estimation techniques within the DIRSIG LIDAR radiance solvers vary for volume versus surface elements. Thus, breaking the photon distribution approximation into two or more maps often avoids confusion and potential simulation artifacts. This feature also allows the user to drive the model to obtain a higher density of photon bundles in critical locations (such as in a gaseous plume) so that the variance of the estimate is greatly reduced. For instance, one might only need 50,000 photon bundles in the surface map, but a good estimate of the return signal from the plume may require 500,000 events due to the large amount of scattering. A similar case can be made for topographic LIDAR simulations of tree canopy penetration. The structure allows the user to specify the desired number of photon events to be recorded in each map. As a safety valve, the user also must specify the maximum number of photons to cast into the scene to avoid trying to fill a photon map that will never be filled (i.e., shooting at a plume that isn't in the transmit beam for this pulse). The cost of this flexibility is complexity within the code. The radiometry solvers must be given the appropriate weighting of each photon bundle to ensure that the numerical estimates remain consistent.

4.2.8.2 Optical Parameter Generation Methodology

The modeling described throughout this chapter demands that accurate physical and optical properties of the plumes or gaseous layers be generated or provided. Figure 68 illustrates the conceptual flow diagram for generating one of these properties, the scattering phase function. The scattering phase function is probably the most involved optical property required and is shown here as an exemplar of the overall approach. Portions of this diagram are not yet fully in place and the majority of the diagram is not automated and requires significant user interaction. One of the future upgrades of the DIRSIG LIDAR model may involve creating a more fluid and automated process; however, the general process and philosophy illustrated in Figure 68 was a driving factor for the front-end design of the LIDAR model.

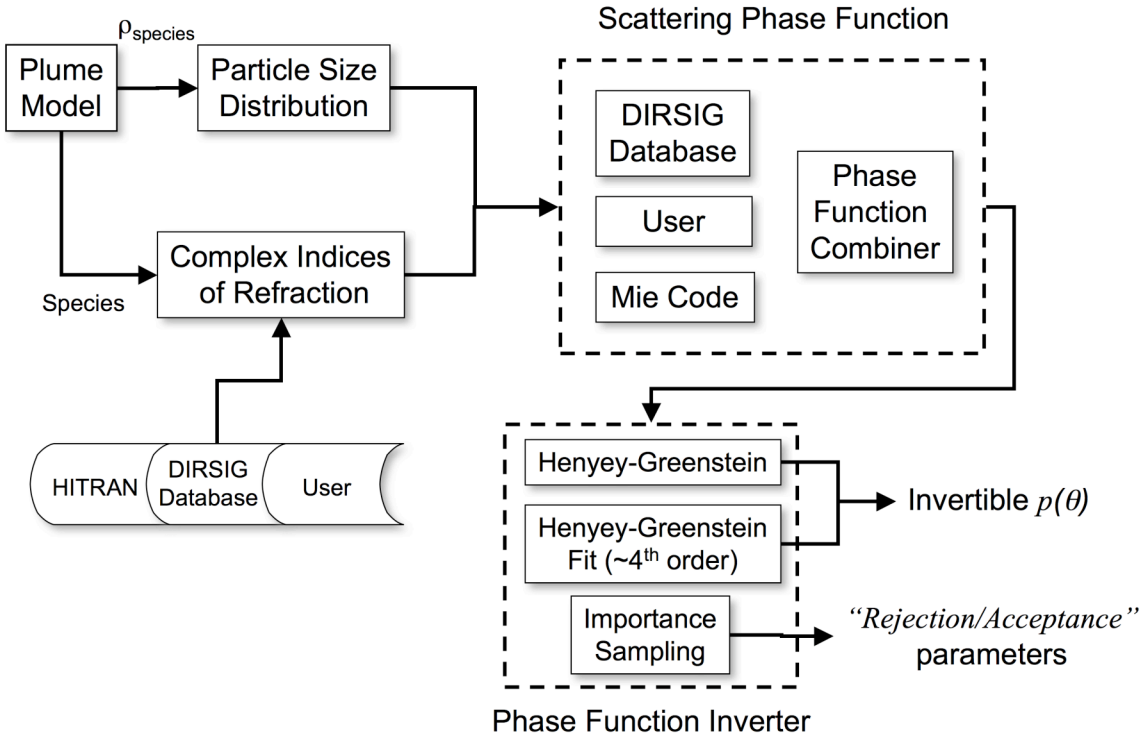


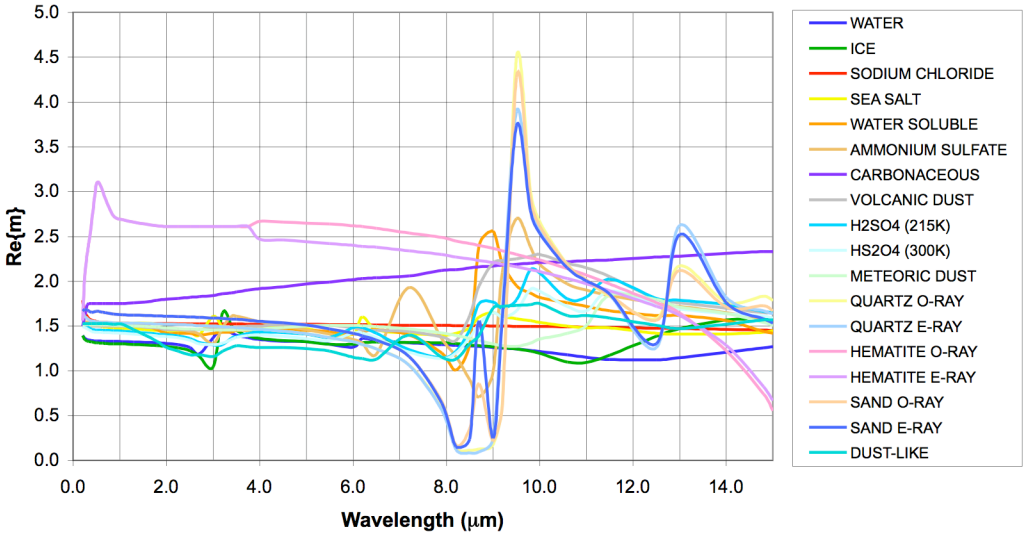
Figure 68: Scattering phase function generation methodology

In this subsection, the process for generating the scattering phase functions used in this research effort and a few of the basic assumptions are discussed. The first piece of information necessary is fairly rudimentary, the species involved. Ideally, we would be interacting with a voxelized plume model so that the inhomogenous optical properties can be

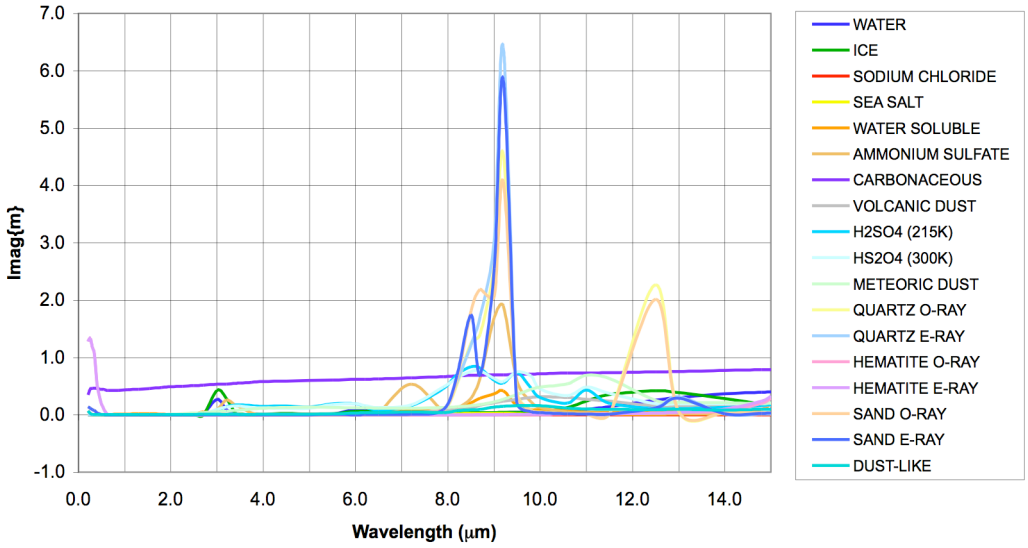
more easily encapsulated for the DIRSIG radiometry solvers. The user either supplies a set of complex indices of refraction for the wavelengths under consideration or the information is pulled from a locally stored database. The plume model or the user also determines the particle size distribution. This may be a localized particle size distribution in the case of a voxelized plume model. The scattering phase function and other associated optical properties are then generated using the MIEDU code discussed in Chapter 3. Alternatively, the DIRSIG input parsers allow a user to input a predefined set of optical properties. Currently, the latter approach is the default mode of operations. If multiple species are present, then some form of linear combiner is used in conjunction with the concentration of each species to generate the actual optical properties, which is the scattering phase function in this case.

Mie codes produce very detailed numerical descriptions of the scattering phase function; however, the functions are not readily reversible which causes some difficulty in the photon mapping paradigm. One option is to use importance sampling to replicate the stochastic behavior of the actual scattering phase function, but the computational time proved to be cost-prohibitive. Therefore, a more reasonable approach was adopted. The Henyey-Greenstein function was used to approximate the actual scattering phase function. The necessary input parameter is the asymmetry parameter which is readily available from the Mie calculations. The Henyey-Greenstein function is reversible and works well for highly forward scattering or nearly isotropic scatterer, but could be a crude approximation for complex scattering phase functions. For many aerosols and plume constituents, the Henyey-Greenstein approximation should be adequate. However, this is not necessarily true for every scattering phase function. This is where caution and discernment must be applied. One should carefully evaluate the degree to which the reversible approximation accurately represents the actual scattering phase function. In the future, one may consider using a higher order combination of Henyey-Greenstein functions to more accurately estimate the scattering phase function, but that was not done for this research effort. The modifications to the DIRSIG model necessary to support higher order Henyey-Greenstein functions are relatively straightforward and could be added as a future enhancement.

As noted previously in this subsection, the critical physical input parameters for a particular species are the particle size distribution and the complex indices of refraction. The complex indices of refraction are typically well known for many constituents of interest, such as atmospheric aerosols. For example, some of the complex indices of refraction for aerosols modeled in MODTRAN for common atmospheric remote sensing applications are plotted in Figure 69. The atmospheric aerosols range from very specific constituents, such as H_2SO_4, to broader categories, such as dust-like aerosols, over the wavelength region of 0.1 μm to 15.0 μm. Unfortunately, the particle size distribution is often more difficult to ascertain for many real-world applications. Table 10 lists the particle size distributions assumed for common plume scatterers, such as soot, fly ash, and water vapor. The distributions do not fully describe the anticipated particle size distribution for a real-world plume, but they are sufficient for the purposes of verification of the model, demonstrating how one might generate the optical characteristics of a participating scene element, and exploring the impacts of scatterers on DIAL measurements.



(a) Real part



(b) Imaginary part

Figure 69: Typical atmospheric complex indices of refraction (MODTRAN database)

Table 10: Particle size distribution description for typical plume constituents

Species	Particle Size Distribution Type	Distribution Parameters
Water Vapor	Gamma	$a_{eff} = 6.0$ $a_0 = 4.0$
Fly Ash	Gamma	$a_{eff} = 6.7$ $a_0 = 10.8$
Fine Soot	Lognormal	$a_m = 0.5$ $\sigma = 1.09527$

Many databases exist for the complex indices of water. The dataset chosen for this effort was the Segelstein dataset published in 1981. Both the real and imaginary components of the indices of refraction are shown in Figure 70 from 0.1 μm to 3.0 μm. The water vapor particle size distribution was based upon the industry standard C1 cloud model, which is gamma distribution and is shown in Figure 71. To simulate a more realistic plume scene, the particle size distribution would likely need to be modified, but the C1 cloud model distribution was deemed adequate for a starting point and to demonstrate DIRSIG's capabilities to model multiple scattering in a plume. The optical parameters of water vapor plotted versus wavelength in Figure 72 and Figure 73 were then generated using the process described in this subsection and the MIEDU code. The water vapor optical properties could then linearly combined with any other constituent based upon the relative and overall concentration. Note that the asymmetry parameter indicates that water vapor is generally forward scattering and could be broadly characterized as having g_{sca}=0.85. For this reason, many of the pulse scattering simulations will involve participating mediums where g_{sca}=0.85.

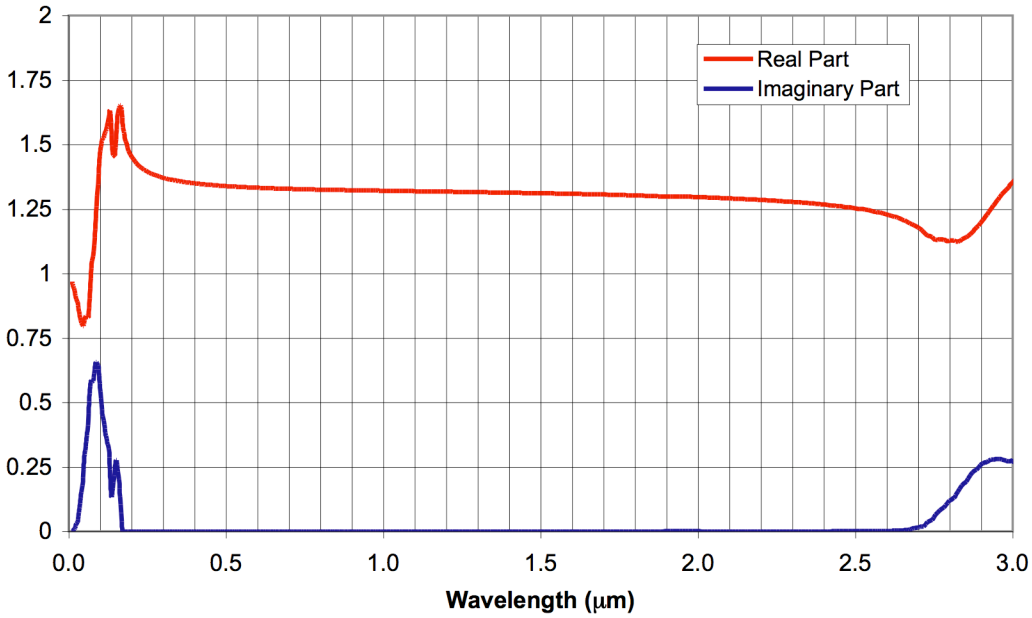
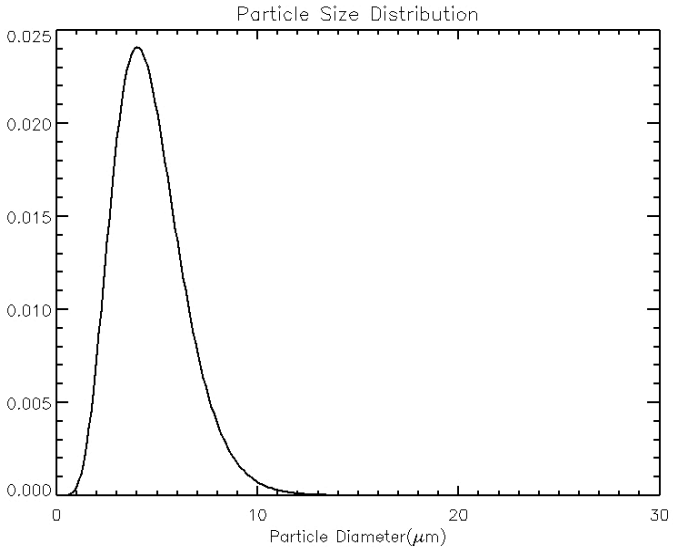


Figure 70: C1 water cloud complex indices of refraction (Segelstein, 1981)



■

Figure 71: Sample particle size distribution for C1 cloud water vapor (gamma[a_{eff}=6.0;a_0=4.0])

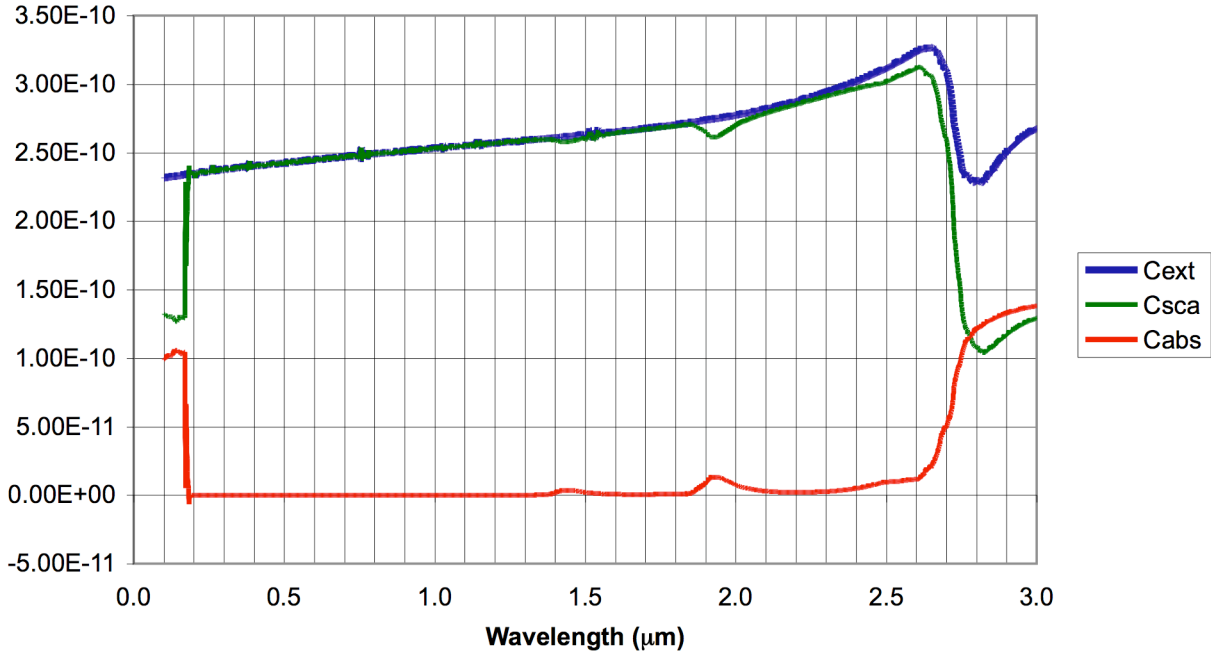


Figure 72: C1 water cloud extinction, scattering, and absorption cross-sections

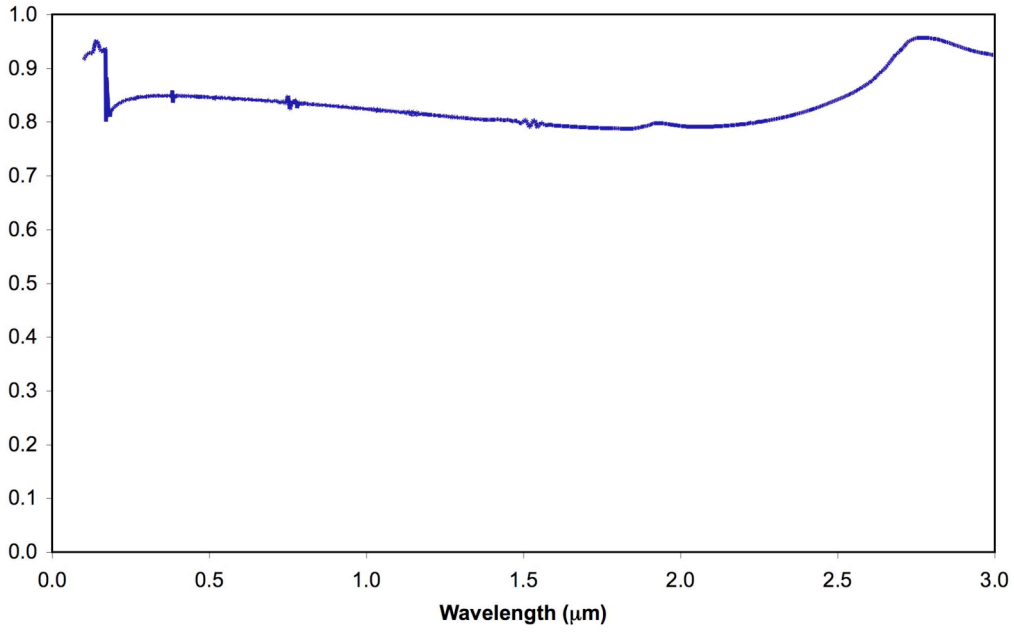


Figure 73: C1 water cloud asymmetry parameter

As with the broader categories of atmospheric aerosols in the MODTRAN database, soot and fly ash are more difficult to define with respect to material makeup and particle size distribution. The primary reason is that the term soot encompasses a wide range of constituents with very different core elements and species. Both the particle size distribution and the complex indices of refraction vary depending upon the process and materials by which the soot is generated and injected into the plume. Figure 74 shows the real and imaginary components for two different kinds of soot as described by Chang (1990) and Kokhanovsky (2001). In particular, the indices are for fine soot particles with a distribution similar to the one described in Table 10 and plotted in Figure 75. The particles are fairly small with a mean around 0.5 μm. The corresponding optical parameters using Kokhanovsky's and Chang's indices of refraction are plotted in Figure 77 and Figure 76 respectively. Although the particle size distribution is the same for each case, the optical cross-sections for Chang's fine soot particles are approximately half the size of Kokhanovsky's and the scattering phase function generally is more in forward-scattering than Kokhanovsky's.

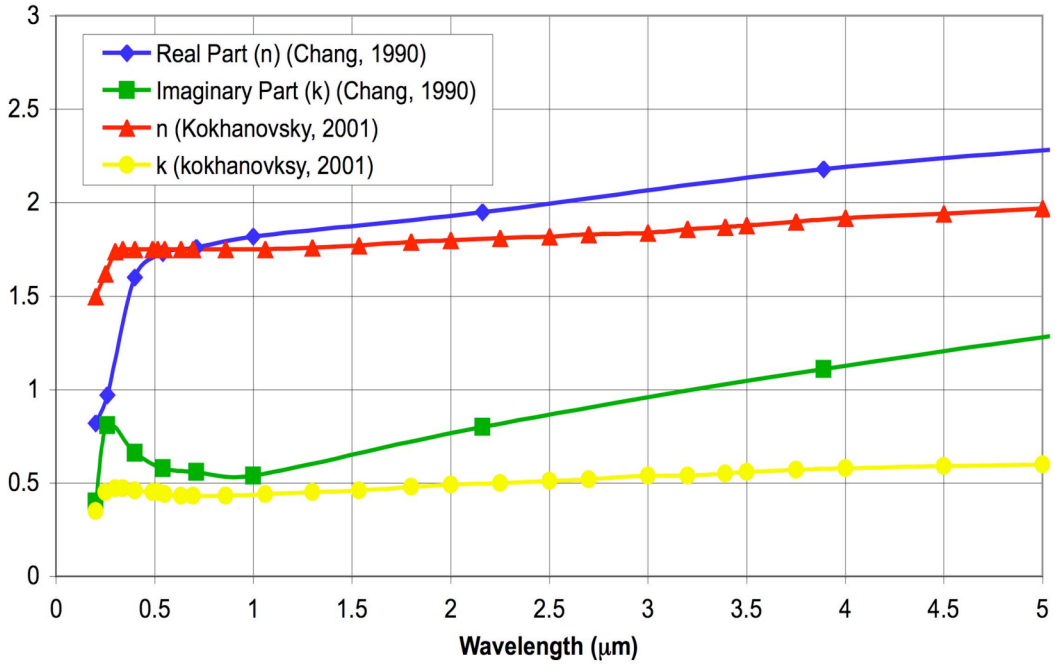


Figure 74: Complex indices of refraction for soot
(Chang, 1990 and Kokhanovsky, 2001)

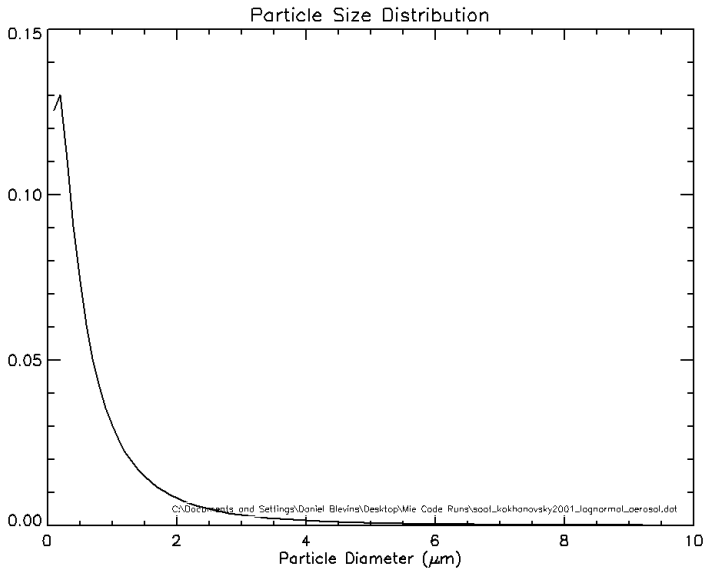
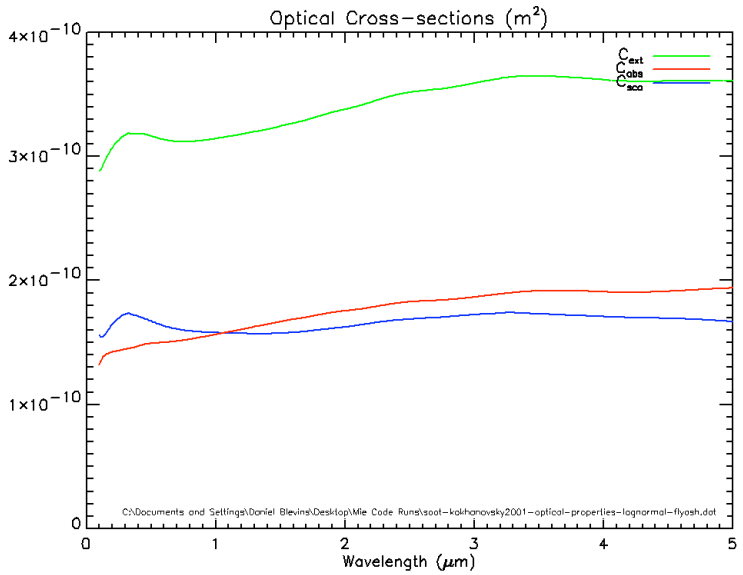
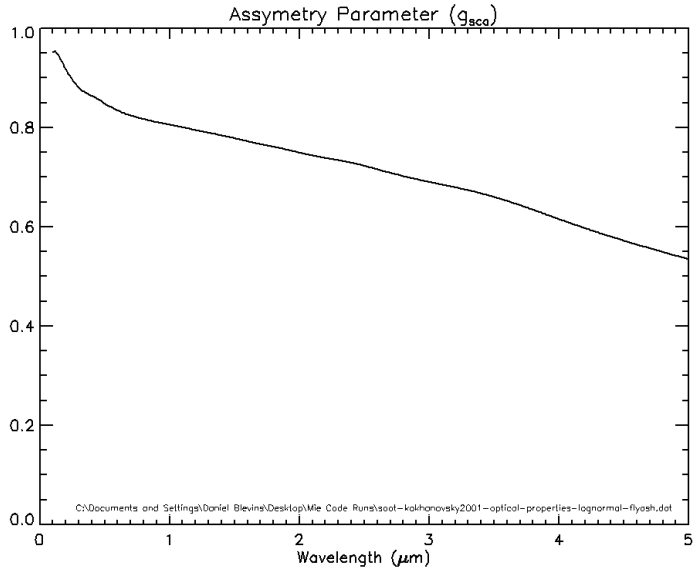


Figure 75: Soot aerosol particle size distribution (lognormal[a_m=0.5;σ=1.09527])

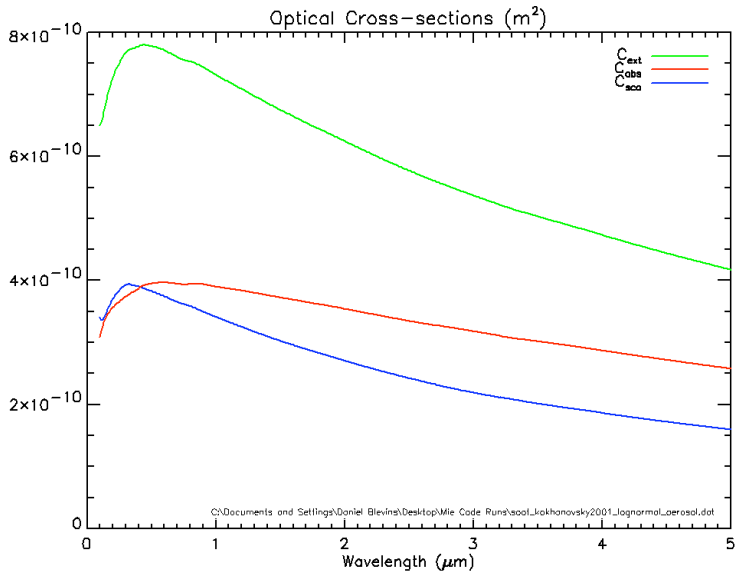


(a) Optical cross-sections

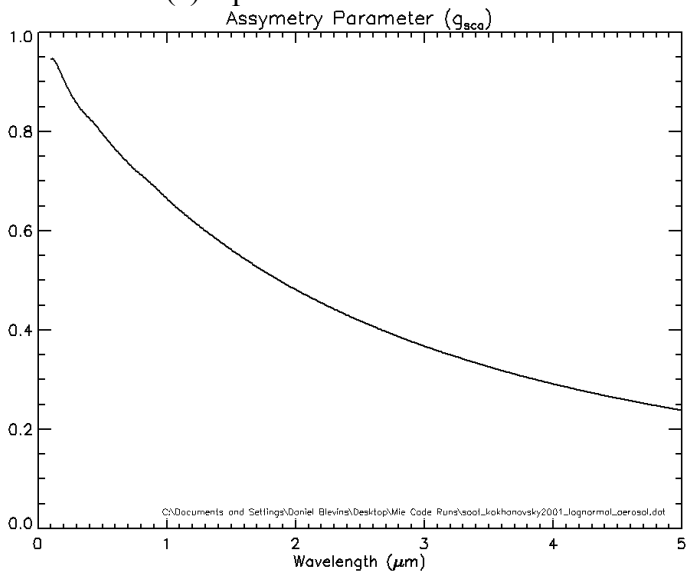


(b) Assymetry parameter

Figure 76: Optical properties for soot using Chang's indices of refraction



(a) Optical cross-sections



(b) Asymmetry parameter

Figure 77: Optical properties for soot aerosol using Kokhanvosky's indices of refraction

A typical factory stack plume is not solely comprised of molecular constituents, some water vapor, and few fine soot particles. In particular, the particle size distribution for the soot-like particles is often bi-modal with fine soot particles and something like fly ash involving larger particles. The fly ash distribution in Table 10 and plotted in Figure 78 are based upon the fly ash particle size distribution measured by WHO??? (WHEN). Since the specific complex indices of refraction were not available, Chang's indices for fine soot particles were used for the optical parameter generation process. The results from MIEDU are shown in Figure 79.

The optical cross-sections for our fly ash are very similar to the fine soot particles based upon Chang's indices of refraction; however, the asymmetry parameter is much closer to 0.9 and thus more forward scattering than our fine soot particles.

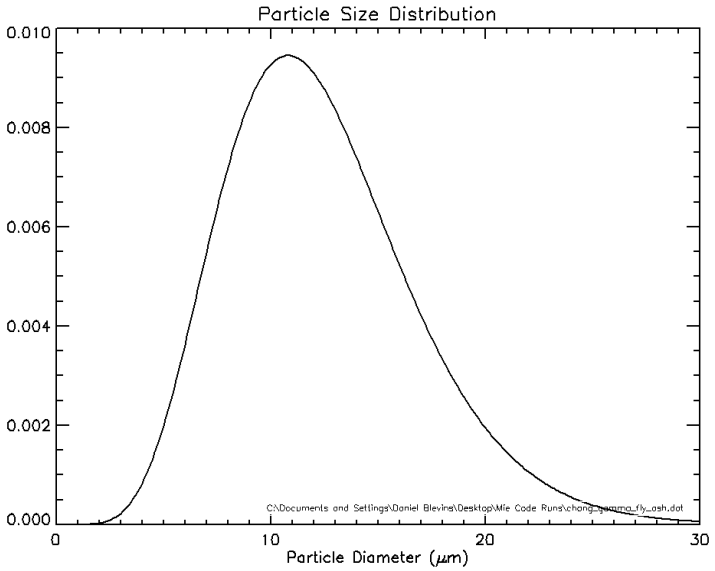
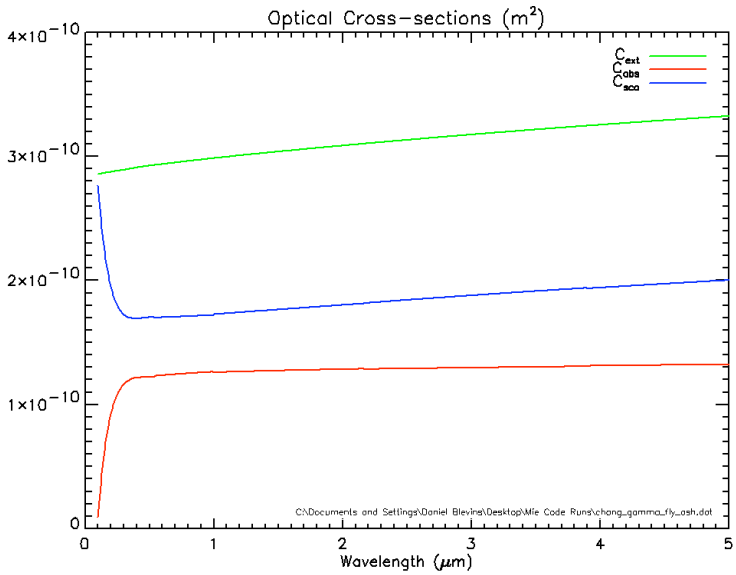
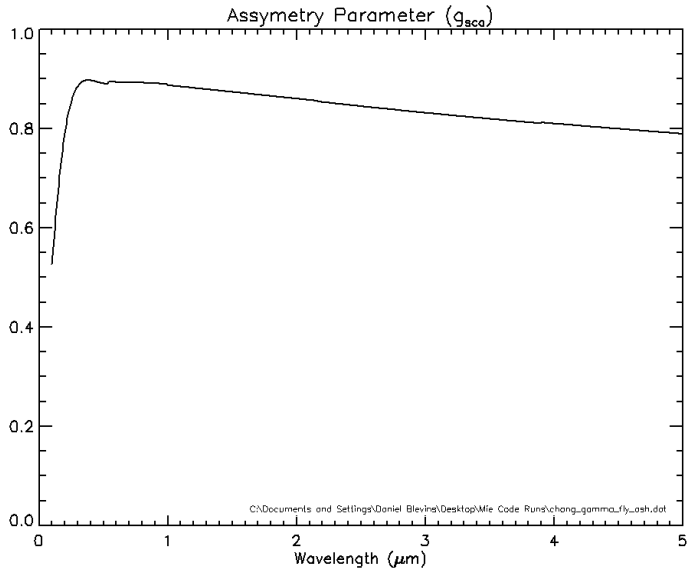


Figure 78: Sample particle size distribution for fly ash (gamma[a_{eff}=6.7; a_0=10.8])



(a) Optical cross-sections



(b) Asymmetry parameter

Figure 79: Optical properties for fly ash using Chang's indices of refraction

4.3 Topographic and DIAL Processor

For the purposes of model verification and demonstration, a simple topographic and DIAL processor were constructed. The fundamental basis and description for both processors was discussed in Chapter 3. Essentially, the processors take the DIRSIG LIDAR cubes, ingest them, process them, and then output the data points into a standard topographic xyz-ASCII data format. The primary difference between the topographic and DIAL output files is that

the DIAL includes a fourth column indicating the measured concentration path length for the associated pulse set. Both processors are based upon very basic detection schemes, either Geiger counting mode or linear mode. Additionally, the processors do not employ co-coincidence processing or pulse averaging to improve the accuracy of the data products. This could certainly be added into the software in the future.

4.4 Model Development and Verification

The DIRSIG LIDAR module was built using a spiral development methodology. The first step was to prioritize the broad range of requirements and identify the initial core photon mapping components that would form the foundation of the DIRSIG LIDAR model. Once those foundational components were put into place, the general development approach was to incrementally add specific capabilities or functionality to that foundation and then perform a series of verification tests at each stage of development. Additionally, the verification tests for the previous stages were repeated to ensure that the modifications to the model did not introduce unforeseen artifacts or errors. This iterative verification process was designed to build up a high level of confidence through analyzing a series of simplified scenes in conjunction with phenomenological demonstrations for more complex scenarios or capabilities. One should note that verification indicates a proper physical basis such that the results are consistent with the underlying physics. Validation would require real world data collection and associated truth data. Such LIDAR datasets were not readily available at the time of this research; however, the DIRSIG LIDAR model was verified at each stage using analytical predictions and qualitative demonstrations.

Imbedded in the phenomenological demonstrations are some of the functional capabilities developed or inherited from the legacy DIRSIG modules. For instance, incorporating the existing moving platform and sensor scanning modules primarily involved developing a time-based, iterative calling interface within the LIDAR radiance solver. The testing of those modifications was focused on confirming that the integration was done properly. In this instance, simulating a scanning flight scenario over Microscene and examining the resulting topographic dataset accomplished the verification. In general, the legacy DIRSIG modules were not re-validated or re-verified unless significant modifications were required to

accommodate interaction with the DIRSIG LIDAR modules. A small fraction of the inherited prototype code, such as the fully developed speckle and turbulence effects components, were not re-verified because they were not utilized in this research initiative.

For the critical analytical verification efforts, the basic plane-parallel light scattering layer setup introduced in Chapter 3 and illustrated in Figure 80 was advantageous. Not only could the scenario be analytically solved for a variety of cases, but the simple setup also decoupled the geometrical effects from the light scattering effects. The simple scene was comprised of either a semi-infinite or finite plane-parallel layer of participating media with an underlying Lambertian surface. For most of the verification runs, the planar surface was Lambertian with a known reflectance and was 1200 m downrange from the co-located transmitter and receiver. Because many of the generalized RTE boundary conditions do not account for any stray light re-entering the layer once it departs, the surface in some instances was defined to be 100% absorbing. Although DIRSIG's BRDF model was tested for functionality, such reflection functions significantly overcomplicate the analytical predictions and were not introduced during the verification process. The homogenous participating layer had a specified optical thickness, a scattering phase function, an absorption cross-section, a scattering cross-section, and a constant particle density. To minimize atmospheric effects, a dry atmosphere was assumed with the extinction coefficient of $1x10^{-5}$ [1/m]. The primary exception was any simulations after the MODTRAN interface was established based upon the legacy passive DIRSIG modules.

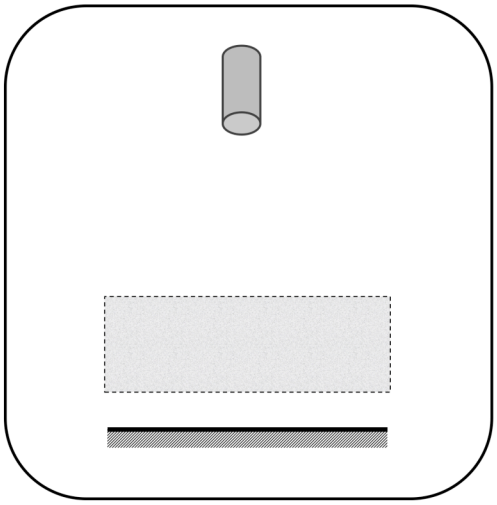


Figure 80: Simplified verification scene setup

The key LIDAR system parameters used for the DIRSIG verification runs are listed in Table 11. The parameters were selected to represent a typical LIDAR system configuration. Due to numerical precision limitations, the optical throughput parameter was adjusted to ensure that the dynamic range of the output LIDAR cubes was accommodated. For comparison to the predictions, the simulated optical throughput was backed out so that the resulting throughput was 1.0. This throughput level was chosen because the results could then easily be scaled for a more realistic throughput. Unfortunately, the scaling operation causes a loss in numerical precision and ultimately accuracy. The specific impact and recommendations will be discussed at length in Chapter 5. The detector size was also varied for some of the verification tests to investigate the photon density required for different scenarios. The full beam could easily be collected from a surface at 1200 m downrange with a 50 mm detector. While DIRSIG supports much more complicated sensor architectures, a single detector element centered on the optical axis was used as often as possible to simplify the analytical predictions.

Table 11: LIDAR system configurations for DIRSIG verification runs

Parameter	Configuration A
Wavelength (λ)	532 nm
Pulse Energy ($P_L=N_L hc/\lambda$)	6 μJ
Pulse Repetition Frequency (PRF)	5 KHz
Pulse Length (τ_D)	1 ns
Aperture Radius (r_0)	100 mm
Focal Length (f)	400 mm
Transmit Beam Radius (w_0)	5 mm
Beam Divergence (ϕ_D)	8.0 mrad
Optical Throughput	0.02 *
Detector Size	50 mm **

* *Throughput selected to ensure dynamic range of output cube was accommodated*
** *50 mm detector represents collection of entire beam*

4.4.1 Time-gated Topographic Return and Temporal Pulse Spread

The first key development milestone was the implementation of the core photon mapping components described previously in this chapter. The shooter function was adapted to handle a wider variety of input parameters, a more faithful representation of the photon mapping architecture was put into place, and the new collection/rendering phase was coded. Although the full capabilities of the model were somewhat limited, a simple topographic LIDAR capability was now available. A suite of verification tests was then established to ensure that the detected topographic return signal was accurately simulated. In particular, two of the most important tests were the temporal pulse spread demonstration and the analysis of the integrated return signal power. The temporal pulse spread demonstration stressed the arbitrary sampling and time-gating requirements, the fidelity of the range return bins, and the validity of the new photon mapping radiance solver approach. A LIDAR pulse was fired at a tipped Lambertian surface and the detected pulse was compared to a perpendicular surface return (illustrated in Figure 81). The latter should have retained the original pulse shape shifted to the range of the target. The tipped plate should result in a spreading of the pulse power over a broader set of range bins. The degree of pulse spread should correspond directly to the beam divergence and the angle at which the surface was tipped. The second set of tests verifies that the integrated return signal power from a surface element is accurate. All of these tests involved either a single or just a few pulses averaged together.

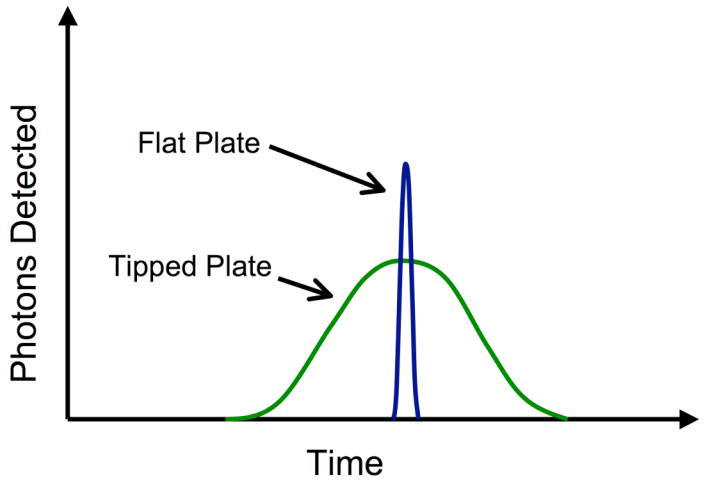


Figure 81: Illustrated comparison of the signal returns from a tipped and flat plate

4.4.2 Impact of an Absorbing Layer

The next development milestone was the addition of signal attenuation due to an absorption layer. While this milestone may appear to be a fairly straightforward, the modifications were fairly extensive because the entire architecture to support volume elements and their associated optical properties had to be developed and then incorporated into the existing model. By limiting ourselves to absorption by a participating layer, we could leverage the previous integrated return signal power tests and analytically predict the attenuation of the signal due to absorption by that layer. Additionally, absorption layers in the absence of scattering exhibit a very predictable exponential event distribution; therefore, statistical analysis of the resulting photon maps and the mean photon path lengths provided us with insight into how well the photon tracing stage was propagating the photons throughout the scene. The results of these tests are discussed further in Chapter 5 and eventually formed the basis for an early DIAL demonstration that was sub sequentially enhanced to form the baseline for the case studies on the impact of scattering on DIAL measurements.

4.4.3 Impact of an Scattering Layer

The next upgrade involved augmenting the volume properties to support scattering optical properties and then upgrading the LIDAR ray tracing engine to use the photon mapping techniques for photon tracing in a scattering medium as described in Chapter 3. In addition to

the scattering cross-section, the optical properties included a scattering phase function. As mentioned previously, the scattering phase function was implemented in two different ways: the Henyey-Greenstein approximation and a full importance sampled scattering phase function. The latter is embedded in the code, but currently lies dormant because the computational run-time was burdensome. Instead, the Henyey-Greenstein function approximation for the scattering phase function was adopted as the default for this research effort and the verification process. This is fairly reasonable for either isotropic or anisotropic scatterers; however, as will be discussed in Chapter 5, the layer statistics exhibit slight artifacts due to the inherent approximation errors.

As discussed thoroughly in Chapter 3, solving the RTE for a non-stationary, directional LIDAR pulse is a formidable task. A straightforward, direct analytical comparison was no longer viable due to the in-scattered radiance and the temporal nature of the photon distribution throughout the scene. In lieu of a robust analytical approximation, the performance was verified using the RTE approximations derived in Chapter 3 for a non-stationary, directional-pulsed source and statistical analysis of the photon events within the layer. Essentially, the model simulated a high-powered pulse that was fired into a weakly absorbing, highly scattering homogenous layer and the time-dependent backscattered signal was compared with the analytical approximations for the RTE: the multiple-scattering LIDAR equation and the non-stationary diffusion approximation. The near-surface returns should follow the multiple-scattering LIDAR equation fairly closely while the backscattered returns from deep within the layer should approach the non-stationary diffusion approximation. The traditional LIDAR equation was also included for reference in the results that are presented in Chapter 5.

The suite of statistical evaluations was designed to determine if the ray tracing process through the scattering layer and in particular the scattering phase function was implemented correctly with respect to the theory described in Chapter 3. The results were not only evaluated qualitatively, but were also compared to specific test cases published in the literature for light scattering in a cloud layer (Platnick, 2001). This provides an excellent basis for asserting that the model is accurately simulating the photon distribution throughout

the scene. Lastly, a general characterization of the photon maps for various scattering phase functions was performed to confirm phenomenological behavior such as beam spreading and blooming due to scattering. Early in the stages of development, the statistical analysis of the photon map combined with the general investigation into the photon bundle tracing engine discovered a potential bias in the random number generation process used by the scattering phase function. The issues were then corrected and the LIDAR model performance was re-verified. The final results for this development milestone were very encouraging and indicated that the modeling approach can indeed accurately model the multiple scattering effects on a LIDAR pulse. Final results from this portion of the verification process is also presented and discussed in more detail in Chapter 5.

4.4.4 Atmospheric, Passive, and Emissive Contributions

The atmospheric, passive, and emissive contributions were incorporated into the LIDAR capture method using the existing DIRSIG framework and community standard models such as MODTRAN and THERM. Since these components have already been validated, the focus of the verification efforts was to ensure that the implementation within the capture method was appropriate. For instance, the difference in the solar contribution for a pulse shot at midnight versus at noon in mid-lattitude summer (presented earlier in Figure 66) was verified against the data within the MODTRAN output file. A similar approach was taken for each of these components.

4.5 Phenomenological Case Studies

Not only were the phenomenological case studies selected to demonstrate the capability of the model to handle complex scenes and properties, but also to showcase the versatility and robust nature built into the new DIRSIG LIDAR module. The case studies explored in Chapter 5 demonstrate a host of the requirements listed previously in Table 9, but emphasize four in particular: complex scenes and properties, multi-bounce effects, arbitrary signal gating, and platform motion and scanning effects. The scenarios were all run utilizing the complete modeling capabilities, including such items as a realistic atmosphere and passive/thermal effects.

The first case study is the multi-bounce and "late" photon demonstration using Microscene area on campus. The scene has been modeled to a very high degree of fidelity such that even the blades of grass have facets. If one temporally oversamples and smartly range-gates over the "grassy" region, a small number of "lost" photons should be able to be observed and they were. The "lost" photons actually represent multiple bounces on a micro-scale. The details are left to Chapter 5. The second case study involved forest canopy penetration. Within the model, a broad single pulse was fired at a single deciduous tree and the time domain return signal was recorded. The anticipated result for the averaged return signal is illustrated in Figure 82. Essentially, we should get a return from the top of the tree, from the ground, and a small return from photons who underwent multiple bounces within the tree canopy. The third case study is simulation of a topographic LIDAR collect against a camouflaged target. The purpose is to demonstrate the high spatial and temporal oversampling capability as well as the arbitrary signal gating.

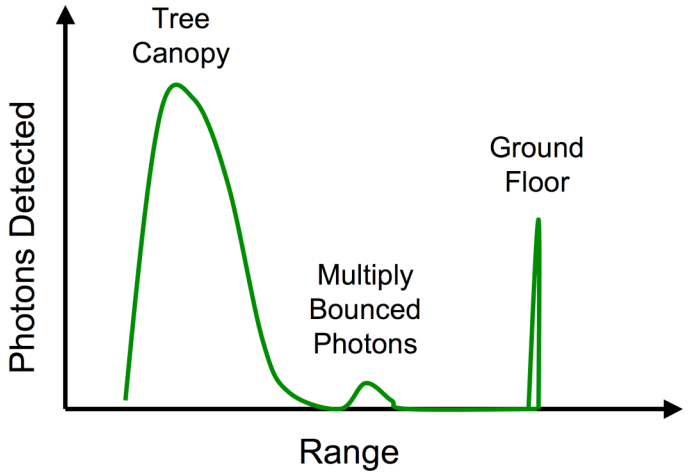


Figure 82: Illustrated averaged return signal from a tree

Thus far, the case studies have only involved a single pulse fired from a fixed position. Once the LIDAR model was modified to utilize the legacy DIRSIG platform and scanning modules, the next two case studies were designed to demonstrate the full capability of the LIDAR model to handle real-world scenarios of moving and scanning systems via an end-to-end topographic mapping simulations. The fourth case study simulated a sinusoidal scanning

LIDAR as it collects during a pass over the microscene area on RIT's campus. The simulated data was then processed through a research partner's topographic processor (ITT) and compared to a real-world topographic data product over the same area. The fifth and final case study was an extended dwell demo. The simulation involved a topographic LIDAR collecting in spotlight mode at a particular grazing angle for a set of concealed targets on the edge of a tree line.

4.6 DIAL Case Studies and Representative Datasets

With a verified LIDAR model, we can now develop a set of simulated DIAL datasets with a gaseous plume or set of voxels suitable to qualitatively confirm whether common scattering constituents, such as water vapor or soot, can significantly degrade a DIAL sensor's ability to accurately detect and measure the concentration level of a particular constituent within the plume. For this research effort, two types of scenes were developed. First, a simplified scene resembling the verification setup illustrated previously in Figure 80 with a few modifications. The modifications were that the Lambertian surface was replaced with a grassy surface with a bump and texture map and the gas box was trimmed down from semi-infinite to 200m x 200m. DIRSIG uses a texture map derived from a real-world image to randomly select from a library of emissivity curves for that material type. Ideally, the approach results in emissivity variability across the ground that is appropriate for the material and wavelength region selected. The texture map used for the grass was derived from one developed by Peterson (2004) for the near-infrared region of the spectrum and is shown in Figure 83. The texture map is not necessarily accurate for the spectral region where we simulated the DIAL collects; however, the intent was merely to provide some emissivity variability and this texture map was sufficient.

Methane (CH_4) is a common gas measured by commercial DIAL systems that monitor natural gas pipelines for leaks and was chosen for that reason to be the constituent of interest for these DIAL scenarios. The specific gas selected is not as important as the relative strength of the absorption and scattering cross-sections of the plume constituents at both the "off" and "on" wavelengths. Water vapor was chosen as the scattering constituent because the optical

properties and particle size distribution functions are fairly well known and because it is very common in plumes.

Based upon methane's absorbance spectrum shown in Figure 85, the MWIR was selected for the demonstrations. Methane has a strong set of features in that region and the optical properties for other materials, such as the sample grass spectra shown in Figure 84 and more importantly water vapor, do not vary greatly. The largest group of absorption features is around 3.31 μm. The wavelengths chosen for the DIAL system were 3.3058 μm and 3.3151 μm. The latter is at the peak of a strong absorption feature and the former resides nearby with a very low absorption cross-section. The rest of the DIAL system parameters are listed in Table 12.

With the methane concentration held constant, the amount of water vapor was varied in the gas box. The simulation results were then run through the simplistic DIAL processor and the output concentration path lengths were compared. The details and results are discussed further in Chapter 5.

The second type of scene was intended to be a more realistic simulation of a DIAL collection against an actual plume. The scene was constructed using RIT's Megascene Tile4 water treatment plant and adding a Blackadar plume with methane and water vapor. A series of pulses were simulated with full platform and scanning motion. In addition, the on/off pulses were offset by 400 nsec, which is representative of the delay for a real DIAL system. Not only did the pulses see different portions of the plume and ground due to the inter-pulse delay, but the plume model was adjusted so that the plume wandered a bit between the pulse pairs. A DIRSIG generated panchromatic snapshot of the scene is shown in Figure 87. As anticipated, the scattering induced by the water vapor did impact the DIAL system's accuracy and will be discussed further in Chapter 5.

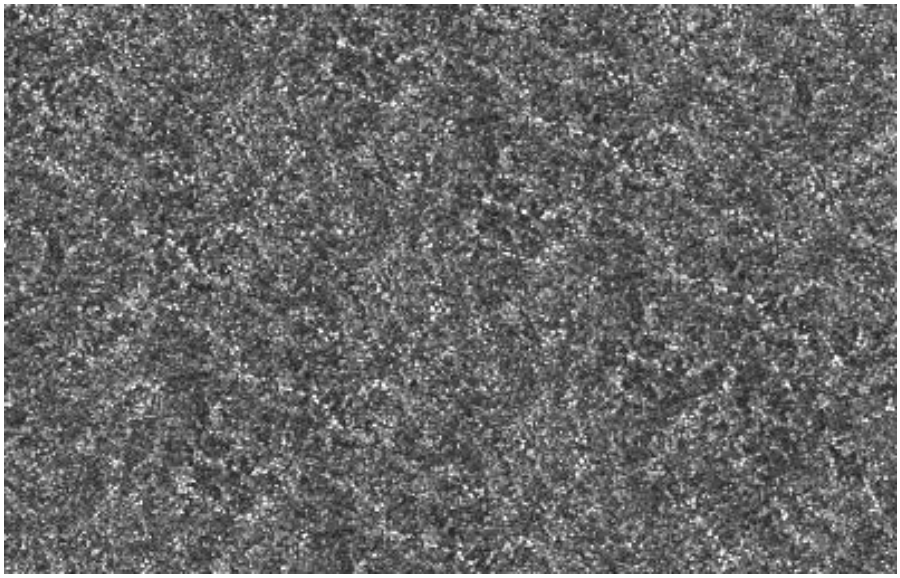


Figure 83: DIRSIG emissivity texture map used for MWIR grass spectrum (Peterson, 2004)

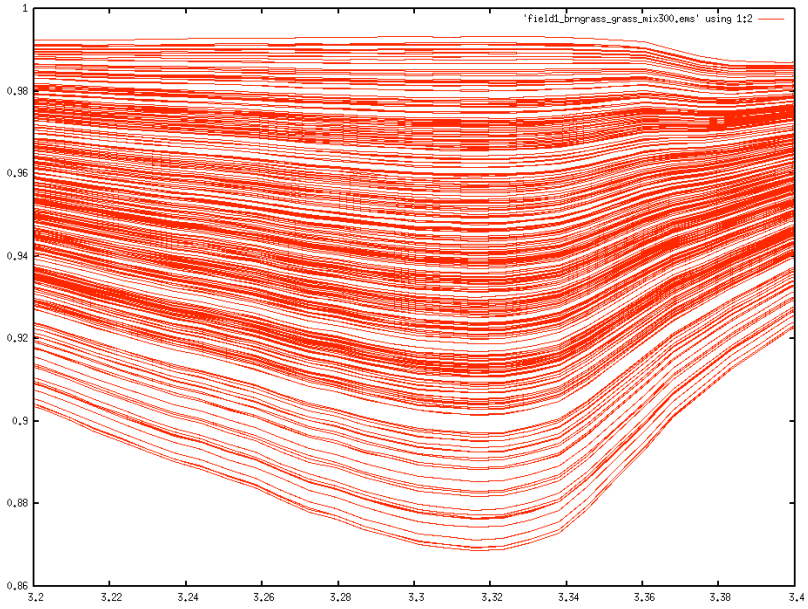
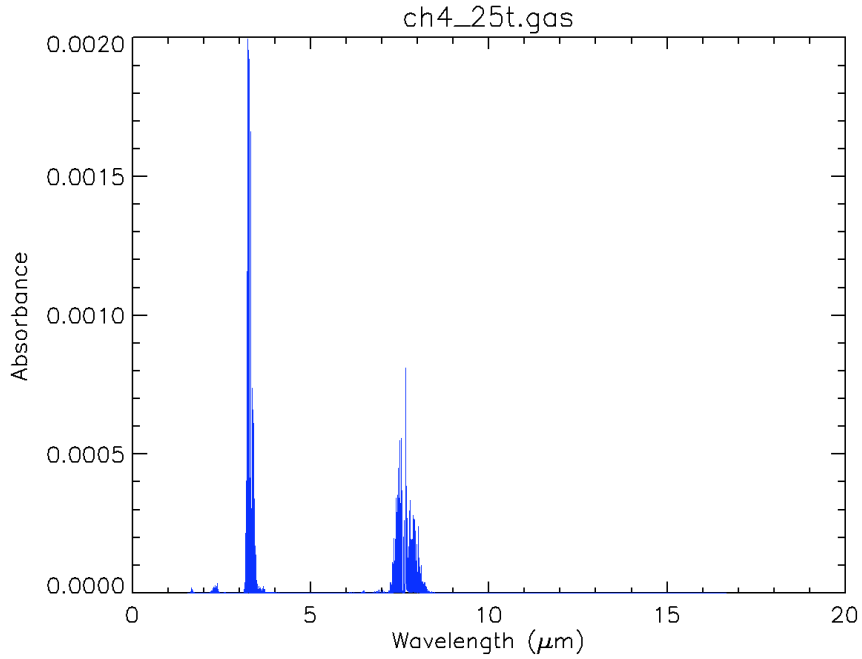
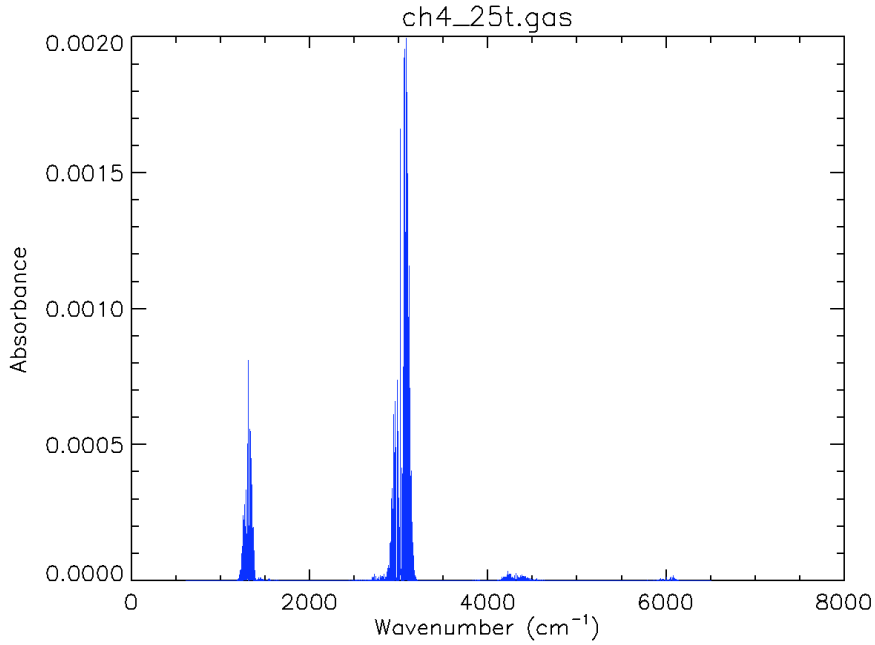


Figure 84: Sample emissivity curves for brown field grass (field1_brngrass_grass_mix300.ems)



(a) Absorbance vs. wavelength



Absorbance vs. wavenumber

Figure 85: Absorbance for CH_4 gas at 25°C in ppm/m

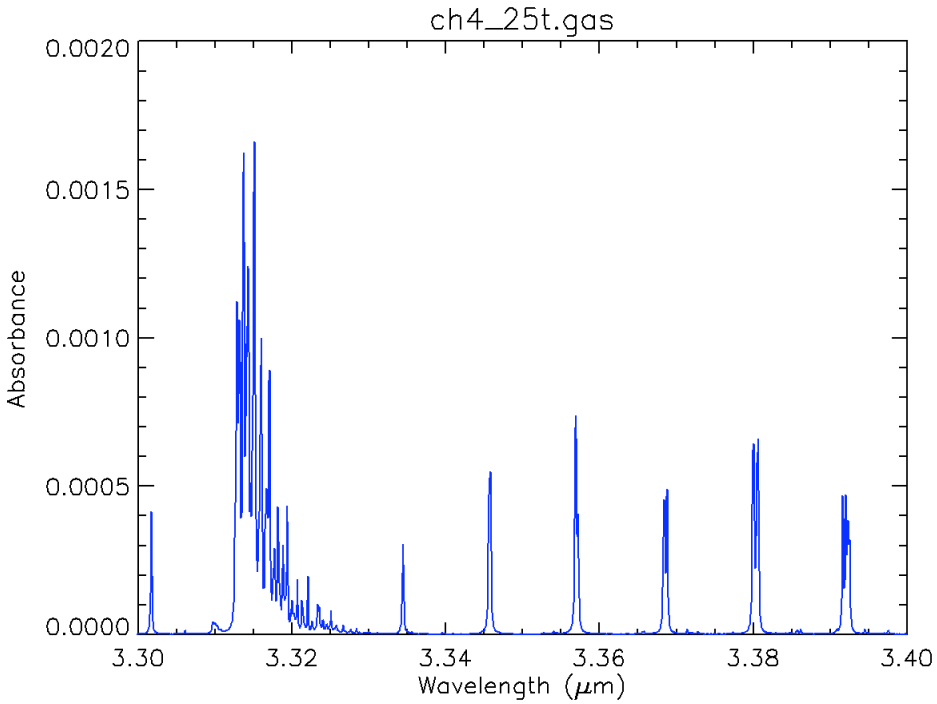


Figure 86: Absorbance for CH_4 gas at 25°C in ppm/m in MWIR region (3.3-3.4 μm)

Table 12: LIDAR system configuration for scattering case study

Parameter	Configuration C
Wavelength (λ_{OFF})	3.3058 μm
Wavelength (λ_{ON})	3.3151 μm
Pulse Energy ($P_L=N_L hc/\lambda$)	6 μJ
Pulse Repetition Frequency (PRF)	5 KHz
Pulse Length (τ_D)	1.5 ns
Aperture Radius (r_0)	100 mm
Focal Length (f)	400 mm
Transmit Beam Radius (w_0)	5 mm
Beam Divergence (ϕ_D)	8.0 mrad
Detector Size	500 μm

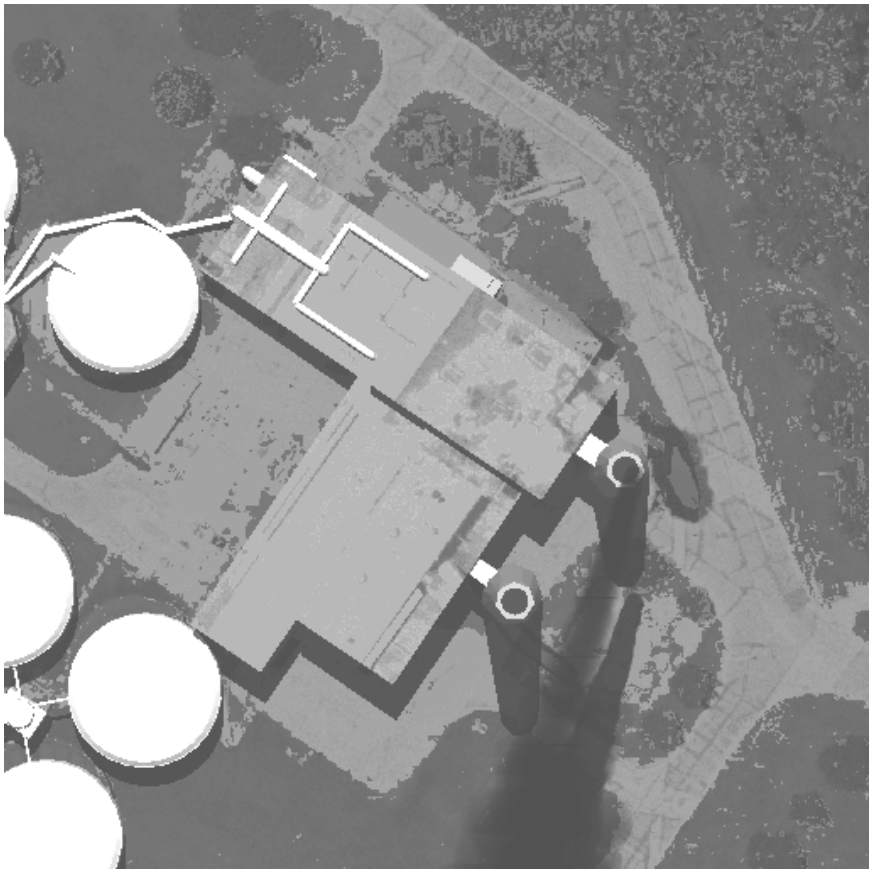


Figure 87: DIRSIG panchromatic image of a CH_4 gas plume inserted into the RIT's Megascene 1 water treatment facility

Chapter 5

Results

Given the DIRSIG LIDAR modeling implementation introduced previously, this chapter details specific results from the spiral development and verification process and from subsequent DIAL case studies of the potential impact of scattering on DIAL measurements. It also presents some exemplar topographic and DIAL simulations to demonstrate the viability of and flexibility of the new DIRSIG modules to generate realistic LIDAR datasets. In general the emphasis of the discussion is on the verification, fidelity, and potential limitations of the new DIRSIG LIDAR module for modeling the multiple scattering and absorption for a DIAL collection scenario. To that end, Section 5.1 below discusses the analytical verification tests that were performed throughout the model's spiral development cycle. Section 5.1 presents simulated results for the geometric-induced temporal pulse spread effects, the signal returns for a topographic LIDAR, the attenuation due to an absorbing layer, and the backscattered signal of a LIDAR pulse from a highly scattering medium. Section 5.2 follows this up with a suite of phenomenological demonstrations, including demonstrations for multiply bounced "lost" photons, camouflaged/concealed hard targets, tree canopy penetration, and end-to-end topographic system. These demonstrations not only showcase DIRSIG's LIDAR modeling capabilities, but also verify that the functional capabilities developed or inherited from the legacy DIRSIG modules are implemented correctly.

With the integrity and/or utility of the overall model established, Section 5.3 explores the impact of scattering on DIAL measurements using a simplified DIRSIG scene. The case study baseline also verifies the modeling accuracy of DIRSIG at least for this type of scene. The case study is not intended to extensively characterize the impacts of scattering on DIAL measurements. Instead, the results in Section 5.3 demonstrate that even a small amount of scattering may impact the DIAL measurement accuracies if left unaccounted for. Finally, Section 5.4 discusses an end-to-end DIAL demonstration using Megascene Tile 4 and the Blackadar plume model introduced earlier in Chapter 3.

5.1 Analytical Model Verification

A wide range of functional and performance requirements were verified throughout the spiral development cycle. This section discusses the critical analytical verification tests and demonstrations that directly address the viability, accuracy, and potential limitations of the photon mapping theory and specifically the new LIDAR modeling approach introduced in Chapters 3 and 4 respectively. The analytical verification tests were purposefully simplified in an attempt to focus on the underlying physic-based modeling approaches and to permit direct analytical verification. Although the verification tests could stand on their own, each was designed to build upon the previous results and thus incrementally increase our confidence in the model. Due to the complexity associated with modeling the propagation of light through participating volumes, the first few verification cases are focused on topographic surface returns. The final two tests demonstrate the accuracy of the model for multiple scattering and absorption due to participating media.

As introduced in Chapter 4, the general verification setup (Figure 80) remained the same for each of the verification tests. For the topographic cases, the gaseous layer was removed or assigned the properties of the atmosphere. The default DIRSIG atmosphere, which is a dry atmosphere with an extinction coefficient of $1x10^{-5}$ [1/m], was used in most of the cases. The planar surface is Lambertian with a known reflectance and is typically 1200 m downrange from the co-located transmitter and receiver. The LIDAR system parameters in Table 13 were selected for most of the verification tests. The one major exception was for the multiple scattering analyses where a much higher powered pulse and different receiver was necessary to simulate the backscattered return from within a cloud layer. Also, the receiver is assumed to be detector limited. This assumption simplifies the geometrical form factor and thus the prediction calculations. For many cases, a baseline was set using the 50 mm detector solely because the collection area encompasses the entire beam footprint.

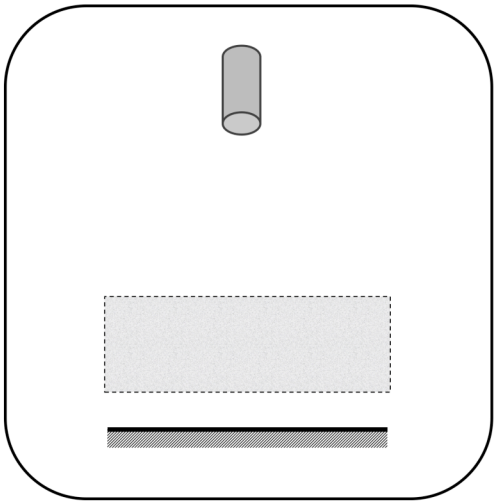


Figure 88: Simplified verification scene setup

Table 13: LIDAR system configurations for DIRSIG verification runs

Parameter	Configuration A	Configuration B
Wavelength (λ)	532 nm	3400 nm
Pulse Energy ($P_L=N_L hc/\lambda$)	6 μJ	6 μJ
Pulse Repetition Frequency (PRF)	5 KHz	5 KHz
Pulse Length (τ_D)	1 ns	1 ns
Aperture Radius (r_0)	100 mm	100 mm
Focal Length (f)	400 mm	400 mm
Transmit Beam Radius (w_0)	5 mm	5 mm
Beam Divergence (ϕ_D)	8.0 mrad	8.0 mrad
Optical Throughput	0.02 *	0.02 *
Detector Size	50 mm **	50 mm **

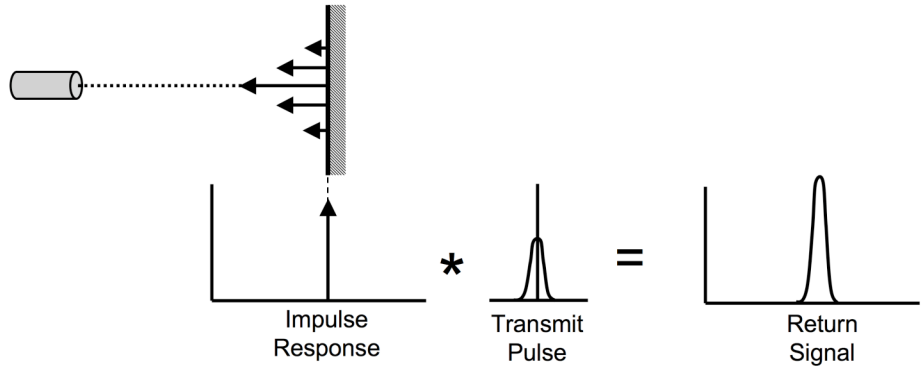
* *Throughput selected to ensure dynamic range of output cube was accommodated*
** *50 mm detector represents collection of entire beam*

5.1.1 Temporal Pulse Broadening

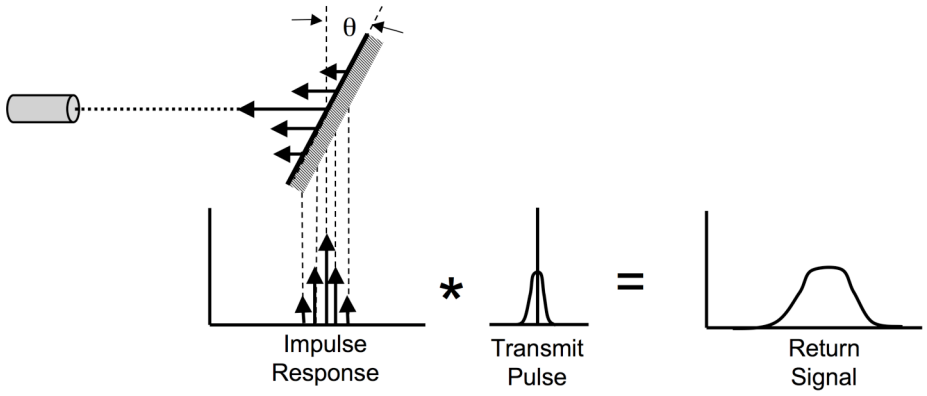
As discussed in Chapter 4, the temporal pulse broadening demonstration verifies the new temporal photon mapping collection method, which is at the core of our model. Because the test case also requires temporal super-sampling, the arbitrary time-gating capabilities are also effectively demonstrated. The primary emphasis was on the temporal aspects of a reflected LIDAR pulse from a flat versus a tipped plate and not the accuracy of the detected number of photons, which will be discussed later in Section 5.1.2. While the test might be stressing for many modeling systems, the setup is fairly straightforward. DIRSIG simulated the return from a 1 ns Gaussian LIDAR pulse that was fired at a Lambertian reflecting plate with a

reflectance of 50%. The reflecting plate was set 1200 m downrange from the co-located transmitter and receiver. The receiver FOV encompassed the entire transmit beam footprint, which was about 10 m wide for the plate that was perpendicular to the optical axis of the LIDAR system. The return signal was highly oversampled at a rate of 10 GHz (~0.1 nsec sample bins) so that we have several samples over the 1 nsec transmit pulse duration. Two pulses were fired and then the results were compared. The first pulse was fired at a plate that was perpendicular to the optical axis. The second pulse was fired at a plate that was tipped 10 degrees around the x-axis. The results shown in Figure 90 are that the "tipped" plate signal is temporally broadened while the flat plate return is a time delayed replica of the transmit pulse. The 10 degree tilt amounts to about a 1 m difference in range; therefore, the return from the "tipped" plate should broaden by approximately 6.666 nsec on both sides. The times at which the 2nd standard deviation points for the "tipped" plate are correctly located at approximately 7.993 μsec and 8.0067 μsec. The flat plate width was also correct at about 1 nsec. In other words, the DIRSIG LIDAR module accurately modeled the temporal aspects for both pulses including the temporal pulse broadening due to the tilted plate.

The results were achieved due to the new photon mapping architecture and in particular due to the temporal photon mapping collection scheme discussed in Chapter 4 and illustrated in Figure 89. For both scenarios, DIRSIG generates a series of randomly generated photon bundles and casts them into the scene. Those bundles intersect the surface and an event is recorded. The events in the photon map illustrated by the arrows at the surfaces are then back-propagated to the receiver and summed. The result is the impulse response of the scene. For the "tipped" plate, the photon events are spread over a broader set of range bins based upon the amount of tilt (Figure 89b). The impulse response of the scene is then convolved with the transmit pulse, windowed, and sampled. The actual collection algorithm performs these operations with each individual event and performs the summation at the end; however, the result is the same for the output signal due to the linearity of the operations.



(a) Flat plate



(b) Tipped Plate

Figure 89: Illustration of temporal pulse broadening due to tilted plate for a Gaussian pulse

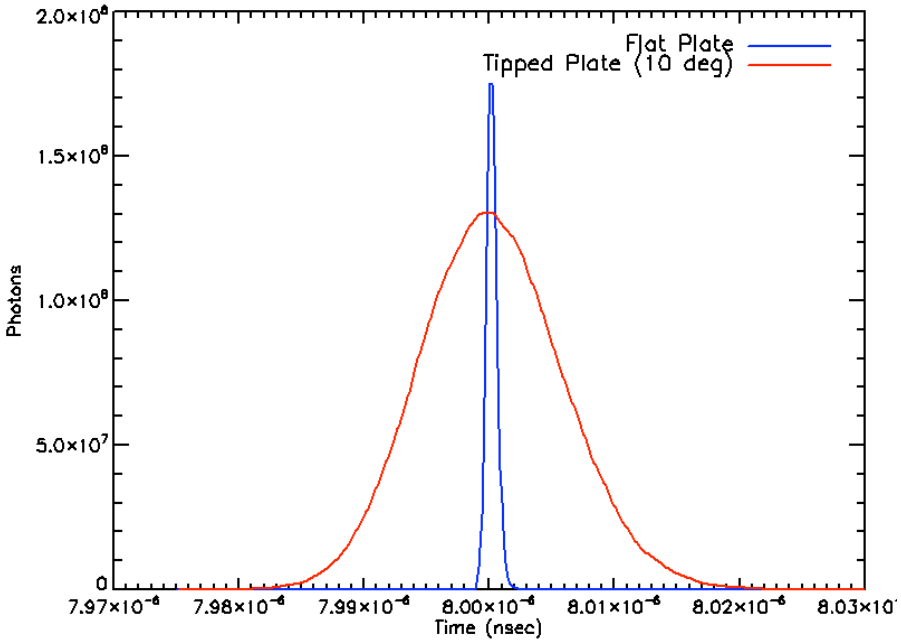


Figure 90: Temporal pulse broadening due to tilted plate for a 1 ns Gaussian pulse (10 deg)

5.1.2 Topographic Return from a Lambertian Plate

The second verification test analyzes the integrated topographic return from a Lambertian plate that is 1200 m downrange from a LIDAR system with the Configuration B operational parameters listed in Table 13. The governing equation for the received signal captured by a LIDAR sensor is derived from the general LIDAR equation for elastic scattering. Based upon Measures (1984), the received number of photons from a range R due to elastic backscattered radiation can be written as:

$$N_{\text{detected}}(\lambda,R) = N_L(\lambda)\xi(\lambda,R)\frac{A_r}{R^2}\frac{\rho_s(\lambda)}{\pi} \times \exp\left[-2\int_0^R \sigma_{ext}(\lambda,r)dr\right] \tag{282}$$

where $\xi(\lambda,R)$ is a system function determined by the geometric considerations of the receiver optics, the quantum efficiency of the detection system at each wavelength, and the overlap between the transmitted laser beam and the field of view of the receiver; A_r/R^2 is the acceptance solid angle of the receiver optics with a collecting area A_r; $N_L(\lambda)$ is the average number of photons in the transmitted pulse at wavelength λ; $\sigma_{ext}(\lambda,r)$ is the extinction coefficient of the participating medium at the wavelength λ for the range r; $\rho_s(\lambda)$ is the backscattering efficiency at of the target surface. $\xi(\lambda,R)$ is usually assumed to be separable into a wavelength dependent weighting; $\xi(\lambda)$, and a geometrical form factor, $\xi(R)$. $\xi(\lambda)$ is dependent primarily upon the receiver design characteristics and for the purposes of this subsection shall be assumed to be unity whereas typical values range from 0.5 to 0.8. The geometrical form factor is used to adjust the equation to account for a variety of factors and is often fairly difficult to evaluate for a real LIDAR system. If one assumes that the laser power distribution is Gaussian in the target plane and that the limiting aperture is the detector size instead of the telescope objective lens (or mirror), then the LIDAR system function can be expressed as:

$$\xi(\lambda,R) = \xi(\lambda)\frac{1}{\pi W^2(R)}\frac{R^2}{\pi r_0^2 f^2}\int_{A_D}\int_{A(r,\psi,r_0)} \exp\left[-\frac{r^2}{W^2(R)}\right] dA\, dA_D \tag{283}$$

where f is the effective focal length of the system, r_0 is the radius of the receive telescope aperture, R is the range, $W(R)$ is the transmit beam waist radius at range R, A_D is the area of the detector in the focal plane, and $A(r,\psi, r_0)$ is a circle of radius r_0 that is centered at (r,ψ) in

the target plane. When equations 282 and 283 are combined, the topographic LIDAR equation can be rewritten as:

$$N_{\text{detected}}(\lambda,R)=N_L(\lambda)\xi(\lambda)\frac{\rho_s(\lambda)}{\pi}\times\exp\left[-2\int_0^R\sigma_{ext}(\lambda,r)dr\right]\times\frac{1}{\pi W^2(R)}\frac{1}{f^2}\int_{A_D}\int_{A(r,\psi,r_0)}\exp\left[-\frac{r^2}{W^2(R)}\right]dA\,dA_D \qquad (284)$$

Using Equation 284 and the system parameters described in Table 13, one can analytically evaluate the number of photons detected from a surface. To minimize atmospheric effects, a dry atmosphere will be assumed with the extinction coefficient of $1\text{x}10^{-5}$ [1/m].

Figure 91 displays both the analytical prediction dictated by equation 284 and DIRSIG's integrated output for a single pixel versus the surface reflectance. As shown in Figure 91, the analytical and numerical results are well-correlated and exhibit appropriate behaviors. Figure 92 displays the error associated with each curve from an absolute and relative perspective. The relative error was calculated with respect to the predicted integrated photon count of the return signal and not from the transmitted photon count. The error is bounded at about less than 0.07% for a 50 mm detector, 0.1 % for a 1 mm detector, and 1-2% for a 0.5 mm detector. In general, the error for these plots was on the order of 10^9 to 10^{10} photons which is less than 0.001 % to 0.0001% of the approximately $1.02\text{x}10^{14}$ photons shot per pulse.

The dominant sources of error are the approximation errors for the calculation of the prediction's geometrical form factor, the errors induced by the user-defined dynamic range scaling operations, the errors due to numerical precision loss inherent within the model, and the errors due to the limited number of photon bundles shot into the scene. The first source affects the analytical prediction, while the others are related to the model and the utilization of the model. Unfortunately, the geometrical form factor approximation error may be a fairly dominant source of error. An error in the fourth or fifth decimal place could potentially generate an error on the order of what is seen in the data; however, this is not the only source of error. We know that the other sources probably contributed significantly.

As indicated previously in Chapter 4, the DIRSIG LIDAR output cubes are output as long integers. To fit the results within the available dynamic range, the optical throughput was

adjusted to 0.00002. This scalar was then backed out in the analytical stages, but there was significant numerical precision loss due to this approach. For instance, if all of the photons were reflected back to the sensor, an error on the order of 10^5 would be exhibited due to rounding caused just by the optical throughput scaling operations. This is less of a concern when the anticipated simulation returns fit within the dynamic range of a long integer. Another alternative method is to over sample the return signal and then integrate the output LIDAR cubes directly. This bypasses the output dynamic range issue somewhat, but complicates the backend processing. The bottom-line is that the user must carefully consider the potential precision losses if scalar inputs, such as the optical throughput, are adjusted merely to ensure that the dynamic range of the output can be represented by a long integer. In the future, the DIRSIG LIDAR capture method could be modified to support doubles for the output data cube as a user-defined option.

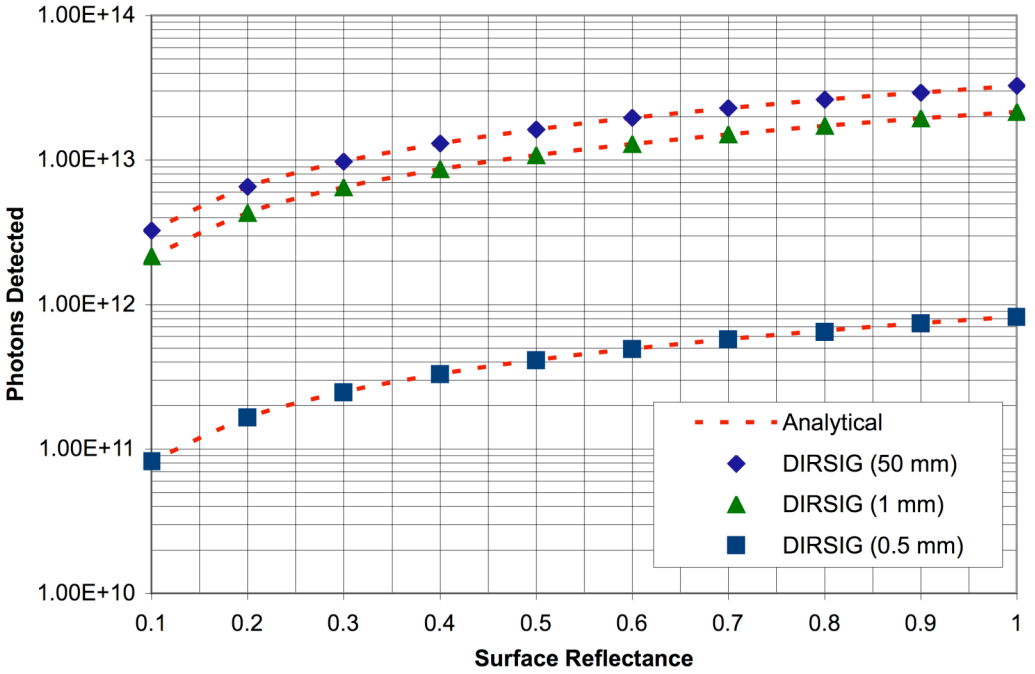
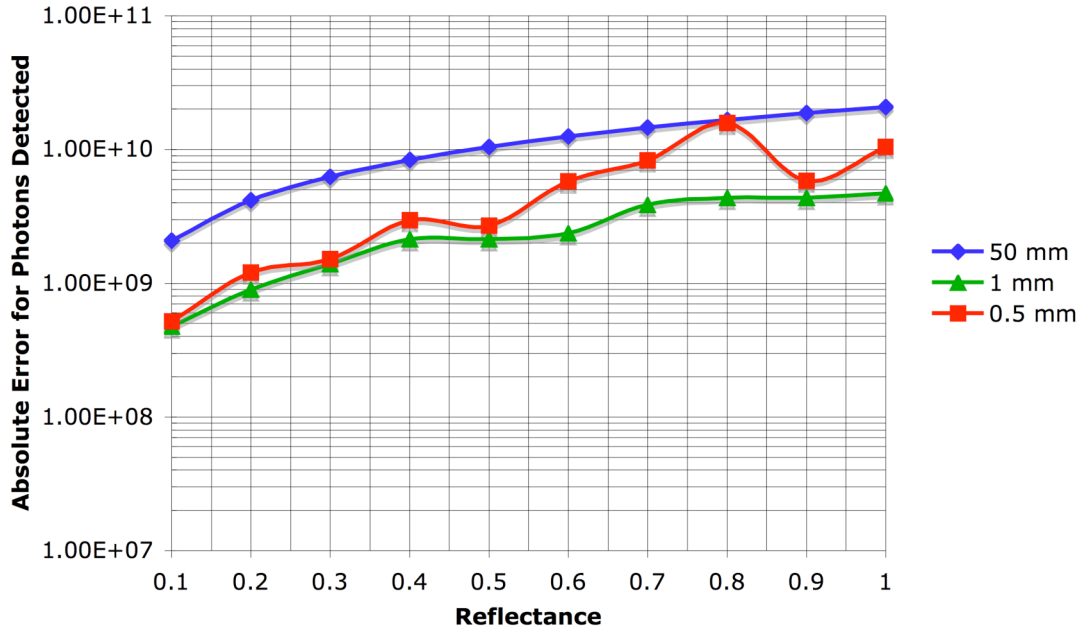
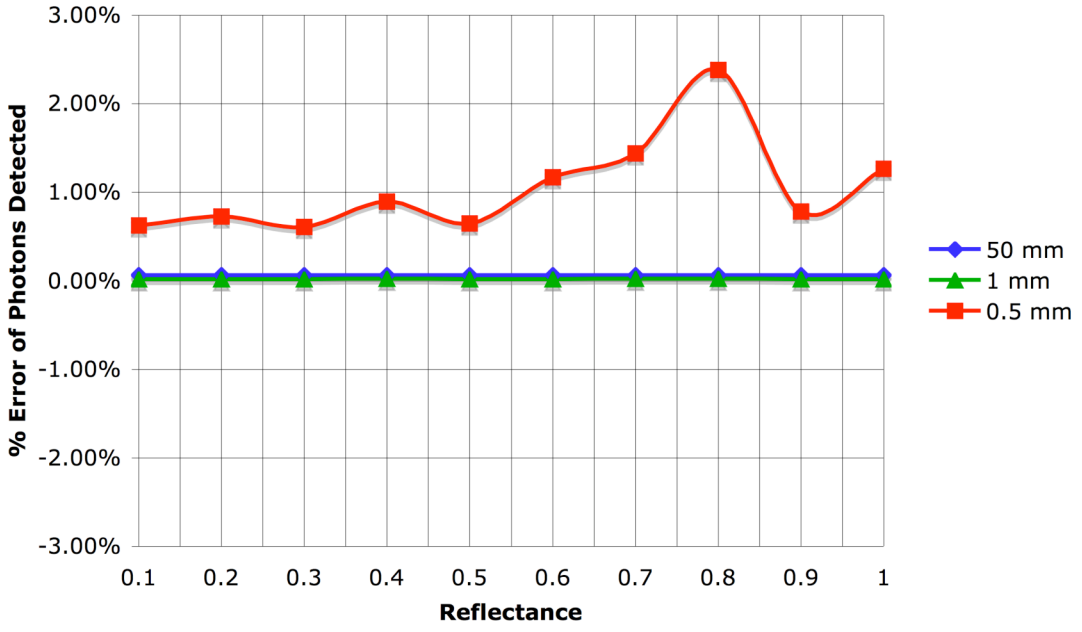


Figure 91: DIRSIG integrated number of photons detected for a single pulse reflected from a Lambertian surface at 1200 m downrange for various detector sizes



(a) Absolute error



(b) Relative error

Figure 92: Error for DIRSIG integrated number of photons detected for a single pulse reflected from a Lambertian surface at 1200 m downrange for various detector sizes

The remaining error sources are somewhat coupled within the model. The number of photon bundles affects both the numerical precision of the internal calculations and also the inaccuracies associated with the random sampling of the surface photon distribution which is driven by the importance sampling of the source function. Despite this fact, some observations can be gleaned by examining the relative and absolute errors for the 50 mm, 1 mm, and 0.5 mm detectors given various numbers of photon bundles shot during the simulation. The results of those simulations are plotted in Figure 93 through Figure 95.

The 50 mm detector cases effectively are not affected by the importance sampling of the surface photon distribution because the detector collects and integrates over the full beam. The location of the photon events on the surface are not as relevant since the surface is Lambertian and all of the events are well within the receiver FOV. The dominant error contributors are the dynamic range compression errors discussed earlier and the inherent computational loss in numerical precision within the model. These errors decrease as the number of photon bundles shot is increased, but unfortunately, the computational burden also increases from 20-30 sec per pulse for 50K to 2-3 minutes per pulse for 500K. This trend is consistent with photon mapping theory introduced in Chapter 3. The loss in numerical precision is directly correlated to the number of photon bundles cast into the scene. For instance, increasing the number of photon bundles cast into the scene reduces the number of photons that each bundle represents. Table 14 lists the number of photons represented by each bundle depending upon the number of photon bundles shot into these scenes. While the number of significant digits is maintained, the importance of the digits that are lost lessens as the number of photon bundles cast increases.

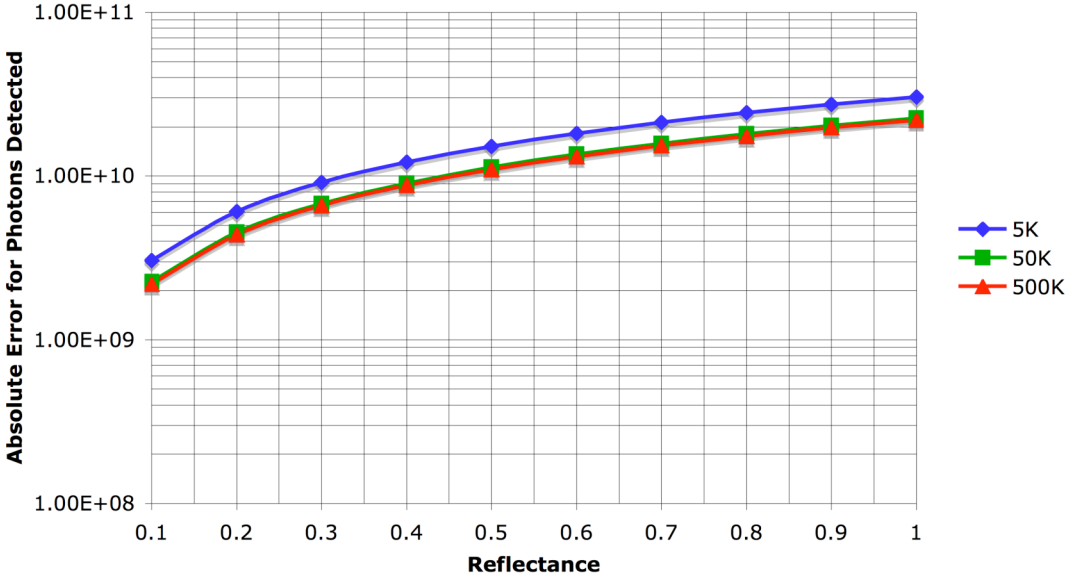
The 1 mm and 0.5 mm results (shown in Figure 94 and Figure 95 respectively) are impacted by the importance sampling of the photon distribution at the surface and the computational error evident in the 50 mm results. Thus, the errors are greater for both of these cases than for the 50 mm case. The variability in the error is related to the random nature of the importance-based sampling of the source function. The detector has a limited FOV that is less than the

full transmit beam. As described in Chapter 4, the ray tracing engine randomly casts photon bundles into the scene based upon a Gaussian laser source function. Those bundles stochastically build up the photon distribution at the surface. For the cases under consideration, we are effectively undersampling that distribution.

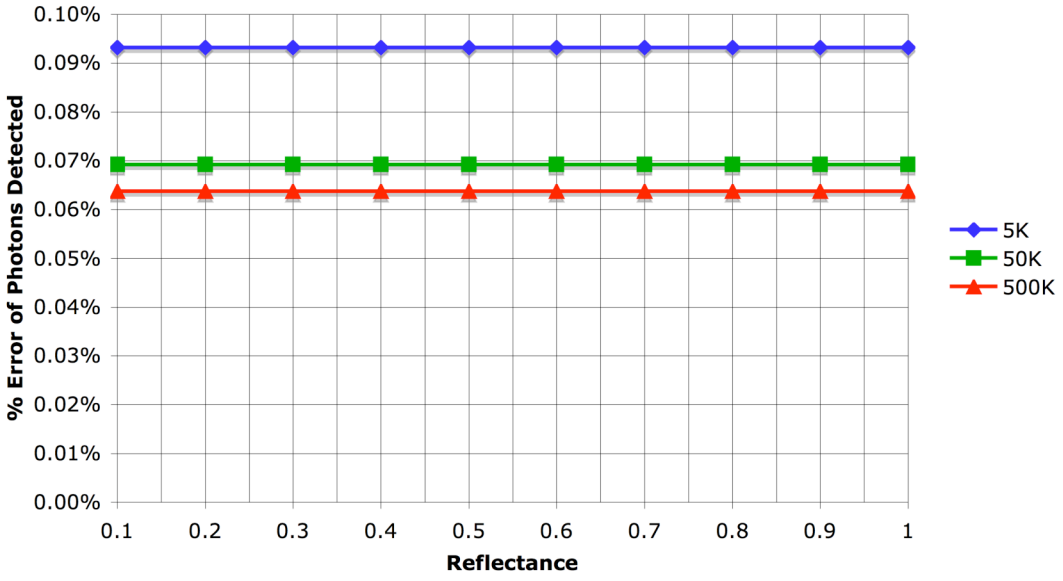
Casting more photon bundles into the scene has two primary effects shown in the normalized photon map histograms in Figure 96. First, we increase the number of samples throughout the beam and inside the detector FOV. Secondly, the photon bundles represent a smaller number of photons as the number cast increases. Thus, if a few bundles randomly land outside instead of inside the detector FOV when we are undersampled, the impact is lessened. In other words, a "misplaced" photon bundle results in a 10^8 instead of 10^{10} error in the number of detected photons. Figure 96b and in Figure 96d are image visualizations of the surface photon distribution and somewhat represent what the intensity of the transmit beam is at the surface. The difference between the two images is that one was generated with 50,000 samples and the other was generated with 1,000,000. The 3D representations are also shown in Figure 96a and in Figure 96c respectively. The 1 mm detector collects about 66% of the surface signal power due to the system's transmit and receive FOV overlap. The 0.5 mm detector only collects about 2% of the surface signal power because of its much smaller FOV. The location of the photon distribution samples is much more critical for the smaller detector. This is amplified for the relative error because the signal power is also much smaller. The result for these cases is that the error is increased from less than 0.1% for the 1 mm detector to something on the order of a 2% to 6% for the 0.5 mm detector. Although the trends indicate that the error is significantly reduced as more photon bundles are cast into the scene, the very small detector collection area to transmit beam footprint ratio would probably require millions of photon bundles to reduce the error down to less than 0.1%.

Table 14: Photons represented by each bundle given the number of bundles shot in DIRSIG

Bundles Shot	Photons/Bundle *(6 μj at 3.4 μm)*
500K	2.0539179012E+08
75K	1.3692786008E+09
50K	2.0539179012E+09
5K	2.0539179012E+10

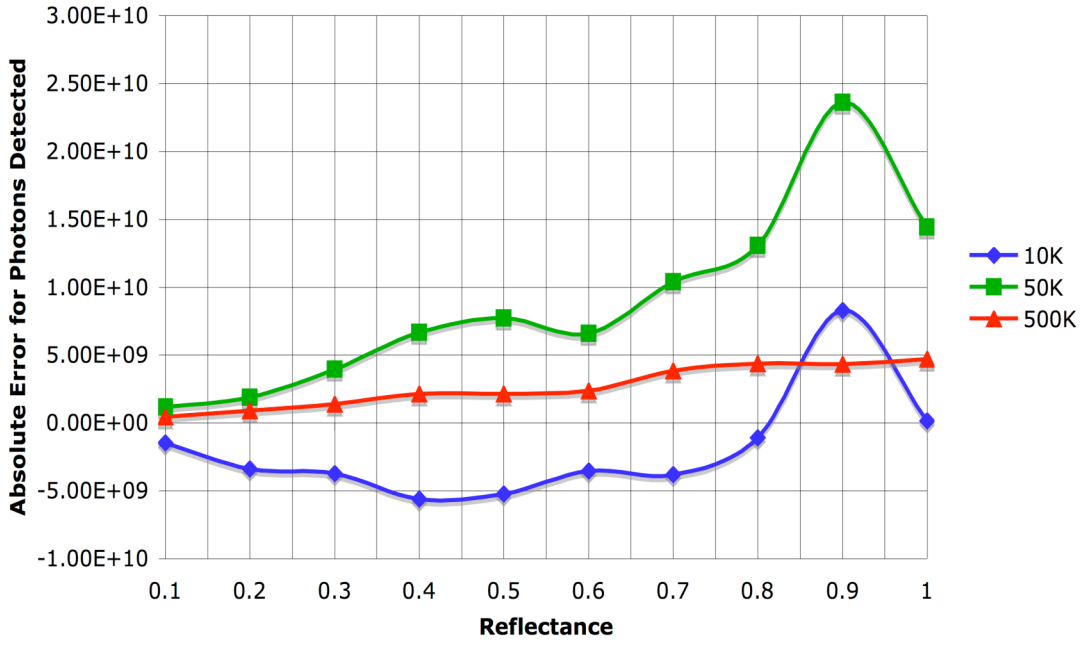


(a) Absolute error

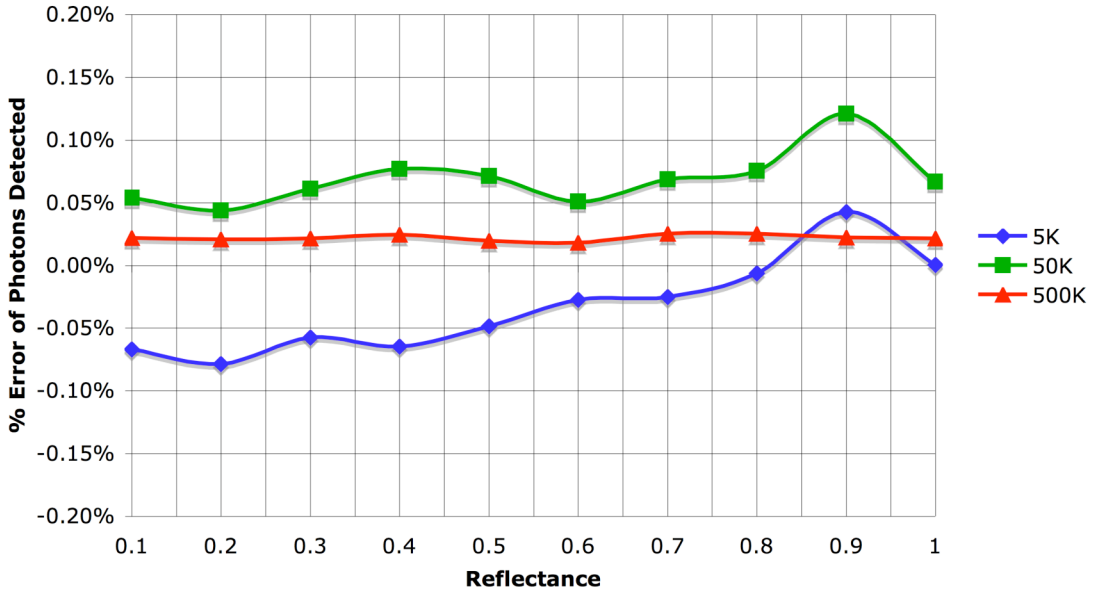


(b) Relative error

Figure 93: Error for DIRSIG integrated number of photons detected for a single pulse reflected from a Lambertian surface at 1200 m downrange for a 50 mm detector

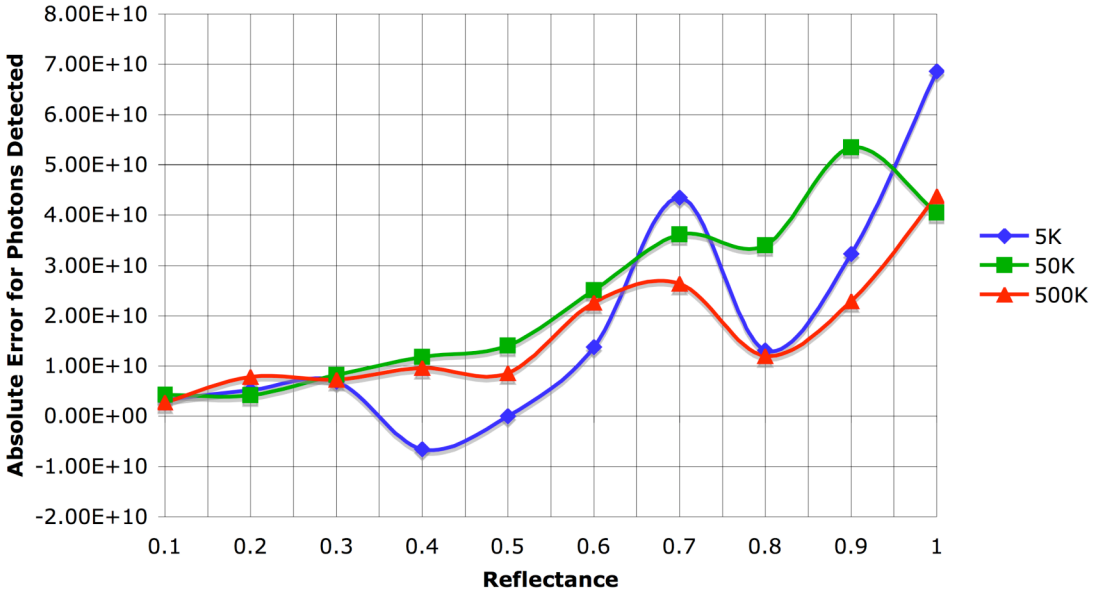


(a) Absolute error

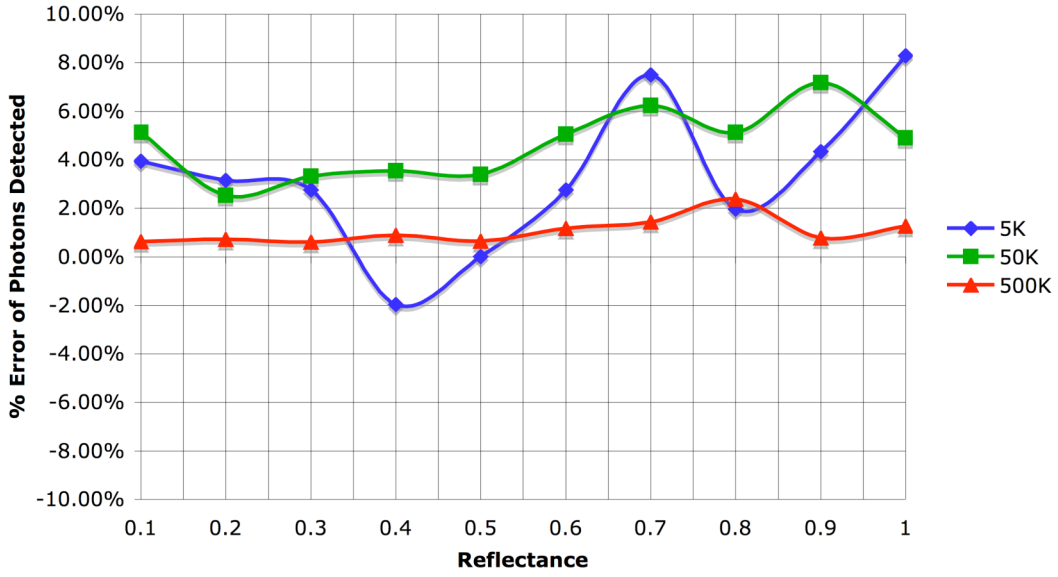


(b) Relative error

Figure 94: Error for DIRSIG integrated number of photons detected for a single pulse reflected from a Lambertian surface at 1200 m downrange for a 1 mm detector

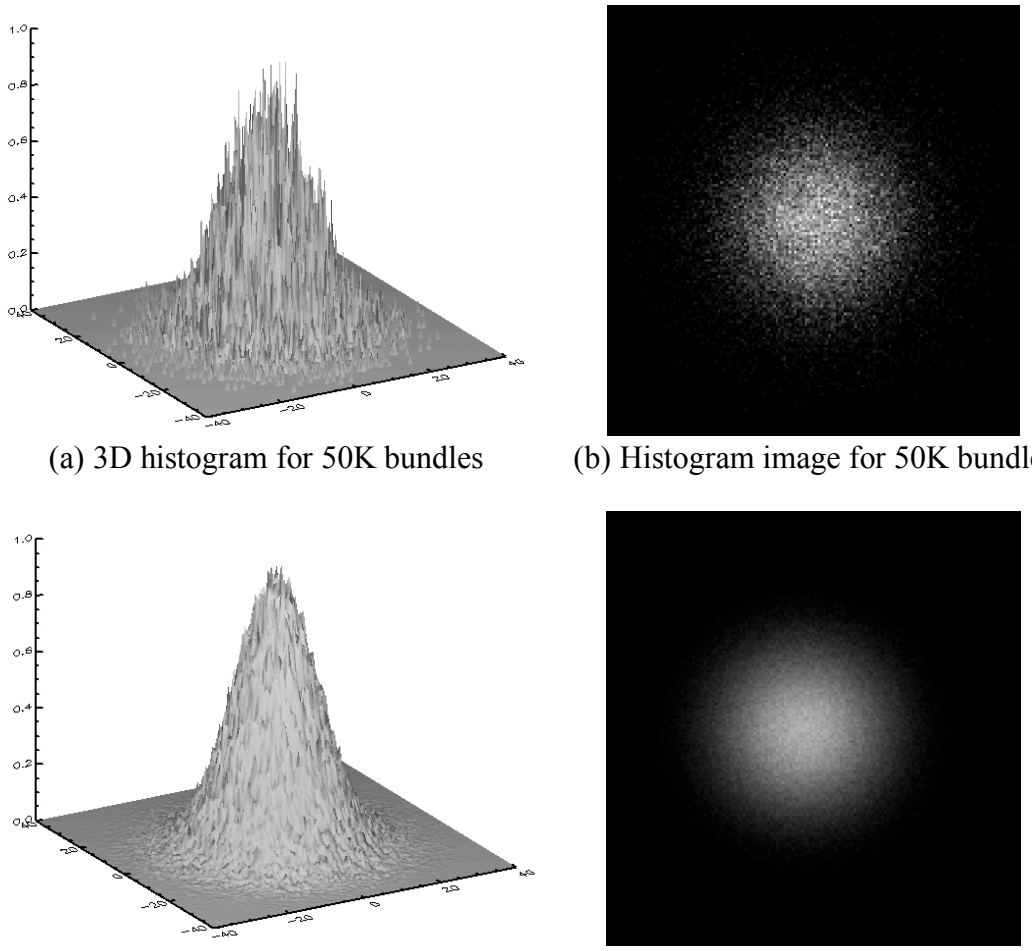


(a) Absolute error



(b) Relative error

Figure 95: Error for DIRSIG integrated number of photons detected for a single pulse reflected from a Lambertian surface at 1200 m downrange for a 0.5 mm detector



(a) 3D histogram for 50K bundles (b) Histogram image for 50K bundles

(c) 3D histogram for 1 million bundles (d) Histogram image for 1 million bundles

Figure 96: Normalized histogram of photon events recorded for a single LIDAR pulse intersecting a flat Lambertian plate 1200 m downrange

Based upon the results achieved for the topographic signal returns, the DIRSIG LIDAR model is accurately simulating the integrated power of the return signal for a topographic LIDAR pulse. Additionally, some practical implementation recommendations and limitations can be identified. First, casting more photon bundles into the scenes improves the accuracy of the results at the expense of computation time. This was expected for a photon mapping based LIDAR modeling approach. Second, casting approximately 50,000 bundles results in a reasonable accuracy (less than 0.1%) if the detector FOV and the beam footprint are fairly well matched. In other cases, the user should carefully consider increasing the number of

photon bundles cast. Thirdly, the model does have some inherent loss in precision during the calculations, which can be minimized to some degree by increasing the number of photon bundles shot into the scene. Fourthly, users must use caution if they elect to use the scalar inputs to ensure that the results fit within the dynamic range of a long integer. Lastly, the stochastic ray tracing approach has some limitations for scenes with very small geometrical form factors. This could be alleviated by adopting alternative shooting approaches such as "guided" photon mapping. "Guided" photon mapping attempts to cast photon bundles into the scene where they are most needed (where they will be eventually seen). The challenge is that the sampling process is no longer truly random and avoiding biases can be problematic. "Guided" photons also require additional computational overhead and were not deemed necessary at this point in the model development.

Another aspect investigated and plotted in Figure 97 was the impact of the detector size on the number of photons detected from the Lambertian surface. For these simulations, the wavelength was set to 532 nm. The upper boundary designated by the dashed line is the number of source photons and the maximum achievable integrated signal power. Once the detectors are collecting the majority of the transmit beam (detector pitch > 3 mm), then the number of photons detected varies linearly with the surface reflectance. However, when the detector sizes are such that the receiver FOVs are small compared to the transmit beam footprint, the geometrical form factor has a greater impact on overall number of detect photons and an incremental increase in detector size results in a dramatic improvement. This trend is consistent with theory and demonstrates that the model is appropriately handling the detector FOV effects for a detector limited system.

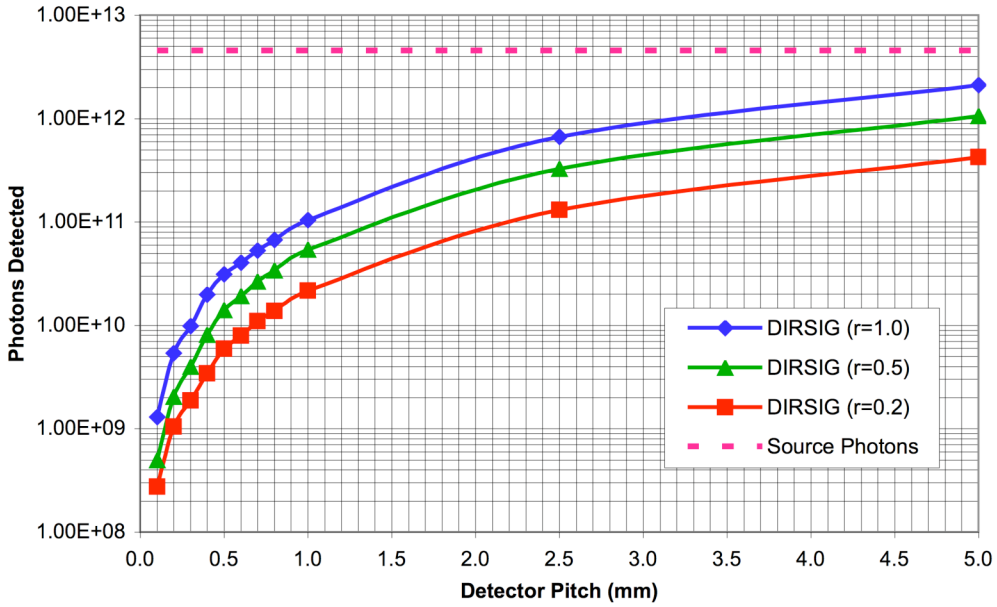


Figure 97: Detector size impact on the integrated number of photons detected from a Lambertian surface of varying reflectances at 1200 m downrange for a single pulse

5.1.3 Absorption by a Gaseous Layer

As discussed in Chapter 4, the verification of the attenuation by an absorbing layer was a direct extension of the topographic surface return analysis and was the first verification step for the new volume propagation components of the DIRSIG LIDAR model. The verification was broken into two distinct stages: verification of the internal ray tracing/propagation implementation and the integrated signal return. The first stage was added to demonstrate that the Monte-Carlo statistics are accurate for the tracing function, while the second confirms that the end-to-end modeling performance is accurate when an absorbing layer is present via analytical calculations using equation 284. Both scenes were setup based upon the baseline verification setup shown previously in Figure 80. To simplify the analysis, only the active LIDAR component was utilized, the number of photon bundles cast into the scene was fixed at approximately 50,000, and the detector FOV was setup to be much larger than the full transmit beam. The latter was done to decouple the detector size effects that were discussed in the previous section. The specific scene and test setup differences will be discussed below in the respective subsections.

5.1.3.1 Statistical Analysis

For the statistical analysis, 50,000 photon bundles or so were cast into a scene comprised of a 1 km thick absorption layer and a 100% absorbing ground plate. The latter mitigated any artifacts that might be induced by photon bundles that actually penetrated the layer and could then be reflected. The absorption coefficient for the homogenous layer was varied for each run over the range 0.005 to 0.1. The vertical distribution and associated statistics of the absorption events within the layer embedded in the photon maps was evaluated. In the absence of scattering and reflections, the histograms should be an exponential distribution with a mean and variance equal to the inverse of the absorption coefficient. The mean and variance results and absolute errors for the different absorption coefficients are plotted in Figure 98 and Figure 99 respectively. Despite only shooting 50,000 photon bundles, the statistics matched very well with the exception of the fairly small absorption coefficients. This is consistent with the photon mapping theory presented in Chapter 3 and the atmospheric implementation discussion in Chapter 4. Less likely events require that a more statistically significant number of photon bundles be cast into the scene.

Since the mean and variance do not necessarily guarantee that the vertical distribution is accurate, we shall now examine the actual distributions for four of those coefficients (0.005, 0.01, 0.05, and 0.1), which are plotted in Figure 100. The corresponding absolute error plots are shown in Figure 101. All of them agree fairly well with the predictions and the events are exponentially distributed in accordance with the absorption coefficient. As noted above, the less absorbing layers do exhibit an increase in error and could likely be improved by casting more photons into the scene. These results strongly indicate that the ray tracing propagation through absorbing media was implemented correctly.

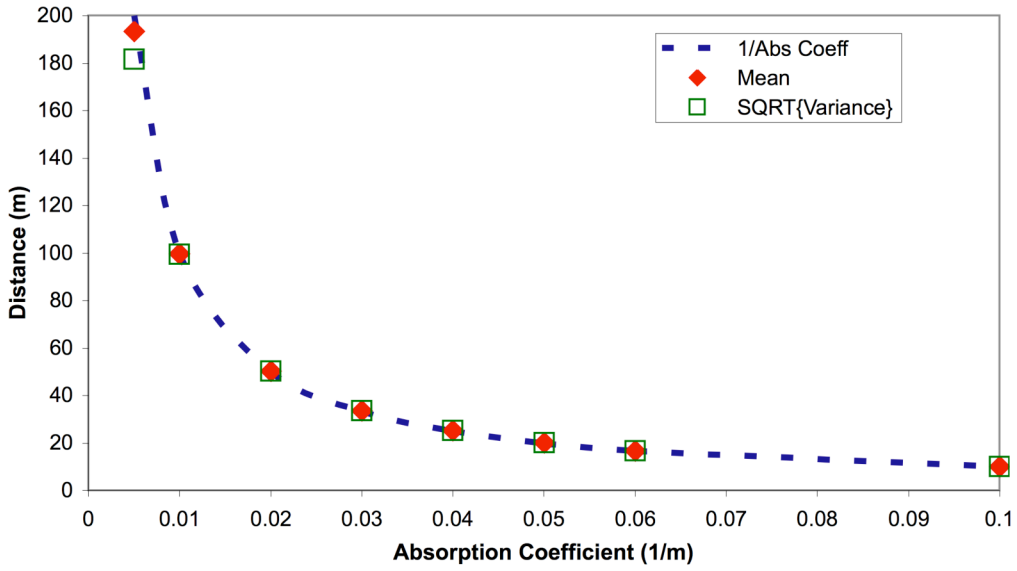


Figure 98: Analytical and modeled vertical distribution statistics of photons fired into different absorbing layers

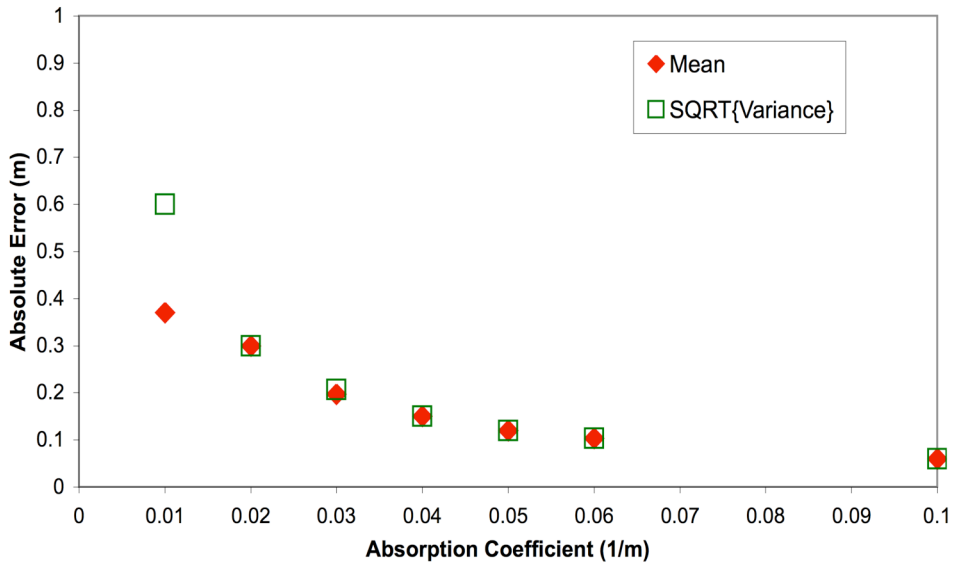


Figure 99: Absolute error for modeled vertical distribution statistics of photons fired into different absorbing layers

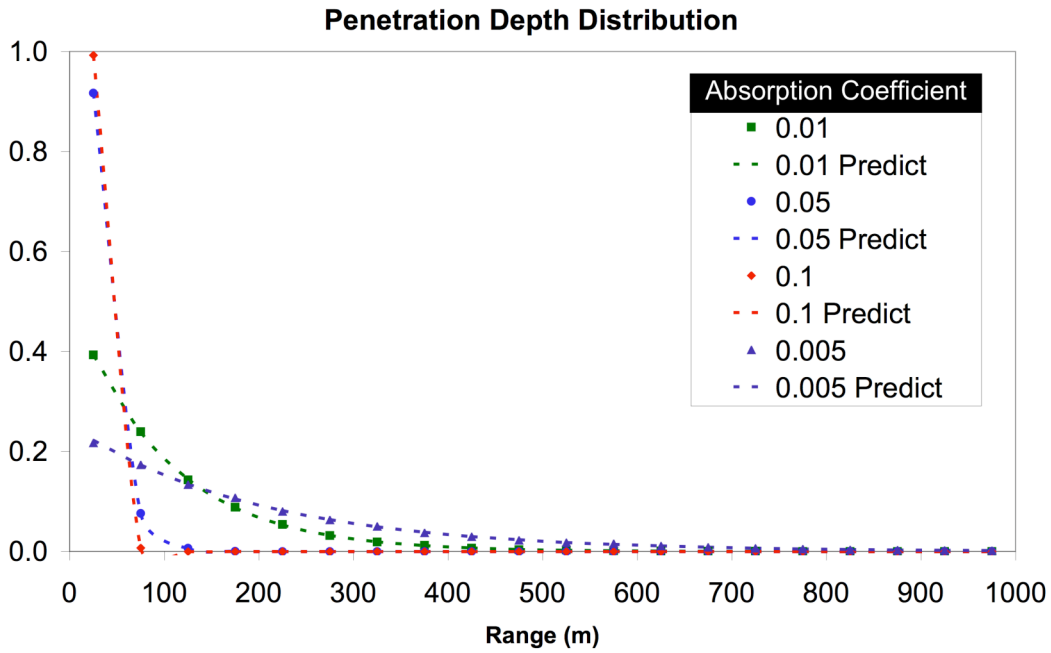


Figure 100: Analytical and LIDAR model vertical distribution of photons for different absorbing layers (penetration depth distribution)

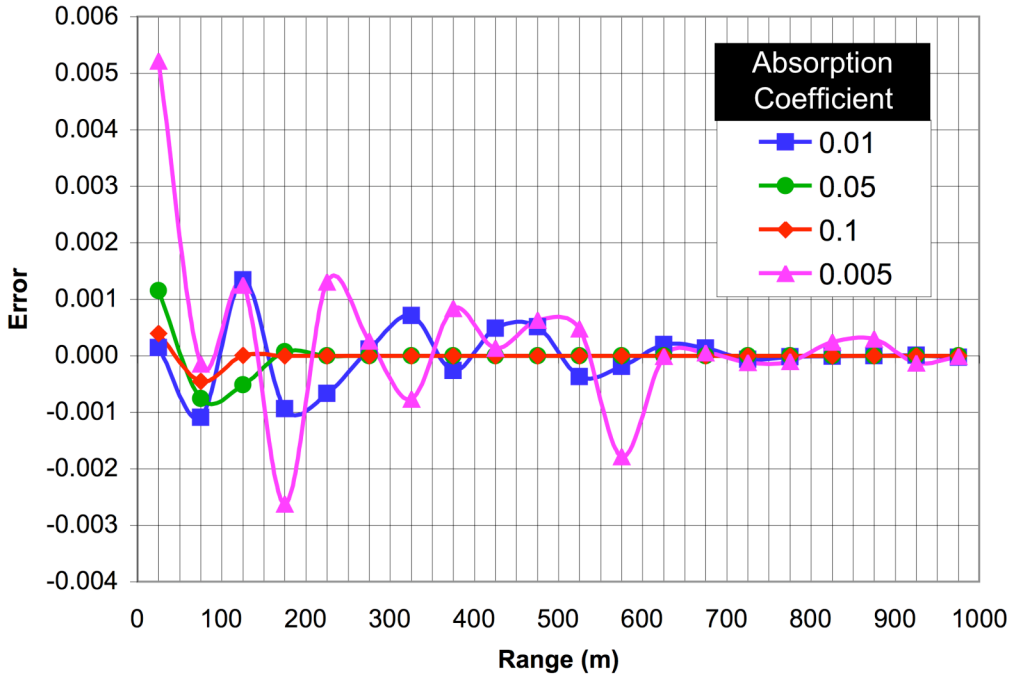


Figure 101: Modeling error for vertical distribution of photons for different absorbing layers (penetration depth distribution)

5.1.3.2 Integrated Return Signal

The analytical predictions for the integrated return signal through an absorbing layer were calculated based upon equation 284 and the LIDAR system parameters for Configuration A in Table 13. For this analysis, the surface reflectance and the optical depth of the absorbing layer were varied. As with the topographic return verification cases, the integrated return signal power was compared to the analytical predictions. Figure 102 and Figure 103 are plots of the DIRSIG results and the associated errors. The returns were plotted for plates with a reflectance of 0.18, 0.5, and 1.0. Consistent with radiative transfer theory, the integrated number of photons exhibits an exponential decay as the optical depth increases. The absolute error is on the order of 10^9 photons (~1.61×10^{13} photons were transmitted). The absolute error is not a significant increase over the error we observed with just surfaces and casting only 50,000 photon bundles. The relative errors are worse than the surface-only errors because of the attenuation of the overall signal, particularly for the thicker optical depths. The absolute error is more significant when compared to the overall received signal power. For this simplistic scene, 50,000 photon bundles were sufficient; however, increasing the number of photon bundles cast will probably be necessary to accommodate a DIAL simulation.

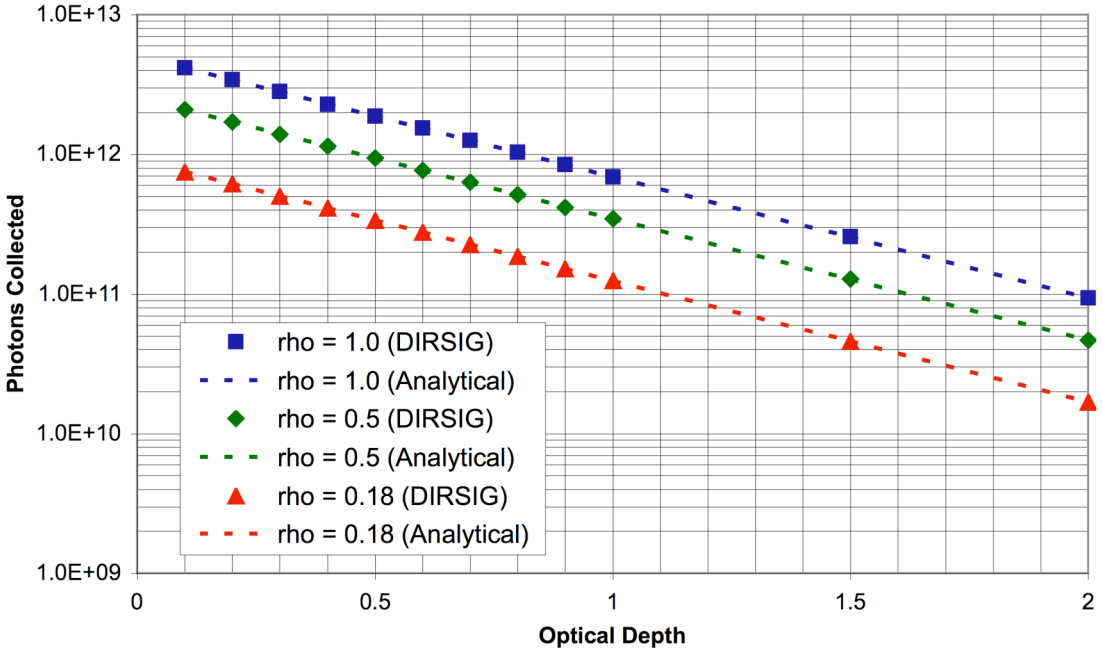
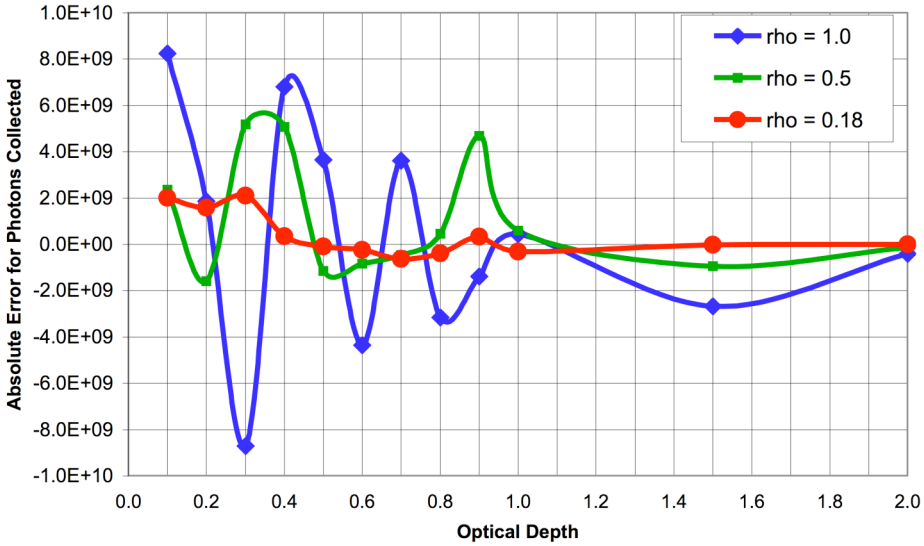
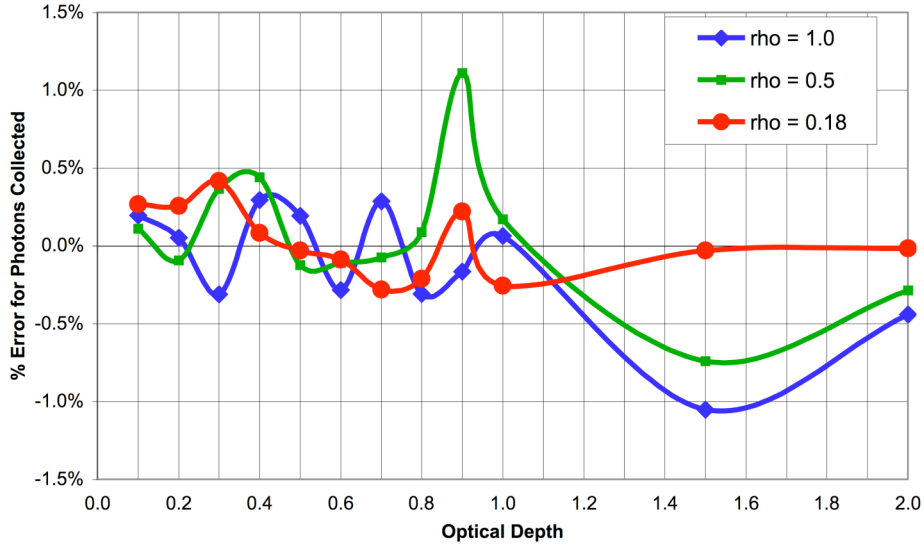


Figure 102: DIRSIG integrated number of photons detected for a single pulse reflected from a Lambertian surface at 1200 m downrange and attenuated by an absorbing gaseous layer of varying optical depths



(a) Absolute error



(b) Relative error

Figure 103: DIRSIG error for integrated number of photons detected for a single pulse reflected from a Lambertian surface at 1200 m downrange and attenuated by an absorbing gaseous layer of varying optical depths

5.1.4 Scattering by a Gaseous Layer

One of the most challenging requirements for the DIRSIG LIDAR module development was to accurately model the effects of multiple scattering for the LIDAR pulses as they interact with a complex scene and in particular scattering media. The previous verification process established that the volume support functionality within DIRSIG was operational and producing accurate results for the simplified case of attenuation due to absorption. This subsection builds upon those results and explores the validity of the photon mapping approach to model multiple scattering for nonstationary directional sources. Similar to the absorption verification process, the scattering verification is broken into two stages: verification of the internal ray tracing/propagation implementation and the comparison of the simulated temporal signature with the BSN approximation and multiply scattered LIDAR equation derived in Chapter 3. The verification of the interal ray tracing/propagation implementation focuses on the core photon mapping architecture that was added to DIRSIG and the results could be extrapolated for other simulation efforts. The evaluation of the simulated temporal signature from a high powered, short duration pulse fired into an optically thick layer directly provides a measure of the applicability of this modeling approach for LIDAR systems and particularly for DIAL sensors.

For all of the results presented in this subsection, the standard verification scene shown previously in Figure 80 was used. In general, photons were cast into an optically thick water cloud over a 100% absorbing surface. The optical parameters of the scattering layer were generally established using Mie codes for most of the results or published literature parameters for direct comparisons to relevant published results. In some instances for the statistical analysis, the asymmetry parameter was intentionally varied over unrealistic values for water clouds because we wanted to characterize the performance and behavior of the model. This performance and behavior could then be qualitatively compared with the foundational principles of light scattering. Consistent with the spiral development philosophy, the passive and thermal radiance contributions were not included for these verification tests and will be discussed independently of these results.

5.1.4.1 Statistical Analysis

The statistical analysis phase of the multiple scattering verification process is based upon published results in the literature for photon scattering statistics in plane-parallel atmospheres and more specifically cloud layers. The initial concepts behind how we would verify the Monte Carlo scattering statistics associated with a DIRSIG LIDAR simulation were specifically based upon the work published by Platnick (2001a, 2001b). Platnick developed an analytical technique using superposition priniciples to calculate the veritical and horizontal distribution of photons within a cloud layer. The technique was specifically designed for atmospheric cloud layers; however, it is applicable to the general parallel-plane layer radiative transfer problems. Although the detailed derivation and discussion of the superposition formulae and validation will be not be covered in this dissertation, comparison of DIRSIG's results with some of Platnick's will be discussed towards the end of this subsection. The scattering statistics can be directly correlated to the resulting radiative transfer of photons within a multiple scattering medium. While Platnick was focused on photon transport in clouds, the techniques and results can be applied to any multiple scattering plane-parallel radiative transfer problem, including scattering of LIDAR pulses. For instance, the number of scattering events is closely linked to the mean photon path length and other moments of the photon path distribution. As discussed in Chapter 3, if the distribution of photons in the scattering layer is known, then the backscattered signal return can be directly determined. Thus, if the Monte Carlo statistics of the photon distribution calculated by DIRSIG is consistent with underlying photon transport theory and associated statistics, then we can have a greater degree of confidence in the new modeling approach. Additionally, the changes in the mean photon path length due to scattering may be a key contributor to potential measurement errors for a DIAL system in the presence of scattering. Therefore, evaluation of these statistics may also provide us insight into how scattering might affect DIAL collection scenarios.

As stated above, the standard simplified verification scene was used. The surface was 100% absorbing and the participating medium is an optically thick, highly scattering, weakly absorbing, homogeneous plane-parallel layer. A specialized mono-directional pulsed laser source was incorporated into the DIRSIG sensor architecture to be used in this analysis. The

mono-directional pulsed laser source randomly casts bundles into the scene parallel to the user-defined optical axis of the system from a user-defined aperture area. Additionally, a detailed events data file was recorded during the propagation of those photon bundles within the scene. The events data file, which includes every decision by DIRSIG during the photon bundle tracing phase, was then processed to generate the statistical results shown in this subsection. The statistics were then subdivided into two groups, reflected photons and transmitted photons. Reflected photons are defined as any photon that entered and subsequentially exited the layer via the top boundary. Transmitted photons are defined as any photon entering the top boundary of the layer and then exiting through the bottom layer of the boundary. The participating layer is semi-infinite in the horizontal direction; therefore, all of the photon bundles cast into the scene are declared reflected, transmitted, or absorbed photons for the purposes of this analysis. The distribution of photons indicated by the events file was evaluated based upon the vertical distribution of scattering events and the horizontal displacement of the reflected and transmitted photons.

For the first set of statistical analyses, calculations are for a homogenous layer with an optical thickness of 10. The scattering albedo was 0.9928 and the asymmetry parameter was varied. The scattering layer has to be sufficiently thick enough to ensure that the photon scatterings are uncorrelated in each dimension (vertical and horizontal) and to ensure that the horizontal transport is driven by the scattering in the layer and not just the geometry of the scenario. In essence, a large number of scatterings for an anisotropic layer are necessary to ensure sufficient directional randomness. Approximately 50,000 photon bundles were cast into the scene at a grazing angle of 45 degrees (μ=0.707).

Figure 104 is a plot of the number of reflected photons and transmitted photons as the asymmetry parameter is varied. For an isotropic scattering phase function, the majority of the photons are reflected. As the scattering becomes more forward, the number of reflected photons decreases and the transmitted photons increase. They are approximately equal when the asymmetry parameter is approximately 0.875. The transition between reflected and transmitted photons is more rapid once the layer is essentially forward scattering (> 0.6) and

is particularly sensitive to any changes in the scattering phase function at around the 0.8 to 1.0 region.

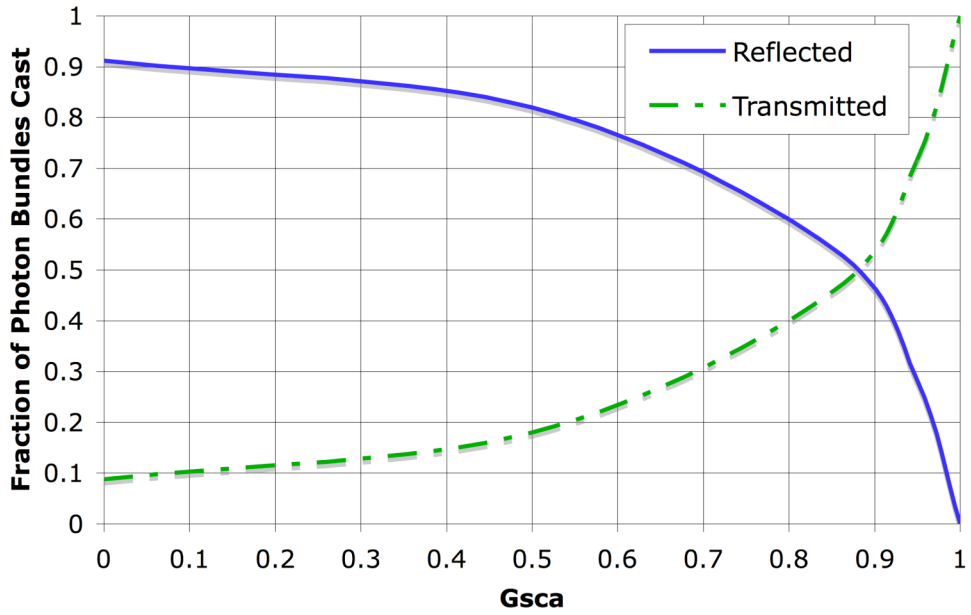


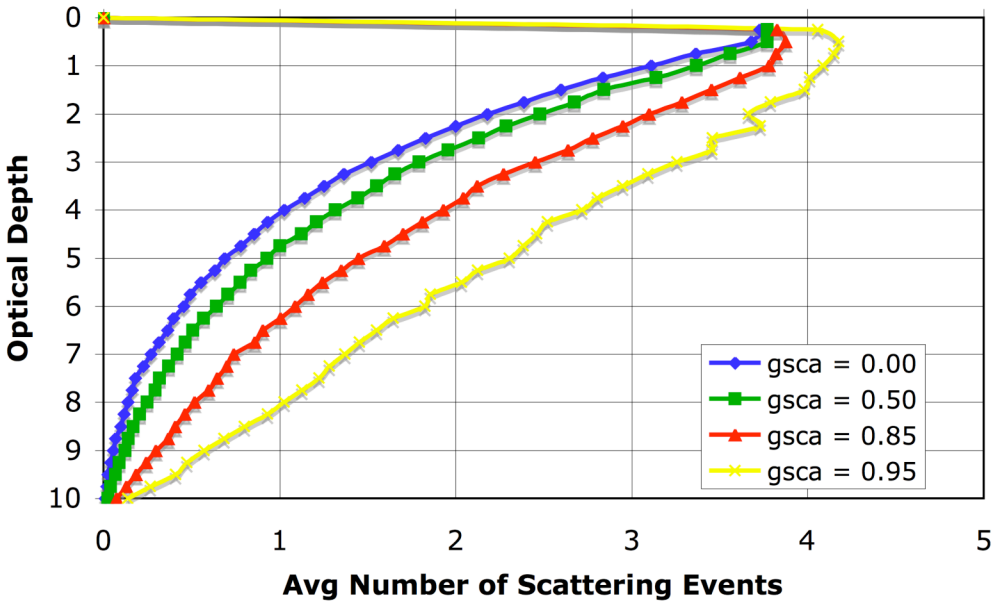
Figure 104: Fraction of photon bundles cast into a thick scattering layer that are reflected or transmitted as the asymmetry parameter is varied (τ = 10.0; ω_0 = 0.9928; μ=0.707)

The average number of scatterings encountered by reflected and transmitted photons within any arbitrary layer of the plane-parallel homogenous medium was also calculated and a subset of the results is shown in Figure 105. The vertical distributions for the reflected photons peaks just below the layer's top and then decrease towards the layer's base. The maximal contribution to the return signal comes from the portion of the layer indicated by the position of the peak in the reflected photon vertical distribution. In contrast, the transmittance distributions are symmetric to some degree and exhibit a broad maximum throughout the middle layers of the cloud. The contributions from the different levels in the layer for transmitted photons are approximately equal. As the asymmetry parameter increases and the scattering phase function scatters more in the forward direction, the reflected photon distribution shifts indicating that the photons spent more time in the middle portion of the layer and the average number of scatterings for a photon increased, which is shown in Figure 106. Thus, the reflected photons experienced a longer mean optical path length. This effect is

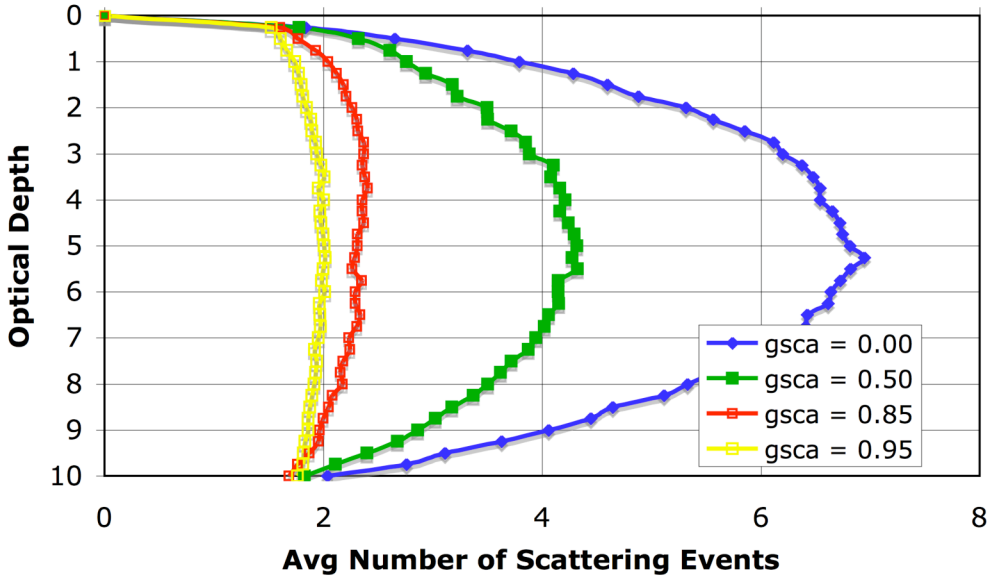
combined with the reduction of the overall number of reflected photons and the backscattered signal discussed earlier.

The average number of scattering events for the transmitted photons in Figure 106 decreases more linearly as the layer scatters more in the forward direction. The photons are essentially spending less time "meandering" in the layer and the mean optical path length is decreasing as the asymmetry parameter increases. It is worth mentioning that other factors, such as the scattering albedo and optical depth, are key factors in determining the average number of scattering events within the layer and additional cases could be pursued in future research efforts to develop a deeper understanding of the underlying physics. At this point, the results indicated that the model's vertical photon distribution statistics were behaving reasonably. The direct comparison of DIRSIG's results to Platnick's published research for the vertical distribution of the reflected and transmitted photons will be discussed later in this subsection.

We now consider the horizontal photon distribution of the reflected and transmitted photons. In particular, we generated the statistical distributions for the horizontal displacement of the photons from their entry point to their departure point at the boundaries of the layer. The results for four different asymmetry parameters (0.0, 0.5, 0.85, and 0.95) are plotted in Figure 107. In general, the horizontal displacement of photons due to a high scattering layer is non-trivial. Based upon both the horizontal and vertical data, as the scattering becomes more forward, the additional reflected photons occur in the shallow region of the layer and the exit point is near the entry point. Therefore, the mean optical path length traveled by the reflected photons decreases as the layer scatters more isotropically. As the asymmetry parameter increases, the transmittance function scales and narrows. The beam is becoming more focused and is diffused less as is shown in the histogram images of the absorption events for the surface which was 2 m below the layer Figure 108. Additionally, the elliptical spread of the beam is primarily due to geometrical projection effects.



(a) Reflected photons



(b) Transmitted photons

Figure 105: Average number of scattering events within a cloud layer with an optical thickness of 10.0 and a scattering albedo of 0.9928 for all (a) reflected and (b) transmitted photons for various asymmetry parameters

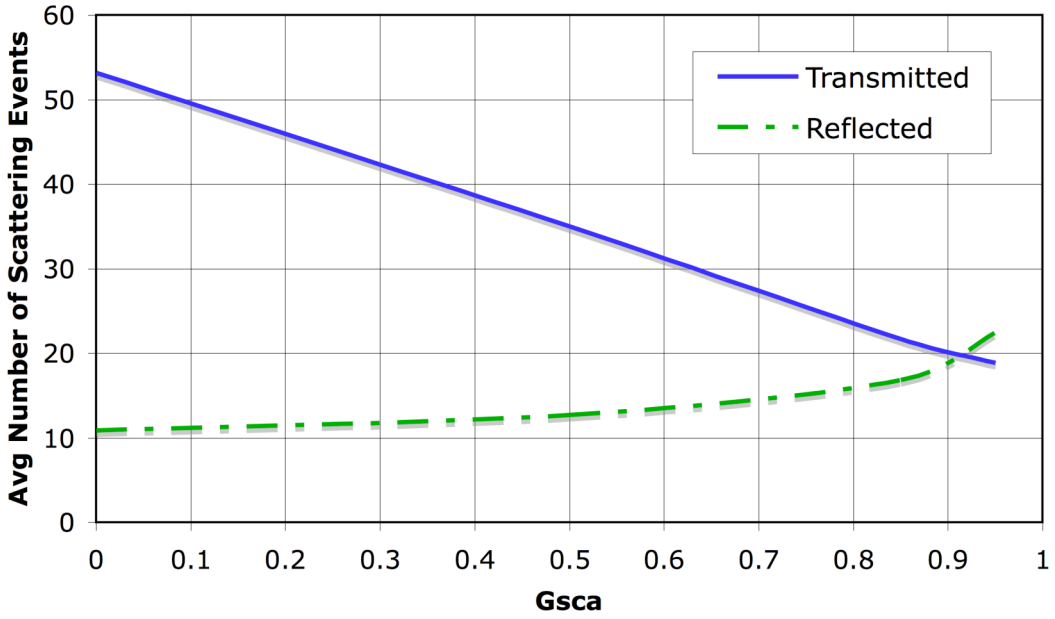
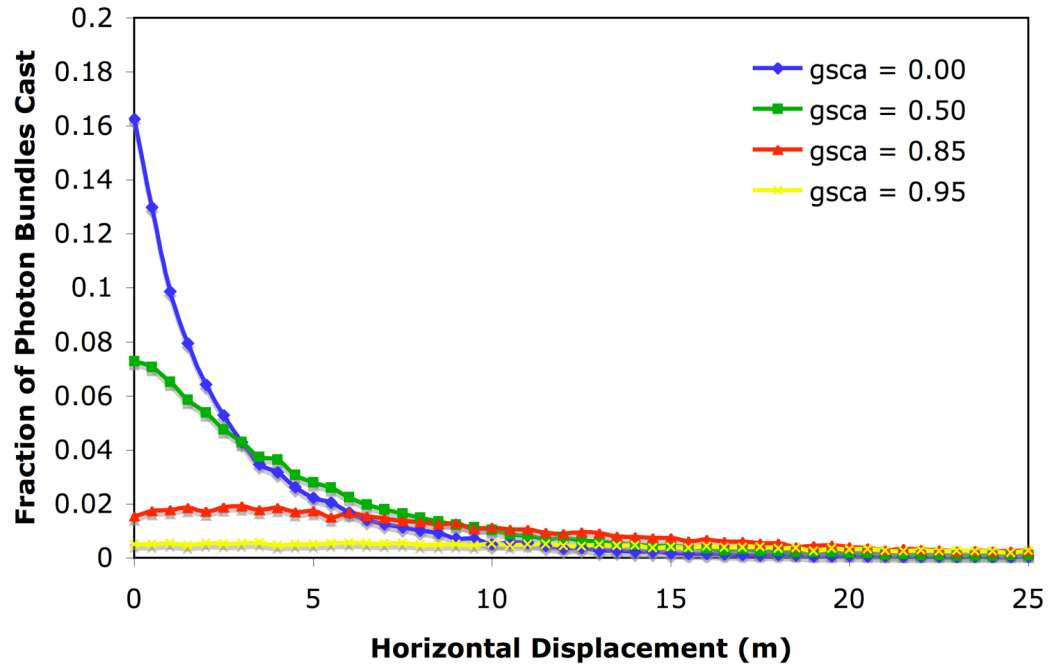
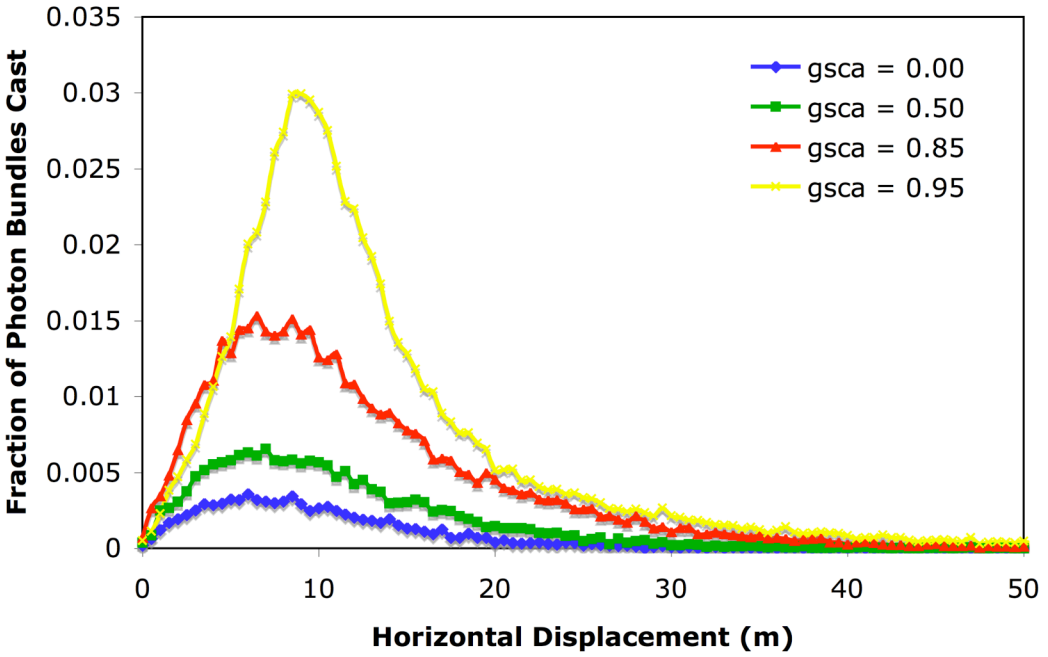


Figure 106: Average number of scattering events in a scattering layer for reflected and transmitted photons as the asymmetry parameter is varied ($\tau = 10.0$; $\omega_0 = 0.9928$; $\mu=0.707$)

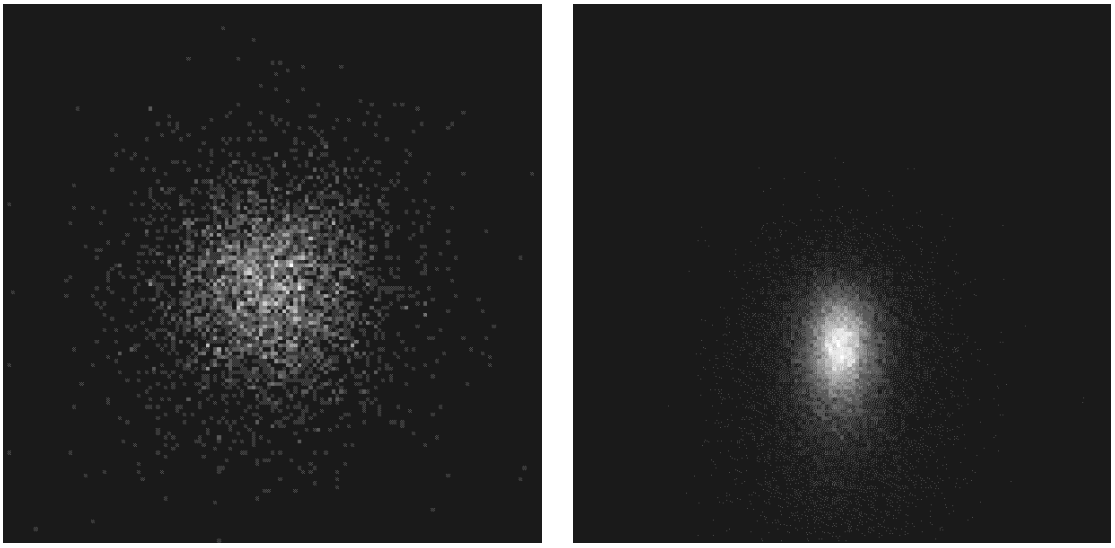


(a) Reflected photons



(b) Transmitted photons

Figure 107: Horizontal displacement distribution for photon bundles cast into a scattering layer ($\tau = 10.0$; $\omega_0 = 0.9928$; ; $\mu=0.707$; $g_{sca} = \{0.0, 0.5, 0.85, 0.95\}$)



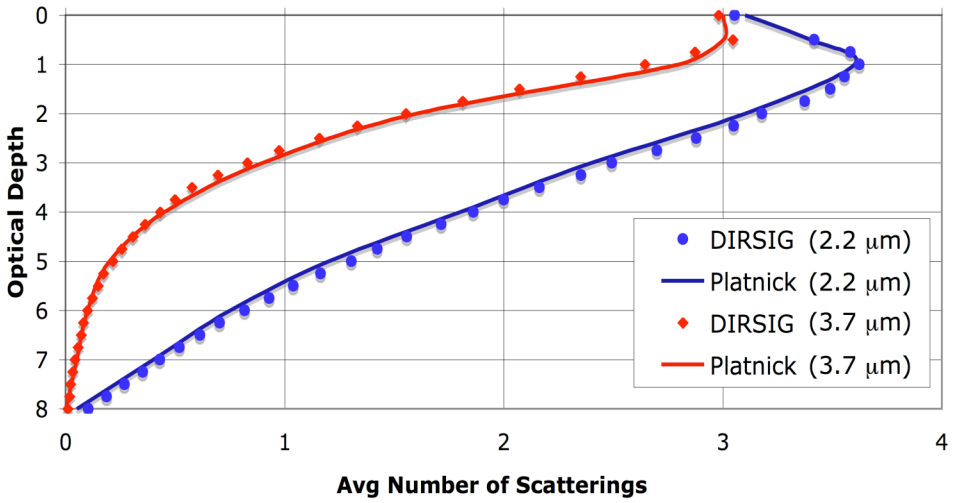
(a) $g_{sca} = 0.00$ (b) $g_{sca} = 0.95$

Figure 108: Histogram image of absorption events at the surface 2 m beneath the layer occurring within ±35 m of the scene center for horizontal displacement calculation ($\tau = 10.0$; $\omega_0 = 0.9928$; μ=0.707)

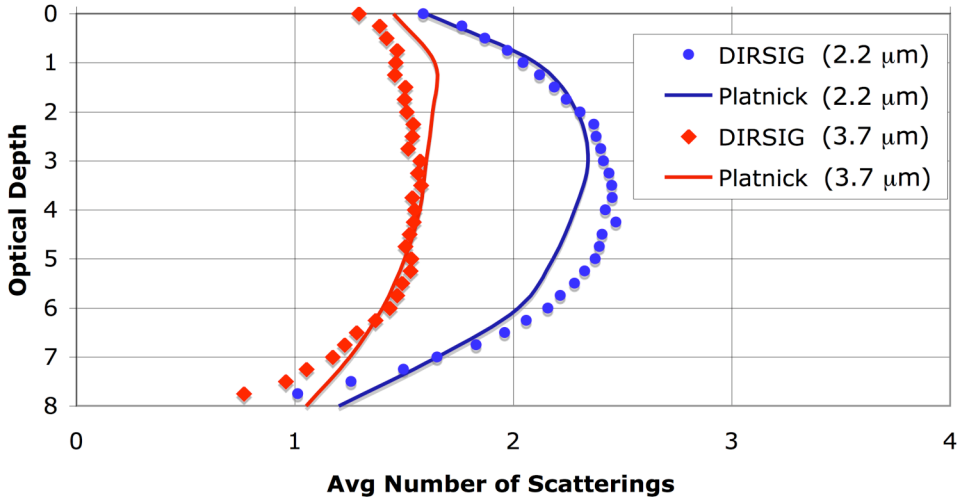
We now shift and compare the results for the vertical distribution of the average number of scatterings per differential layer for reflected and transmitted photons calculated from DIRSIG's events file with the results obtained using Platnick's superposition technique (2001). The scene is comprised of a liquid water cloud layer with an optical depth of 8. The cloud droplet particle size distribution is a gamma distribution with a 10mm effective radius and an effective variance of 0.1. The cosine of the incidence angle was 0.65. The optical properties used by Platnick are listed in Table 15 and were generated using a Mie code and were averaged over two of the typical atmospheric remote sensing instrument spectral response functions (Platnick, 2001). These same parameters were used for the DIRSIG simulations and new parameters were not re-generated. DIRSIG's and Platnick's results for the two spectral bands (2.2 and 3.7 μm) are shown in Figure 109. The predictions using Platnick's superposition formulae and DIRSIG's Monte Carlo approach are quite different, but produce very similar results. The integration of theses curves provide us with the average number of scattering events for a reflected and/or transmitted photon and are listed in Table 16. Once again, the DIRSIG results are fairly comparable to Platnick's. Some of the small discrepancies are likely due to differences of the layer's scattering phase function. In particular, the use of the Henyey-Greenstein approximation instead of a Mie code generated scattering phase function probably introduced some error into these calculations.

Table 15: Scattering parameters averaged over typical remote sensing instrument spectral response functions for a cloud droplet size spectra (Platnick, 2001)

Spectral Band (μm)	Scattering Albedo (ω_0)	Assymetry Parameter (g_{sca})
2.2	0.979	0.834
3.7	0.900	0.794



(a) Reflected photons



(b) Transmitted photons

Figure 109: Theoretical and DIRSIG average number of scattering events within a cloud layer with an optical thickness of 8.0 for all (a) reflected and (b) transmitted photons for two common remote sensing spectral bands (Platnick, 2001)

Table 16: Average number of scattering events for reflected and transmitted photons cast into cloud layer with an optical thickness of 8.0 and optical parameters in Table 15

Wavelength (μm)	Platnick (2001)			DIRSIG		
	Reflected (N_r)	Transmitted (N_t)	Total (N_{total})	Reflected (N_r)	Transmitted (N_t)	Total (N_{total})
2.2	14.6	16.5	31.1	12.48	17.4	29.9
3.7	7.2	12.2	19.4	7.9	12.2	20.1

5.1.4.2 Temporal Signature of Backscattered Power

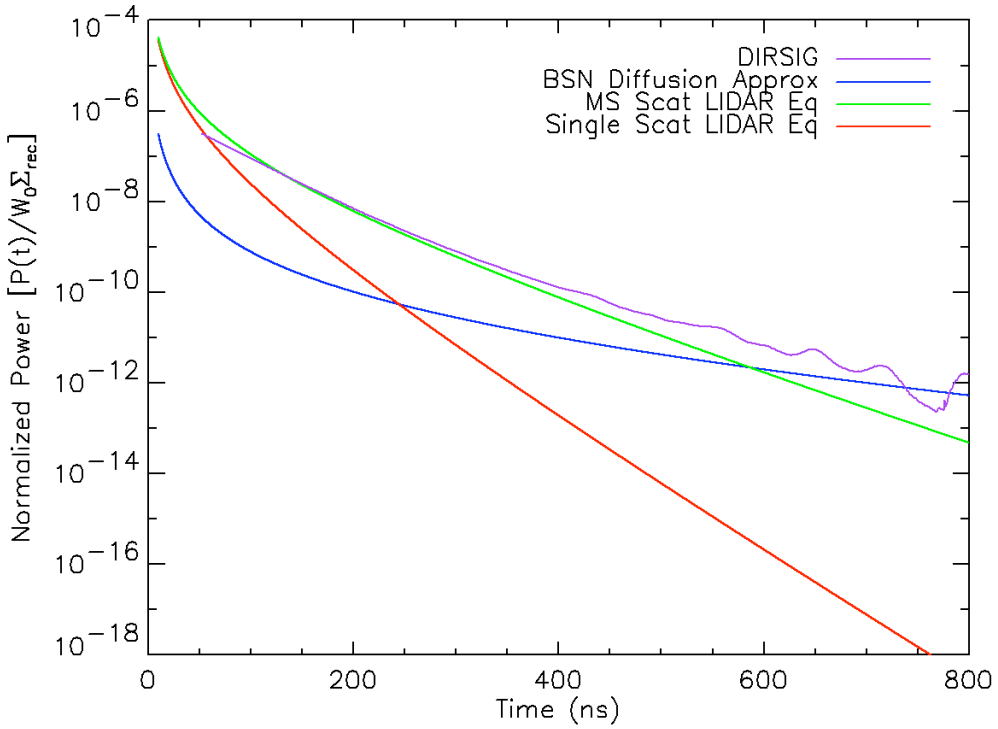
In Chapter 3, the multiply scattered LIDAR equation and the non-stationary diffusion approximation were developed as a reasonable benchmark for the verification of the model to accurately simulate backscattered returns, particularly deep from within a scattering layer. Each approximation has its strengths and weaknesses. In particular, the diffusion approximation significantly underestimates the received power from ranges near the boundary edge. The singly and multiply scattering equations provide a much better estimate for the top of the layer. In contrast, the multiply scattering LIDAR equation underestimates the backscattered return from deep within the layers. Additionally, Chapter 3 compared the predictions of these approximations for backscattered return from a high-powered mono-directional pulse fired into a semi-infinite scattering layer. In this subsection, the DIRSIG results for that same scenario are presented.

The scene is comprised of a semi-infinite scattering layer and a 100% absorbing planar surface. The scattering layer is optically thick enough so that the pulse never reaches the absorbing plate. The participating layer was modeled after a C1 cloud and had an extinction coefficient of 0.1 m^{-1} and a scattering albedo of 0.9. The asymmetry parameter was 0.863. The incident beam was collimated, and the co-located receiver and transmitter were located at the boundary for the top of the layer. DIRSIG's LIDAR module then simulated the backscattered return from the high-powered pulse. The time-domain signal return was highly oversampled and then normalized to eliminate the detector effects and to enable direct comparison to the non-stationary diffusion approximation. To ensure adequate statistics for the photon distribution deep within the scattering layer, approximately 3 million photon

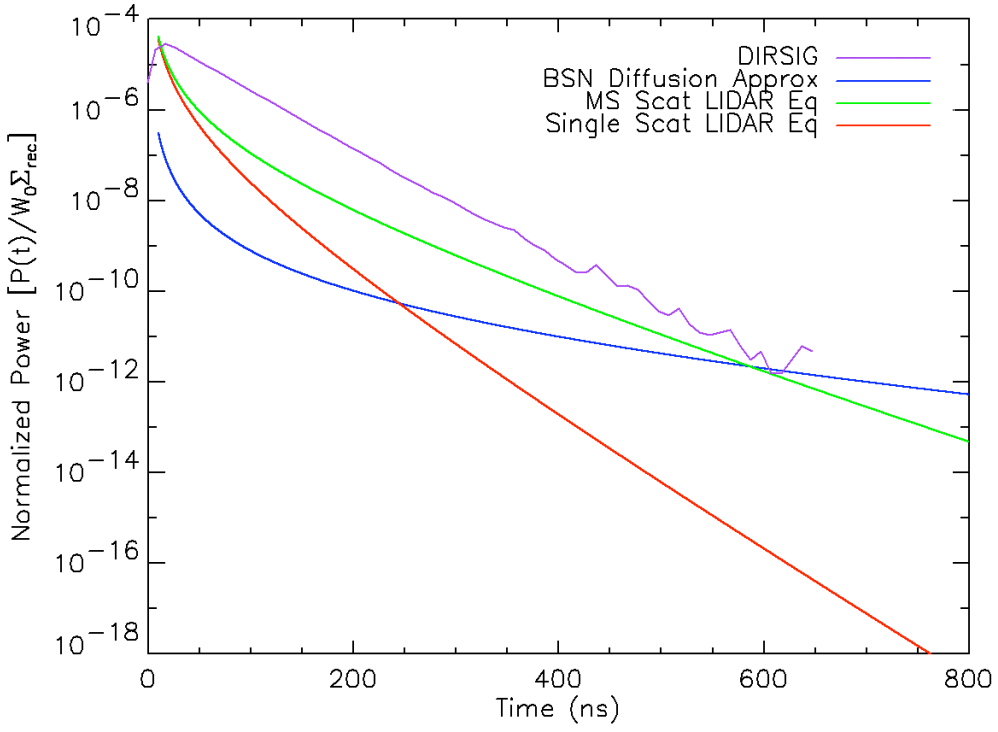
bundles were shot into the scene. DIRSIG's backscattered return along with the singly scattered LIDAR equation, multiply scattered LIDAR equation, and the non-stationary diffusion approximation (evaluated using the BSN approximation) are shown in Figure 110(a). For Figure 110(b), the scattering phase function for the layer was isotropic.

As anticipated, DIRSIG's results track Eloranta's multiply scattered LIDAR equation for returns from the top portion of the layer and eventually transition to the non-stationary diffusion approximation at an optical depth of 10, which is somewhere around 600 ns. The simulated returns from areas in close proximity to the receiver at the top of the layer do not appear to be as accurate. This is likely due to the receiver FOV convention used by DIRSIG. DIRSIG assumes that the FOV is a pyramid and does not fully account for the receive aperture collection area very close to the receiver. In essence, DIRSIG doesn't collect all of the photons really close to the aperture.

For the isotropic scattering case, the multiply scattered LIDAR approximation under-predict the return because it is based upon a forward scattering assumption. As demonstrated with the statistical analysis of the scattering events within a participating layer, the number of reflected photons near the top of the boundary are greater for an isotropic scattering phase function than for a forward scattering phase function. For the backscattered return from deep within the layer, the non-stationary diffusion approximation should still represent an asymptotic boundary and the DIRSIG results appear to be converging as expected. To accumulate sufficient statistics for the photon distribution deeper in the layer than what is shown or to reduce the variability (the "wiggle") in the simulated backscattered return would require increasing the number of photon bundles cast into the scene.



(a) Forward scattering layer (g_{sca}=0.863)



(b) Isotropic scattering layer (g_{sca}=0.0)

Figure 110: Normalized backscattered power from a semi-infinite scattering layer

5.1.5 Passive/Thermal Contributions

One of the advantages of the new DIRSIG LIDAR module is that the LIDAR radiance solver has direct access to both of the legacy passive and thermal radiance solvers. These radiance solvers offer a great deal of flexibility and fidelity to the model. The purpose of the passive and thermal contributions demonstration is to verify that the passive and thermal radiance solvers were incorporated into the model correctly. To accomplish this objective, the integrated topographic signal return from a Lambertian planar surface was simulated at noon and midnight. MODTRAN was used to build the DIRSIG atmospheric input files for a mid-lattitude summer atmosphere in Rochester, NY. The key LIDAR system and the scenario's atmospheric parameters are listed in Table 17. The direct solar, downwelled, and upwelled radiance listed are averaged values from the MODTRAN output files. A single pulse was simulated and the output LIDAR cube was generated for a short 0.2 μsec listening window.

The equation used to calculate the predicted total radiance at the detector including the passive and emissive contributors was:

$$L_{total} = \tau_1\tau_2 \frac{E_s}{\pi}\rho_{surf}\Delta t + \tau_2 L_{up}\Delta t + \tau_2 L_{down}\frac{\rho_{surf}}{\pi}\Delta t + \tau_2\tau_2 L_{LIDAR}\frac{\rho_{surf}}{\pi} + \tau_2 L_e \Delta t \qquad (285)$$

where E_s is the irradiance from the sun, ρ_{surf} is the reflectance of the surface, τ_1 is the downward optical transmission for the sun to the target, τ_2 is the upward path transmission from the target to the sensor, L_{up} is the upwelled radiance from the atmosphere, L_{down} is the downwelled radiance from the atmosphere, L_{LIDAR} is the radiance of the LIDAR pulse, L_e is the thermally radiance emitted towards the receiver, and Δt is the length of the listening window. Based upon this equation and the MODTRAN generated atmospheric parameters, the breakdown of the contributions to the integrated signal return are listed in Table 18. The values listed are the contributions at the detector due to the respective sources. Note that the thermal model was disabled to simplify the analysis. Thus, the emissive term was zero.

The comparison between DIRSIG and the analytical predictions is shown in Figure 111 and the corresponding error plots are included in Figure 112. Based upon the predictions, the

noon and midnight curve are accurately offset on a log-plot by about 2.11×10^{13} photons. The averaging of the downwelled radiance for the prediction calculations contributed to the final error and is probably the driver behind the surface reflectance dependence of the error. However, the overall accuracy of the model is very good and the errors are generally consistent with the results shown previously.

Table 17: LIDAR system parameters and MODTRAN output data for solar verification scenes

Parameters	Noon	Midnight
Pulse Power	6.0 μJ	6.0 μJ
Wavelength (λ)	532 nm	532 nm
Integration time (t)	2 μsec	2 μsec
Detector Pitch (x_a)	50 mm	50 mm
Solar Path Attenuation (τ_1)	0.8648	0.7005
Sensor Path Attenuation (τ_2)	0.9847	0.9853
Direct Solar Irradiance (E_s)	0.183 W/cm^2	2.34E-07 W/cm^2
Upwelled Irradiance (E_{up})	2.59E-04 W/cm^2	1.67E-10 W/cm^2
Downwelled Irradiance (E_{down})	1.90E-03 W/cm^2	1.32E-09 W/cm^2

Table 18: Breakdown of key contributors for solar verification scenes

Contributor	Noon (photons)	Midnight (photons)
LIDAR	4.97E+12	4.97E+12
Solar	2.09E+13	2.16E+07
Upwelled	3.47E+10	2.20E+04
Downwelled	2.50E+11	1.74E+05
Total Passive	2.11E+13	2.18E+07
Total Detected	2.61E+13	4.97E+12

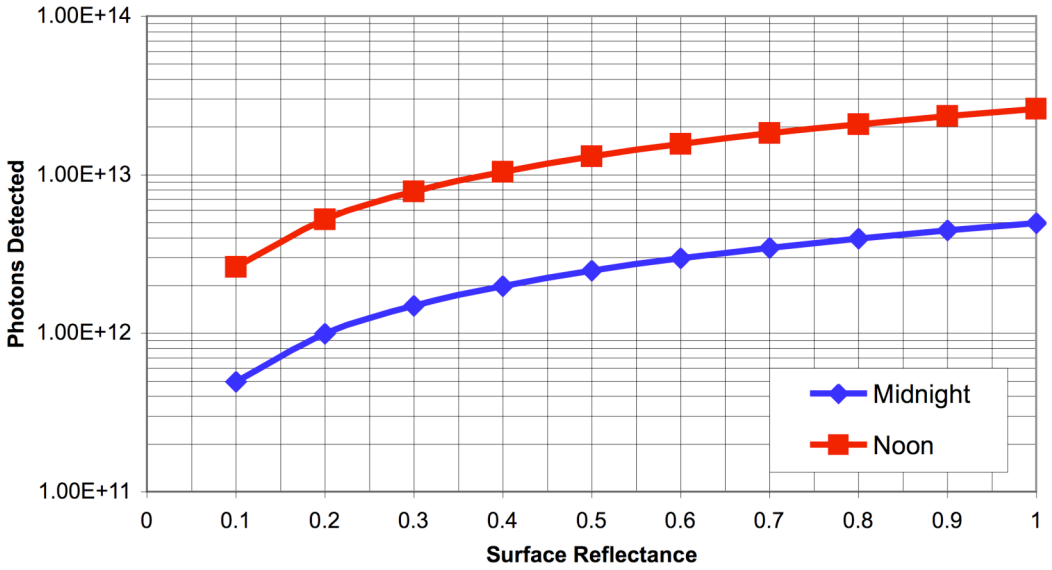
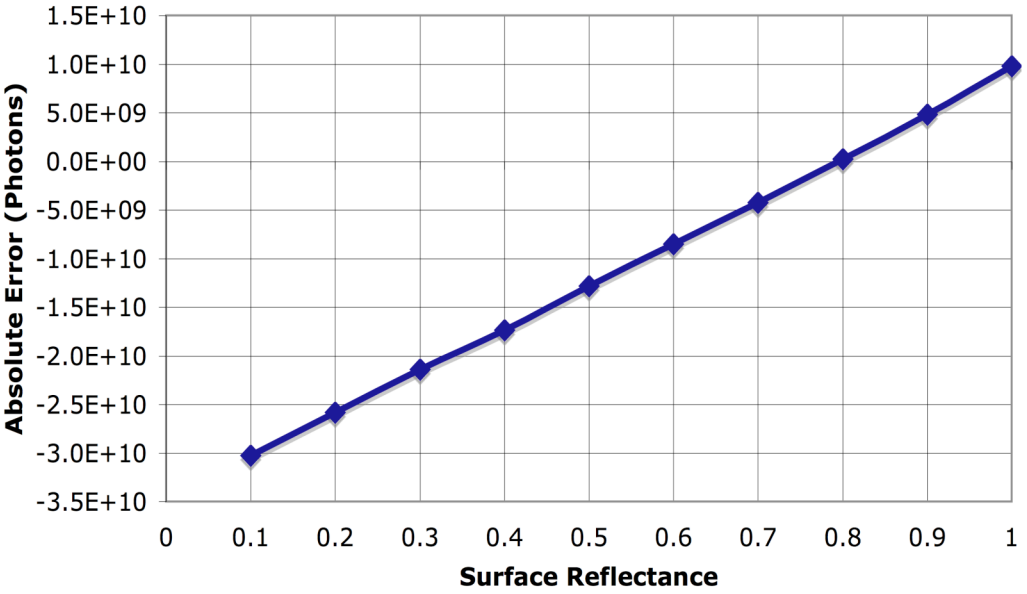
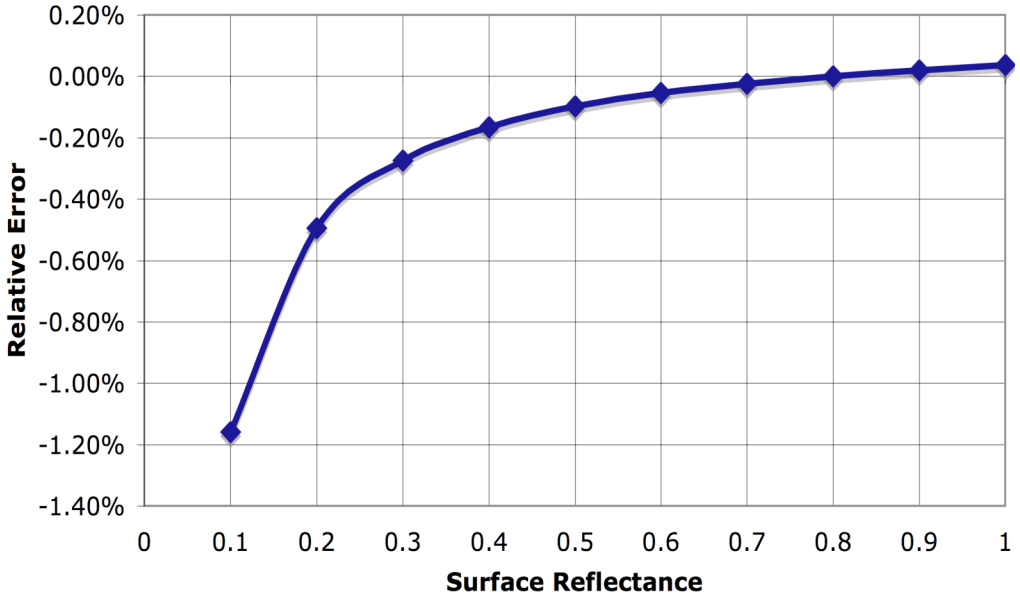


Figure 111: Passive solar contribution for a pulse fired a Lambertian plate with different reflectances (mid-latitude summer atmosphere; Rochester, NY)



(a) Absolute error



(b) Relative error

Figure 112: Error for passive solar contribution for a pulse fired a Lambertian plate with different reflectances (mid-latitude summer atmosphere; Rochester, NY)

As a demonstration of the inclusion of the thermal model and emissive radiance solver into the DIRSIG LIDAR module, simulated data sets were generated while varying the absorption coefficient for a gaseous layer at various temperatures positioned 100 m above a 18% Lambertian planar surface. The LIDAR system used the standard Configuration A described

previously in Table 13. Similar to the passive simulations run earlier, MODTRAN was used to build the atmospheric table for a mid-lattitude summer night in Rochester, NY. The signal was integrated over a short listening window of 0.2 μsec. The simulated photons collected at midnight for different temperatures and absorption coefficients are shown in Figure 113. The increase in temperature effectively bends the curve upward and the emissive term eventually dominates for layers with higher absorption coefficients and temperatures. This is one reason why DIAL measurements are often performed downwind and not at the release point for hot factory stacks.

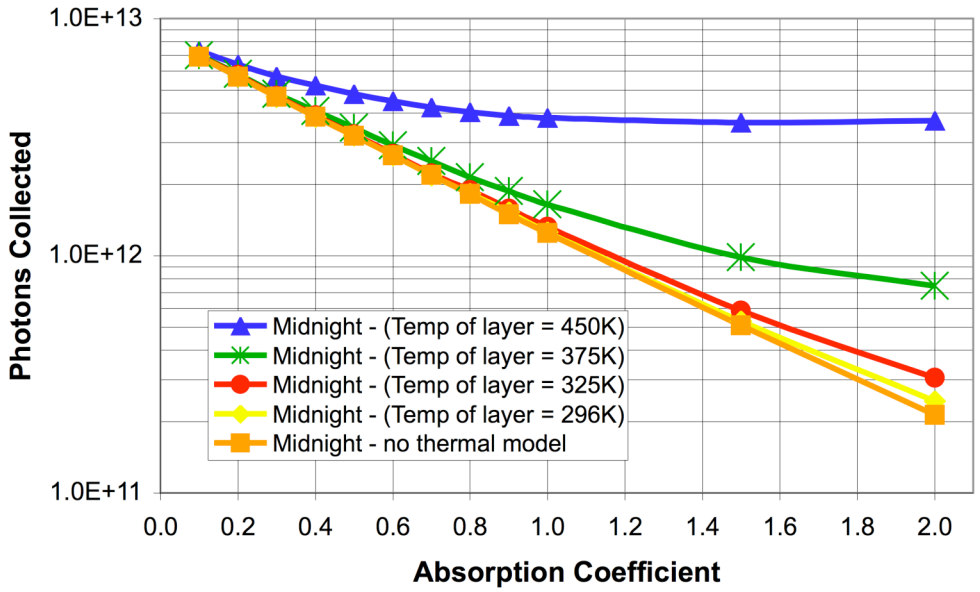


Figure 113: Photons collected at midnight from a pulse fired at a Lambertian plate with a 1m gaseous layer for different absorption coefficients including the thermal contributions (mid-latitude summer atmosphere; Rochester, NY)

5.2 Phenomenological Demonstrations

Up until this point, the DIRSIG simulations have been greatly simplified to facilitate verification efforts. The next few subsections present a series of phenomenological demonstrations that involve more complex scenes and eventually multiple pulses and platform and scanning motion. Although most of these demonstrations focus on topographic LIDAR applications, the underlying capabilities and techniques are directly applicable to

modeling a realistic DIAL sensor and data collection. In addition, these demonstrations identified some potential areas for future upgrades to the DIRSIG LIDAR module.

5.2.1 Multi-Bounce and "Late" Photons

During the early development stages for the topographic LIDAR demonstrations, we conducted preliminary testing of the model on existing scenes from the DIRSIG scene database. One of the premiere scenes is known as Microscene and was used for an end-to-end topographic LIDAR demonstration discussed later in this Chapter. Microscene was built to be utilized for high resolution imagery simulations and is based upon a particular area of RIT's campus. The CAD models for all of the objects within the scene have a very high degree of spatial detail. For instance, the grass added to the terrain model of the burm was "grown" by Barcomb as part of his master's defense. Each blade of grass is modeled with facets in the CAD model (shown in Figure 114) and then attributed with appropriate optical properties. This is important for a phenomenon that we observed in the topographic LIDAR time intensity slices.

A single pulse was fired into the scene and the return signal was highly oversampled. Figure 115 shows a sample of the time intensity slices for the returns. Each intensity slice is scaled independently to enhance the contrast and does not necessarily indicate relative strength of the returns between slices. As expected, we saw the returns for the objects within the scene at the appropriate ranges; however, a very small number photons were returning from beneath the surface of the burm. When traced within the code, the photons who appeared to be "lost" were actually delayed due to multiple bounces within the grass blades. The number of photons who were bouncing around in the grass was very small, but this was an early indicator of the potential capabilities of the DIRSIG LIDAR modeling approach.

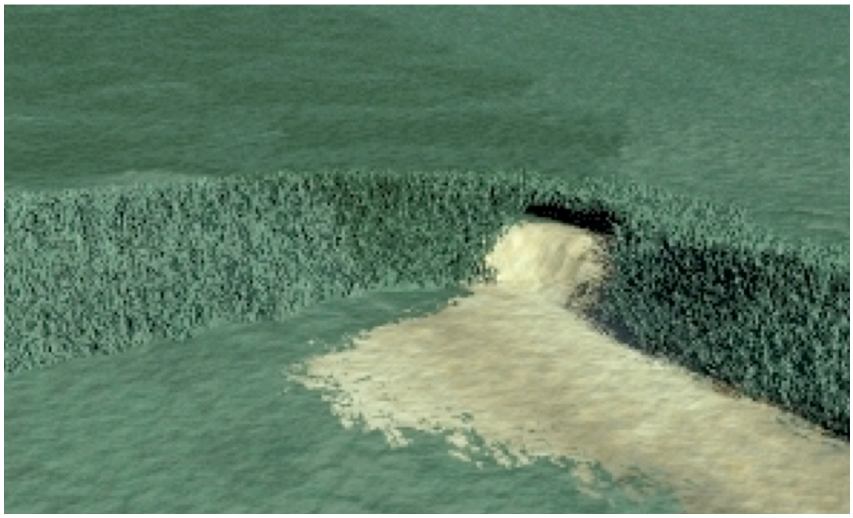


Figure 114: CAD model of "grown" grass blades for Microscene burm (Barcomb, 2004)

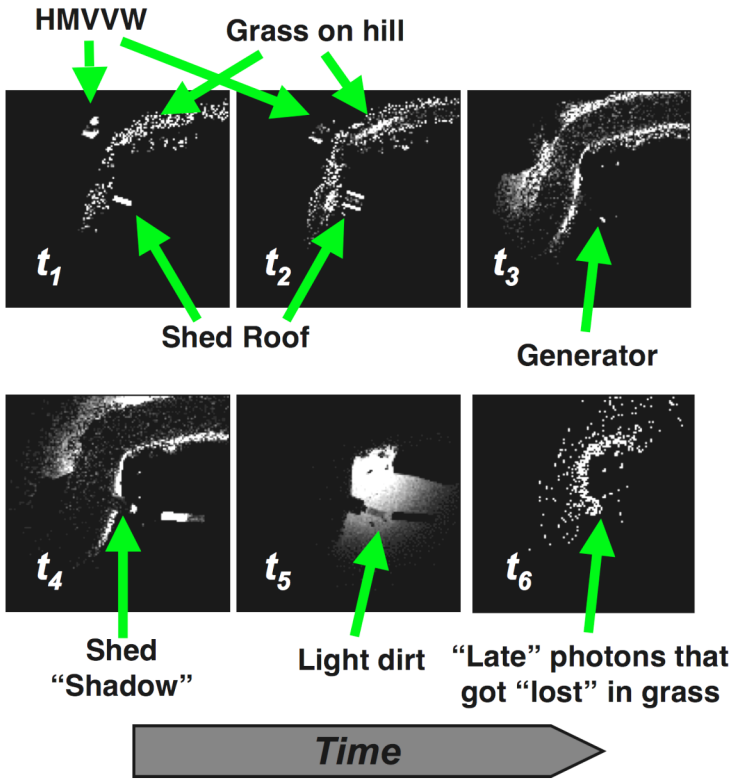


Figure 115: Microscene topographic LIDAR time-gated returns with "late" photons

5.2.2 Forest Canopy Penetration

The next phenomenology demonstration will address laser radar returns from a tree crown. For this example, a single tree is modeled and the temporal structure of the reflected photon counts will be explored. The geometry of the tree was created using a software package called OnyxTREE (http://www.onyxtree.com) and the surfaces were attributed with leaf spectral reflectance and transmission measurements made at RIT. The OnyxTREE software is capable of producing physically realistic tree geometries using detailed descriptions of tree growth patterns.

Figure 116 illustrates the general scene simulation setup. Figure 117 includes a 3D photon map density plot resulting from a single pulse modeled with 1,000,000 photon bundles. In the plot of the photon map, the shape and detail of the tree crown can be seen as well as the resulting shadow on the ground. Within the tree shadow there are some areas with increased photon counts that are evidence of direct illumination via foliage "poke through" and indirect illumination due to multiple reflections. The plot of the photon counts as a function of time/distance in Figure 118 results from spatially integrating a region encompassing most of the tree (refer to the highlighted box in the photon count frames). This magnitude vs. time plot shows a steady decay within the tree crown due to absorption and reflection, the late arrival of photons from ranges between the crown and the ground due to multiple bounces within the crown and the ground return itself. The magnitude of the ground return indicates a non-trivial probability of photons reflecting off the ground beneath the tree itself. The magnitude of this return would be a function of the tree's optical properties and leaf density (leaf area index). The images in the lower portion of Figure 118 are temporal slices of the photons counts arriving at the sensor. These spatial count density maps reveal horizontal and vertical structure of the tree that can be utilized to reconstruct the tree height and shape. The modeling of a tree canopy (instead of a single tree) is included in the end-to-end topographic scene simulation later in this chapter.

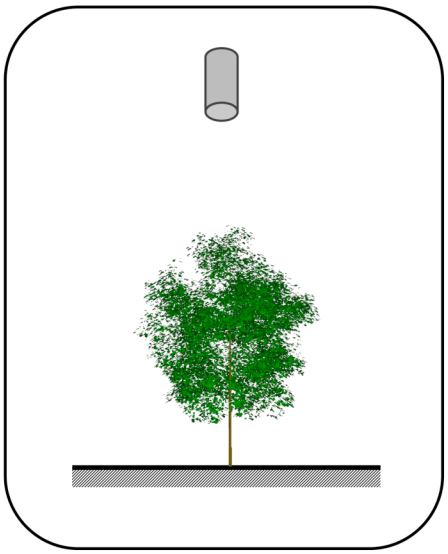


Figure 116: Canopy penetration/multi-bounce demonstration setup

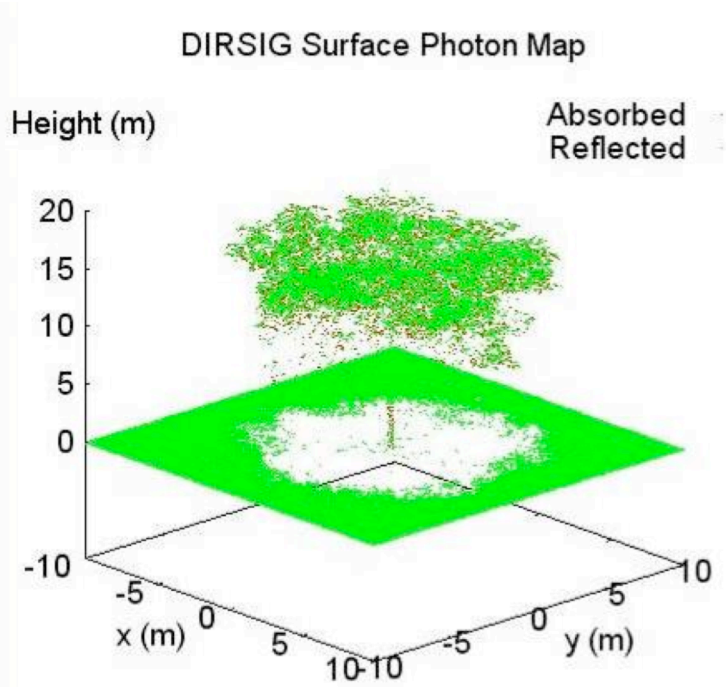


Figure 117: DIRSIG photon map for canopy penetration/multi-bounce demonstration

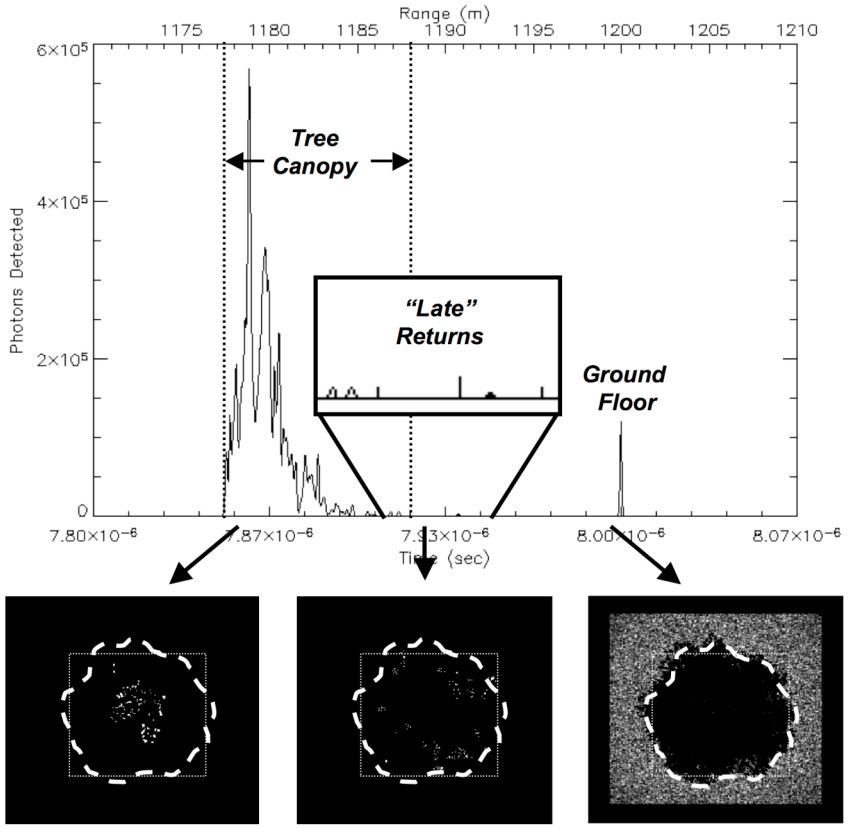
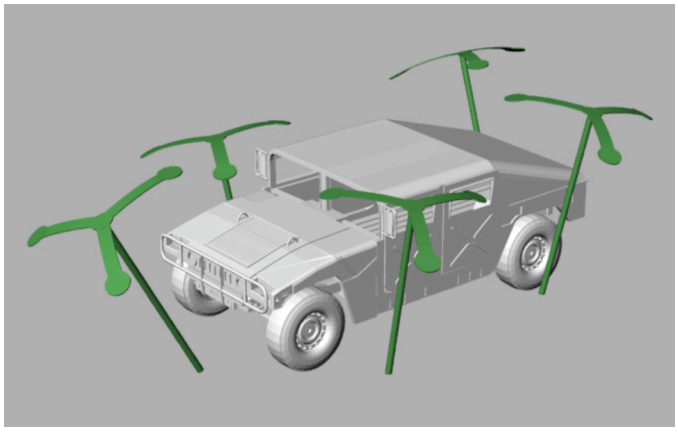


Figure 118: Canopy penetration and multi-bounce demonstration for a single, deciduous tree

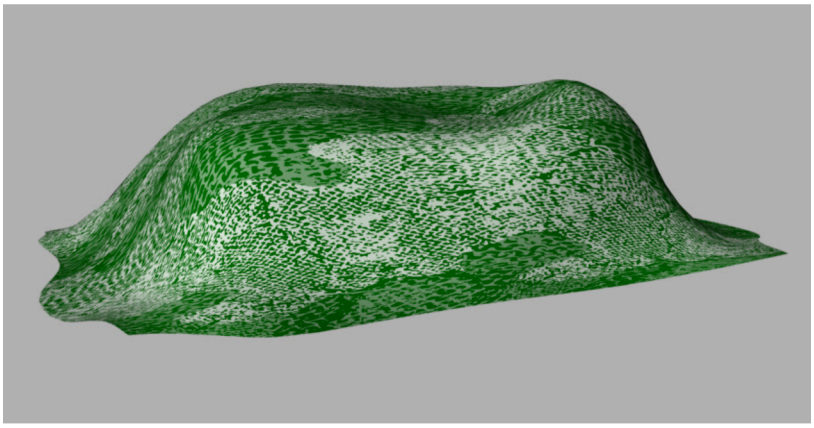
5.2.3 Camouflage/Concealed Hard Targets

Another common application area for topographic laser radar systems is for camouflage penetration problems. To demonstrate the use of the DIRSIG model for this task, a small scene was constructed that contains a HMMWV ("hum-vee") under a camouflage net held in place by supports on a terrain. The camouflage net is modeled as a continuous surface that has holes cut into it using a high spatial resolution "hole mask" that introduces geometric transmission due to spatial variations in fill factor. The solid areas of the net are attributed with a set of three fabric materials that have different reflectance and transmission factors. The vehicle and surrounding terrain is also fully attributed with appropriate surface optical properties. A rendering of the high-fidelity CAD models including the camouflage net and spreaders used for the DIRSIG simulation are shown in Figure 119. Figure 120 displays the results from DIRSIG overhead passive simulations of a HMVVV out in the open and the camouflaged HMVVV scene for this demonstration.

The DIRSIG model produced a highly oversampled, time-gated, photon count cube for this scene. For visual reference, the DIRSIG model also produced the height "truth map" shown in the Figure 121 that illustrates the amount of camouflage "poke through" that can be expected and the visibility of net supports and vehicle underneath. The series of images in Figure 122 show the spatial photon densities as a function of time. At this high temporal sampling rate, small differences in vertical structures can be easily resolved including variations in the net surface, the net support, the roof and hood of the vehicle and the terrain beneath. The ability to model scenes with these complex interactions and surface properties accentuates the benefit of physics based approach over what analytical or statistical models can provide.

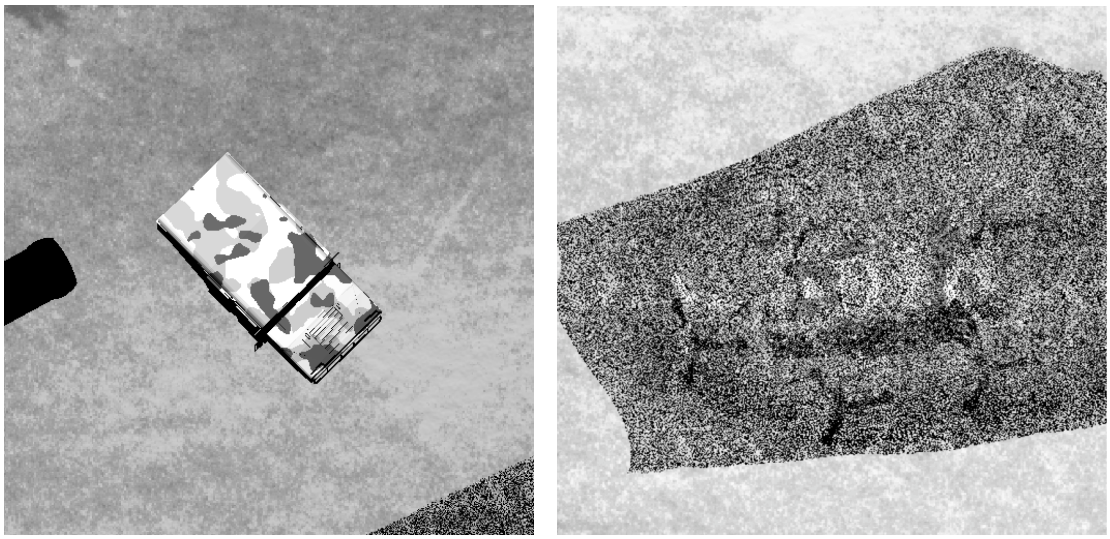


(a) HMVVV and spreaders



(b) Camouflage netting

Figure 119: HMVVV, spreaders, and camouflage netting CAD models for DIRSIG simulation (Barcomb, 2004)



(a) HMVVV (λ=732 nm) (b) Camouflaged HMVVV (λ=732 nm)

Figure 120: DIRSIG overhead passive simulation of HMVVV and camouflaged HMVVV

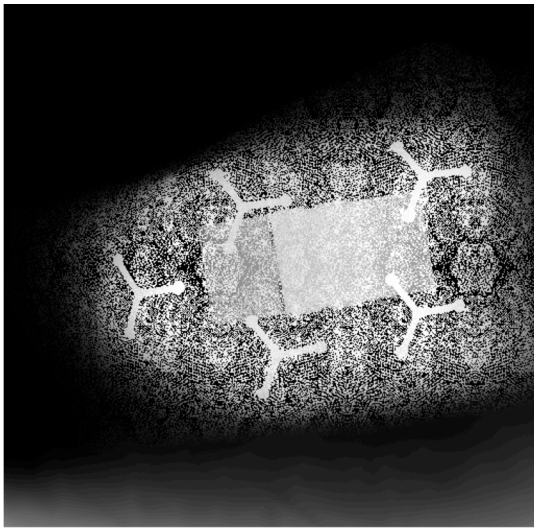


Figure 121: DIRSIG scene distance truth map for camouflaged HMVVV

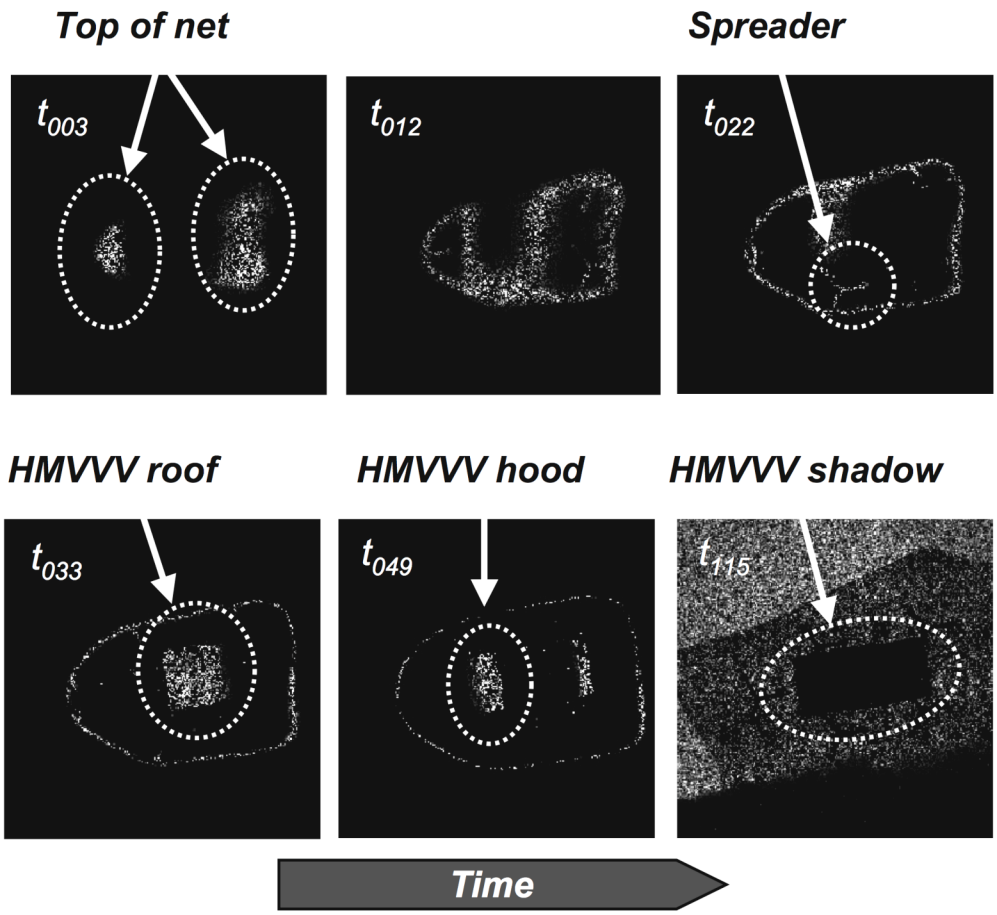


Figure 122: DIRSIG time-gated LIDAR returns for camouflaged HMVVV

5.2.4 End-to-End Topographic Mapping Demonstrations

5.2.4.1 Microscene

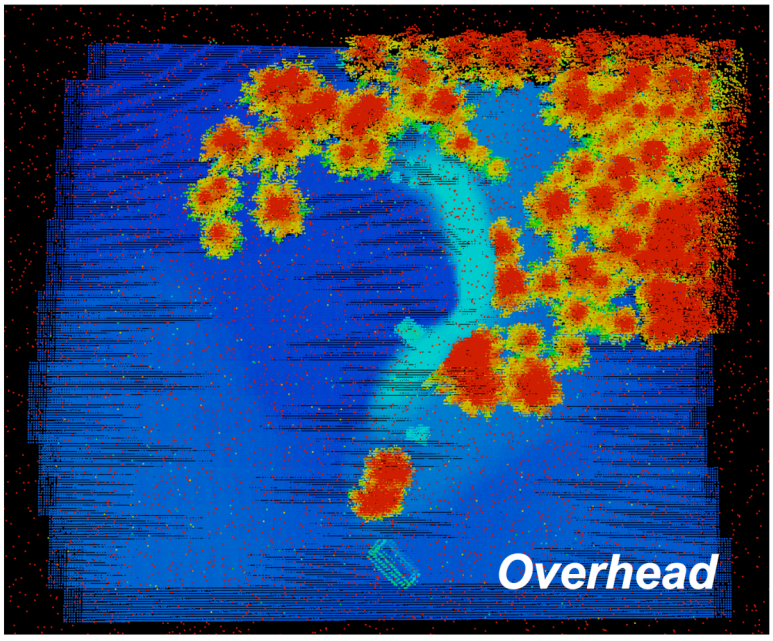
As described in Chapter 4, the end-to-end modeling of operational systems entails using the DIRSIG model to create time-gated photon counts that can be processed by an external sensor model to produce simulated raw instrument data. These simulated instrument data sets can then be used with conventional data processing tools to create topographic data products. For this demonstration, a data collection of the ALIRT system developed at MIT Lincoln Laboratories was simulated over a small scene located on the RIT campus. The DIRSIG scene database used in this end-to-end simulation was originally developed for passive, tower-based collections for the purpose of camouflage and landmine algorithm testing. The entire scene is approximately 300 x 300 meters and contains terrain, trees, and man-made

elements. The operational ALIRT system was flown during the winter of 2004 over the corresponding portion of the RIT campus to capture reference data sets for future validation efforts. The original scene database was modified to reflect the scene as it appeared during the data collection by the actual ALIRT sensor with the exception of a few feet of snow.

The ALIRT instrument uses a spatial array that is scanned in the across-track direction from an airborne platform. The across-track scan speed is slower than the laser pulse repetition rate so that the collected area overlaps significantly from pulse to pulse. The ALIRT instrument and collection characteristics were modeled using laser and instrument properties supplied by MIT Lincoln Laboratories. The simulated data cubes produced by the DIRSIG model utilized the flight data from the actual ALIRT over-flight of the scene. The resulting time-gated, photon count cubes were then processed using a detailed sensor model developed by ITT Industries, Space Systems Division, that features a rigorous treatment of the ALIRT focal plane and instrument. The resulting simulated raw instrument data streams were then post-processed using QT Viewer (developed at Johns Hopkins Applied Physics Laboratory) to view the resulting topographic products (see Figure 123 and Figure 124). The scan sweeps of the system are clearly visible in the overhead and slant topographic projections. The data appears synthetic because of the even-spaced grid nature of the points. These artifacts arise due to the noise-free knowledge of the platform location and platform relative pointing of the instrument during scanning. Future simulations may include a noise and/or jitter term for these quantities to introduce the inherent uncertainty in these values.



(a) Passive simulation

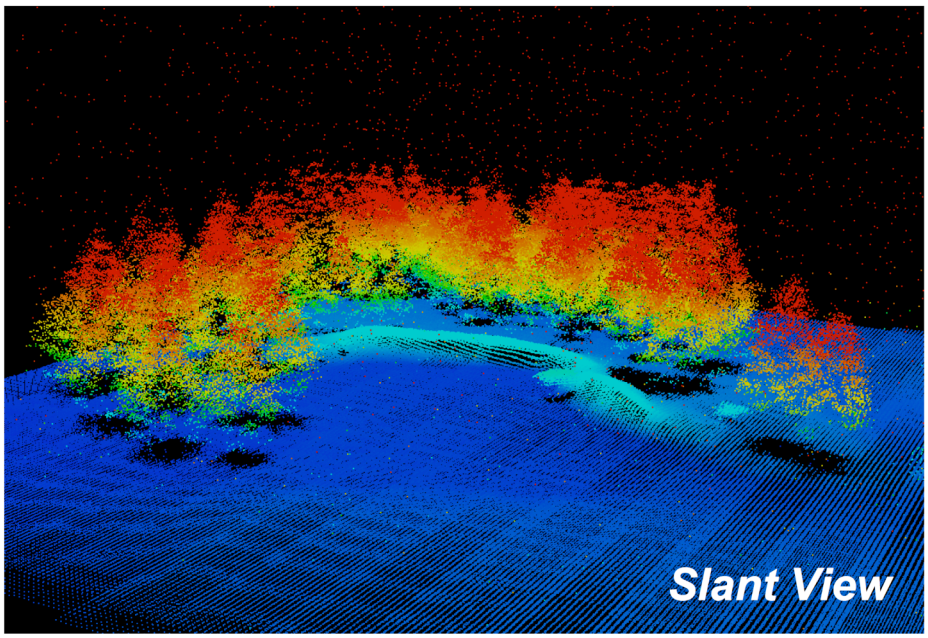


(b) Topographic LIDAR product

Figure 123: Microscene topographic LIDAR product and passive simulation (overhead)



(a) Passive simulation (Barcomb, 2004)



(b) Topographic LIDAR product

Figure 124: Microscene topographic LIDAR product and passive simulation (slant view)

5.2.4.2 Spotlight-mode, Extended Dwell and Canopy Penetration

The final phenomenological demonstration is the simulation of a topographic LIDAR collection in spotlight-mode for an extended dwell against a series of targets under a tree canopy. The scene is comprised of a T-72 tank, a HMVVV, and a concealed target in a tent on the edge of a deciduous tree line. The LIDAR configuration for this demonstration was based upon the ALIRT sensor described in the previous end-to-end topographic simulation of the Microscene area. The primary difference was that a customized sensor pointing and platform motion description file was created instead of relying upon one of the standard DIRSIG scanning platform descriptions. This was possible because of the inherent flexibility of the DIRSIG platform and sensor motion modules. The LIDAR system was flown over the scene in spotlight-mode at a grazing angle of 30 degrees with an extended dwell of 45 degrees. A simplistic Geiger counter detector model and topographic processor then processed the DIRSIG LIDAR data cubes. The final topographic product is shown in Figure 125. Figure 126 shows some close-ups for the T-72 tank and the HMVVV. The scan pattern and broadening of that pattern in the direction away from the sensor is evident in the processed data and accurately reflects what would be observed in a real data collect. The topographic product also contains a significant number of noisy or erroneous data points due to the multiple bounce effects. Most of these points would probably be removed if co-coincidence processing was used and are generally not simulated by many of the common LIDAR models. DIRSIG's LIDAR module would permit a researcher to verify the performance of the various co-coincidence processing algorithms using a more stressing data set.

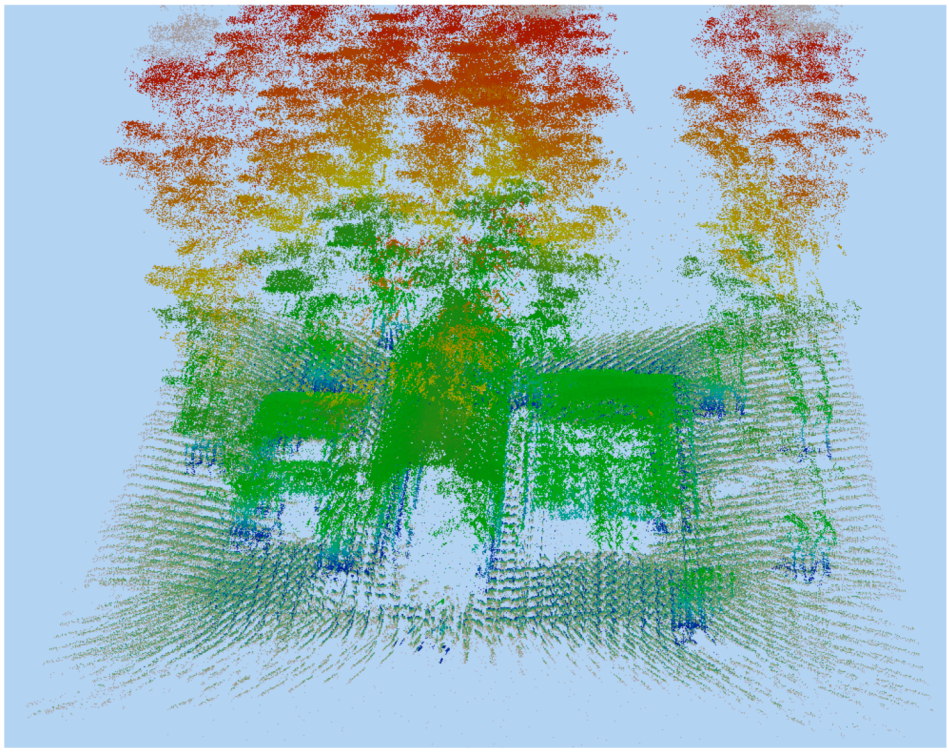


Figure 125: Topographic product for extended dwell (45 deg) collect of concealed targets at 30 deg grazing angle

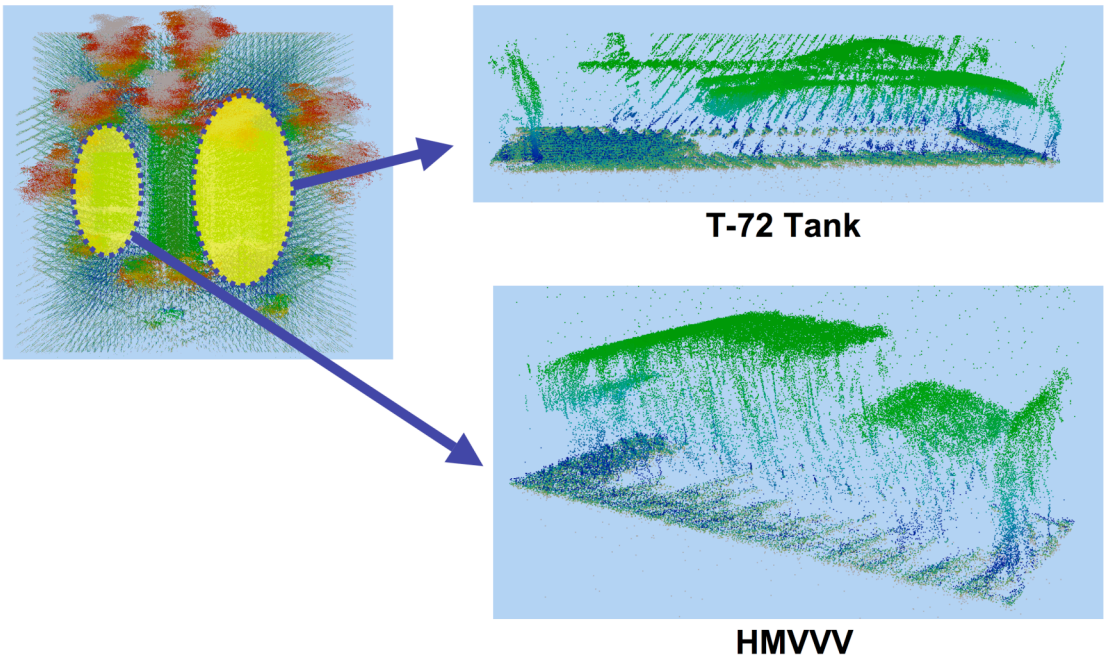


Figure 126: Vehicle close-ups for extended dwell (45 deg) topographic product

5.3 Impact of Scattering Constituents on DIAL Measurements

While the majority of this research effort was focused on developing and verifying a LIDAR model within DIRSIG that can accurately model multiple scattering and absorption for a DIAL system, a critical objective was to qualitatively demonstrate the impact of scattering constituents on DIAL measurements. Injection of common scattering media, such as water vapor or soot, into a gaseous plume can significantly degrade the ability of a DIAL sensor to detect and measure the concentration of individual constituents within the plume. Based upon the scattering verification analysis, the impacts of scattering on the photon distribution within a scene and the related return signal from a LIDAR pulse can be fairly significant and depend greatly upon a variety of factors. An increase in the scattering cross-section can drive the number of reflected and transmitted photons and their associated distributions within the scene. The increase in optical depth due to the additional scatterers also plays a factor since the mean optical path lengths generally increase. Additionally, the scattering phase function can impact the way in which the backscattered signal from the scattering constituents manifests itself.

This section presents the results from two different DIAL case studies that explore the impact scattering can have on DIAL concentration path length measurements for a wide range of parameters. As described in Chapter 4, the first scene is modeled after the simplified verification scene used throughout the verification process. A series of enhancements were made to the scene and collection scenario to increase the realism of the simulations while maintaining a fairly well-controled, well known environment. The second scene, which was introduced previously in Chapter 4, is much more complex and utilizes the new Blackadar plume model. Unfortunately, applicable truth data from the Blackadar plume model was not yet available. Therefore, while the data set confirms the importance of multiple scattering, additional investigation is warranted in the future when appropriate truth data can be generated and provided to the user.

The constituent of interest for both scenes is methane, and the scattering agent was water vapor droplets modeled after the C1 cloud properties. As described in Chapter 4, the sensors for both scenes use the same wavelengths, but the general setup was modified to

accommodate the requirements for each of the demonstrations. To enhance the "realism" for the DIAL sensor concept of operations, a 400 nsec delay was inserted between the firing of the "ON/OFF" pulses. In other words, the system fired an "ON" pulse, waited 400 nsec, and then fired an "OFF" pulse. The full LIDAR module was used during these demonstrations including a mid-lattitude summer atmosphere in Rochester, NY at midnight. The passive and thermal radiance solvers were activated and the results include those contributors.

5.3.1 Controlled Scattering Case Study

The controlled scattering case study was designed to confirm that scattering has a perceivable impact on DIAL concentration measurements. The DIAL sensor was modeled using the configuration parameters listed in Table 19, which were discussed briefly in Chapter 4. The scene was comprised of a homogenous box of mixed methane and water vapor at 100 m above a flat grass plate. The grass plate used a texture map to spatially vary the emissivity across the plate to simulate the texture of grass in the MWIR. Although the texture was not entirely accurate for the MWIR, the texture map did induce more realistic variability in the topographic target background as the platform moved between ON/OFF pulses than a constant emissivity across the plate would have.

Table 20 and Table 21 list the vertical optical depths of the homogeneous gas box for each test case. In addition to varying the methane concentration, various concentrations of water vapor were added to the gas box. The water vapor concentrations fell into four general categories: baseline, thin, medium, and thick. The naming convention was selected based upon the rough order of the optical depth contribution by the water vapor. An additional case was added to investigate the impact of the scattering phase function on the DIAL measurements. A medium case was run with an isotropic scattering phase function substituted for the actual forward scattering phase function calculated by MIEDU.

Enough photon bundles were cast into the scene to generate approximately 500,000 events in the gas box. Based upon the verification results, the accuracy loss should be minimal except for the strong scattering cases. The 500,000 events requirement was primarily set based upon computational time. For the strong scattering cases, generating and evaluating 500,000 events

takes about 20+ minutes per pulse. A 50,000 events requirement results in about 5 minutes per pulse. Although somewhat desirable for accuracy considerations, a 1 million events requirement took about 45 minutes per pulse in a preliminary run.

A single pulse was simulated for both the OFF and ON wavelengths and the resulting data cubes were processed using a simplified DIAL processor described in Chapter 4. Figure 127 compares the concentration path length error of the processed data for each of the test cases and different methane concentrations. Figure 127(b) is a rescaled version of Figure 127(a) that can be used to examine the less dramatic scattering cases. The baseline case's CPL error is very consistent regardless of the methane concentration. The 6 ppm error is likely due too differences in the atmospheric attenuation for the two wavelengths, spectral and spatial variability in the topographic target background between the pulses due to platform motion, and the modeling errors discussed previously in the verification section. The CPL errors for the forward scattering medium and thick cases demonstrate the potential devastating effect that scattering can have on DIAL measurements. Although in general the CPL is over-estimated, two of the cases do not exhibit the same behavior. In particular, a small amount of scattering in the thin cases eventually results in an under-estimation of the CPL for larger methane concentrations. For the baseline cases, the OFF and ON receive signal is dominated by the transmitted photons that reflect off of the surface and then return back through the gas box. When a small amount of scattering is introduced, the transmit beams are effectively broadened and the OFF wavelength detected signal is reduced. For the ON wavelength, the small increase in backscatter from the top of the gas box layer is significant and may counter-balance the losses due to beam broadening. The result is that the effective relative difference between those signals decreases and the CPL also decreases.

Another interesting observation is that isotropic scattering appears to cause less measurement accuracy degradation than forward scattering in the medium cases. The inclusion of isotropic scattering into the gas box appears to have little effect on the DIAL measurements for this data set. Consistent with the scattering verification analysis, an isotropic scattering layer tends to balance the longer mean path lengths of the transmitted photons with the reflected photons that leave the medium more quickly due to the scattering phase function. This

counter-balancing effect is the underlying explanation for the minimal impact of scattering on the measured CPL if the gas mixture scatters isotropically.

Table 19: LIDAR system configuration for scattering case study

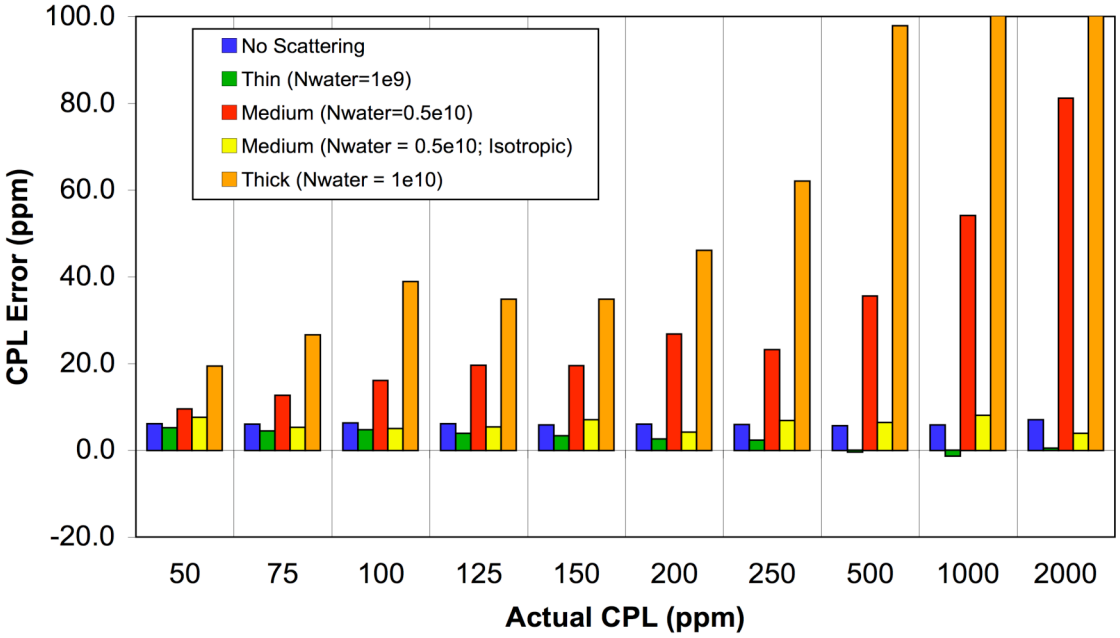
Parameter	Configuration C
Wavelength (λ_{OFF})	3.3058 μm
Wavelength (λ_{ON})	3.3151 μm
Pulse Energy ($P_L=N_L hc/\lambda$)	6 μJ
Pulse Repetition Frequency (PRF)	5 KHz
Pulse Length (τ_D)	1.5 ns
Aperture Radius (r_0)	100 mm
Focal Length (f)	400 mm
Transmit Beam Radius (w_0)	5 mm
Beam Divergence (ϕ_D)	8.0 mrad
Detector Size	500 μm

Table 20: Optical depth of gas box for DIAL and scattering case study at the OFF wavelength

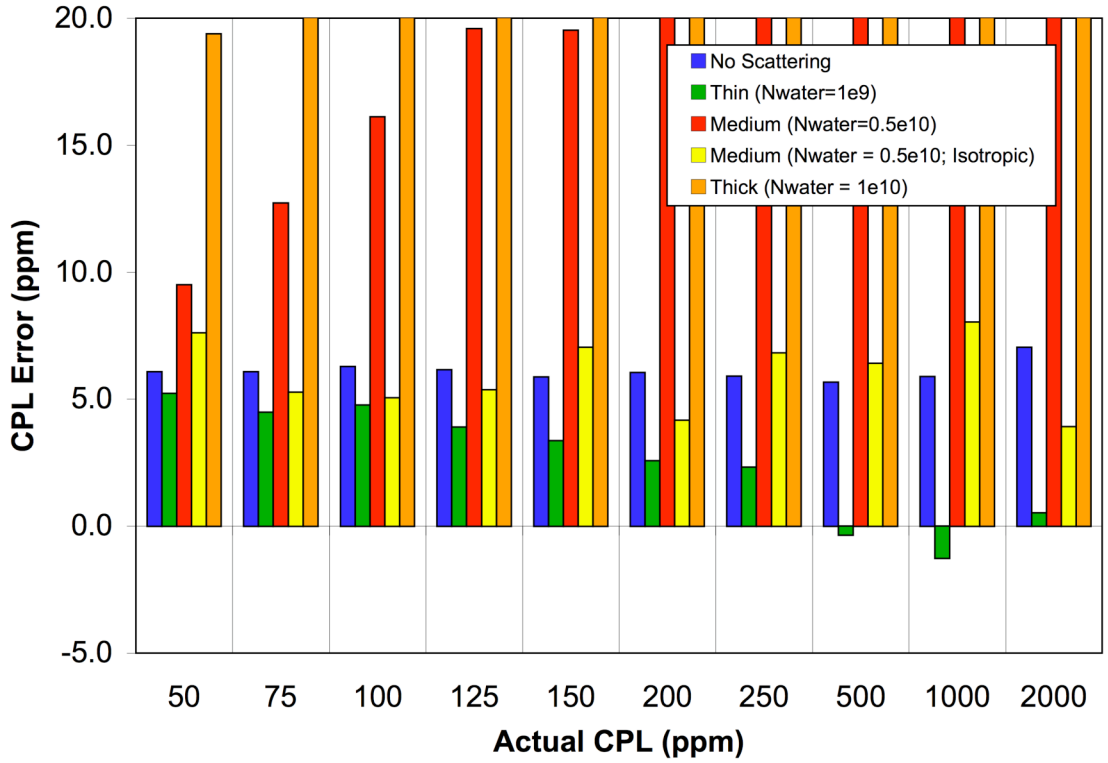
(λ_{OFF})		DIAL Scattering Test Cases				
		Baseline	Thin	Medium	Medium (Isotropic)	Thick
		Water Vapor Nc (1/m^3)				
		0	1.00E+09	5.00E+09	5.00E+09	1.00E+10
Methane Nc (ppm)	50	1.16E-04	2.39E-01	1.19E+00	1.19E+00	2.39E+00
	75	1.74E-04	2.39E-01	1.19E+00	1.19E+00	2.39E+00
	100	2.33E-04	2.39E-01	1.19E+00	1.19E+00	2.39E+00
	125	2.91E-04	2.39E-01	1.19E+00	1.19E+00	2.39E+00
	150	3.49E-04	2.39E-01	1.19E+00	1.19E+00	2.39E+00
	175	4.07E-04	2.39E-01	1.19E+00	1.19E+00	2.39E+00
	200	4.65E-04	2.39E-01	1.19E+00	1.19E+00	2.39E+00
	250	5.82E-04	2.39E-01	1.19E+00	1.19E+00	2.39E+00
	500	1.16E-03	2.40E-01	1.19E+00	1.19E+00	2.39E+00
	1000	2.33E-03	2.41E-01	1.19E+00	1.19E+00	2.39E+00
	2000	4.65E-03	2.43E-01	1.20E+00	1.20E+00	2.39E+00

Table 21: Optical depth of gas box for DIAL and scattering case study at the ON wavelength

(λ_{ON})		DIAL Scattering Test Cases				
		Baseline	Thin	Medium	Medium (Isotropic)	Thick
		Water Vapor Nc (1/m^3)				
		0	1.00E+09	5.00E+09	5.00E+09	1.00E+10
Methane Nc (ppm)	50	8.31E-02	3.22E-01	1.28E+00	1.28E+00	2.47E+00
	75	1.25E-01	3.63E-01	1.32E+00	1.32E+00	2.51E+00
	100	1.66E-01	4.05E-01	1.36E+00	1.36E+00	2.55E+00
	125	2.08E-01	4.46E-01	1.40E+00	1.40E+00	2.59E+00
	150	2.49E-01	4.88E-01	1.44E+00	1.44E+00	2.63E+00
	175	2.91E-01	5.30E-01	1.48E+00	1.48E+00	2.68E+00
	200	3.33E-01	5.71E-01	1.53E+00	1.53E+00	2.72E+00
	250	4.16E-01	6.54E-01	1.61E+00	1.61E+00	2.80E+00
	500	8.31E-01	1.07E+00	2.02E+00	2.02E+00	3.22E+00
	1000	1.66E+00	1.90E+00	2.86E+00	2.86E+00	4.05E+00
	2000	3.33E+00	3.56E+00	4.52E+00	4.52E+00	5.71E+00



(a) Concentration path length error



(b) Concentration path length error (zoomed in plot)

Figure 127: DIAL concentration path length error due to scattering for a gaseous layer 100 above a grassy surface

5.4 End-to-end DIAL Demonstration

5.4.1 Megascene Tile 4 Water Treatment Plant with a CH_4 Plume

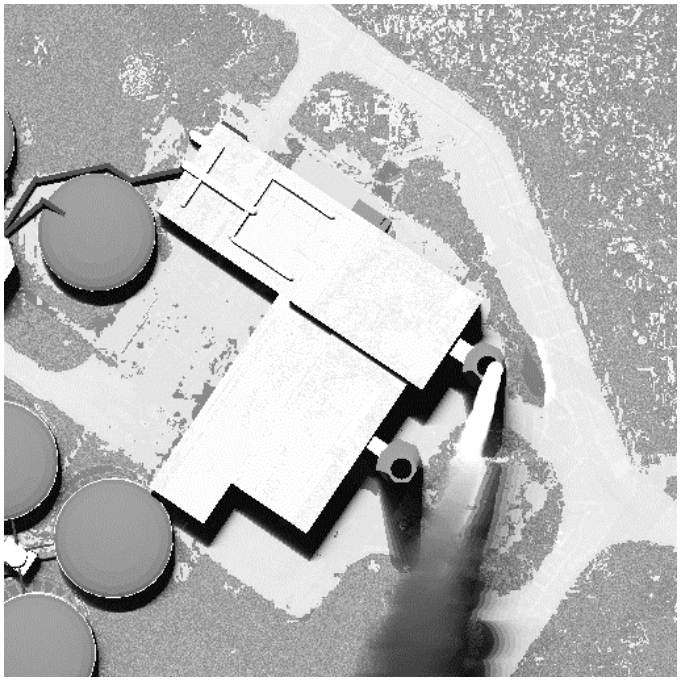
The second demonstration is an end-to-end DIAL demonstration that displays the current modeling capabilities for a complex scene within DIRSIG including scanning and platform motion, a realistic atmosphere, the passive and emissive radiance solvers, the Blackadar plume model, and a simplistic DIAL processor. In addition, the importance of modeling the effects of multiple scattering for DIAL collections for plumes with water vapor is reinforced. The Megascene Tile 4 water treatment plant in the DIRSIG scene database was built upon a water plant in Rochester, NY and has been used frequently by researchers in the past for passive plume algorithm development and generating algorithm training data sets. A Blackaddar plume with methane was added to the scene with a release concentration of 10,000 ppm-m stepped every 0.5 secs. The release temperature was nominally 450K at the stack. The scanning DIAL system parameters used are listed in Table 22. Passive MWIR simulated images of the Megascene Tile 4 water plant with the Blackadar plume for the ON/OFF wavelengths are shown Figure 128. In addition to the emissive and absorption phenomena, a neutral transition region is appropriately evident for the Blackadar plume.

Because concentration truth data for the scene was not available, two DIAL data sets were generated: one without any water vapor and one with water vapor. The processed results are shown in Figure 129 and Figure 130 respectively. The gray-scale images indicate the relative CPL based upon the processed synthetic data. The darker dots are actually negative CPLs and indicate strong thermal emission from the background. We are also getting some potential poke-through in the plume where it is a bit thinner, but this is not as apparent because the data is undersampled spatially. The baseline CPL was measured to be about 250 to 275 ppm of methane in the non-scattering plume. The measured CPL was reduced to 10 to 30 ppm for the scattering plume. The reduction in apparent CPL due to the scattering is consistent with the results from the previous scattering case studies. Based upon the effective

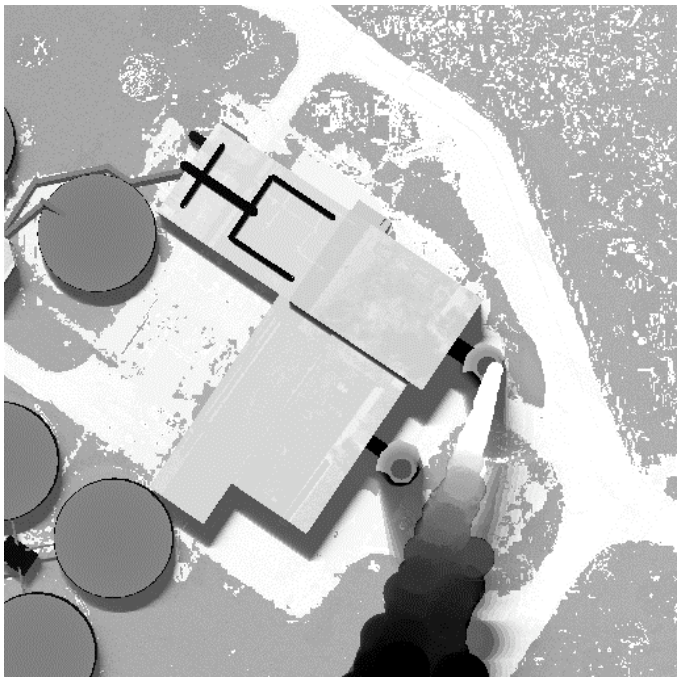
down-wind dilution of the methane concentrations, the amount of water vapor is fairly small, but sufficient to impact the DIAL measurements.

Table 22: LIDAR system configuration for Megascene-Tile4 simulation

Parameter	Configuration D
Wavelength (λ_{OFF})	3.3058 μm
Wavelength (λ_{ON})	3.3151 μm
Pulse Energy ($P_L=N_L hc/\lambda$)	6 μJ
Pulse Repetition Frequency (PRF)	400 Hz
Pulse Length (τ_D)	1.5 ns
Aperture Radius (r_0)	100 mm
Focal Length (f)	400 mm
Transmit Beam Radius (w_0)	5 mm
Beam Divergence (ϕ_D)	8.0 mrad
Detector Size	100 μm
Array Size	32 x 32



(a) λ=3.3060 μm



(b) λ=3.3160 μm

Figure 128: DIRSIG MWIR image of Megascene-Tile4 waterplant with a Blackadar plume

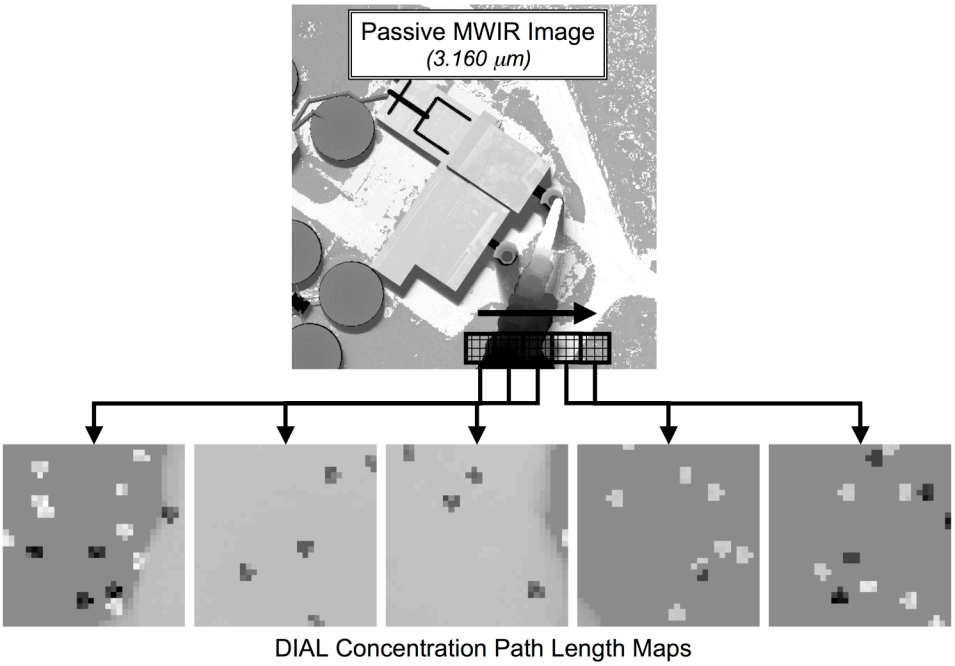


Figure 129: Processed CPL maps from DIRSIG LIDAR cubes for Megascene-Tile4 waterplant with a CH_4 Blackadar plume (λ_{off}=3.3060 μm; λ_{on}=3.3151 μm)

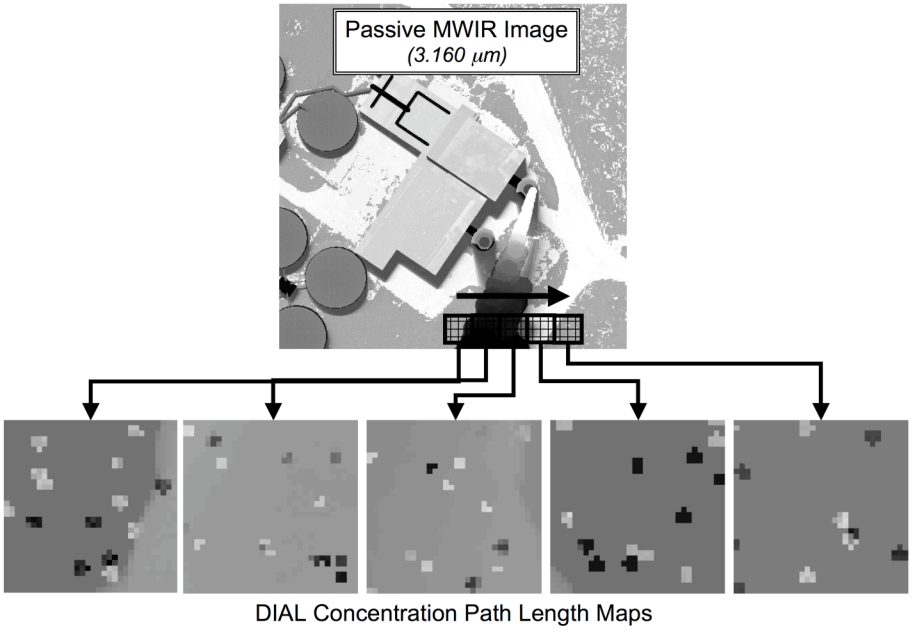


Figure 130: Processed CPL maps from DIRSIG LIDAR cubes for Megascene-Tile4 waterplant with a CH_4 and water vapor Blackadar plume (λ_{off}=3.3060 μm; λ_{on}=3.3151 μm)

Chapter 6

Conclusions

Previous research has indicated that multiple scattering effects could impact a DIAL sensor's ability to detect and quantify effluents of interest within participating medium. The non-stationary nature and complex temporal structure of factory stack plumes complicates the analysis of potential multiple scattering effects or the development of advanced algorithms to counter the effects. Synthetic data sets would be beneficial for investigation of the underlying physic-based root causes, quantification of the effects and general trends, and DIAL processing algorithm development. Unfortunately, extending traditional modeling techniques to model multiple scattering and absorption of an arbitrary time-gated LIDAR pulse accurately and efficiently within a non-homogenous, finite volume, such as a plume, is non-trivial and problematic. Another modeling approach was needed.

Leveraging the photon mapping techniques used by the computer graphics community, this dissertation effort adds to the existing body of knowledge by extending the traditional photon mapping techniques to support a new physics-based modeling approach capable of accurately handling multiple scattering and absorption of LIDAR pulses within a complex, extended scene including a realistic plume. Additionally, the available tools to simulate LIDAR scenes do not support rigorous atmospheric interactions, participating media, multiple bounce/scattering, thermal and reflective region passive returns, complex scene geometries, moving platform and scanning effects, detailed optical descriptions of materials (e.g., BRDF and scattering models), and time-gated returns. Such requirements were deemed crucial to fully address future research problems and accurately model the observable signatures of gaseous plumes under a variety of complex scene conditions, including multiple scattering. By incorporating the new photon mapping variant into the existing passive DIRSIG framework, the new DIRSIG LIDAR module is meets these challenging requirements as was demonstrated in Chapter 5.

Based upon the underlying theoretical basis for the new LIDAR modeling approach presented in this thesis, the DIRSIG LIDAR module was verified against a suite of analytical

and statistical benchmarks. As discussed in Chapter 5, the results confirm that the DIRSIG LIDAR module can accurately predict sensor-reaching photon counts for a LIDAR system, including the effects of multiple scattering and absorption within a realistic plume. In addition, the phenomenological case studies demonstrated its capabilities to model a wide array of topographic LIDAR and DIAL systems, including an exemplar dataset for a complex plume scene that exhibits the effects of multiple scattering on DIAL concentration measurements. Because the new core LIDAR components model the low-level physics-based interactions and utilize the surrounding modular infrastructure that has been built up over decades of research at RIT, the DIRSIG LIDAR module now enables researchers to explore not only the root causes of the effects of multiple scattering on DIAL system performance, but also to generate accurate synthetic datasets of very complex scenes and collection scenarios for direct passive vs. active comparisons and DIAL algorithm development. Specific research findings and recommendations for future work appear in the sections that follow.

6.1 Findings

Upon review of the primary objectives in Chapter 2, the research effort conducted for this dissertation exceeded the stated requirements and in addition accomplished several of the research goals. The theory presented in Chapter 3 in conjunction with the modeling approach in Chapter 4 and the results in Chapter 5 fulfilled the requirement to develop a firm understanding of the mathematical and theoretical basis, viability, and practical limitations of photon mapping to numerically model multiple scattering and absorption in a dispersive, gaseous participating medium. The foundational theory for the new photon mapping approach was presented in Chapter 3 and shown to be consistent with the underlying physics and radiative transfer theory for gaseous media. The accuracy of photon mapping for simulating a LIDAR pulse in a participating medium was verified in Chapter 5 using analytical means (where tractable) augmented by statistical analysis commonly used in the literature for multiple scattering. In addition, the phenomenological case studies substantiated the photon mapping approach for more complex scenes. The exemplar scenes included full complex backgrounds and targets and demonstrated the interactions between the participating medium and a more realistic surrounding environment. To support the simulation of more

complex scenes, a practical methodology for generating the critical optical properties of mixed gases required for the propagation of photons through the scene and estimating the observed radiance was presented in Chapter 4 and utilized for the scene development in Chapter 5. The approach was based upon the Mie scattering theory and MIEDU code discussed in Chapter 3 and Appendix A.

Three of the requirements revolve around developing a set of representative DIAL simulations that utilize the DIRSIG LIDAR sensor module, contain gaseous plumes or voxels, and are then processed by a DIAL processor. The simulations and associated datasets were presented in the latter portion of Chapter 5 and demonstrate how to generate end-to-end DIAL simulations using the DIRSIG LIDAR module. In addition, the results in Chapter 5 qualitatively confirm that common scattering constituents, such as water vapor or soot, can significantly degrade a DIAL sensor's ability to accurately detect and measure the concentration level of a particular constituent within a plume. Although the DIAL processor was based upon a simple band ratio algorithm, it was used to augment the qualitative assessments of the impact of plume scattering on the quantification of plume effluents and demonstrated a sufficient level of accuracy for the investigations undertaken in this research effort.

With regards to the research goals listed Chapter 2, emphasis was placed on extending DIRSIG's LIDAR module capability to model topographic scenarios. While the focus of the research was on DIAL systems, the underlying physics inherently drives a level of fidelity in the modeling that incorporates sufficient capability to mode topographic LIDAR sensors. In the process, a topographic processor was developed and test that displayed sufficient flexibility to incorporate various detector modes. The results of the phenomenological case studies in Chapter 5 included standard terrain topography, forest canopy penetration, and camouflaged hard targets. In addition, an initial library of scattering phase functions for standard gases and aerosols of interest were developed and a representative set were presented in Chapter 4.

6.2 Recommendations for Future Research

The recommendations for future research fall into three primary categories: model validation, model enhancements, and model applications. The model validation addresses the continuation of the verification efforts in this proposal to demonstrate the accuracy of the DIRSIG LIDAR modeling approach and the applicability for specific research application areas. The model enhancements build upon the current DIRSIG model and continue the spiral development of the model to either improve performance or provide new capabilities. The modeling applications area recommends research areas for which the model has been demonstrated in this dissertation and could be directly used to generate synthetic datasets for analysis.

6.2.1 Model Validation

The first recommendation is to perform an extensive model validation. As a first step, a commercially available topographic LIDAR system could be used to collect over a scene already constructed in the DIRSIG scene database, such as Megascene 1 or Microscene. The datasets could be statistically compared at the end product and at the raw data level. In addition, the multiple bounce phenomenology demonstrated in this dissertation could be compared with observable tree canopy signatures. Although this would directly address most of the LIDAR module's performance, the accuracy of the multiple scattering and absorption components would probably require a controlled environment such as a lab for validation efforts to be successful. This ensures that the gas concentrations are known or well characterized and are adequately mixed. If available, another potential source of validation data would be the water vapor DIAL measurements for various clouds. In either case, the multiple scattering or absorption could be directly compared and statistically evaluated. Alternatively, further confidence could be gained by employing cloud droplet size measurement algorithms to the synthetic datasets and compare the results with the known inputs. In conjunction with validation of the current DIRSIG LIDAR module, the multiply scattered LIDAR equation could be evaluated as an alternative for improved computational performance under certain circumstances where the accuracy was deemed.

6.2.2 Model Enhancements

With regards to recommended future model enhancements, they can be grouped into two primary categories, performance improvements and expanded capabilities. All of these enhancements are naturally extensions of the core LIDAR modeling approach and associated software code. In many instances, the underlying architecture was specifically designed with the intent of enabling pursuit of these enhancements in future research efforts. Others were discovered during the spiral development process as various technical challenges were overcome.

The focus of the performance improvements is to reduce in computational run-time and efficiencies as well as decrease the inherent precision loss noted in Chapter 5. The current LIDAR model represents a vast improvement in computational efficiency and speed over the previous prototype model. A single pulse simulation for a simplified target at a very coarse range resolution using the prototype model used to take between 24-48 hours to generate. The new DIRSIG LIDAR module generates a much higher fidelity data cube for a single pulse from a more complex topographic scene in approximately 2-4 minutes per pulse. Simulation of a single pulse involving multiple scattering nominally completes in approximately 10-20 minutes per pulse due to an increase in the required number of photon bundles cast into the scene. This improvement is considerable considering that the fidelity and complexity of the new LIDAR module. In large part, the improvement is due to the new photon mapping approach developed for this model. However, some potential opportunities for improvement were identified. First, the volumetric radiance solvers could be augmented with a user-activated option to use the multiply scattered LIDAR equation instead of the photon mapping radiance solver for the effects of the participating medium. If a reduced level of accuracy for the participating medium was acceptable, a user could select this option and fire just an adequate number of photon bundles for a topographic scene. Secondly, the concept of "guided" photons could be incorporated into the source model. Essentially, an additional pass is added before the current two-pass photon mapping approach to determine which elements within the scene need a higher photon density. During the tracing stage, the photon bundles are statistically "guided" into those areas of the scene. Although the speed improvements are dramatic, the complications and overhead to keep the statistics accurate for

the entire scene are non-trivial and are potentially compounded by the temporal nature of the scene and source.

To decrease the precision loss in the system demonstrated in Chapter 5, the LIDAR data cube output could be permitted to be double precision if specified by the user. This would effectively decrease the precision loss in the system due to dynamic range constraints on the output. The downside is that the size of the cubes and the read/write time for the output will dramatically increase. Additionally, there may be ways to decrease the inherent precision loss in the calculations within the model. For instance, instead of photons, the photon bundles could be represented in terms of watts per bundle until the very end and then converted by the user. The actual benefit may be fairly small, but should be considered.

The performance enhancements build upon the baseline DIRSIG module developed and verified in this dissertation to either provide new capabilities or improve the fidelity of the current model. Some new capabilities that could be added are a polarmetric LIDAR module, Raman scattering and florescence phenomenology, and a coherent LIDAR module. Although the addition of these new capabilities is not necessarily simple, the current DIRSIG LIDAR module was built with the hooks embedded in the code to facilitate the improvements. To improve the existing fidelity of the model, one should consider a series of options. First, the current model simulates a monochromatic source. The detector module can already be defined spectrally because it is based upon the legacy passive modules. The spectral width of the laser source and photon bundles could be added into the architecture. This would probably have to be done parametrically to avoid an unacceptable increase in computational time. Secondly, some user-defined, pulse-to-pulse variability could be added to the source. For instance, the pulse power, duration, and departure time actually vary from pulse-to-pulse for a real LIDAR system. These three components could be randomly modified based upon some established statistics such as a Gaussian random variable within the code and the truth data could be stored in the LIDAR data cube header file. Thirdly, other beam shapes and/or modes could be added to the Gaussian and top-hat source functions. Fourthly, the sensor jitter could be added to the sensor motion module. The jitter can currently be generated outside of DIRSIG via a detailed sensor pointing input file; however, this is not in general an

easy task for most users. A default user-controlled random jitter could be added directly to the platform and sensor motion modules within DIRSIG. Lastly, the available options for inputting the scattering phase functions should be expanded to include direct importance-based sampling of a user-supplied scattering phase function and higher-order Henyey-Greenstein approximations. These options will likely be necessary for successfully validating the model when multiple scattering is present.

6.2.3 Model Applications

From an applications perspective, a wide range of possible research applications of the model was demonstrated in this research effort. For instance, the effects of multiple scattering on DIAL concentration measurements could now be pursued more thoroughly using this model as a tool to generate a host of synthetic datasets for analysis. The key would be to generate appropriate truth data for the current DIRSIG compatible voxelized plume models. In a similar fashion, the camouflage/concealed target and tree canopy penetration demonstrations showcased the module's capabilities with regards to topographic LIDAR applications and could be expanded to examine particular tasking strategies against concealed hard targets. Lastly, the model could be used to generate datasets for a direct comparison between passive and active methods of identifying and quantify the constituents within a gaseous plume. Eventually, synergy between passive and active collection and processing techniques could be explored using the DIRSIG LIDAR module.

Appendix A - Mie Code Performance

A.1 Accuracy and Precision

The accuracy of a Mie code is dependent upon a lot of key factors, but is a part of the design process. In other words, the desired accuracy and precision over a target range of input parameters drives the algorithm design and number of iterations for each loop. MIEV0's published accuracy for any calculated optical parameter is to 5-6 significant digits or better for particle size parameters from $0.1 \le x \le 20{,}000$ and indices of refraction $1 \le Real\{m\} \le 9$, $0 \le Imag\{m\} \le 10$. According to Wiscombe (1996), the MIEV0 code accuracy reduces to 3-4 significant digits for very small particle size parameters ($0.01 \le x \le 0.2$). The Fortran or IDL version of the BHMIE code has a similar 5-6 significant digit accuracy or better for particle size parameters from $1 \le x \le 1{,}000$ and indices of refraction $1 \le Real\{m\} \le 2.5$, $0 \le Imag\{m\} \le 2$. The accuracies of both of these codes are more than sufficient for most applications and this is why they are used so frequently in atmospheric optics. Note that all of the codes under consideration were designed to handle wavelengths from the UV to the visible to the microwave and longwave regions of the spectrum. In fact, the development of Mie codes in the late 1970s was driven by investigations into propagation of longwave and solar radiation in clouds and the upper atmosphere. Du claims in his paper (2004) that his algorithm provides accuracy of greater than 6 significant digits for particle size parameters from $0.001 \le x \le 20{,}000$ and indices of refraction $1 \le Real\{m\} \le 10$, $0 \le Imag\{m\} \le 10$. Because of the dial-able accuracy/precision, he also provides examples where the accuracy was 10 orders greater than MIEV0; however, the computational cost was extreme. Additionally, Du demonstrates that his code may be able to handle particle sizes up to 1,000,000. The difficulty with the latter claim is that it is not easily verified, but the result presented in 2004 is reasonable. One should note that these accuracies were quoted for code written in C++ on very high precision computer systems. The subsequent discussion shall be of the accuracy of Du's algorithm as implemented on an ordinary PC laptop in IDL (denoted MIEDU). As will be shown shortly, MIEDU's maintains the consistency with at least the 5-6 significant digit accuracy claim. A summary of the overall operational restrictions and accuracies for the various Mie codes presented (MIEV0, BHMIE, and MIEDU) are shown in

Table 23 below. One should use this table as a reference for the following discussion of the specific accuracy test results.

Table 23: Operational restrictions for MIEV0, BHMIE, and MIEDU

	Size Parameter (um)	Indices of Refraction		Accuracy
MIEV0	0.02 < x < 20,000	1 < Re{m} < 9	0 < Imag{m} < 10	>6
IDL BHMIE	1 < x < 1,000	1 < Re{m} < 2.5	0 < Imag{m} < 2	5 to 6
IDL MIEDU	0.02 < x < 20,000	1 < Re{m} < 9	0 < Imag{m} < 10	dialable up to 14

Before we go and discuss some comparisons of these codes, let's establish the underlying source of inaccuracies and operational restrictions for Mie codes and then the design of these codes specifically.

As introduced in Section 3.6.1, the core Mie mathematical relationships are:

(1) Scattering Amplitudes

$$S_1(\theta) = \sum_{n=1}^{\infty} \frac{2n+1}{n(n+1)} \left[a_n \pi_n(\cos\theta) + b_n \tau_n(\cos\theta) \right] \tag{286}$$

$$S_2(\theta) = \sum_{n=1}^{\infty} \frac{2n+1}{n(n+1)} \left[b_n \pi_n(\cos\theta) + a_n \tau_n(\cos\theta) \right] \tag{287}$$

where a_n and b_n are known as the Mie coefficients and π_n and τ_n are Legrendre associated polynomials.

(2) Extinction Efficiency Factor

$$Q_{ext} = \frac{2}{x^2} \sum_{n=1}^{\infty} (2n+1) \mathrm{Re}\{a_n + b_n\} \tag{288}$$

where x is the particle size parameter.

(3) Scattering Efficiency Factor

$$Q_{sca} = \frac{2}{x^2} \sum_{n=1}^{\infty} (2n+1) \left(|a_n|^2 + |b_n|^2 \right) \tag{289}$$

(4) Scattering Phase Function

$$p(\theta) = \frac{2\left(|S_1^2| + |S_2^2| \right)}{k^2 a^2 Q_{sca}} \tag{290}$$

(5) Asymmetry Factor

$$g_{sca} = \frac{4}{x^2 Q_{sca}} \sum_{n=1}^{\infty} \left[\frac{n(n+2)}{n+1} \mathrm{Re}\left\{ a_n a_{n+1}^* + b_n b_{n+1}^* \right\} + \frac{2n+1}{n(n+1)} \mathrm{Re}\left\{ a_n b_n^* \right\} \right] \tag{291}$$

The primary challenge of Mie codes is to structure the computation such that the desired accuracy is maintained, numerical instability and ill-conditioned calculations are avoided, and maximum efficiency is achieved. The accuracy is primarily determined by how the codes handle four potential pitfalls. First, the upward calculation for A_n is very unstable if the imaginary component of the indices of refraction is large enough. Fortunately, the downward recurrence is always stable, but is fairly computationally intense. Most Mie codes, such as MIEV0 and BHMIE, utilize a criterion established a priori based upon the value of x and m to determine when to use the downward recurrence relationship for A_n. Others, such as MIEDU, rely on a ratio (r_n in Du's case) that has a stable upward recurrence formula. The criterion-based approach is typically based upon the desired accuracy for the overall algorithm. For instance, MIEV0's criteria was set such that the relative error for the Mie quantities did not exceed 10^{-6}. According to Wiscombe, this was done by a thorough study for values of x ranging from 1 to 10,000. For the downward recurrence calculation, one needs to decide where to start the iterations. MIEV0 uses a convergence criteria of 10^{-8} to determine the starting point.

The second potential pitfall can be in the calculation of the spherical Bessel functions. These functions are also numerically unstable for the upward recurrence; however, the downward recurrence is very stable. Generally, Mie codes restrict the errors for the spherical Bessel functions to be no larger than 0.002% of the actual value.

The third potential pitfall is the determination of the cutoff for the infinite series calculations required. Older Mie codes stopped the summations for the Mie series at the first value of n for which:

$$|a_n|^2 + |b_n|^2 < 10^{-14} \tag{292}$$

This criterion corresponds to 6 significant digits for the output results. To speed things up, MIEV0 and BHMIE utilize an a priori estimate of the required number of terms in the Mie series. This empirical estimate is based upon runs that were made in the early 1980s for a wide range of parameters ($0.1 \le x \le 20{,}000$ and indices of refraction $1.05 \le Real\{m\} \le 2.5$, $0 \le Imag\{m\} \le 1$). The older criterion was used after replacing the 10^{-14} with $5\text{x}10^{-14}$. Based upon these runs, a new criterion was established. MIEV0 sets the number of terms as:

$$N_{\max} = \begin{cases} x + 4x^{1/3} + 1 & 0.02 \le x \le 8 \\ x + 4.05x^{1/3} + 2 & 8 < x < 4200 \\ x + 4x^{1/3} + 2 & 4200 \le x \le 20{,}000 \end{cases} \tag{293}$$

BHMIE sets the number of terms as:

$$N_{\max} = x + 4x^{1/3} + 2 \tag{294}$$

regardless of the x parameter. As stated in Section 3.6.2, Du's algorithm uses the estimate of the number of significant digits lost based upon Kapteyn's inequality to decide how many terms to use in the series (and also when to use the upward or downward recurrences of the spherical Bessel functions).

The fourth potential pitfall is how one handles very small particles ($x \to 0$). The issue is that the calculation for A_n is numerically ill-conditioned as the particle size parameter gets very small. Secondly, the subtraction in the numerator for b_n becomes ill-conditioned and thirdly, the subtraction for the upward recurrence of the spherical Bessel functions loses significant digits at every step. MIEV0 incorporates a different set of relationships for calculating very small particles ($x < 0.2$) and has been shown to retain 3-5 significant digits for very small particle size parameters. Bohren and Huffman have not made any such claim about the BHMIE code and test data for these small sizes was not available. Du claims the same accuracy as the MIEV0 code. Note that due to the introduction of the ratio, r_n, the issues associated with A_n are not present for the MIEDU code; however, the other constraints are still present.

Although no published data exists over most of the ranges for which the codes claim to be accurate, some general principles can be applied:

(1) Q_{ext} should go to 2 and Q_{sca} and g_{sca} should asymptote as $x \to \infty$

(2) The asymptotic approaches should be more rapid as $Imag\{m\}$ gets larger

(3) Increasing $Imag\{m\}$ should damp out the ripple structure

When examined, the trends for all three codes (MIEV0, BHMIE, and MIEDU) behave in accordance to these guidelines. Leveraging published test data for MIEV0, BHMIE and MIEDU can be compared for a set of stressing cases. The baseline test data for MIEV0 is supported by an extensive evaluation of its accuracy by Wiscombe (NCAR report, 1979). The results are shown in Table 24, Table 5, Table 6, and Table 27. Note that differences in results for the codes are highlighted in red for comparison sake. MIEDU is very consistent with MIEV0 and produces very accurate results in every test case. Table 5 and Table 6 show that MIEDU is very consistent with the BHMIE code for a wide range of situations with the exception of when the imaginary component of the index of refraction is very small (but not zero). The same results can be seen in the comparison between the MIEV0 and BHMIE calculations. This would appear to contradict the performance claims for the IDL implementation of BHMIE. In general, we retain about 5 or 6 significant digits of accuracy for MIEDU or MIEV0.

Table 24: Comparison of MIEDU and MIEV0 results

			IDL version of Du's Algorithm				Wiscombe's MIEV0 (FORTRAN)			
Re{m}	Imag{m}	x	Qext	Qsca	Qabs	gsca	Qext	Qsca	Qabs	gsca
0.75		0.099	7.41786E-06	7.41786E-06	0.00000E+00	0.001448	7.41786E-06	7.41786E-06	0.00000E+00	0.001448
0.75		0.101	8.03354E-06	8.03354E-06	0.00000E+00	0.001507	8.03354E-06	8.03354E-06	0.00000E+00	0.001507
0.75		10	2.23226E+00	2.23226E+00	0.00000E+00	0.896473	2.23227E+00	2.23227E+00	0.00000E+00	0.896473
0.75		1000	1.99791E+00	1.99791E+00	0.00000E+00	0.845093	1.99791E+00	1.99791E+00	0.00000E+00	0.844944
1.33	-1.0E-05	1	9.39520E-02	9.39233E-02	2.86810E-05	0.184517	9.39520E-02	9.39230E-02	2.90000E-05	0.184517
1.33	-1.0E-05	100	2.10132E+00	2.09659E+00	4.72690E-03	0.868961	2.10132E+00	2.09659E+00	4.72700E-03	0.868959
1.33	-1.0E-05	10000	2.00409E+00	1.72386E+00	2.80232E-01	0.907784	2.00409E+00	1.72386E+00	2.80232E-01	0.907840
1.50	-1.0E+00	0.055	1.01491E-01	1.13169E-05	1.01480E-01	0.000491	1.01491E-01	1.10000E-05	1.01480E-01	0.000491
1.50	-1.0E+00	0.056	1.03347E-01	1.21631E-05	1.03335E-01	0.000509	1.03347E-01	1.20000E-05	1.03335E-01	0.000509
1.50	-1.0E+00	1	2.33632E+00	6.63454E-01	1.67287E+00	0.192136	2.33632E+00	6.63454E-01	1.67287E+00	0.192136
1.50	-1.0E+00	100	2.09750E+00	1.28370E+00	8.13805E-01	0.850252	2.09750E+00	1.28370E+00	8.13805E-01	0.850252
1.50	-1.0E+00	10000	2.00437E+00	1.23657E+00	7.67793E-01	0.846272	2.00437E+00	1.23657E+00	7.67793E-01	0.846310
10.00	-1.0E+01	1	2.53299E+00	2.04941E+00	4.83588E-01	-0.110664	2.53299E+00	2.04941E+00	4.83588E-01	-0.110664
10.00	-1.0E+01	100	2.07112E+00	1.83679E+00	2.34339E-01	0.556215	2.07112E+00	1.83679E+00	2.34339E-01	0.556215
10.00	-1.0E+01	10000	2.00591E+00	1.79539E+00	2.10521E-01	0.548191	2.00591E+00	1.79539E+00	2.10521E-01	0.548194

Table 25: Comparison of MIEDU and BHMIE results

			Wiscombe's MIEV0 (FORTRAN)				IDL version of Bohren/Huffman Algorithm			
Re{m}	Imag{m}	x	Qext	Qsca	Qabs	gsca	Qext	Qsca	Qabs	gsca
0.75		0.099	7.41786E-06	7.41786E-06	0.00000E+00	0.001448	7.41786E-06	7.41786E-06	0.00000E+00	0.001448
0.75		0.101	8.03354E-06	8.03354E-06	0.00000E+00	0.001507	8.03354E-06	8.03354E-06	0.00000E+00	0.001507
0.75		10	2.23227E+00	2.23227E+00	0.00000E+00	0.896473	2.23226E+00	2.23226E+00	0.00000E+00	0.896473
0.75		1000	1.99791E+00	1.99791E+00	0.00000E+00	0.844944	1.99791E+00	1.99791E+00	0.00000E+00	0.844944
1.33	-1.0E-05	1	9.39520E-02	9.39230E-02	2.90000E-05	0.184517	2.02490E+00	2.02490E+00	0.00000E+00	0.184517
1.33	-1.0E-05	100	2.10132E+00	2.09659E+00	4.72700E-03	0.868959	2.15784E+00	2.15335E+00	4.49140E-03	0.859799
1.33	-1.0E-05	10000	2.00409E+00	1.72386E+00	2.80232E-01	0.907840	2.00436E+00	1.93166E+00	7.26961E-02	0.887362
1.50	-1.0E+00	0.055	1.01491E-01	1.10000E-05	1.01480E-01	0.000491	1.01491E-01	1.13169E-05	1.01480E-01	0.000491
1.50	-1.0E+00	0.056	1.03347E-01	1.20000E-05	1.03335E-01	0.000509	1.03347E-01	1.21631E-05	1.03335E-01	0.000509
1.50	-1.0E+00	1	2.33632E+00	6.63454E-01	1.67287E+00	0.192136	2.33632E+00	6.63454E-01	1.67287E+00	0.192136
1.50	-1.0E+00	100	2.09750E+00	1.28370E+00	8.13805E-01	0.850252	2.09750E+00	1.28370E+00	8.13805E-01	0.850252
1.50	-1.0E+00	10000	2.00437E+00	1.23657E+00	7.67793E-01	0.846310	2.00437E+00	1.23657E+00	7.67793E-01	0.846310
10.00	-1.0E+01	1	2.53299E+00	2.04941E+00	4.83588E-01	-0.110664	2.53299E+00	2.04941E+00	4.83588E-01	-0.110664
10.00	-1.0E+01	100	2.07112E+00	1.83679E+00	2.34339E-01	0.556215	2.07116E+00	1.83683E+00	2.34327E-01	0.556209
10.00	-1.0E+01	10000	2.00591E+00	1.79539E+00	2.10521E-01	0.548194	2.00591E+00	1.79539E+00	2.10521E-01	0.548194

Table 26: Comparison of MIEV0 and BHMIE results

			IDL version of Du's Algorithm				IDL version of Bohren/Huffman Algorithm			
Re{m}	Imag{m}	x	Qext	Qsca	Qabs	gsca	Qext	Qsca	Qabs	gsca
0.75		0.099	7.41786E-06	7.41786E-06	0.00000E+00	0.001448	7.41786E-06	7.41786E-06	0.00000E+00	0.001448
0.75		0.101	8.03354E-06	8.03354E-06	0.00000E+00	0.001507	8.03354E-06	8.03354E-06	0.00000E+00	0.001507
0.75		10	2.23226E+00	2.23226E+00	0.00000E+00	0.896473	2.23226E+00	2.23226E+00	0.00000E+00	0.896473
0.75		1000	1.99791E+00	1.99791E+00	0.00000E+00	0.845093	1.99791E+00	1.99791E+00	0.00000E+00	0.844944
1.33	-1.0E-05	1	9.39520E-02	9.39233E-02	2.86810E-05	0.184517	2.02490E+00	2.02490E+00	0.00000E+00	0.184517
1.33	-1.0E-05	100	2.10132E+00	2.09659E+00	4.72690E-03	0.868961	2.15784E+00	2.15335E+00	4.49140E-03	0.859799
1.33	-1.0E-05	10000	2.00409E+00	1.72386E+00	2.80232E-01	0.907784	2.02447E+00	2.01513E+00	9.33560E-03	0.883624
1.50	-1.0E+00	0.055	1.01491E-01	1.13169E-05	1.01480E-01	0.000491	1.01491E-01	1.13169E-05	1.01480E-01	0.000491
1.50	-1.0E+00	0.056	1.03347E-01	1.21631E-05	1.03335E-01	0.000509	1.03347E-01	1.21631E-05	1.03335E-01	0.000509
1.50	-1.0E+00	1	2.33632E+00	6.63454E-01	1.67287E+00	0.192136	2.33632E+00	6.63454E-01	1.67287E+00	0.192136
1.50	-1.0E+00	100	2.09750E+00	1.28370E+00	8.13805E-01	0.850252	2.09750E+00	1.28370E+00	8.13805E-01	0.850252
1.50	-1.0E+00	10000	2.00437E+00	1.23657E+00	7.67793E-01	0.846272	2.00437E+00	1.23657E+00	7.67793E-01	0.846310
10.00	-1.0E+01	1	2.53299E+00	2.04941E+00	4.83588E-01	-0.110664	2.53299E+00	2.04941E+00	4.83588E-01	-0.110664
10.00	-1.0E+01	100	2.07112E+00	1.83679E+00	2.34339E-01	0.556215	2.07116E+00	1.83683E+00	2.34327E-01	0.556209
10.00	-1.0E+01	10000	2.00591E+00	1.79539E+00	2.10521E-01	0.548191	2.00591E+00	1.79539E+00	2.10521E-01	0.548194

As mentioned previously in this subsection, small particles present special challenges for Mie codes. Figure 131 is a polar plot of the normalized amplitude functions for a very small particle with an index of refraction of 1.77 and a particle size parameter of ~0.05. This example is well within the region where the Rayleigh approximation is valid. As one might expect, the behavior for the unpolarized, perpendicular, and parallel amplitude functions as predicted by MIEDU are consistent with scattering behavior in the Rayleigh scattering regime.

While Figure 131 represents a qualitative assessment, Table 27 is a very special set of stressing cases designed to test the calculations for very small particles. Wiscombe conducted a detailed study (NCAR report, 1979) of the actual results in the process of developing his own algorithm. The results for all three codes is in the table. Notice that all of them work very well, even for very small x. Any lost digits result in minor errors. The strong correlation between the two IDL implementations may be due to some shared IDL computational artifact or process. For instance, the *tan*( ) function and the *exp*( ) in IDL do have some limitations

when evaluating very small or very large inputs. This could potentially be a source of the errors. Note that the errors are very minor.

Overall, all of the Mie codes evaluated have demonstrated a very high degree of accuracy for the calculating the scattering and absorption properties of a spherical particle over a very wide range of input parameters. The advantages of Du's algorithm are that it is simple, accurate, and robust for a wide range of operational inputs. The precision and accuracy is also truly deterministic and could be increased if necessary or reduced for improved computational efficiency.

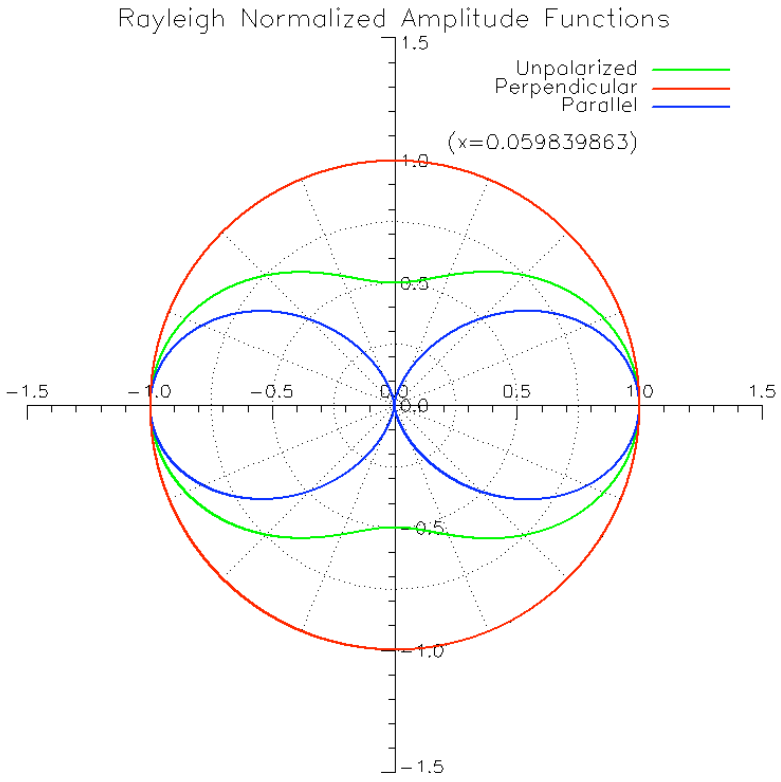


Figure 131: Normalized Rayleigh scattering amplitude functions

Table 27: Comparison of values of Q_{ext} in the small particle limit

x	Re{m}	Imag{m}	abs(m)*x	Exact	MIEV0	MIEDU	BHMIE
0.02	1.50	-1.E-06	0.030	7.67805E -08	7.67805E -08	7.6780 4E-08	7.6780 4E-08
	1.95	-1.E-06	0.039	1.27355E -07	1.27355E -07	1.27355E -07	1.27355E -07
	1.95	-1.E-05	0.039	3.77355E -07	3.77355E -07	3.77 659E-07	3.77 659E-07
0.04	1.05	-1.E-06	0.042	1.12179E -07	1.12179E -07	1.12179E -07	1.12179E -07
	1.50	-1.E-06	0.060	6.70403E -07	6.70403E -07	6.70403E -07	6.70403E -07
	1.50	-1.E-04	0.060	8.57008E -06	8.57008E -06	8.5700 7E-06	8.5700 7E-06
	1.90	-1.E-04	0.076	7.16259E -06	7.16259E -06	7.16259E -06	7.16259E -06
0.08	1.05	-1.E-06	0.084	3.28478E -07	3.28478E -07	3.28478E -07	3.28478E -07
	1.50	-1.E-06	0.120	9.61292E -06	9.6129 1E-06	9.61292E -06	9.61292E -06
	1.50	-1.E-04	0.120	2.54547E -05	2.54547E -05	2.54547E -05	2.54547E -05
	1.95	-1.E-04	0.156	3.67336E -05	3.6733 5E-05	3.67336E -05	3.67336E -05
0.2	1.05	-1.E-02	0.210	5.25263E -05	5.252 56E-05	5.25263E -03	5.25263E -03
	1.05	-1.E+00	0.290	5.78539E -01	5.785 32E-01	5.78539E -01	5.78539E -01
	1.95	-1.E-02	0.390	3.90548E -03	3.905 26E-03	3.90548E -03	3.90548E -03
	1.95	-1.E+00	0.438	2.58637E -01	2.586 26E-01	2.58637E -01	2.58637E -01

A.2 Computational Performance

One of the common concerns with Mie Codes is computational run-time. Mie codes have a reputation for being very time consuming, particularly when one is calculating over 100s of wavelengths for 100s of different particle sizes. Due to the improvements in processor speed, memory, and vectorized coding possibilities, computational time is not as significant factor as previously. Table 28 is a sample timing comparison of the IDL implementations of Du's algorithm and the BHMIE code. The driving factor for the run-time of Mie codes is the particle size parameter. Note that the nominal run-time for plume and atmospheric constituents is about 0.1-0.2 sec for each radius using Du's algorithm. In general, the BHMIE code takes about twice as long as Du's. For a run for a nominal gamma particle size distribution containing 1200 different radii, my implementation of Du's algorithm took about 2.1 sec. Du notes in his paper that the MIEV0 code is a little bit faster due to its vector optimization. The BHMIE code could definitely be optimized better for the IDL operating environment and one could further optimize the IDL implementation of Du's algorithm. Currently, the code is optimized for calculation of numerous angles. In hindsight, the code could have been optimized for calculating over a large number of particle sizes and/or wavelengths. However, the times listed are very acceptable for most research efforts. Generating the optical properties of the plume constituents is intended to be on off-line activity that feeds the DIRSIG configuration file. Additionally, if a database of optical

parameters for standard gases were built, then the Mie codes would not need to be run directly.

Table 28: Timing comparison for IDL Mie and IDL BHMIE implementations
(m = 10-10i, 65 angles)

x	IDL Mie (sec)	IDL BHMIE (sec)
0.1	0.016	0.026
1	0.018	0.028
10	0.023	0.037
100	0.049	0.106
1000	0.296	0.559
10000	2.018	4.177

References

[1] Argall, P.S., and R.J. Sica (2002). "LIDAR," *Encyclopedia of Atmospheric Sciences*, Academic Press, London, pp. 869-889.

[2] Barcomb, K. (2004). *High-resolution, slant-angle scene generation and validation of concealed targets in DIRSIG.* M.S. Thesis, Rochester Institute of Technology, NY.

[3] Bennet, M. (1998). "The effect of plume intermittency upon differential absorption lidar measurements". *Atmospheric Environment*, vol 32, pp. 2423-2427.

[4] Berk, A., G.P. Anderson, L.S. Bernstein, P.K. Acharya, H. Dothe, M.W. Matthew, S.m. Adler-Golden, J.H. Chetwynd Jr, S.C. Richtsmeier, B. Pukall, C.L. Allred, L.S. Jeong, and M.L. Hoke (2000). "MODTRAN4 Radiative Transfer Modeling for Atmospheric Correction". MODTRAN documentation, Air Force Research Laboratory, Hanscom AFB.

[5] Bishop, Jonathan. (2001). *Modeling of Plume Dispersion for Synthetic Imaging Applications.* PhD dissertation, Rochester Institute of Technology, NY.

[6] Bissonnette, L.R. (1996). "Multiple-scatter lidar equation," *Applied Optics* (35), pp. 6449-6465.

[7] Bissonnette, L.R. and G. Roy (1998). "Multiple scattering in lidar remote sensing: nuisance and benefit," *SPIE Proceedings of EUROPTO Conference on Atmospheric Propagation, Adaptive Systems, and Laser Radar Techniques for Remote Sensing II*, Barcelona, Spain, v3494, pp. 305-313.

[8] Blackadar, A. K. (1997). *Turbulence and Diffusion in the Atmosphere*. Springer-Verlag, New York.

[9] Bohren, C. F. and D. R. Huffman (1998). *Absorption and Scattering of Light by Small Particles*. John Wiley & Sons, Inc., New York.

[10] Burton, R. (2002). *Elastic LADAR Modeling for Synthetic Applications*. PhD dissertation, Rochester Institute of Technology.

[11] Cammarano, M. and H.W. Jensen (2002). "Time Dependent Photon Mapping". *The Eurographics Association*, California.

[12] Chang, H. and T. T. Charalampopoulos (1990). "Determination of the Wavelength Dependence of Refractive Indices of Flame Soot". *Proceedings of the Royal Society of London Series a-Mathematical and Physical Sciences*, London.

[13] Chandrasekhar, S. (1950). *Radiative Transfer*, Oxford University Press, Oxford.

[14] Cohn, D.B., E.J. Griffin, L.F. Klaras, M.E. Ehritz, C.R. Swim, J.A. Fox (2001). "WILDCAT chemical sensor development," *Proceedings of SPIE Conference on Chemical and Biological Sensing II*, v 4378, pp. 34-42.

[15] Cohn, D.B., J.M. Fukumoto, J.A. Fox, C.R. Swim (2001). "Compact DIAL sensor: SHREWD," *Proceedings of SPIE Conference on Chemical and Biological Sensing II*, v 4378, pp. 43-49.

[16] Dave, J.V., (1969). "Scattering of electromagnetic radiation by a large absorbing sphere". IBM J. Res. Dev. 13, pp. 302-313.

[17] Debevec, P. and S. Gibson (2002). "Time Dependent Photon Mapping". *Thirteenth Eurographics Workshop on Rendering*, pp 135-142,326.

[18] Debevec, P. and S. Gibson (2002). "Time Dependent Photon Mapping". *Thirteenth Eurographics Workshop on Rendering*, pp 135-142,326, WHERE, WHEN.

[19] Dobashi, Y., K. Kaneda, T. Okita, and T. Nishita (2000). "A Simple, Efficient Method for Realistic Animation of Clouds". *Proceedings of SIGGRAPH 2000 Conference*, pp. 19–28, July 2000.

[20] Du, H. (2004). "Mie-scattering calculation". Applied Optics, 43, pp. 1951-1956.

[21] Elorante, E.W. (1991). "Practical Model for the calculation of multiple scattering lidar returns*". Journal of the Optical Society of America*, vol. 3, no. 12, pp. 2464-247.

[22] Elorante, Edwin W. (1972). *Calculation of Doubly Scattering lidar returns.* PhD dissertation, University of Wisconsin, WI.

[23] Fedkiw, R. and J. Stam (2001). "Visual Simulation of Smoke," *Proceedings of SIGGRAPH 2001 Conference*, pp. 15-22.

[24] Foster, N. and D. Metaxas (1996). "Realistic Animation of Liquids," *Graphical Models and Image Processing*, 58(5), pp.471-483.

[25] Foster, N. and D. Metaxas (1997). "Modeling the motion ofa hot, turbulent gas," *Proceedings of SIGGRAPH 1997*, pp. 181-188.

[26] Heino, J., S. Aridge, J. Sikora, and E. Somersalo (2003). "Anisotropic effects in highly scattering media," Physical Review, v68, The American Physical Society, pp. 031908-1 – 031908-8.

[27] Holtkämper, T. (2003). "Real-Time Gaseous Phenomena: A Phenomenological Approach to Interactive Smoke and Steam," *Proceedings of the 2nd international Conference on Computer Graphics, Virtual Reality, Visualization, and Interaction in Africa*, Cape Town, South Africa, pp. 25-30.

[28] van de Hulst, H.C. (1957). *Light Scattering by Small Particles*, John Wiley & Sons, Inc., New York.

[29] van de Hulst, H.C. (1957). *Light Scattering by Small Particles*, John Wiley & Sons, Inc., New York.

[30] Ishimaru, A. (1978). Wave Propagation and Scattering in Random Media. Academic Press, New York.

[31] Jensen, H.W. and P.H. Christensen (1998). "Efficient Simulation of Light Transport in Scenes with Participating Media using Photon Maps". *Proceedings of SIGGRAPH 1998 Conference*, pp. 311-320, WHERE, Jul 1998.

[32] Jensen, H.W. (2001). *Realistic Image Synthesis Using Photon Mapping*, A K Peters Natick, MA.

[33] Jensen, H.W. (1996). *The photon map in global illumination.* PhD dissertation, Technical University of Denmark.

[34] Kajiya, J.T. and B.P. von Herzen (1984). "Ray Tracing Volume Densities", *Proceedings of SIGGRAPH 1984 Conference*, 18(3), pp. 165-174, July 1984.

[35] Kokhanovsky, A. A. (1998). "Variability of the Phase Function of Atmospheric Aerosols at Large Scattering Angles," *Journal of Atmospheric Sciences*, vol. 55, pp. 314-321.

[36] Kokhanovsky, A. A. (2001). *Optics of Light Scattering Media*. Springer-Verlag, Chichester, UK.

[37] Kokhanovsky, A. A. (2002). "Simple approximate formula for the reflection function of a homogeneous, semi-infinite turbid medium," *Journal of the Optical Society of America*, vol. 19, no. 5, pp. 957-961.

[38] Kokhanovsky, A. A. (2002). "Statistical properties of a photon gas in random media," *Physical Review*, 66, pp. 037601-1 – 037601-4.

[39] Kokhanovsky, A. A. (2003). "Analytical solutions of multiple light scattering problems: a review," *Measurement Science Technology*, 13, pp. 233-240.

[40] Kokhanovsky, A. A. and B. Mayer (2003). "Light reflection and transmission by non-absorbing turbid slabs: simple approximations," *Journal of Optics A: Pure and Applied Optics*, 5, pp. 43-46.

[41] Kokhanovsky, A. A. and R. Weichert (2001). "Multiple light scattering in laser particle sizing," *Applied Optics*, vol. 9, no. 5, pp. 1507-1514.

[42] Kokhanovsky, A. A., R. Weichert, M. Heuer, and W. Witt (2001). "Angular spectrum of light transmitted through turbid media: theory and experiment," *Applied Optics*, vol. 40, no. 16, pp. 2595-2600.

[43] Kokhanovsky, A. A. and E.P. Zege (1998). "On Remote Sensing of Water Clouds from Space," *Advanced Space Remote Sensing*, vol. 21, no. 3, pp. 425-428.

[44] Kokhanovsky, A. A. and E.P. Zege (1998). "Optical Properties of Aerosol Particles: A Review of Approximate Analytical Solutions," *Journal of Aerosol Sciences*, vol. 28, no. 1, pp. 1-21.

[45] Kuo, Didi S. (1997). *Synthetic Image Generation of Factory Stack and Water Cooling Tower Plumes.* PhD Thesis, Rocheseter Institute of Technology, New York.

[46] Liou, K. and R.M. Schotland (1971). "Multiple Backscattering and Depolarization from Water Clouds fro a Pulsed Laser," Journal of Atmospheric Science, vol. 28, p. 772.

[47] Max, N. (1994). "Efficient Light Propagation for Multiple Anisotropic Volume Scattering". *Proc. of the Fifth Eurographics Workshop on Rendering*, pp. 87-104.

[48] Measures, R. M. (1984). *Laser Remote Sensing: Fundamentals and Applications*. John Wiley & Sons, Inc., New York.

[49] Measures, R.M. (1988). *Laser Remote Chemical Analysis*, John Wiley & Sons, New York.

[50] Messinger, D.W. and J.R. Schott (2004). "Minimum Detectable Target Concentrations of Gaseous Plumes: A Comparison of Active and Passive Systems," submitted to *Journal of the Intelligence Community Research and Development*.

[51] OnyxTREE Software, information available online at http://www.onyxtree.com

[52] Peterson, E.D. (2004). *Synthetic Landmine Scene Development and Validation.* Masters Thesis, Rocheseter Institute of Technology, NY.

[53] de Rooij, W.A. and C.C.A.H van der Stap (1984). "Expansion of Mie scattering matrices in generalized spherical functions," *Astronomy Astrophysics*, vol. 131, pp. 237-248.

[54] Rozanov, V.V. and A.A. Kokhanovsky (2005). "The average number of photon scattering events in vertically inhomogeneous atmospheres". PhD dissertation, University of Bremen, Germany.

[55] Scharlemann, E.T. (2003). "Chemical detection sensitivities of active and passive remote sensing systems". *Proceedings of SPIE: Lidar Remote Sensing for Environmental Monitoring IV*, vol 5154, August 2003, San Diego, CA, pp. 126-137.

[56] Schmitt, M., B. McVey, B. Cooke, and G. Busch (1996). "Comprehensive system model for CO_2 DIAL". *Proceedings of SPIE : Gas and Chemical Lasers*, vol 2702, pp. 95-103.

[57] Schott, J. R. (1997). *Remote Sensing: The Image Chain Approach*. Oxford University Press, New York.

[58] Schotland, R. M. (1966). "Some observations of the vertical profile of water vapor by a laser optical radar". Proceedings of the 4th Symposium on Remote Sensing of the Environment. University of Michigan Press, Ann Arbor, MI, pp. 273.

[59] Siegel, R. and J. Howell (1992). *Thermal Radiation Heat Transfer*, Hemisphere Publishing Corp, Washington, DC.

[60] Sobolev, V.V. (1963). *A Treatise on Radiative Transfer.* D. Van Nostrand Company, Inc., New York.

[61] Stamnes K. and H. Dale (1981). "A new look at the discrete ordinate method for radiative transfer calculation in anisotropically scattering atmospheres. II: Intensity computations". *Journal of Atmospheric Sciences,* vol. 38, 2696-2706.

[62] Szirmay-Kalos, L. (2003). "Monte-Carlo global illumination methods, state of the art and new developments". Technical University of Budapest, Budapest, Hungary.

[63] Szirnay-Kalos, L. (1998). *Stochastic Methods of Global Illumination State of the Art Report.* Technical University of Budapest, Hungary.

[64] Stam, J. (1999). "Stable Fluids". *Proceedings of SIGGRAPH 1999 Conference*, pp. 121-128, Aug 1999.

[65] U.S. Congress, Office of Technology Assessment (1993). *Technologies Underlying Weapons of Mass Destruction,* OTA-BP-ISC-115. Government Printing Office, Washington, DC.

[66] Watson, G.N. (1966). *Treatis on Theory of Bessel Functions*, Cambridge Univ Press, London.

[67] Williams, M.D., M.J. Brown, B. Singh, and D. Boswell (2004). "QUIC-PLUME Theory Guide". Memorandum LA-UR-04-0561 dated Jan 26, 2004. Los Alamos National Laboratory, Los Alamos, NM.

[68] Williams, M.D., M.J. Brown, B. Singh, and D. Boswell (2004). "Testing of the QUIC-PLUME model with wind-tunnel measurements fro a highrise building". *13th Conference on the Applications of Air Pollution Meterology with the Air and Waste Management Association*, 5th Conference on the Urban Environment. Los Alamos National Laboratory, Los Alamos, NM.

[69] Wiscombe, W.J. (1980). "Improved Mie Scattering Algorithms". *Applied Optics*, 19, pp. 1505-1509.

[70] Zanzottera, E. (1990). "Differential absorption Lidar techniques in the determination of trace pollutants and physical parameters of the atmosphere". *Critical reviews in analytical chemistry*, vol 21, CRC Press, Boca Raton, FL, pp. 279-319.

[71] Zege, E.P., A.P. Ivanov, and I.L. Katsev (1991). *Image Transfer through a Scattering Medium.* Springer-Verlag, New York. 2